

**WA School of Mines: Minerals, Energy and Chemical Engineering**

**Photochemical and Thermal Energy Transformation for Hydrogen  
Generation**

**Xiaojie Li**

**This thesis is presented for the Degree of  
Doctor of Philosophy  
of  
Curtin University**

**July 2020**

## **Declaration**

To the best of my knowledge and belief, this thesis contains no material previously published by any other person except where due acknowledgment has been made. This thesis contains no material which has been accepted for the award of any other degree or diploma in any university.

Signature: \_\_\_\_\_ (Xiaojie Li)

Date: \_\_\_\_\_

## **Acknowledgment**

At first, I would like to express my sincere gratitude to my Principal Supervisor, Prof. Shaobin Wang. With an excellent vision, a wealth of knowledge, and academic enthusiasm, Prof. Wang has guided me towards the frontier of the academic field. His academic rigour and meticulousness have deeply influenced me. From him, I have learned how to systematically acquire knowledge in a certain domain, how to complete a project with high quality, and how to study an issue in depth. He is definitely my academic model, and I will follow his footsteps for the rest of my academic career.

Equally, I owe my great thanks to my Co-Supervisor, Prof. Hongqi Sun. Prof. Sun is a gentle, erudite, and versatile scholar. He always provides practical advice for my experiments and articles. From him, I have learned how to think about an issue from different viewpoints and how to design an experiment with more details to be considered so that high-quality work can be realized.

I would like to thank Prof. Shaomin Liu, who always helps me both in my experiments and my life.

I would also like to thank Dr Xiaoguang Duan and Dr Huayang Zhang. Dr Duan has a profound theoretical foundation. He helped me detailedly

explain experimental results. Dr Zhang owns ample experimental experience. He gave me a great deal of significant advice for my work.

I am also grateful to Prof. Peiqiang Li, Dr Liang Zhao, Dr Wenjie Tian, Dr Xiaochen Guo, Dr Jian Kang, Dr Yazhi Liu, Dr Chen Wang, Dr Heng Ye, and my other colleagues, Ms Li Zhou, Mr Zhengxin Yao, Mr Jiaquan Li, Mr Jinqiang Zhang, Mr Hong Wu, Mr Xinyuan Xu, Mr Kai Wang, Mr Changya Deng, Mr Shiyong Zhao, Mr Kunsheng Hu, Mr Yangyang Yang, and Ms Panpan Zhang. They gave me lots of help in my academic study and life.

I appreciate lab technicians, Roshanak, Jimmy, Jason, Andrew, Ann, and Araya and thank them for providing technical supports for my experiments.

Lastly, I owe my great gratefulness to my parents, my elder brother and sister-in-law, and my nephew, Kunyi Li. Without their supports, I cannot cross the ocean to Australia to pursue my PhD degree. Thank you pretty much!

## Abstract

Low emission, environmental protection, and renewable energy are three major themes of the 21st century. Photocatalytic hydrogen evolution (PC-HER), exploiting solar energy to obtain hydrogen from water, fully contributes to these subjects. As a result, many efforts have been devoted to this area. One of the most significant developments is the application of graphitic carbon nitride ( $g\text{-C}_3\text{N}_4$ ) in PC-HER owing to the easy preparation, proper bandgap, nontoxicity, and physicochemical stability of  $g\text{-C}_3\text{N}_4$ . In this PhD study, the PC-HER and influences of solar-heat on PC-HER were investigated with different nanomaterials as photocatalysts. Meanwhile, novel  $g\text{-C}_3\text{N}_4$  based nanomaterials, including NiO quantum dots decorated  $g\text{-C}_3\text{N}_4$ , single-atom Ag modified  $g\text{-C}_3\text{N}_4$ , and K doped  $g\text{-C}_3\text{N}_4/g\text{-C}_3\text{N}_4$  nanosheets van der Waals type II junctions, were developed and applied in PC-HER processes. Various characterization techniques combined with density functional theory calculations were utilized to explore the structures and properties of these composites. The loading amounts, substance ratios, and reaction temperatures were optimized to maximize PC-HER efficiency. The electrochemical tests and photoluminescence experiments were taken to probe the inner mechanisms of the enhanced PC-HER performance of these materials. Our research not only helps broaden the sources of photocatalysts for PC-HER but also assists to better understand the PC-HER process from varying aspects.

## Publications by the Author

### Published and Accepted:

1. **Xiaojie Li**, Huayang Zhang, Yazhi Liu, Xiaoguang Duan, Xinyuan Xu, Shaomin Liu, Hongqi Sun, Shaobin Wang. Synergy of NiO quantum dots and temperature on enhanced photocatalytic and thermophoto hydrogen evolution. *Chemical Engineering Journal*, 2020, 390, 124634.
2. Jingui Zheng<sup>†</sup>, **Xiaojie Li**<sup>†</sup>, Yuhu Qin, Shuqin Zhang, Mingsheng Sun, Xiaoguang Duan, Hongqi Sun, Peiqiang Li, Shaobin Wang. Zn phthalocyanine/carbon nitride heterojunction for visible light photoelectrocatalytic conversion of CO<sub>2</sub> to methanol. *Journal of Catalysis*, 2019, 371, 214.
3. Wei Chen<sup>†</sup>, **Xiaojie Li**<sup>†</sup>, Fei Wang, Shaghrif Javaid, Shaobin Wang, Yunguo Li, Guohua Jia. Non-Epitaxial Gold-Tipped ZnSe Hybrid Nanorods for Efficient Photocatalytic Hydrogen Production. *Small*, 2020, 16, 1902231.
4. Shishu Zhu, **Xiaojie Li**, Jian Kang, Xiaoguang Duan, Shaobin Wang. Persulfate Activation on Crystallographic Manganese Oxides: Mechanism of Singlet Oxygen Evolution for Nonradical Selective Degradation of Aqueous Contaminants. *Environmental Science Technology*, 2019, 53, 307.
5. Liang Zhao, Muhammad R. Azhar, **Xiaojie Li**, Xiaoguang Duan, Hongqi Sun, Shaobin Wang, Xiangchen Wang. Adsorption of cerium

- (III) by HKUST-1 metal-organic framework from aqueous solution. *Journal of Colloid and Interface Science*, 2019, 542, 421.
6. Yazhi Liu, Xinyuan Xu, Jinqiang Zhang, Huayang Zhang, Wenjie Tian, **Xiaojie Li**, Moses O. Tade, Hongqi Sun, Shaobin Wang. Flower-like MoS<sub>2</sub> on graphitic carbon nitride for enhanced photocatalytic and electrochemical hydrogen evolutions. *Applied Catalysis B: Environmental*, 2018, 239, 334.
  7. Shaghrif Javaid, **Xiaojie Li**, Fei Wang, Wei Chen, Yingping Pang, Shaobin Wang, Guohua Jia, Franca Jones. Controlled and facile approach for the synthesis of magnetically separable Fe<sub>3</sub>O<sub>4</sub>-Au-CdS heterotrimers incorporating plasmonic and semiconductor functionalities. *Journal of Materials Chemistry C*, 2019, 7, 14517.
  8. Yazhi Liu, Jinqiang Zhang, **Xiaojie Li**, Zhengxin Yao, Li Zhou, Hongqi Sun, Shaobin Wang. Graphitic Carbon Nitride Decorated with CoP Nanocrystals for Enhanced Photocatalytic and Photoelectrochemical H<sub>2</sub> evolution. *Energy & Fuels*, 2019, 33, 11663.
  9. Peng Zhou, Wei Ren, Gang Nie, **Xiaojie Li**, Xiaoguang Duan, Yongli Zhang, Shaobin Wang. Fast and Long-Lasting Iron(III) Reduction by Boron Toward Green and Accelerated Fenton Chemistry. *Angewandte Chemie International Edition*, 2020, DOI: 10.1002/anie.202007046 and 10.1002/ange.202007046.

## Contents

<b>Declaration</b> .....	<b>I</b>
<b>Acknowledgment</b> .....	<b>II</b>
<b>Abstract</b> .....	<b>IV</b>
<b>Publications by the Author</b> .....	<b>V</b>
<b>Contents</b> .....	<b>VII</b>
<b>Chapter 1 Introduction</b> .....	<b>1</b>
1.1 Background.....	1
1.2 Research objectives.....	4
1.3 Thesis organization.....	5
References.....	7
<b>Chapter 2 Literature Review</b> .....	<b>12</b>
2.1 Introduction.....	12
2.2 Basic concepts.....	13
2.3 Fundamentals of PC-HER.....	16
2.4 Fundamentals of g-C <sub>3</sub> N <sub>4</sub> .....	17
2.4.1 Structure and morphology.....	17
2.4.2 Physicochemical properties.....	18
2.4.3 Preparation of g-C <sub>3</sub> N <sub>4</sub> .....	24
2.5 Sacrificial agents for g-C <sub>3</sub> N <sub>4</sub> in PC-HER.....	26
2.6 Cocatalysts for g-C <sub>3</sub> N <sub>4</sub> in PC-HER.....	32

2.6.1 Metal cocatalysts.....	34
2.6.2 Single-atom cocatalysts .....	36
2.6.3 Transition metal based cocatalyst .....	39
2.6.4 Metal-free cocatalysts .....	52
2.6.5 Metal organic framework (MOF) cocatalysts.....	55
2.7 Different nanostructures of g-C <sub>3</sub> N <sub>4</sub> for PC-HER.....	56
2.7.1 Different morphologies of g-C <sub>3</sub> N <sub>4</sub> for PC-HER .....	56
2.7.2 Porous g-C <sub>3</sub> N <sub>4</sub> for PC-HER .....	60
2.7.3 Crystalline g-C <sub>3</sub> N <sub>4</sub> for PC-HER.....	63
2.7.4 Doped g-C <sub>3</sub> N <sub>4</sub> for PC-HER.....	64
2.8 g-C <sub>3</sub> N <sub>4</sub> based heterostructure for PC-HER.....	67
2.8.1 Schottky junction .....	67
2.8.2 Type II junction .....	68
2.8.3 Z-scheme junction.....	70
2.8.4 PN junction .....	72
2.8.5 Van der Waals junction.....	74
2.8.6 Summary of heterojunctions .....	74
2.9 Other factors for g-C <sub>3</sub> N <sub>4</sub> based PC-HER.....	75
2.9.1 Quantity of photocatalysts .....	75
2.9.2 Light sources .....	76
2.10 Conclusions and perspectives .....	76
References .....	79

<b>Chapter 3 Solar-heat temperature effect on photocatalytic hydrogen evolution.....</b>	<b>108</b>
Abstract .....	108
3.1 Introduction.....	109
3.2 Experimental .....	112
3.3 Results and discussions.....	115
3.4 Conclusions.....	128
References .....	129
<b>Chapter 4 Synergy of NiO quantum dots and temperature on enhanced photocatalytic and thermophoto hydrogen evolution .....</b>	<b>139</b>
Abstract .....	139
4.1 Introduction.....	140
4.2. Experimental .....	142
4.3 Results and Discussion.....	147
4 Conclusions .....	171
References .....	172
<b>Chapter 5 Solar-heat-assisted single-atom catalysis for photocatalytic hydrogen evolution .....</b>	<b>182</b>
Abstract .....	182
5.1 Introduction.....	183
5.2 Methods.....	186

5.3 Results and Discussion.....	192
4 Conclusion.....	222
References .....	222
<b>Chapter 6 g-C<sub>3</sub>N<sub>4</sub> self-based van der Waals type II junctions for photocatalytic hydrogen evolution .....</b>	<b>236</b>
Abstract .....	236
6.1 Introduction.....	237
6.2 Experimental .....	239
6.3 Results and discussions.....	244
6.4 Conclusion.....	264
References .....	265
<b>Chapter 7 Conclusions and perspectives .....</b>	<b>275</b>
7.1 Conclusions.....	275
7.2 Perspectives.....	280
<b>APPENDIX I: ATTRIBUTION TABLES.....</b>	<b>283</b>
<b>APPENDIX II: COPYRIGHT PERMISSION STATEMENTS .....</b>	<b>287</b>

## **Chapter 1 Introduction**

### **1.1 Background**

For the sustainable development of human society, tremendous issues facing us should be resolved. Currently, energy crisis[1–4] and environmental pollutions[5–8] together threaten human's long-term wellbeings. Therefore, strategies must be taken to overcome those problems. As it is known, the entire earth belongs to the solar system. In essence, the Sun provides us with all kinds of energy, because all other forms of energies are transformed from solar energy.[9,10] From this point of view, how to effectively and cleanly utilize solar power is one of the most significant challenges for human progress. Traditionally, natural photosynthesis combines  $\text{CO}_2$  and  $\text{H}_2\text{O}$  towards organics under solar irradiation.[11,12] Ancient forests, after complex natural processes, became coal, petroleum, and natural gas, which have been exploited as energy sources presently.[13,14] However, these fossil fuels take millions of years to form, making them be labelled unrenewable energy resources.

After Fujishima and Honda found the phenomenon of photocatalytic water splitting with a titania photoelectrode in 1972,[15] a brand new way to develop solar energy was opened and has shown great prospects. In this process, as shown in Figure 1.1, the photoelectrode is an n-type  $\text{TiO}_2$

semiconductor while a platinum plate as the counter electrode. When UV light ( $< 415 \text{ nm}$ ) illuminates the photoelectrode, electrons jump from the valence band (VB) towards the conduction band (CB). Then, the so-called photo-excited electrons transfer to the Pt counter electrode via an external circuit and react with water to produce hydrogen on the surface of the Pt plate. On the other hand, water near the  $\text{TiO}_2$  photoelectrode is oxidized to be oxygen by the photo-excited holes.

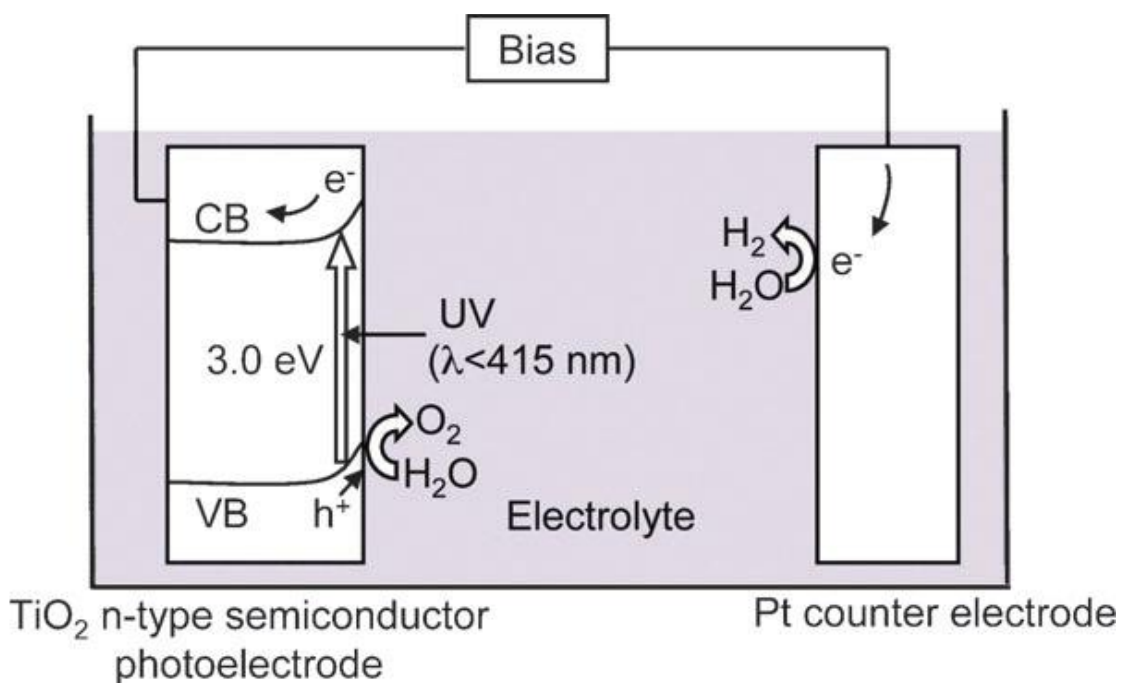


**Figure 1.1** Schematic illustration of photocatalytic water splitting with  $\text{TiO}_2$  photoelectrode via Honda-Fujishima effect.[16]

In this process, hydrogen as one of the cleanest fuels is generated by photocatalysis, one of the most environmentally friendly methods, which is prominent to effectively resolve the issues of the energy crisis and environmental pollution.

Ever since then, massive efforts were devoted to the field of photocatalytic hydrogen evolution reaction (PC-HER) via water splitting and abundant semiconductors were applied in this area. Among them, Wang et al. for the first time reported a polymeric semiconductor, graphitic carbon nitride ( $g\text{-C}_3\text{N}_4$ ), as a visible-light-driven photocatalyst for PC-HER in 2009.[17] Thereafter,  $g\text{-C}_3\text{N}_4$  became a superstar in photocatalysis because of its easy fabrication, nontoxicity, proper band structure, and physicochemical stability.

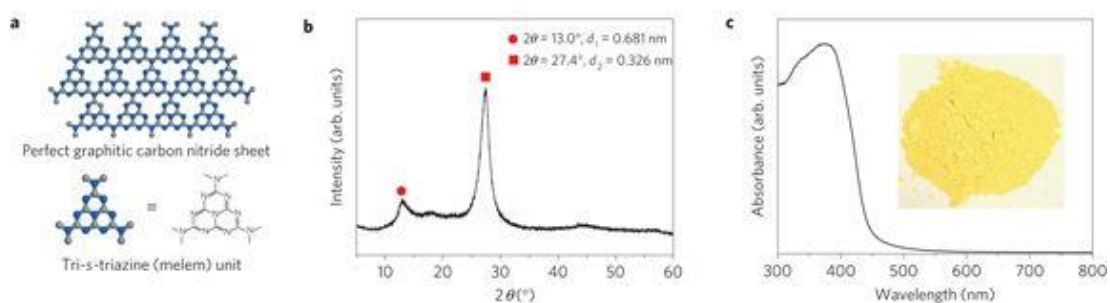


**Figure 1.2** **a**, Illustrative structure of  $g\text{-C}_3\text{N}_4$  with melem as units; **b**, XRD patterns of  $g\text{-C}_3\text{N}_4$ ; **c**, UV-vis diffuse reflectance spectral of  $g\text{-C}_3\text{N}_4$ . [17]

As displayed in Figure 1.2a, the perfect  $g\text{-C}_3\text{N}_4$  sheet is constructed with tri-s-triazine (melem) as units. At 27.4 degree on XRD patterns (Figure 1.2b), the sharp peak originates from the (002) crystal plane for 0.336 nm interlayer spacing of  $g\text{-C}_3\text{N}_4$ , and the UV-vis spectrum in Figure 1.2c shows that the absorption edge is about 540 nm and the bandgap can be calculated as 2.7 eV. For the enhancement of photocatalytic water splitting

for g-C<sub>3</sub>N<sub>4</sub>, the following aspects should be highly considered: 1) cocatalysts[18–21] are almost indispensable for hydrogen evolution to inhibit the recombination of photo-excited charge pairs; 2) heteroatom doping[22–24] can improve the photocatalytic performance via increasing light absorption range, tuning band structure and advancing electrical conductivity; 3) heterojunctions between g-C<sub>3</sub>N<sub>4</sub> and other photocatalysts[25–27] can also help the improvement in light absorption, electrical conductivity and inhibition of photo-excited electron-hole pairs; and 4) reduced thickness[28–30] via thermolysis or other exfoliation methods mainly enlarges surface area, providing more active sites for photocatalysis.

What is more, infrared light accounts for 43% of the solar spectrum. It cannot excite most semiconductors to generate photoelectrons but can raise the reaction-solution temperature.[31,32] It is of vital industrial significance to have insights into the solar-heat influences on PC-HER processes.

## **1.2 Research objectives**

The main intention is to fabricate novel g-C<sub>3</sub>N<sub>4</sub> based materials, for example, heteroatom doped g-C<sub>3</sub>N<sub>4</sub> and g-C<sub>3</sub>N<sub>4</sub> based heterojunctions, and utilize them in photocatalytic and solar-heat-assisted photocatalytic hydrogen evolution. Specific objectives are listed below.

1. Synthesizing NiO quantum dots decorated g-C<sub>3</sub>N<sub>4</sub>, single-atom Ag modified g-C<sub>3</sub>N<sub>4</sub>, and g-C<sub>3</sub>N<sub>4</sub> self-based Van der Waals junctions;
2. Investigating the morphology, structure, and properties in light absorption, electrical conductivity and photoluminescence of the as-prepared materials.
3. Employing those materials for photocatalytic and solar-heat-assisted photocatalytic water splitting, and testing their hydrogen evolution performance and the temperature effect on their performance.
4. Using density functional theory (DFT) calculations to explore the mechanisms of the photocatalytic or solar-heat-assisted photocatalytic behaviour of the novel materials and exemplifying their advantages compared with other existing materials.

### **1.3 Thesis organization**

This thesis is composed of seven chapters, including introduction, literature review, results and discussions (four chapters), conclusions and perspectives for future studies.

**Chapter 1 – Introduction** – displays the background of photocatalytic hydrogen evolution via water splitting. Objectives and thesis structure are also included in this chapter.

**Charter 2** – *Literature Review* – comprehensively summarizes the research advances of photocatalytic hydrogen evolution on g-C<sub>3</sub>N<sub>4</sub> based materials, from the perspectives of basic principles, main influence factors, material fabrication methods and relevant characterizations.

**Charter 3** – Solar-Heat-Temperature Effect on Photocatalytic Hydrogen Evolution via Water Splitting. The solar-heat-assisted temperature effect in PC-HER was thoroughly discussed from different aspects, such as photoabsorption, electrical impedance and thermal agglomeration.

**Charter 4** – Synergy of NiO Quantum Dots and Temperature on Enhanced Photocatalytic and Thermophoto Hydrogen Evolution. The chemical structure changes and the origins of enhanced photocatalytic and thermophoto performance are discussed.

**Charter 5** – Solar-Heat-Assisted Single-Atom Catalysis for Photocatalytic Hydrogen Evolution. The structure of single-atom Ag modified g-C<sub>3</sub>N<sub>4</sub> is demonstrated theoretically and experimentally. A new mechanism is proposed for its PC-HER application, and the special advantages of the single-atom system in solar-heat-assisted photocatalysis is emphasized.

**Charter 6** – g-C<sub>3</sub>N<sub>4</sub> Self-based Van der Waals Type II Junctions for Photocatalytic Hydrogen Evolution. The structure of g-C<sub>3</sub>N<sub>4</sub> self-based

Van der Waals type II junction is demonstrated theoretically and experimentally, and a new mechanism is proposed.

**Chapter 7 – *Conclusion and Perspectives*** – gives a summary of the results and provides perspectives for the future development of photocatalytic water splitting.

## References

- [1] A. Vilenkin, The vacuum energy crisis, *Science*. 312 (2006) 1148–1149.
- [2] J. Tollefson, Energy crisis upsets platinum market, *Nature*. 451 (2008) 877.
- [3] K.E. Boulding, The social system and the energy crisis, *Science*. 184 (1974) 255–257.
- [4] R. Dalton, Californian labs feel the heat of energy crisis, *Nature*. 411 (2001) 227.
- [5] X. Ren, C. Chen, M. Nagatsu, X. Wang, Carbon nanotubes as adsorbents in environmental pollution management: A review, *Chem. Eng. J.* 170 (2011) 395–410.
- [6] J.L. Martinez, Environmental pollution by antibiotics and by antibiotic resistance determinants, *Environ. Pollut.* 157 (2009) 2893–2902.
- [7] H. Resources, Potential Hire 's Expectations from Life & Corporate Author ( s ): Vijaya Mani and Vaishnavi A Source : Indian Journal of

Industrial Relations , Vol . 49 , No . 1 ( July 2013 ), pp . 148-156 Published by : Shri Ram Centre for Industrial Relations and Hum, 49 (2019) 148–156.

[8] Does Japan have acid rain ? (1986) 1986.

[9] D.G. Nocera, M.P. Nash, For the ““In This Issue”” summary, 104 (2007).

[10] M. Grätzel, Solar energy conversion by dye-sensitized photovoltaic cells, *Inorg. Chem.* 44 (2005) 6841–6851.

[11] W. Tezara, V.J. Mitchell, S.D. Driscoll, D.W. Lawlor, Water stress inhibits plant photosynthesis by decreasing coupling factor and ATP, *Nature.* 401 (1999) 914–917.

[12] E.H. Murchie, K.K. Niyogi, Manipulation of photoprotection to improve plant photosynthesis, *Plant Physiol.* 155 (2011) 86–92.

[13] J. Tomić, H.H. Schobert, Coal/petroleum residuum interactions during coprocessing under noncatalytic, low solvent/coal ratio conditions, *Energy and Fuels.* 11 (1997) 116–125.

[14] E.D. Sloan, Fundamental principles and applications of natural gas hydrates, *Nature.* 426 (2003) 353–359.

[15] A. Fujishima, K. Honda, Electrochemical Photolysis of Water at a Semiconductor Electrode, *Nature.* 238 (1972) 38–40.

[16] A. Kudo, Y. Miseki, Heterogeneous photocatalyst materials for water splitting, *Chem. Soc. Rev.* 38 (2009) 253–278.

[17] X. Wang, M. Kazuhiko, T. Arne, T. Kazuhiro, X. Gang, C.J. M., D. Kazunari, A. Markus, A metal-free polymeric photocatalyst for hydrogen

- production from water under visible light, *Nat. Mater.* 8 (2009) 76–80.
- [18] J. Ran, J. Qu, H. Zhang, T. Wen, H. Wang, S. Chen, L. Song, X. Zhang, L. Jing, R. Zheng, S.Z. Qiao, 2D Metal Organic Framework Nanosheet: A Universal Platform Promoting Highly Efficient Visible-Light-Induced Hydrogen Production, *Adv. Energy Mater.* 9 (2019) 1–8.
- [19] J. Ran, G. Gao, F.T. Li, T.Y. Ma, A. Du, S.Z. Qiao,  $\text{Ti}_3\text{C}_2$  MXene co-catalyst on metal sulfide photo-absorbers for enhanced visible-light photocatalytic hydrogen production, *Nat. Commun.* 8 (2017) 1–10.
- [20] J. Ran, W. Guo, H. Wang, B. Zhu, J. Yu, S.Z. Qiao, Metal-Free 2D/2D Phosphorene/g- $\text{C}_3\text{N}_4$  Van der Waals Heterojunction for Highly Enhanced Visible-Light Photocatalytic  $\text{H}_2$  Production, *Adv. Mater.* 30 (2018).
- [21] J. Ran, J. Zhang, J. Yu, M. Jaroniec, S.Z. Qiao, Earth-abundant cocatalysts for semiconductor-based photocatalytic water splitting, *Chem. Soc. Rev.* 43 (2014) 7787–7812.
- [22] Y. Zhang, T. Mori, J. Ye, M. Antonietti, P doped g- $\text{C}_3\text{N}_4$ (*J. AM. CHEM. SOC.* 2010, 132, 6294–6295).pdf, (2010) 6294–6295.
- [23] J. Ran, T.Y. Ma, G. Gao, X.W. Du, S.Z. Qiao, Porous P-doped graphitic carbon nitride nanosheets for synergistically enhanced visible-light photocatalytic  $\text{H}_2$  production, *Energy Environ. Sci.* 8 (2015) 3708–3717.
- [24] Y. Wang, H. Li, J. Yao, X. Wang, M. Antonietti, Synthesis of boron doped polymeric carbon nitride solids and their use as metal-free catalysts for aliphatic C-H bond oxidation, *Chem. Sci.* 2 (2011) 446–450.

- [25] W. Yu, J. Chen, T. Shang, L. Chen, L. Gu, T. Peng, Direct Z-scheme g-C<sub>3</sub>N<sub>4</sub>/WO<sub>3</sub> photocatalyst with atomically defined junction for H<sub>2</sub> production, *Appl. Catal. B Environ.* 219 (2017) 693–704.
- [26] A. Kumar, A. Kumar, G. Sharma, A.H. Al-Muhtaseb, M. Naushad, A.A. Ghfar, F.J. Stadler, Quaternary magnetic BiOCl/g-C<sub>3</sub>N<sub>4</sub>/Cu<sub>2</sub>O/Fe<sub>3</sub>O<sub>4</sub> nano-junction for visible light and solar powered degradation of sulfamethoxazole from aqueous environment, *Chem. Eng. J.* 334 (2018) 462–478.
- [27] L.K. Putri, B.J. Ng, W.J. Ong, H.W. Lee, W.S. Chang, S.P. Chai, Engineering nanoscale p-n junction: Via the synergetic dual-doping of p-type boron-doped graphene hybridized with n-type oxygen-doped carbon nitride for enhanced photocatalytic hydrogen evolution, *J. Mater. Chem. A.* 6 (2018) 3181–3194.
- [28] T.Y. Ma, S. Dai, M. Jaroniec, S.Z. Qiao, Graphitic carbon nitride nanosheet-carbon nanotube three-dimensional porous composites as high-performance oxygen evolution electrocatalysts, *Angew. Chemie - Int. Ed.* 53 (2014) 7281–7285.
- [29] L. Shi, T. Wang, H. Zhang, K. Chang, J. Ye, Electrostatic Self-Assembly of Nanosized Carbon Nitride Nanosheet onto a Zirconium Metal-Organic Framework for Enhanced Photocatalytic CO<sub>2</sub> Reduction, *Adv. Funct. Mater.* 25 (2015) 5360–5367.
- [30] B. Lin, H. An, X. Yan, T. Zhang, J. Wei, G. Yang, Fish-scale structured g-C<sub>3</sub>N<sub>4</sub> nanosheet with unusual spatial electron transfer property for high-efficiency photocatalytic hydrogen evolution, *Appl.*

Catal. B Environ. 210 (2017) 173–183.

[31] Y. Li, L. Zhong, B. Gautam, H.J. Bin, J.D. Lin, F.P. Wu, Z. Zhang, Z.Q. Jiang, Z.G. Zhang, K. Gundogdu, Y. Li, L.S. Liao, A near-infrared non-fullerene electron acceptor for high performance polymer solar cells, Energy Environ. Sci. 10 (2017) 1610–1620.

[32] L. Zhang, Y. Li, C. Li, Q. Chen, Z. Zhen, X. Jiang, M. Zhong, F. Zhang, H. Zhu, Scalable Low-Band-Gap  $\text{Sb}_2\text{Se}_3$  Thin-Film Photocathodes for Efficient Visible-Near-Infrared Solar Hydrogen Evolution, ACS Nano. 11 (2017) 12753–12763.

*Every reasonable effort has been made to acknowledge the owners of copyright material. I would be pleased to hear from any copyright owner who has been omitted or incorrectly acknowledged.*

## **Chapter 2 Literature Review**

### **2.1 Introduction**

Fujishima and Honda, for the first time, reported the phenomenon of photocatalytic (PC) water splitting in 1972, which created a sensation all over the world.[1] After that, massive efforts were devoted to the area of PC-based hydrogen evolution reaction (HER) because of its great significance to human society in the following directions.[2–4] First, hydrogen is one of the cleanest renewable energy resources, and the energy crisis can be eased to a large extent if industrial PC water splitting can be realized. What is more, no pollution is associated with both the generation and the application of hydrogen as an energy source, and water is the only product from hydrogen combustion.

In this process, photocatalysts, including homogeneous and heterogeneous components, play the core role in providing electrons and holes for redox reactions under light illuminations.[5–9] Heterogeneous catalysts, mainly as semiconductors, with the edge of reusability, attract much more attention in the past several decades.[10–13] Graphitic carbon nitride (g-CN) owns merits in cheapness, robustness, nontoxicity, non-metal nature and appropriate band structure, distinguishing itself from other semiconductors. It has aroused widespread interests after the first

study in photocatalytic water splitting in 2009.[14] To enhance the activity of g-CN, researchers developed diverse routes mainly by widening photo absorption range, tuning band structure, decreasing electric impedance, inhibiting the recombination of photo-motivated charges, enlarging surface areas, and advancing water absorption.[15–20] Those strategies contain nanostructure changing, cocatalyst, heterojunctions, and their combinations.[21–25]

Herein, the fundamentals and impact factors of PC-HER are reviewed, and all kinds of g-CN relevant materials are summarized in synthesis, properties, and mechanisms.

## **2.2 Basic concepts**

***Photocatalyst:*** A material that can be excited by photons with higher energy than the bandgap to produce electron and hole charges, which can participate in redox reactions.

***Bandgap:*** The distance between the valence band maximum and the conduction band bottom of a photocatalyst.

***Valence band:*** The energy band occupied by valence electrons.

**Conduction band:** The energy space formed by free electrons. That is the energy range of free-moving electrons in a solid structure.

**SHE:** The abbreviation of “Standard Hydrogen Electrode”. A platinum electrode composed of an ideal solution with a hydrogen ion activity of 1 mol/L (pH = 0) (current zero-potential standard).

**NHE:** The abbreviation of “Normal Hydrogen Electrode”. The electrode composed of a platinum electrode in 1 M strong acid solution (pH = 0) (historical standard, now **abandoned**).

**RHE:** Reversible Hydrogen Electrode (RHE) used in electrochemistry to indicate that the electrode potential is the standard "zero potential". The term comes from an article in JPCC.[26] In electrochemical papers, the reference electrode of the RHE calibration system is frequently used as a common unit for comparison.

$$E(\text{RHE}) = E(\text{SCE}) + 0.0591\text{pH} + 0.24 \quad \text{Eq. 2.1}$$

$$E(\text{RHE}) = E(\text{SHE}) + 0.0591\text{pH} \quad \text{Eq. 2.2}$$

$$E(\text{SHE}) = E(\text{Ag/AgCl}) + 0.197 \quad \text{Eq. 2.3}$$

**Cocatalyst:** A material combined with the main photocatalyst, which can

transfer photo-encouraged electrons or holes into reactants, such as a proton or a water molecule. Cocatalyst can help inhibit the recombination of photo-stimulated electric charges.

***Sacrificial agent:*** As half-reaction of water splitting, hydrogen evolution reaction (HER) only requires photoelectrons while photo-holes are applied for oxygen evolution reaction (OER). As a result, the holes in HER and electrons in OER should be deleted. Otherwise, they will recombine with the useful charges. Then, sacrificial agents are necessary to consume those charges.

**AQY:** The abbreviation of “Apparent Quantum Efficiency”.

$$\text{AQY (\%)} = \frac{2 \times 100 \times \text{number of generated H molecules}}{\text{number of incident photons}} \quad \text{Eq. 2.4}$$

***Gibbs free energy of the intermediate state ( $\Delta G_{H^*}$ ):*** For photocatalytic HER,  $H^+$  firstly combines with an active site to form  $H^*$ , and after acquiring a photoelectron, the obtained H atom is desorbed. The Gibbs free energy of the intermediate state  $H^*$  is the so-called  $\Delta G_{H^*}$  and the optimized value should be zero, at which the absorption of  $H^+$  and desorption of H atom could reach the best balance.

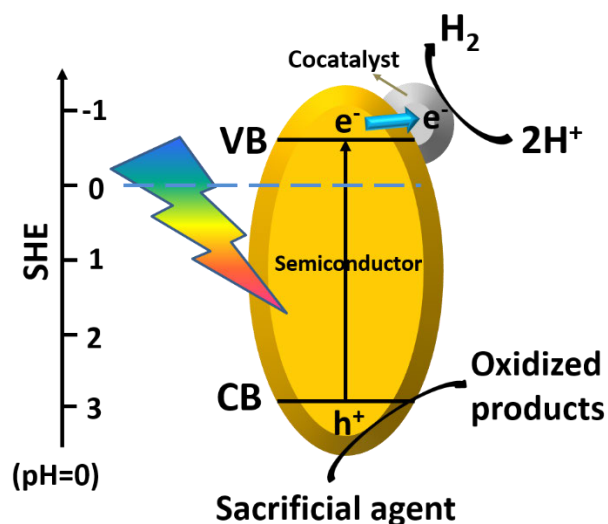


**Figure 2.1** The scheme of PC-HER.

### 2.3 Fundamentals of PC-HER

In the half-reaction of photocatalytic hydrogen evolution via water splitting (Figure 2.1), the photocatalyst, i.e. a semiconductor, absorbs photons with energy higher than its bandgap, and some electrons of the semiconductor can then be stimulated from the valence band (VB) towards the conduction band (CB).[27–30] Herein, the CB value of the semiconductor must be less than zero vs standard hydrogen electrode (SHE) at pH 0 so that the semiconductor has enough potential to reduce a proton. The photo-motivated electrons are then transferred from CB towards the cocatalyst, which can efficiently restrain the recombination of photoelectron-hole pairs. The protons ( $H^+$ ) in water are firstly attached on the surface of the cocatalyst and then reduced to a hydrogen atom by photoelectrons obtained by the cocatalyst. The left holes of the

semiconductor are usually consumed by sacrificial agents, which have a strong reducing capacity.[31–34] This process can also dramatically enhance PC-HER efficiency. That is the procedure of photocatalytic hydrogen evolution.

## **2.4 Fundamentals of g-C<sub>3</sub>N<sub>4</sub>**

The fundamentals, including the structure, preparation, and physicochemical characters of g-C<sub>3</sub>N<sub>4</sub>, are summarized in this part.

### **2.4.1 Structure and morphology**

g-C<sub>3</sub>N<sub>4</sub>, in the form of light-yellow powders, has a planar two-dimensional layered structure similar to graphene, with interlayer spacing about 0.326 nm. There are two types of basic units, triazine ring (C<sub>3</sub>N<sub>3</sub>, left) and 3-s-triazine ring (C<sub>6</sub>N<sub>7</sub>, right). Density functional theory (DFT) calculations by Kroke et al. proved that the g-C<sub>3</sub>N<sub>4</sub> with the 3-s-triazine ring is more stable than that connected by the triazine ring.[35] The basic structural units then extend indefinitely to form a network structure, and the two-dimensional nanosheets are combined by van der Waals forces. Film-like morphologies with wrinkles can be found on the SEM and TEM images. HRTEM image displays a lattice distance about 0.33 nm, corresponding to the (002) peak at about 27.5° in XRD pattern, denoting the interlayer piling of the conjugated double bonds for graphitic materials as mentioned

above, while (100) peak at  $13.0^\circ$  is stemming from the sequencing of tri-s-triazine units at 0.675 nm within a plane.[36–39]

#### 2.4.2 Physicochemical properties

In the TGA test, g-C<sub>3</sub>N<sub>4</sub> from urea can keep stable up to 500 °C, above which the decomposition begins and full decay occurs at ~ 650 °C.[40]

The specific surface area is 47 m<sup>2</sup>/g, with pore volume about 0.31 cc/g and pore diameter about 26 nm. Loose density could be 0.114 g/cm<sup>3</sup>.

The bandgap was reported to be ~ 2.7 eV, with CB of -1.27 V and VB of 1.39 V vs SHE, at pH = 7,[41] while the photoluminescence (PL) peak is emerging at 463 nm under incident light of 330 nm.[42]

XPS studies: 1) There are 2 peaks for C 1s. The one at 287.8 eV accords with sp<sup>2</sup> carbon jointed to the three nitrogen atoms (C–N–C) in the g-C<sub>3</sub>N<sub>4</sub> grid. The other at 284.6 eV is the result of the unavoidably loaded graphitic carbon atoms (C–C). 2) We can find 4 peaks for N 1s. The peak at 398.8 eV is from sp<sup>2</sup>-bonded N atoms in the graphite-like g-CN framework (C–N=C). The peak at 399.6 eV stands for ternary groups (N–(C)<sub>3</sub>). The peak at 401.0 eV originates from amino-functional groups (C–N–H). The peak at 404.5 eV is the result of the characteristic  $\pi$ -excitation (Figure 2.2).[5,43,44]

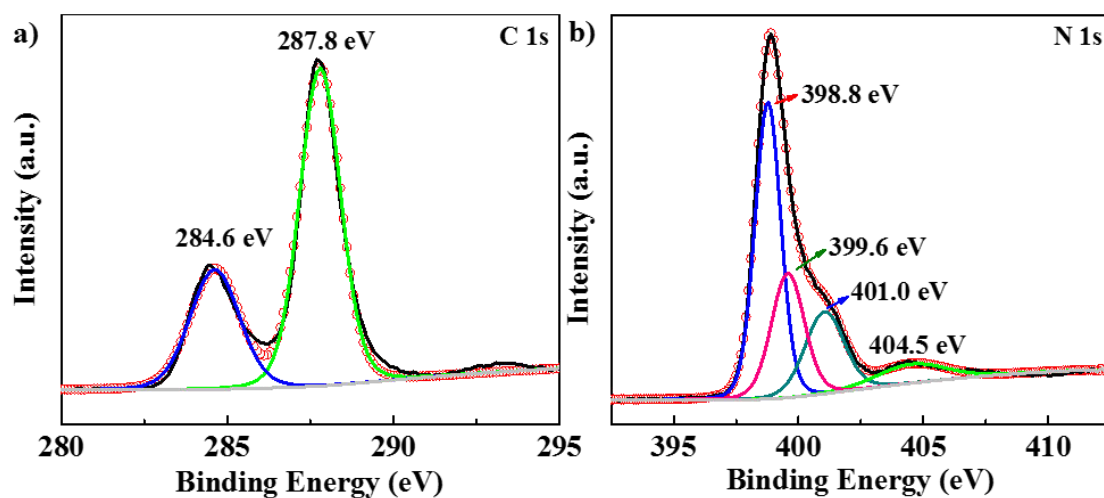


**Figure 2.2** The XPS results of g-C<sub>3</sub>N<sub>4</sub>. [45]

NEXAFS results: Taking g-C<sub>3</sub>N<sub>4</sub> from DCD as an example. 1) C K-edge has 2  $\pi^*$  resonances. 286.0 eV is attributed to  $\pi^*_{C=C}$  (C1) while 288.0 eV is the result of  $\pi^*_{C=N-C}$  (C2). 2) There are 4  $\pi^*$  resonances for N K-edge. 399.3 eV is the result of C–N=C in one tri-*s*-triazine heterocycle (N1). 400.5 eV is due to terminal C–N–H (N2). 401.3 eV comes from the N–3C (N3). 402.3 eV originates from  $sp^3$  N–3C connecting the three tri-*s*-triazine moieties (N4) (Figure 2.3). [37]

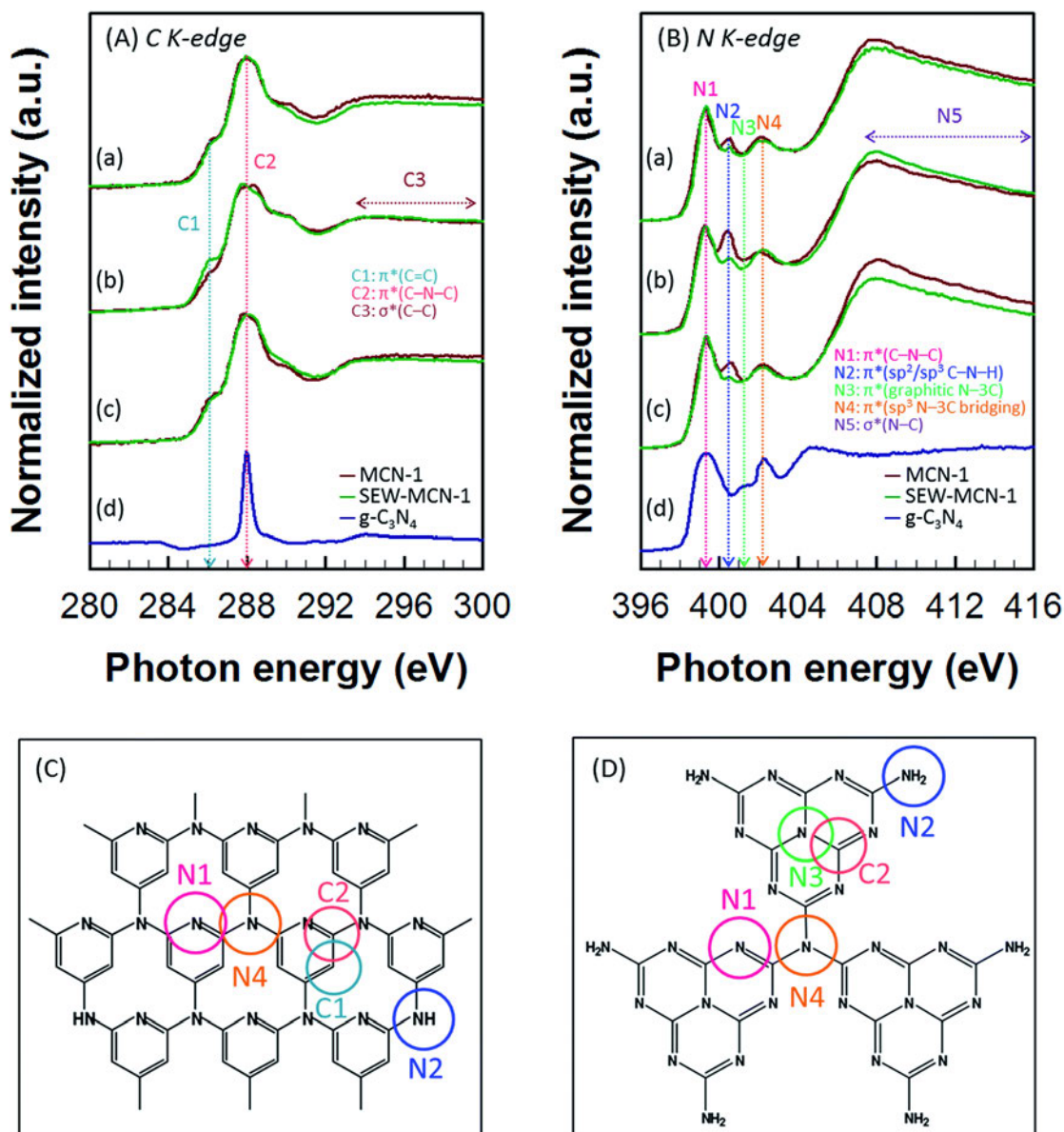


**Figure 2.3** NEXAFS results of g-C<sub>3</sub>N<sub>4</sub>. [37]

FT-IR spectra: 3300 to 3000  $\text{cm}^{-1}$  indicates terminal C–N–H, which is stretching vibration. 806  $\text{cm}^{-1}$  originates from the breathing mode of tri-*s*-triazine units. 889  $\text{cm}^{-1}$  is the result of the deformation mode of N–H. 1700–1200  $\text{cm}^{-1}$  comes from the stretching modes of CN heterocycles (Figure 2.4). [46]

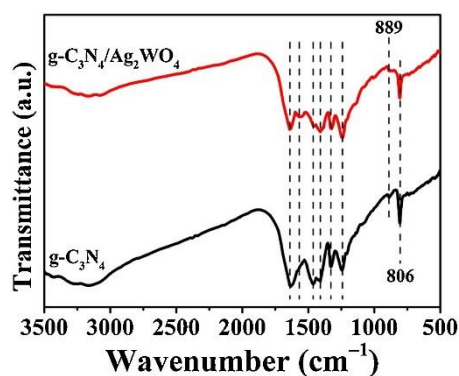


**Figure 2.4** FT-IR results of g-C<sub>3</sub>N<sub>4</sub>. [46]

Raman spectra: 472, 712, 980, and 1226 cm<sup>-1</sup> are the characteristic peaks of g-C<sub>3</sub>N<sub>4</sub>. 544, 751, and 1152 cm<sup>-1</sup> are the results of A<sub>1</sub>' oscillations of the tri-s-triazine loop. 980 cm<sup>-1</sup> indicates the breathing mode of the triazine loop (Figure 2.5). [47]

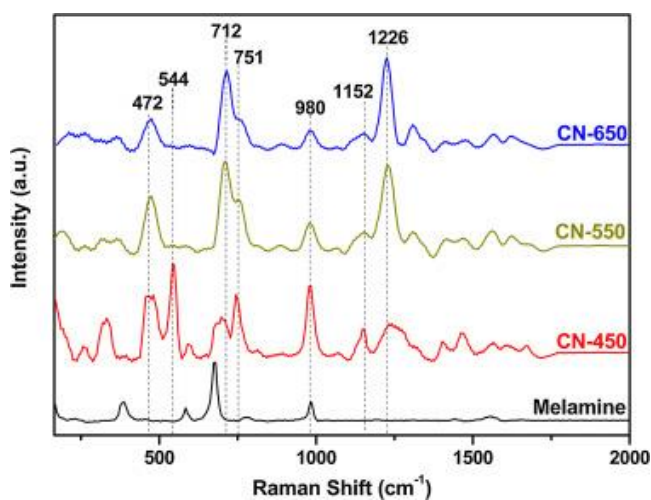


**Figure 2.5** Raman results of g-C<sub>3</sub>N<sub>4</sub>. [47]

EPR: There is one single Lorentzian line of g-C<sub>3</sub>N<sub>4</sub> originating from unpaired electrons in carbon atoms of the aromatic loops, and its *g* value is 2.0033. Larger specific surface area and more structure defects can be

signified by the enhanced intensity of the EPR signal (Figure 2.6).[48]  
 Whereas a weaker intensity can suggest less carbon amount, thus more carbon vacancies (Figure 2.7).[39]

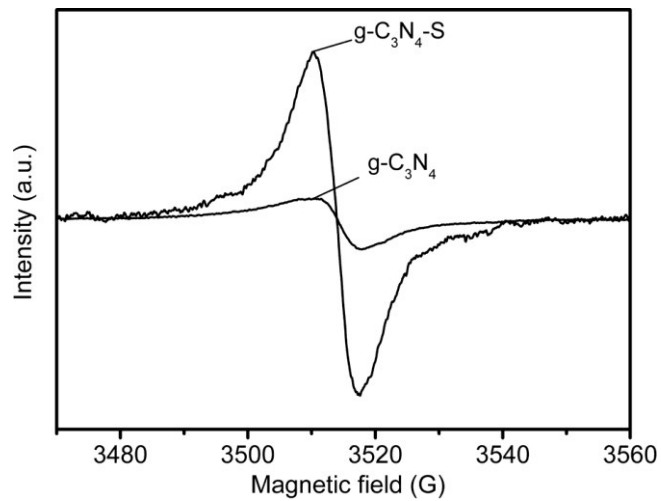


**Figure 2.6** EPR images of g-C<sub>3</sub>N<sub>4</sub> and g-C<sub>3</sub>N<sub>4</sub> nanosheets.[48]

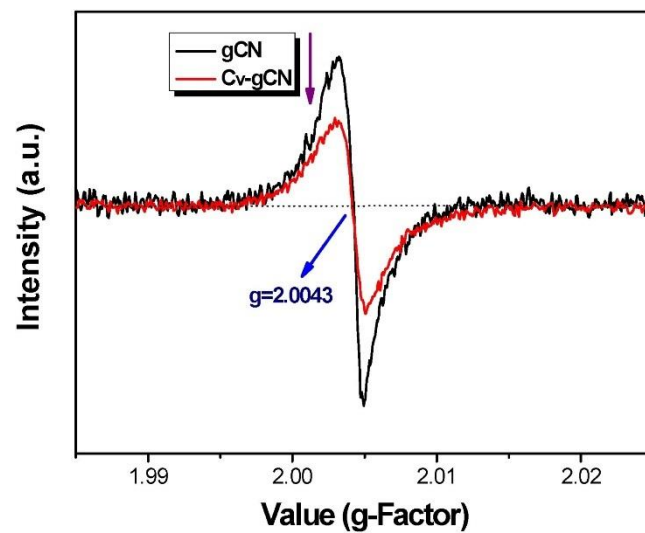


**Figure 2.7** EPR images of g-C<sub>3</sub>N<sub>4</sub> and carbon-vacancies-g-C<sub>3</sub>N<sub>4</sub>. [39]

HOMO-LUMO: DFT calculations displayed that the single layer g-C<sub>3</sub>N<sub>4</sub> is an indirect bandgap semiconductor, unlike bulk g-C<sub>3</sub>N<sub>4</sub>. Its bandgap

energy ( $E_g$ ) is 1.18 eV. The HOMO (corresponding to VB) is distributed on N2 atoms (Figure 2.8 and 2.9a), while the LUMO (according to CB) mainly consists of C1 and C2 atoms and moderately occupies N1 and N2 atoms (Figure 2.8 and 2.9b). It is worth noting that tri-coordinated bridge N (N3) atoms take part neither HOMO nor LUMO. As a result, the photo-excited electron-hole pairs are restricted in each heptazine unit, and their recombination is quite severe, leading to weak photocatalytic performance.[49]

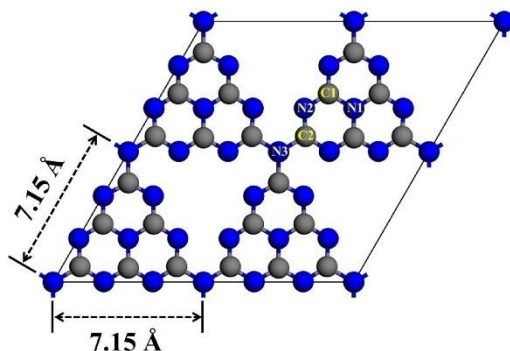


**Figure 2.8** The framework of  $g\text{-C}_3\text{N}_4$ . [49]

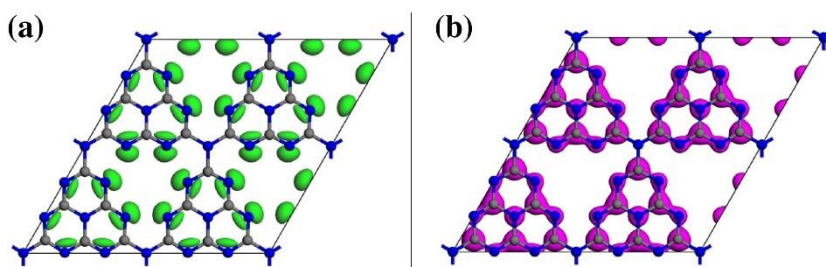


**Figure 2.9** HOMO (a) and LUMO (b) of  $g\text{-C}_3\text{N}_4$ . [49]

### 2.4.3 Preparation of g-C<sub>3</sub>N<sub>4</sub>

The most commonly used and facile strategy to fabricate g-C<sub>3</sub>N<sub>4</sub> is polymerization of N-rich materials, including urea, melamine, dicyandiamide, cyanamide, and thiourea, under 500-600 °C.[6,50–52] However, some weaknesses of this strategy, such as residual intermediates and low crystallinity, impede g-C<sub>3</sub>N<sub>4</sub> photocatalytic efficiency. Thus other synthesis methods were developed to overcome these weak points.[53]

#### 2.4.3.1 Supramolecular pre-assembly method

This method refers to pre-assembling precursors into supra-molecules via non-covalent connection, such as hydrogen bond, before polymerization. The advantage of this strategy lies in the intactness of the prepared g-C<sub>3</sub>N<sub>4</sub>. This is mainly because the structure of the supramolecular complex is much more similar to the target product of g-C<sub>3</sub>N<sub>4</sub> than ordinary precursors.[53] For example, Thomas's group firstly exploited this strategy and used melamine–cyanuric acid compounds as the so-called “supramolecular complex” to fabricate g-C<sub>3</sub>N<sub>4</sub>, which showed enhanced photocatalytic performance.[54] Then, Takahashi et al. used a liquid state reaction to acquire supramolecular complex from ethanol solution of melamine and 2,4,6-triaminopyrimidine,[55] which furtherly increased the crystallinity of g-C<sub>3</sub>N<sub>4</sub>. The PC-HER rate of the as-prepared g-C<sub>3</sub>N<sub>4</sub> could even achieve 8160 μmol h<sup>-1</sup> g<sup>-1</sup>, 14-fold of that of bulk g-C<sub>3</sub>N<sub>4</sub>.

#### 2.4.3.2 Microwave-assisted heating method

This method can obtain high-crystalline g-C<sub>3</sub>N<sub>4</sub> within only several minutes with the assistance of microwave.[53] Du et al. firstly developed this strategy, which helped boost the PC-HER rate 1.5 times higher than that of the material from the traditional polymerization route.[56]

#### 2.4.3.3 Template-assisted method

This strategy contains both hard and soft template routes to synthesize mesoporous g-C<sub>3</sub>N<sub>4</sub>, which can remarkably enlarge the specific surface area, expand pore volume, and thus facilitate photocatalysis.[53] Hard templates involve materials with high hardness, such as SiO<sub>2</sub> nanoparticles[57] and SBA-15.[58] Soft templates, like Pluronic P123[59] and gas bubbles, are more flexible and can shun impurities.[60]

#### 2.4.3.4 Molten salt method

This method refers to using a kind of molten salt as the solvent in the fabrication procedure of g-C<sub>3</sub>N<sub>4</sub>. In this way, the obtained g-C<sub>3</sub>N<sub>4</sub> can own better electrical conductivity, charge mobility, and firmness. Moreover, the strategy can also be regarded as one of the soft-template routes since the mesoporous structure can also be acquired through this approach.[53] One of the most often used molten salts is LiCl/KCl with a melting point (58.6 at% LiCl: 353 °C) much lower than that of each of them (LiCl: 605 °C,

KCl: 770 °C).[61]

#### 2.4.3.5 Ionic liquid method

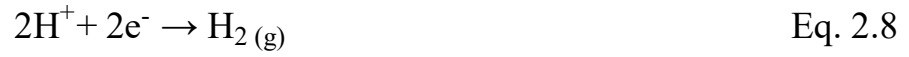
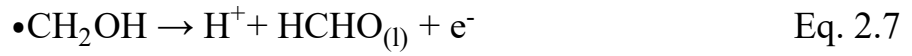
This strategy involves mixing soluble ionic compounds and the precursor of g-C<sub>3</sub>N<sub>4</sub> into water, which is then evaporated and calcined, to fabricate mesoporous or heteroatom doped g-C<sub>3</sub>N<sub>4</sub>. Herein, the ionic compound can also be viewed as a soft template to generate pores. Compared to molten salt route, this strategy does not require a high temperature in the mixing step.[53]

### 2.5 Sacrificial agents for g-C<sub>3</sub>N<sub>4</sub> in PC-HER

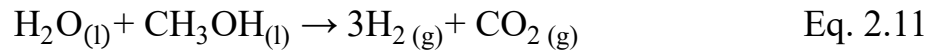
For the half-reaction of photocatalytic hydrogen evolution, sacrificial agents are almost indispensable to consume the photo-generated holes. Then, the left photoelectrons can reduce H<sup>+</sup> towards H<sub>2</sub>, without being recombined with the holes.

The most-commonly-used sacrificial agents for g-C<sub>3</sub>N<sub>4</sub> include methanol, lactic acid (LA), triethanolamine (TEOA), sodium sulfide (Na<sub>2</sub>S), sodium sulfite (Na<sub>2</sub>SO<sub>3</sub>) and the mixture of Na<sub>2</sub>S and Na<sub>2</sub>SO<sub>3</sub>. The processes for these scavengers are shown below.[62]

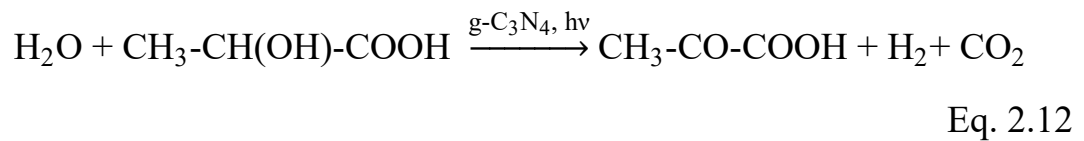
#### **Methanol (MeOH):**



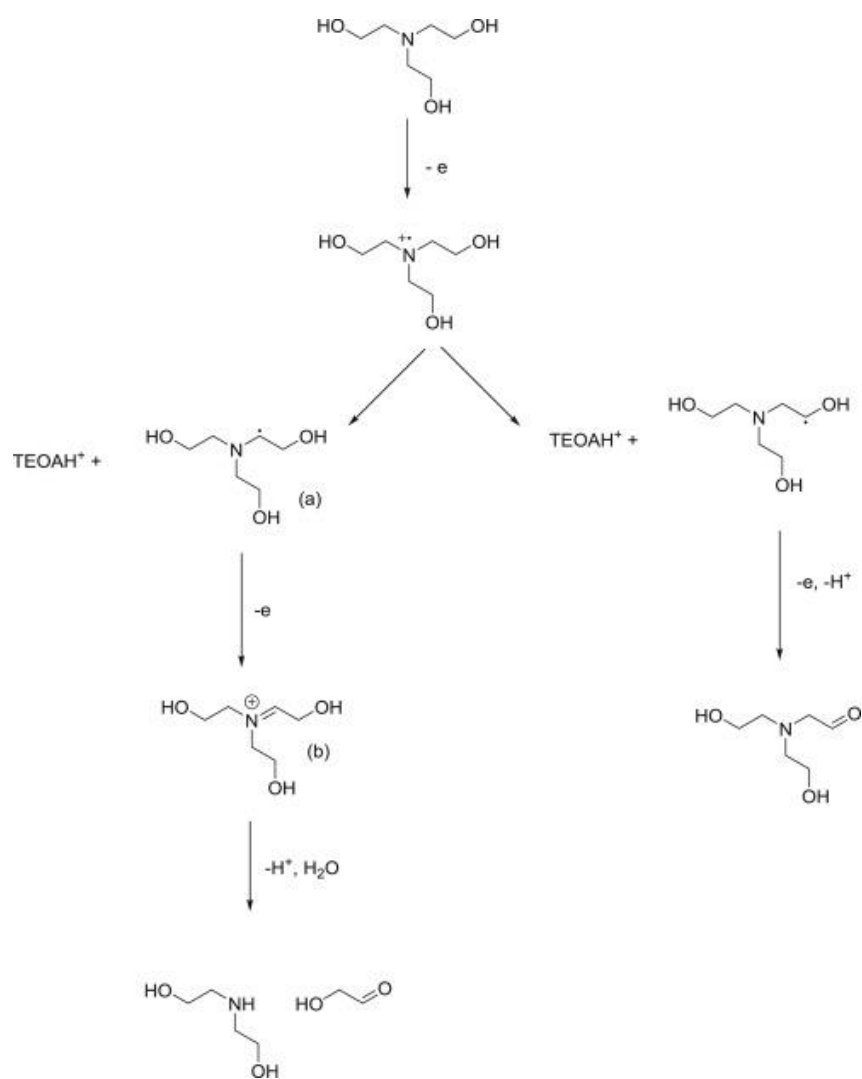
Overall reaction:



**Lactic acid (LA):**



**Triethanolamine (TEOA):**



Eq. 2.13[63]

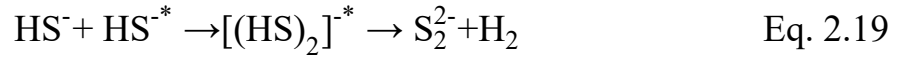
Overall reaction (Path A):



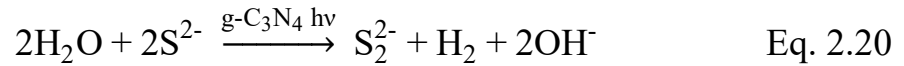
Overall reaction (Path B):



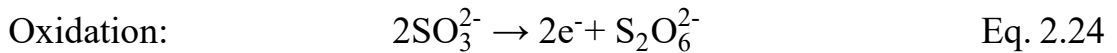
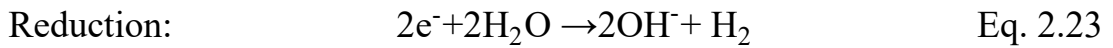
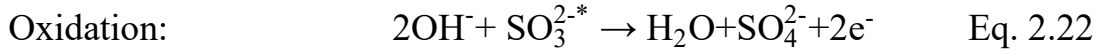
**Sodium sulfide (Na<sub>2</sub>S):**



Overall reaction:



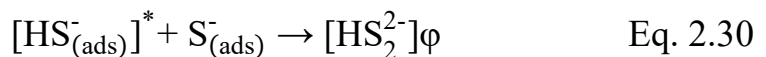
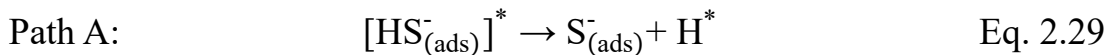
**Sodium sulfite ( $\text{Na}_2\text{SO}_3$ ):**



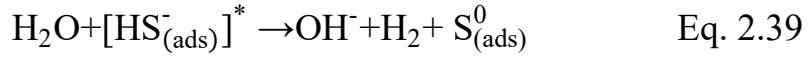
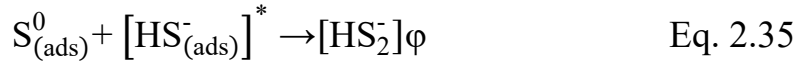
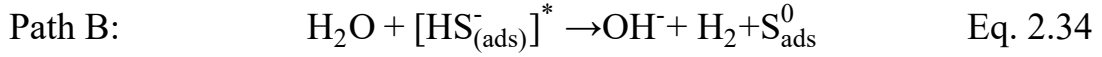
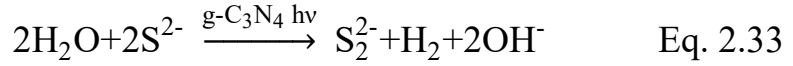
Overall reaction:



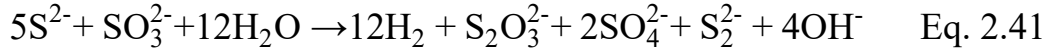
**The mixture of  $\text{Na}_2\text{S}$  and  $\text{Na}_2\text{SO}_3$ :**



Overall reaction (Path A):



Overall reaction (Path B):



Specifically, even without a photocatalyst, hydrogen can be produced with  $\text{Na}_2\text{S}$ ,  $\text{Na}_2\text{SO}_3$ , or their mixture under UV or full-range light irradiations, as shown in Figure 2.10. This point advises that when conducting photocatalytic hydrogen evolution with these three sacrificial agents, only visible light is recommended as a light source. Otherwise, hydrogen from the sacrificial agents' photolysis will cover up the function of photocatalysts.

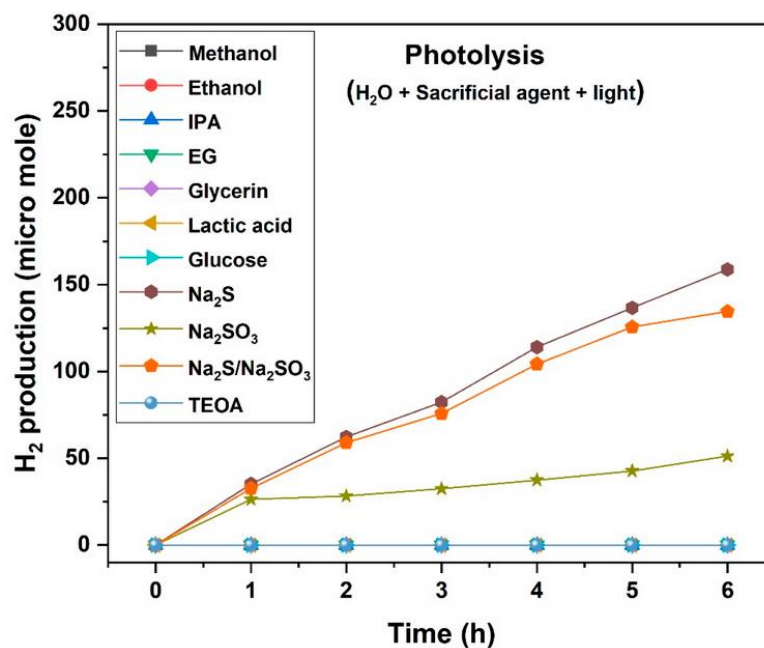


**Figure 2.10** Comparison of PC-HER performance over different sacrificial agents without any photocatalysts.[62]

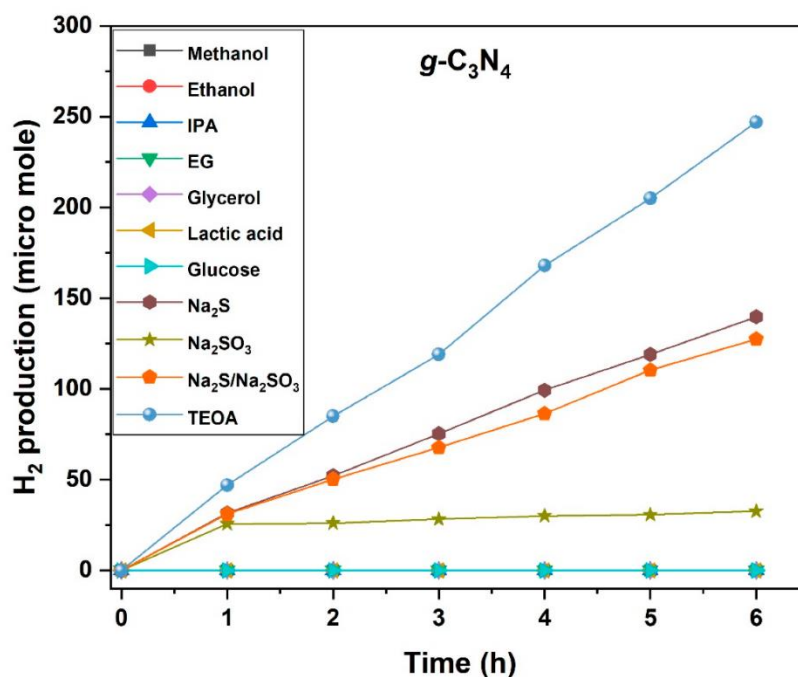


**Figure 2.11** The contrast of PC-HER performance over diverse sacrificial agents with g-C<sub>3</sub>N<sub>4</sub> as a photocatalyst.[62]

According to Figure 2.11, without any cocatalyst, most of the sacrificial agents do not work for g-C<sub>3</sub>N<sub>4</sub> based PC-HER system. Only four of them have apparent hydrogen evolutions. Comparing those data with Figure 2.10, we can find that with or without g-C<sub>3</sub>N<sub>4</sub> as the photocatalyst, the PC-HER performances of Na<sub>2</sub>S, Na<sub>2</sub>SO<sub>3</sub> and their mixture do not show a significant difference, indicating that the hydrogen evolution in Figure 2.11 should originate from the sacrificial agent's photolysis, rather than the photocatalysis based on g-C<sub>3</sub>N<sub>4</sub>. Specifically, TEOA shows the best performance compared to the other scavengers for carbon nitride. In other words, the most efficient sacrificial agent for g-C<sub>3</sub>N<sub>4</sub> is TEOA. The results are, in fact, from the advantage of amine groups in TEOA. In detail, the amine rich nature of g-C<sub>3</sub>N<sub>4</sub> leads to its photo corrosion, which can be overcome by TEOA, because the more reactive amine groups of TEOA can help protect g-C<sub>3</sub>N<sub>4</sub>.

## **2.6 Cocatalysts for g-C<sub>3</sub>N<sub>4</sub> in PC-HER**

In the half-reaction of photocatalytic hydrogen evolution by water splitting, cocatalysts play the second most crucial role in PC-HER, since they can improve the PC-HER rate in several to even thousands times.[64–67] The main function of cocatalysts lies on their ability to transfer photoelectrons from the main photocatalyst towards protons to produce hydrogen.[43,65,68] In this process, the recombination of photo-

motivated electron-hole pairs of the main catalyst can be effectively inhibited by the electron-transferring function of cocatalysts. Meantime, active sites for a proton to be reduced to hydrogen atom are also provided by cocatalysts. Besides, cocatalysts can help lessen the photo-corrosion of main catalysts as well, since they can extract photoelectrons to prevent main catalysts from being reduced.

Generally, the parameters to evaluate the quality of cocatalysts mainly include their work function, Gibbs free energy of the intermediate state ( $|\Delta G_{H^*}|$ ), electric conductivity, and stability.[69,70] Larger work function means a lower Fermi level, which makes it easier for cocatalysts to extract electrons from the main catalyst. Therefore, the larger the work function, the better the cocatalyst in PC-HER is.  $H^*$  is formed in the combination of proton and active site. The optimized value of  $\Delta G_{H^*}$  should be zero, at which the absorption of  $H^+$  and desorption of H atom could reach the best balance. The electric conductivity of cocatalysts is mainly reflected by their bandgap. In general, the narrower the bandgap, the higher the electric conductivity is. The stability of cocatalysts depends on their physicochemical properties. Here, the cocatalysts for carbon nitride primarily contain metal, metal oxide, metal sulfide, metal carbide, and non-metal materials.

### 2.6.1 Metal cocatalysts

Metal cocatalysts are usually excellent conductors. Those quite active metals like alkali and alkaline-earth metals can be excluded. Then the work function and  $\Delta G_{H^*}$  should be carefully considered. Figure 2.12 and Table 2.1 display those two parameters of some important metals. In Figure 2.12, the X-axis is work function while the Y-axis is  $\Delta G_{H^*}$ . It can be seen that the  $\Delta G_{H^*}$  values of Ir, Pt, Rh, Pd are close to zero. However, the work function of Pt is much larger than that of the other three metals. As a result, Pt is definitely the most suitable cocatalyst for PC-HER, which has been adequately demonstrated by previous researches.

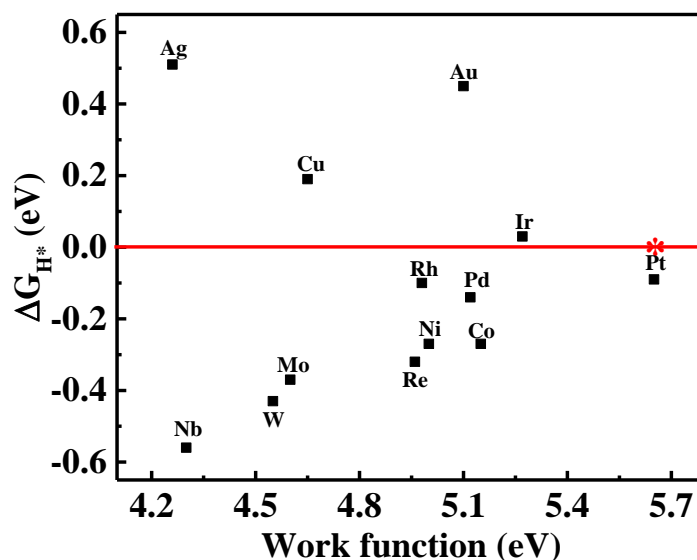


**Figure 2.12** The  $\Delta G_{H^*}$ [71] versus the work function of metal cocatalysts.

**Table 2.1** Values for Figure 2.4.

WF (eV) \ $\Delta G_{\text{H}^*}$ (eV)	4.26	4.3	4.55	4.6	4.65	4.96	4.98	5	5.1	5.12	5.15	5.27	5.65
0.51	Ag												
0.45									Au				
0.19					Cu								
0.03												Ir	
-0.09													Pt
-0.1							Rh						
-0.14										Pd			
-0.27								Co					
-0.27											Ni		
-0.32						Re							
-0.37				Mo									
-0.43			W										
-0.56		Nb											

The PC-HER performance of metal cocatalysts for g-C<sub>3</sub>N<sub>4</sub> is displayed in Table 2.2. Only data of Pt, Au and Ag can be collected from the web of science. Specifically, the data for Au and Ag is very scarce, and most reports relevant to g-C<sub>3</sub>N<sub>4</sub> for PC-HER are utilizing Pt as the cocatalyst. Although PC-HER data of noble metals, Ir, Rh and Pd as cocatalysts can be found for other photocatalysts, no research for these three noble metal modified g-C<sub>3</sub>N<sub>4</sub> can be acquired. This probably results from that the first application of g-C<sub>3</sub>N<sub>4</sub> in PC-HER is in 2009, at that time, those metals had already been tested with other photocatalysts, and the obtained conclusion was that platinum is the most suitable cocatalyst in PC-HER. From Table 2.2, it can also be seen that the ranking for these three metals in PC-HER is Pt, Au, Ag, which is consistent with the ranking of their  $\Delta G_{\text{H}^*}$ .

**Table 2.2** Metal cocatalysts of g-C<sub>3</sub>N<sub>4</sub> for PC-HER.

Cocatalyst	Main catalyst	Catalyst amount (mg)	Optical source	Sacrificial agent	H <sub>2</sub> evolution (μmol·h <sup>-1</sup> ·g <sup>-1</sup> )	Enhanced degree	Ref.
3 wt% Pt	g-C <sub>3</sub> N <sub>4</sub>	50	(300W, >420 nm) Xe lamp	10% TEOA	365	122	[38]
1 wt% Au	g-C <sub>3</sub> N <sub>4</sub>	80	(420–760 nm) Visible light	6% TEOA	91.7	Unknown	[72]
8 wt% Ag	g-C <sub>3</sub> N <sub>4</sub>	100	(300W, >420 nm) Xe lamp	20% Methanol	14.8	8.7	[73]

### 2.6.2 Single-atom cocatalysts

Single-atom catalysis has attracted massive attention after Zhang et al. firstly put forward the concept of “single-atom catalysis” in 2011. They proved that this new type of catalysts can stably exist and that single-atom catalysts can maximize the atomic efficiency to an extremely large extent.

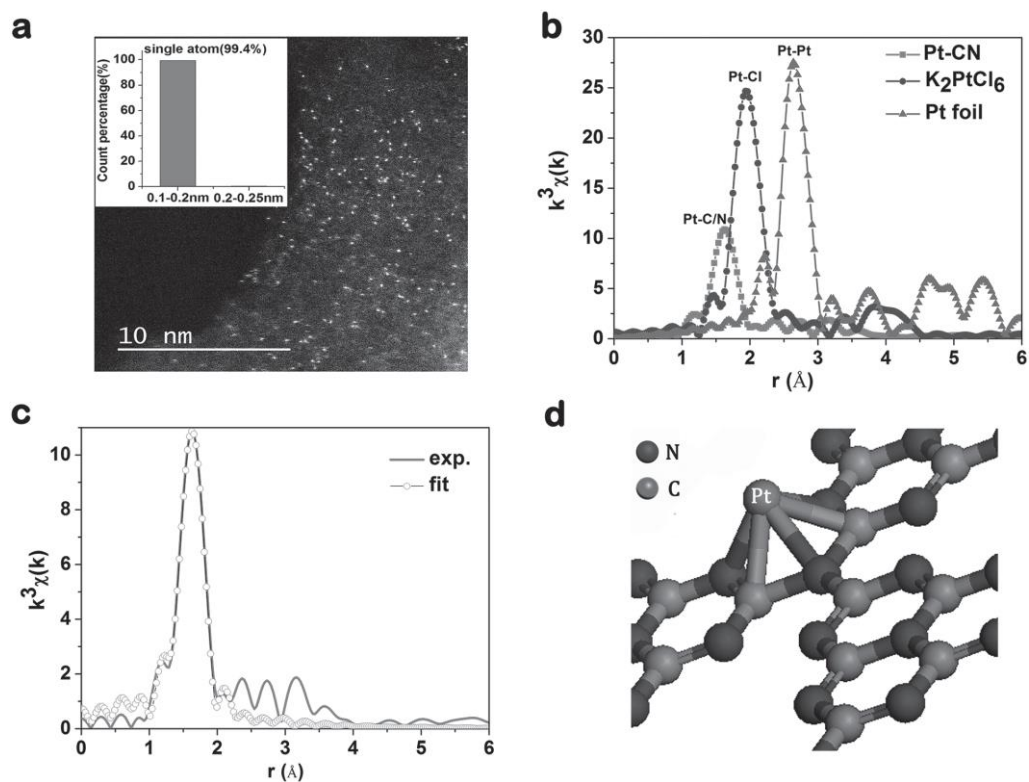


**Figure 2.13 a**, HR-TEM image of 0.16 wt% Pt single-atom modified g-C<sub>3</sub>N<sub>4</sub>. **b**, FT-EXAFS of Pt-CN, K<sub>2</sub>PtCl<sub>6</sub>, and Pt foil. **c**, The corresponding EXAFS r space fitting curves of Pt-CN. **d**, The structure of Pt-CN.[74]

Li et al. firstly introduce single-atom Pt onto g-C<sub>3</sub>N<sub>4</sub> (Figure 2.13a) to take on the role of cocatalyst for PC-HER in 2016.[74] Synchrotron-based extended X-ray absorption fine structure (EXAFS) spectroscopy (Figure 2.13b), combined with the fitted results in the r-space provided by the IFEFFIT software (Figure 2.13c), confirmed the Pt-N and Pt-C bonds-based structure (Figure 2.13d). The PC-HER experiments demonstrated the efficiency of single-atom Pt cocatalyst is 8.6 times that of Pt nanoparticle cocatalyst. The ultrafast transient absorption (TA) test helps support the mechanism that the near band-edge electron trap state can trap

photo-excited electrons so that they have a longer lifetime, and more opportunities to reduce  $H^+$ .

Cao et al. designed and fabricated single-atom Pd decorated g- $C_3N_4$  in 2018.[75] It is deemed that part of Pd single-atoms are located between adjacent layers of g- $C_3N_4$ , while others are trapped in the six-fold cavity of the g- $C_3N_4$  plane. The former is based on Pd-C and Pd-N bonds and plays the role of electron bridge between layers, while the latter helps g- $C_3N_4$  to improve its ability to adsorb water molecules. The PC-HER performance almost doubles that of single-atom Pt decorated g- $C_3N_4$ .

In 2019, Zeng et al. successfully synthesized high-loading-amount single-atom Pt modified g- $C_3N_4$  via a facile ion-exchange method.[76] The platinum atoms can be locked in the interlayer nano-space of g- $C_3N_4$  so that the single-atom Pt loading amount can reach as high as 8.7 wt%. The PC-HER performance can even be  $22650 \mu\text{mol g}^{-1} \text{h}^{-1}$ , resulting from that the interaction between Pt and interlayer space (Pt-N bond) helps reshape the charge distribution of g- $C_3N_4$ , leading to more proton absorption and lowered energy barrier for hydrogen production.

In summary, single-atom-based cocatalysts modified g- $C_3N_4$  are usually based on chemical bonding, and new mechanisms for enhanced PC-HER

performance are often proposed to be different from that of traditional metal nanoparticle cocatalysts. Their PC-HER performance is listed below.

**Table 2.3** Single-atom cocatalysts for PC-HER

Single-atom cocatalyst	Main catalyst	Catalyst amount (mg)	Optical source	Sacrificial agent	H <sub>2</sub> evolution (μmol·h <sup>-1</sup> ·g <sup>-1</sup> )	Enhanced degree	Ref.
0.16 wt% Pt	g-C <sub>3</sub> N <sub>4</sub>	50	(300 W) Xe lamp	10% TEOA	6360	50	[74]
0.33 wt% Pd	g-C <sub>3</sub> N <sub>4</sub>	50	Solar simulator	10% TEOA	6688	unknown	[75]
0.96 wt% Pt	g-C <sub>3</sub> N <sub>4</sub>	50	Solar simulator	10% TEOA	3716	unknown	[75]
8.7 wt% Pt	g-C <sub>3</sub> N <sub>4</sub>	10	(300W, >420 nm) Xe lamp	10% TEOA	22650	unknown	[76]

## 2.6.3 Transition metal based cocatalyst

There are plenty of transition metal based cocatalysts that have been reported, including transition metal oxide, hydroxide, sulfide, carbide, nitride, and phosphide.

### 2.6.3.1 Transition metal oxide and hydroxide cocatalysts

Transition metal oxide and hydroxide cocatalysts for photocatalytic hydrogen evolution mainly include NiO, NiOH, Co<sub>3</sub>O<sub>4</sub>, and Co(OH)<sub>2</sub>. Some others, like Ag<sub>2</sub>O, can also be found in previous reports.

Zhang et al. exploited an in-situ immersion approach to load NiO nanoparticles onto g-C<sub>3</sub>N<sub>4</sub>. The PC-HER rate of the obtained photocatalyst reached more than 6 times higher than that of pure g-C<sub>3</sub>N<sub>4</sub>. [77] The increased charge-transfer ability and decreased overpotential were

considered as the main factors for enhanced performance. Liu et al. utilized a wetness impregnation and thermal oxidation method to prepare amorphous NiO modified g-C<sub>3</sub>N<sub>4</sub>. [78] The amorphous NiO endows more exposed active sites, improved visible light absorption, and thus enhanced PC-HER performance than crystal NiO. In these two studies, NiO with a large bandgap was excited by photons and only transferred photoelectrons from g-C<sub>3</sub>N<sub>4</sub> to H<sup>+</sup> to enhance efficiency, as shown in Figure 2.14. However, some other studies suggested that NiO is responsible for photo-excited holes transfer. Shi et al. developed NiO/g-C<sub>3</sub>N<sub>4</sub> p-n junction and found that the photoinduced holes firstly entered onto NiO from g-C<sub>3</sub>N<sub>4</sub> via p-n junction, and then reacted with sacrificial agents (Figure 2.15). [79] The difference between these two theories might be due to their different structures originating from their different synthesis strategies.

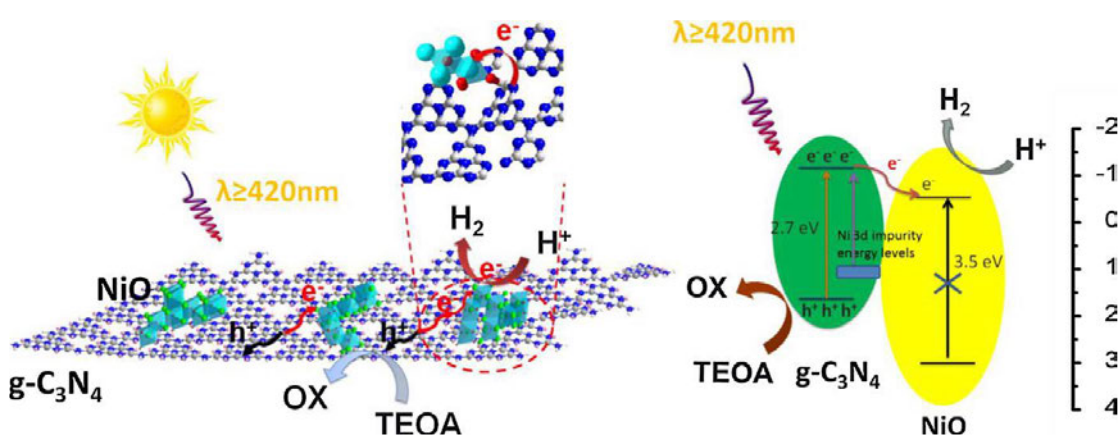


**Figure 2.14** The proposed mechanism for PC-HER process of amorphous NiO modified g-C<sub>3</sub>N<sub>4</sub>. [78]

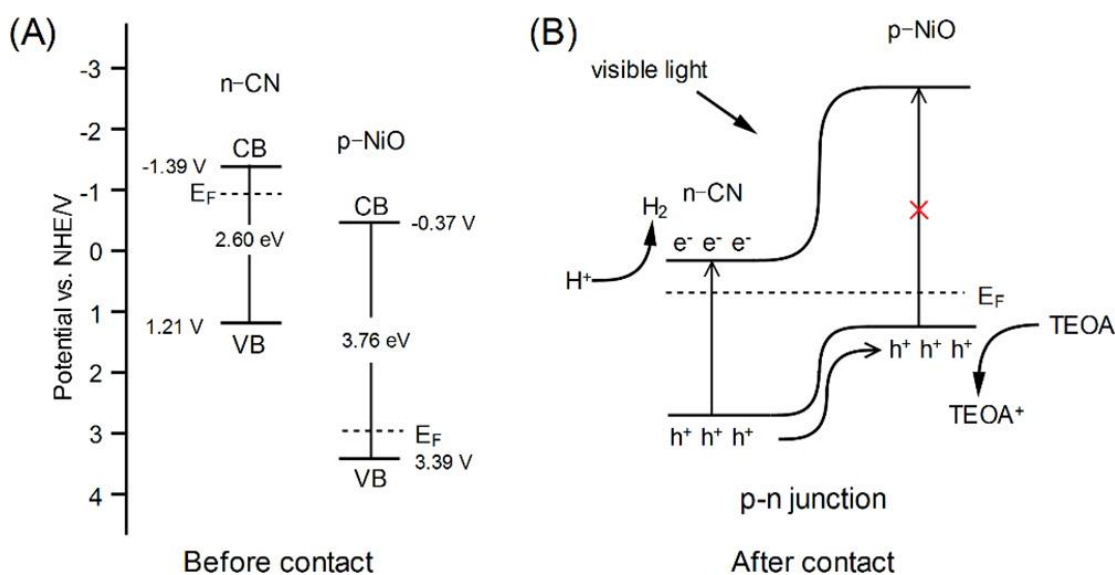


**Figure 2.15** The proposed mechanism for PC-HER process of NiO/g-C<sub>3</sub>N<sub>4</sub> p-n junction.[79]

Moreover, Yang et al. fabricated a series of nickel species as cocatalysts for g-C<sub>3</sub>N<sub>4</sub> and found that Ni(OH)<sub>2</sub> has better PC-HER performance due to its more lowered electrical impedance.[80]

Co<sub>3</sub>O<sub>4</sub> was applied as the cocatalyst of mesoporous g-C<sub>3</sub>N<sub>4</sub> (mpg-C<sub>3</sub>N<sub>4</sub>) in PC-HER by Kheradmand et al.[81] The enhanced charge transfer and the PN junction formed between Co<sub>3</sub>O<sub>4</sub> and g-C<sub>3</sub>N<sub>4</sub> primarily accounted for the improvement of PC-HER production compared with pure mesoporous g-C<sub>3</sub>N<sub>4</sub>. Yang et al. embedded Co<sub>3</sub>O<sub>4</sub> into g-C<sub>3</sub>N<sub>4</sub> by in-situ thermopolymerization.[4] Both the extended light absorption and formed PN junction improve the PC-HER rate of the synthesized material by 5 times as compared to pristine g-C<sub>3</sub>N<sub>4</sub>. It is worth noting that, unlike NiO, which

cannot be activated by visible light owing to the wide bandgap,  $\text{Co}_3\text{O}_4$ , with a bandgap of 2.07 eV, can be stimulated by visible light. Thus, it can not only accept photoelectrons from the CB of  $\text{g-C}_3\text{N}_4$  but also inject its holes towards the VB of  $\text{g-C}_3\text{N}_4$ .

Moreover, Wu et al. utilized a facial hydrothermal method to fabricate  $\text{Ag}_2\text{O}$  decorated  $\text{g-C}_3\text{N}_4$ . [3] The obtained hybrid showed excellent PC-HER performance, over 274 times as high as that of pristine  $\text{g-C}_3\text{N}_4$ , even much better than Pt modified  $\text{g-C}_3\text{N}_4$ . What is more, the recycled  $\text{Ag}_2\text{O/g-C}_3\text{N}_4$  still showed much higher ability than  $\text{Pt/g-C}_3\text{N}_4$ . The mechanism analysis revealed that, unlike most cocatalysts for PC-HER, which are responsible for transferring electrons from main catalysts to  $\text{H}^+$ , the  $\text{Ag}_2\text{O}$  cocatalyst accepts photo-encouraged holes and makes them react with sacrificial agents as shown in Figure 2.16.

Table 2.4 lists the oxide cocatalysts of PC-HER performance in references. Specifically, the much higher HER rate of 5.0 wt%  $\text{Co}_3\text{O}_4$  than that of others should be due to the application of mesoporous carbon nitride (MCN) as the primary catalyst.

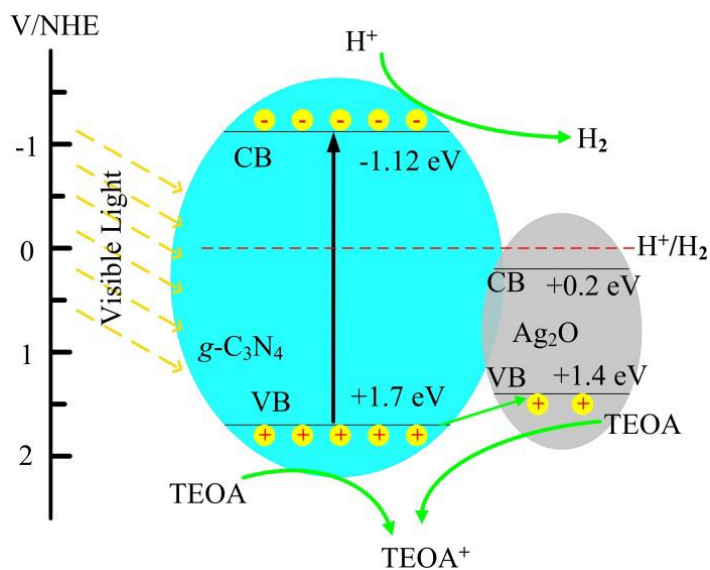


**Figure 2.16** The proposed mechanism for PC-HER process of  $\text{Ag}_2\text{O}/\text{g-C}_3\text{N}_4$ . [3]

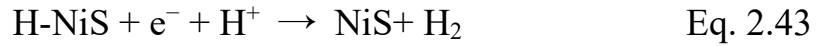
**Table 2.4** Transition metal oxide and hydroxide cocatalysts for PC-HER.

Sulfide Cocatalyst	Main catalyst	Catalyst amount (mg)	Optical source	Sacrificial agent	$\text{H}_2$ evolution ( $\mu\text{mol h}^{-1} \text{g}^{-1}$ )	Enhance d degree	Ref
2 wt% NiO	$\text{g-C}_3\text{N}_4$	50	(300 W, >420 nm) Xe lamp	10% TEOA	120	6	[77]
1 wt% NiO	$\text{g-C}_3\text{N}_4$	10	(300 W, >420 nm) Xe lamp	10% TEOA	29	7.25	[79]
NiO	$\text{g-C}_3\text{N}_4$	40	(300 W, >400 nm) Xe lamp	20% Methanol	82.88	unknown	[80]
9 wt% NiO	$\text{g-C}_3\text{N}_4$	50	(300 W, >420 nm) Xe lamp	10% TEOA	68.8	430	[78]
0.5 wt% $\text{Ni}(\text{OH})_2$	$\text{g-C}_3\text{N}_4$	40	(300 W, >400 nm) Xe lamp	20% Methanol	185.13	unknown	[80]
5.0 wt% $\text{Co}_3\text{O}_4$	mpg- $\text{C}_3\text{N}_4$	40	(300 W, >420 nm) Xe lamp	10% TEA	865	2.05	[81]
1 wt% $\text{Co}_3\text{O}_4$	$\text{g-C}_3\text{N}_4$	50	Unknown	10% TEOA	50	100	[4]
0.83 wt% $\text{Ag}_2\text{O}$	$\text{g-C}_3\text{N}_4$	50	(300 W, >420 nm) Xe lamp	10% TEOA	330.4	unknown	[3]

### 2.6.3.2 Transition metal sulfide cocatalysts

Many transition metal sulfides have been applied as the cocatalysts of  $\text{g-C}_3\text{N}_4$  for PC-HER, including  $\text{NiS}$ ,  $\text{NiS}_2$ ,  $\text{CoS}$ ,  $\text{Ag}_2\text{S}$ ,  $\text{MoS}_2$ ,  $\text{WS}_2$ ,  $\text{VS}_2$ , and  $\text{PtS}_2$ .

Hong et al. developed noble-metal-free NiS grafted g-C<sub>3</sub>N<sub>4</sub> via a hydrothermal method, which can boost the PC-HER performance by 253 times compared to pure g-C<sub>3</sub>N<sub>4</sub> at the optimal loading ratio of 1.1 wt% NiS on g-C<sub>3</sub>N<sub>4</sub>. [2] Chen et al. also obtained a high-performance g-C<sub>3</sub>N<sub>4</sub>/NiS hybrid using a template-free ion-exchange strategy and proposed the reaction processes as below. [82]



Lu et al. decorated g-C<sub>3</sub>N<sub>4</sub> nanosheets with NiS to further enhance the PC-HER rate. [83] Zhao et al. used a facile photochemical method to realize the precise loading NiS onto g-C<sub>3</sub>N<sub>4</sub> nanosheets, which dramatically improved the PC-HER performance by more than 2500 times higher. [84] All those four studies on NiS/g-C<sub>3</sub>N<sub>4</sub> suggested that the electron transfer from g-C<sub>3</sub>N<sub>4</sub> towards NiS mainly led to the higher PC-HER efficiency; however, none of them focused on the process of H<sup>+</sup> attachment on NiS. Therefore, it is worth calculating and discussing the ΔG<sub>H\*</sub> of NiS in the future study.

Yin et al. successfully prepared NiS<sub>2</sub>/g-C<sub>3</sub>N<sub>4</sub> hybrids and demonstrated that the PC-HER rate of 2 wt% NiS<sub>2</sub>/g-C<sub>3</sub>N<sub>4</sub> was four times as high as that

of Pt/g-C<sub>3</sub>N<sub>4</sub>, fully proving the high co-catalytic capacity of NiS<sub>2</sub>. [67] Xue et al. fabricated NiS<sub>2</sub> quantum dots modified g-C<sub>3</sub>N<sub>4</sub>, and the inhibited electron-hole recombination and reduced water reduction barrier were deemed as the reasons for an enhanced PC-HER rate. [51] In addition, bimetallic nickel-iron sulfide was combined with g-C<sub>3</sub>N<sub>4</sub> through a two-step hydrothermal method by Wang et al. [85] The prolonged lifetime of photo-generated carriers, the economic effectiveness and the adjustability of morphologies are major advantages of the synthesized catalyst.

CoS serving as a cocatalyst for g-C<sub>3</sub>N<sub>4</sub> based PC-HER was reported by Zhu et al. [43] Through facilitating photo-excited electrons shift from mesoporous g-C<sub>3</sub>N<sub>4</sub> to CoS and providing active sites for H<sup>+</sup> reduction, CoS can significantly improve the PC-HER performance. An Ag<sub>2</sub>S/g-C<sub>3</sub>N<sub>4</sub> composite photocatalyst was synthesized by Jiang et al. [50] At the beginning of PC-HER process, partial Ag<sup>+</sup> was reduced to Ag atom by the photo-stimulated electrons, which helped notably accelerate the PC-HER process, since the photo-electrons transfer from g-C<sub>3</sub>N<sub>4</sub>, through Ag<sub>2</sub>S, towards Ag, can efficiently help separate photoelectron-hole pairs.

In recent years, with the rapid development of two-dimensional materials, transition metal disulfide compounds have been received colossal attention, especially the new emerging star after graphene, molybdenum

disulfide ( $\text{MoS}_2$ ). Computational studies proved that this material owns  $\Delta G_{\text{H}^*}$  of 0.07 eV, quite close to zero, indicating its quite suitability as the cocatalyst for PC-HER.

Afterwards, bunches of researches about  $\text{MoS}_2$  cocatalysts gushed. Zheng et al. utilized hard-templating and impregnation-sulfidation to bond hollow  $g\text{-C}_3\text{N}_4$  (H- $g\text{-C}_3\text{N}_4$ ) with  $\text{MoS}_2$ .<sup>[65]</sup> The enhanced PC-HER performance of the hybrid should be owing to the thin layered junctions between the two materials and the lowered overpotential resulting from excellent active sites provided by  $\text{MoS}_2$ . 1T  $\text{MoS}_2$  was applied as a cocatalyst for  $g\text{-C}_3\text{N}_4$  in PC-HER by Xu et al. It should be noticed that 2H  $\text{MoS}_2$  is a semiconductor while 1T  $\text{MoS}_2$  has metallic properties. Therefore, Schottky junction was formed between 1T  $\text{MoS}_2$  and oxygenated monolayer  $g\text{-C}_3\text{N}_4$  (O- $g\text{-C}_3\text{N}_4$ ), which had a minimized Schottky barrier because of the van der Waals interactions between 2D 1T  $\text{MoS}_2$  and 2D O- $g\text{-C}_3\text{N}_4$ .<sup>[86]</sup> The hybrid's PC-HER rate can even surpass 1841  $\mu\text{mol/g/h}$ . Further, Liang et al. fabricated metallic 1T  $\text{MoS}_2$  quantum dots and loaded them onto  $g\text{-C}_3\text{N}_4$ .<sup>[87]</sup> On the one hand, the quantum size of  $\text{MoS}_2$  helped provide more exposed catalytic edge sites. On the other hand, the metallicity of 1T  $\text{MoS}_2$  made photoelectrons more quickly transfer onto the active sites on  $\text{MoS}_2$ .

The second hottest 2D disulfide material is WS<sub>2</sub>, with  $\Delta G_{H^*}$  of 0.22 eV, indicating its potential of being a cocatalyst in PC-HER. Hou et al. exploited an impregnation-sulfidation method to fabricate WS<sub>2</sub> decorated mesoporous g-C<sub>3</sub>N<sub>4</sub> (mpg-C<sub>3</sub>N<sub>4</sub>).[66] Like the mechanism of MoS<sub>2</sub>/mpg-C<sub>3</sub>N<sub>4</sub>, the enhanced PC-HER performance of WS<sub>2</sub>/mpg-C<sub>3</sub>N<sub>4</sub> could be owing to the formed layer junction between WS<sub>2</sub> and mpg-C<sub>3</sub>N<sub>4</sub>. Then, 1T WS<sub>2</sub> modified g-C<sub>3</sub>N<sub>4</sub> for PC-HER was reported by Yi et al.[68] They argued that unlike 2H WS<sub>2</sub>, whose active sites are only located on its edge sites, 1T WS<sub>2</sub> owns active sites on both its edge sites and basal plane, which remarkably increases the number of active sites for PC-HER.

Other disulfide materials bedecked g-C<sub>3</sub>N<sub>4</sub> can also be found in previous researches, like VS<sub>2</sub> and PtS<sub>2</sub>. Shao et al. fabricated VS<sub>2</sub>/g-C<sub>3</sub>N<sub>4</sub> via a one-pot hydrothermal method. In fact, 2H VS<sub>2</sub> has metallic properties, which is different from the semiconductor of 2H MoS<sub>2</sub>. [88] Thus, the excellent electrical conductivity can better help charge transfer from the main catalyst to cocatalyst. Besides, there are active sites on both basal plane and edge sites of VS<sub>2</sub>, and the  $\Delta G_{H^*}$  of VS<sub>2</sub> is even comparable to that of Pt cocatalyst. In addition, Liu et al. synthesized defect-riched ultrathin PtS<sub>2</sub> nanosheets decorated g-C<sub>3</sub>N<sub>4</sub>. The formed heterojunction facilitates photoinduced charges separation and transfer.[64]

There are also some other transition metal disulfides, like 2H-NbS<sub>2</sub> and 2H-TaS<sub>2</sub>, which have the potential to become cocatalysts for PC-HER. Both the materials have a metallic property and suitable  $\Delta G_{H^*}$  value. Perhaps, their application as cocatalysts for PC-HER will emerge in the near future.

The PC-HER performances of transition metal sulfide cocatalysts are listed in below Table 2.5.

**Table 2.5** Transition metal sulfide cocatalysts for PC-HER.

Sulfide Cocatalyst	Main catalyst	Catalyst amount (mg)	Optical source	Sacrificial agent	H <sub>2</sub> evolution ( $\mu\text{mol h}^{-1} \text{g}^{-1}$ )	Enhanced degree	Ref
1 1 wt% NiS	mpg-C <sub>3</sub> N <sub>4</sub>	100	(300 W, >420 nm) Xe lamp	15% TEOA	482	250	[2]
1 5 mol% NiS	g-C <sub>3</sub> N <sub>4</sub>	100	(300 W, >420 nm) Xe lamp	10% TEOA	447 7	59	[82]
1 0 wt% NiS	g-C <sub>3</sub> N <sub>4</sub> NS	50	(150 W, > 400 nm) Xe lamp	10% TEOA	84	unknown	[83]
0 76 wt% NiS	g-C <sub>3</sub> N <sub>4</sub> NS	5	(300 W, AM 1 5 G filter) Xe lamp	10% TEOA	16 400	2500	[84]
2 wt% NiS <sub>2</sub>	g-C <sub>3</sub> N <sub>4</sub>	10	(300 W, >420 nm) Xe lamp	15% TEOA	406	unknown	[67]
25 3 wt%-NiS <sub>2</sub>	g-C <sub>3</sub> N <sub>4</sub>	5	(300 W, >420 nm) Xe lamp	10% TEOA	968 2	unknown	[51]
1 0 wt% CoS	mpg-C <sub>3</sub> N <sub>4</sub>	50	(300 W, >420 nm) Xe lamp	10% TEOA	740	13	[43]
5% Ag <sub>2</sub> S	g-C <sub>3</sub> N <sub>4</sub>	50	(3 W, 420 nm) 4 UV-LEDs	25% methanol	500	100	[50]
0 5 wt% MoS <sub>2</sub>	H-g-C <sub>3</sub> N <sub>4</sub>	20	(300 W, >420 nm) Xe lamp	10% lactic acid	1340	unknown	[65]
0 2 wt% 1T MoS <sub>2</sub>	O-g-C <sub>3</sub> N <sub>4</sub>	10	(300 W, > 400 nm) Xe lamp	10% TEOA	1841 72	unknown	[86]
15 wt% 1T MoS <sub>2</sub> QD	g-C <sub>3</sub> N <sub>4</sub> NS	20	(300 W, AM 1 5 G filter) Xe lamp	20% TEOA	1857	37 9	[87]
0 3 at% WS <sub>2</sub>	mpg-C <sub>3</sub> N <sub>4</sub>	50	(300 W, >420 nm) Xe lamp	10% lactic acid	240	unknown	[66]
15 wt% 1T WS <sub>2</sub>	g-C <sub>3</sub> N <sub>4</sub>	10	(300 W, > 400 nm) Xe lamp	10% TEOA	331 09	43 3	[68]
2 8 wt% VS <sub>2</sub>	g-C <sub>3</sub> N <sub>4</sub>	50	Unknown	10% TEOA	1748	26	[88]
1 wt% 1T PtS <sub>2</sub>	mpg-C <sub>3</sub> N <sub>4</sub>	50	(300 W, > 400 nm) Xe lamp	10% TEOA	292	unknown	[64]

### 2.6.3.3 Transition metal carbide and nitride cocatalysts

A few transition metal carbides and nitrides can also play the role of cocatalyst for g-C<sub>3</sub>N<sub>4</sub> in PC-HER, such as W<sub>2</sub>N, W<sub>2</sub>C, Mo<sub>2</sub>C, and Ti<sub>3</sub>C<sub>2</sub>

(Mxene).

Shao et al. compared the PC-HER performances of  $W_2C$ ,  $WS_2$ , and  $W_2N$  decorated  $g-C_3N_4$  and found that all the three materials have the ability as cocatalysts.[89] The PC-HER rate of  $W_2N$  is very close to that of  $WS_2$ , while the rate of  $W_2C$  is even 4 times higher than that of those two materials, because  $W_2C$  can significantly increase charge separation and transfer and surface hydrogen evolution rate.

After Ran et al. firstly introduced  $Ti_3C_2$  Mxene as a cocatalyst for PC-HER in 2017, this material has been received much attention in this area.[90] Li et al. loaded  $Ti_3C_2$  Mxene quantum dots (QDs) onto  $g-C_3N_4$  and found PC-HER rate of the composite was even 3 times higher than that of Pt/ $g-C_3N_4$ .[91] This excellent performance could be owing to the metallic nature, a high surface area, and the prominent  $\Delta G_{H^*}$  of  $Ti_3C_2$  Mxene QDs.

**Table 2.6** Transition metal carbide and nitride cocatalyst for PC-HER.

Cocatalyst	Main catalyst	Catalyst amount (mg)	Optical source	Sacrificial agent	H <sub>2</sub> evolution ( $\mu\text{mol h}^{-1} \text{g}^{-1}$ )	Enhanced degree	Ref
7 wt% $W_2N$	$g-C_3N_4$	50	AM 1.5 solar simulator	10% TEOA	500	12.5	[89]
2 wt% $W_2C$	$g-C_3N_4$	50	AM 1.5 solar simulator	10% TEOA	1960	49	[89]
$Ti_3C_2$ Mxene QDs	$g-C_3N_4$	10	(300 W, AM 1.5 G filter) Xe lamp	15% TEOA	5111.8	26	[91]

#### 2.6.3.4 Transition metal phosphide cocatalysts

Apart from sulfide cocatalysts, there are also many phosphide cocatalysts owning the capacity to be cocatalysts in PC-HER.

Ni<sub>2</sub>P was firstly deposited onto mpg-C<sub>3</sub>N<sub>4</sub> for PC-HER by Indra et al. Time-resolved photoluminescence combined with electron paramagnetic resonance (EPR) demonstrated that the improved carrier transfer at the heterojunction between the Ni<sub>2</sub>P and mpg-C<sub>3</sub>N<sub>4</sub> are mainly responsible for the enhanced PC-HER performance.[92] Wang et al. used a hydrothermal method to fabricate Ni<sub>2</sub>P/g-C<sub>3</sub>N<sub>4</sub>, and they believed that the formed Z-scheme structure resulted in the upgraded PC-HER performance.[93] Then Zeng et al. employed a solution-phase strategy to attach zero-dimensional (0D) Ni<sub>2</sub>P nanoparticles onto two-dimensional (2D) g-C<sub>3</sub>N<sub>4</sub> nanosheets and high-efficiency PC-HER performance was obtained.[94] Peng et al. exploited an in-situ incorporation route to synthesize the compound of Ni<sub>2</sub>P/g-C<sub>3</sub>N<sub>4</sub>, which achieved a very high PC-HER rate of 2849.5 μmol g<sup>-1</sup> h<sup>-1</sup>. [95]

CoP/g-C<sub>3</sub>N<sub>4</sub> was firstly reported by Yi et al., and they proved that the widened optical absorption range and the accelerated charge transfer should be the reasons for an excellent PC-HER performance.[96] After that, Zeng et al. utilized a two-step strategy of in-situ electrostatic

adsorption, and phosphate treatment at low temperature to prepare CoP quantum dots (QDs) decorated g-C<sub>3</sub>N<sub>4</sub> fiber (CNF). The PC-HER rate of the synthesized material was even 34.9 times as high as that of Pt/CNF.[97]

In the work of Zeng et al., 0D FeP nanodots decorated porous g-C<sub>3</sub>N<sub>4</sub> was acquired via phosphate treatment of Fe<sub>3</sub>O<sub>4</sub>/g-C<sub>3</sub>N<sub>4</sub>. [8] The  $\Delta G_{H^*}$  of FeP was calculated to be 0.17 eV, much closer to zero than that of g-C<sub>3</sub>N<sub>4</sub> (-0.58 eV). In the meantime, Sun et al. loaded Fe<sub>2</sub>P onto g-C<sub>3</sub>N<sub>4</sub> and also proved its prominent PC-HER performance, which was even comparable to Pt/g-C<sub>3</sub>N<sub>4</sub>. [98] Nanosized MoP modified g-C<sub>3</sub>N<sub>4</sub> was realized by Cheng et al. using phosphorization, which obtained a PC-HER rate as high as 3868  $\mu\text{mol g}^{-1} \text{h}^{-1}$  resulted from the enforced photoabsorption and lowered H<sub>2</sub> evolution barrier. [7] The amorphous Ru<sub>2</sub>P quantum dots were attached to g-C<sub>3</sub>N<sub>4</sub> based on an in-situ phosphorization route by Wang et al., and the PC-HER rate of the hybrid was more than doubling that of Pt/g-C<sub>3</sub>N<sub>4</sub>. [99]

From the literature of phosphide cocatalysts of g-C<sub>3</sub>N<sub>4</sub> for PC-HER, several points are worth noting. a) Low-temperature phosphorization of oxide/g-C<sub>3</sub>N<sub>4</sub> is usually exploited to fabricate the compound of phosphide/g-C<sub>3</sub>N<sub>4</sub>. b) 0D nanosized or quantum dots are frequently adopted to furtherly enhance their performance. c) The PC-HER rate of

some phosphide/g-C<sub>3</sub>N<sub>4</sub>, such as Fe<sub>2</sub>P, Ru<sub>2</sub>P or CoP decorated g-C<sub>3</sub>N<sub>4</sub>, is even comparable or much higher than that of Pt/g-C<sub>3</sub>N<sub>4</sub>, demonstrating the high capacity of phosphide as cocatalysts for PC-HER. The list below is the comparison of their PC-HER performance.

**Table 2.7** Transition metal phosphide cocatalyst for PC-HER.

Phosphide Cocatalyst	Main catalyst	Catalyst amount (mg)	Optical source	Sacrificial agent	H <sub>2</sub> evolution ( $\mu\text{mol h}^{-1} \text{g}^{-1}$ )	Enhanced degree	Ref
2 wt% Ni <sub>2</sub> P	mpg-C <sub>3</sub> N <sub>4</sub>	50	(300 W, >420 nm) Xe lamp	10% TEOA	644	unknown	[92]
1 wt% Ni <sub>2</sub> P	g-C <sub>3</sub> N <sub>4</sub>	40	(300 W, >420 nm) Xe lamp	10% TEOA	362.4	22	[93]
3.5 wt% Ni <sub>2</sub> P	g-C <sub>3</sub> N <sub>4</sub> NS	50	(300 W, >420 nm) Xe lamp	10% TEOA	474.7	unknown	[94]
14.9 wt% Ni <sub>2</sub> P	g-C <sub>3</sub> N <sub>4</sub>	50	(300 W, >420 nm) Xe lamp	10% TEOA	2849.5	12.4	[95]
0.25 wt% CoP	g-C <sub>3</sub> N <sub>4</sub>	100	(300 W, >420 nm) Xe lamp	10% TEOA	474.4	131	[96]
7 wt%-CoP QDs	g-C <sub>3</sub> N <sub>4</sub> fiber	20	(300 W, >420 nm) Xe lamp	15% TEOA	2420	201.7	[97]
2.19 wt% FeP	g-C <sub>3</sub> N <sub>4</sub>	60	(300 W, >420 nm) Xe lamp	10% TEOA	177.9	unknown	[8]
10 wt% Fe <sub>2</sub> P	g-C <sub>3</sub> N <sub>4</sub>	2	(300 W, >420 nm) Xe lamp	10% TEOA	214	15	[98]
5 wt% MoP	g-C <sub>3</sub> N <sub>4</sub>	10	(300 W, >400 nm) Xe lamp	10% TEOA	3868	unknown	[7]
0.1 wt% Ru <sub>2</sub> P	g-C <sub>3</sub> N <sub>4</sub>	10	(300 W, >420 nm) Xe lamp	10% TEOA	2110	113.4	[99]

## 2.6.4 Metal-free cocatalysts

There are also some metal-free cocatalysts like carbon and phosphide-based materials, including carbon dots, carbon nanotube, doped graphene and black phosphorous.

In the study of Fang et al., carbon dots were decorated onto g-C<sub>3</sub>N<sub>4</sub> by adding them to the precursor of g-C<sub>3</sub>N<sub>4</sub>, dicyandiamide. About 0.25 wt% carbon dots could help improve the PC-HER rate of pristine g-C<sub>3</sub>N<sub>4</sub> at about 2.4 times.[9] It is recognized that carbon dots can play the role of

electron-sinks to prevent the recombination of electron-hole pairs, but too many carbon dots will become recombination centers. Multi-wall carbon nanotubes (MWCNT) modified  $g\text{-C}_3\text{N}_4$ , which can double the PC-HER rate of  $g\text{-C}_3\text{N}_4$ , was reported by Suryawanshi et al.[5] They deemed that the MWCNTs can not only help the process of charge transfer but also moderately change the morphology of  $g\text{-C}_3\text{N}_4$ , which is favorable to PC-HER process. Li et al. systematically compared the PC-HER performance of different graphene-based cocatalysts modified  $g\text{-C}_3\text{N}_4$ . Those cocatalysts are graphene (GR), and O-, S-, N-, B-doped graphene (OGR, SGR, NGR, BGR).[6] The experimental results showed that the PC-HER order is  $\text{NGR}/g\text{-C}_3\text{N}_4 > \text{BGR}/g\text{-C}_3\text{N}_4 > \text{GR}/g\text{-C}_3\text{N}_4 > \text{OGR}/g\text{-C}_3\text{N}_4 > \text{SGR}/g\text{-C}_3\text{N}_4 > g\text{-C}_3\text{N}_4$ . Among them, NGR can help increase the PC-HER rate of  $g\text{-C}_3\text{N}_4$  by more than 46 times. Besides, those cocatalysts can help  $g\text{-C}_3\text{N}_4$  keep stable in the PC-HER process. In the report of Shinde et al., S, Se co-doped graphene (S-Se-GR) was applied as a cocatalyst of  $g\text{-C}_3\text{N}_4$  for PC-HER, and they proved that the synergistic effect of S and Se could help S-Se-GR/ $g\text{-C}_3\text{N}_4$  better performed than S-GR/ $g\text{-C}_3\text{N}_4$  and Se-GR/ $g\text{-C}_3\text{N}_4$ . [52]

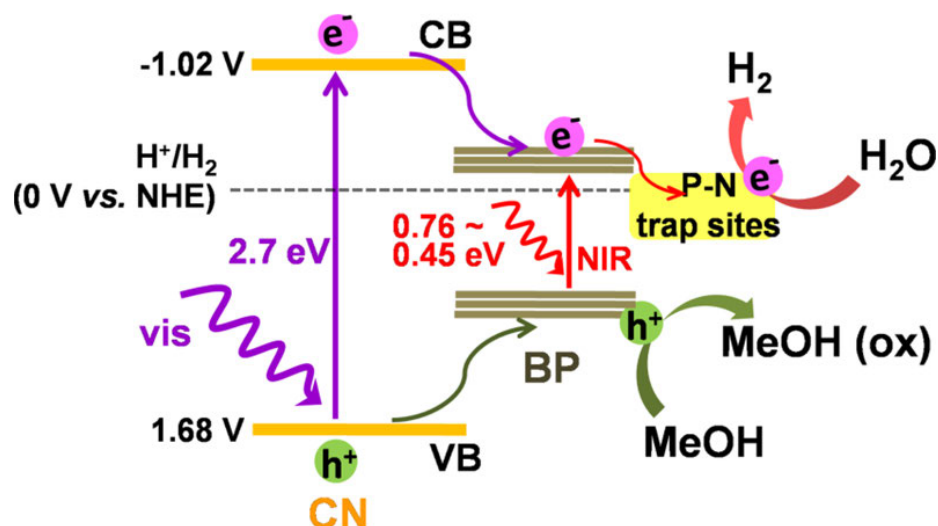


**Figure 2.17** The proposed mechanism of black phosphorous/g-C<sub>3</sub>N<sub>4</sub> for PC-HER.[100]

Black phosphorous (BP) was first attached to g-C<sub>3</sub>N<sub>4</sub> for PC-HER by Zhu et al.[100] The PC-HER results demonstrated that the composite exhibited an excellent performance under not only visible light (> 420 nm) but also infrared (IR) light (> 780 nm). As shown in Figure 2.17, under visible light, BP serves as the cocatalyst of g-C<sub>3</sub>N<sub>4</sub>, and the P–N coordinative bond between BP and g-C<sub>3</sub>N<sub>4</sub> acts as the trap site of electrons. Under IR light, BP becomes the main catalyst and photo-excited electrons from the conduction band (CB) of BP can be trapped by the interfacial P–N defects, boosting its PC-HER performance. Then, Ran et al. synthesized 2D/2D Phosphorene/g-C<sub>3</sub>N<sub>4</sub> van der Waals junction as a metal-free photocatalyst for PC-HER and revealed the brilliant performance of this heterojunction.[101]

**Table 2.8** Metal-free cocatalyst for photocatalytic hydrogen evolution.

Phosphide Cocatalyst	Main catalyst	Catalyst amount (mg)	Optical source	Sacrificial agent	H <sub>2</sub> evolution (μmol h <sup>-1</sup> g <sup>-1</sup> )	Enhanced degree	Ref
0.25 wt% Carbon dots	g-C <sub>3</sub> N <sub>4</sub>	50	(350 W, > 420 nm) Xe lamp	10% TEOA	218	2.4	[9]
0.5 wt% MWCNT	g-C <sub>3</sub> N <sub>4</sub>	100	(300 W, > 395 nm) Xe lamp	23% Methanol	42	1.9	[5]
N doped graphene	g-C <sub>3</sub> N <sub>4</sub>	1	(350 W, > 395 nm) Hg lamp	10% TEOA	1380	46	[6]
B doped graphene	g-C <sub>3</sub> N <sub>4</sub>	1	(350 W, > 395 nm) Hg lamp	10% TEOA	400	13.3	[6]
Graphene	g-C <sub>3</sub> N <sub>4</sub>	1	(350 W, > 395 nm) Hg lamp	10% TEOA	380	12.7	[6]
O doped graphene	g-C <sub>3</sub> N <sub>4</sub>	1	(350 W, > 395 nm) Hg lamp	10% TEOA	90	3	[6]
S doped graphene	g-C <sub>3</sub> N <sub>4</sub>	1	(350 W, > 395 nm) Hg lamp	10% TEOA	60	2	[6]
S doped graphene	g-C <sub>3</sub> N <sub>4</sub> NS	100	(500 W, > 420 nm) Xe lamp	20% Lactic acid	1850	2.3	[52]
Se doped graphene	g-C <sub>3</sub> N <sub>4</sub> NS	100	(500 W, > 420 nm) Xe lamp	20% Lactic acid	2200	2.8	[52]
S-Se-GR	g-C <sub>3</sub> N <sub>4</sub> NS	100	(500 W, > 420 nm) Xe lamp	20% Lactic acid	2590	3.2	[52]
25 wt% BP	g-C <sub>3</sub> N <sub>4</sub>	1.5	(320 W, > 420 nm) Xe lamp	20% Methanol	427	unknown	[100]
25 wt% BP	g-C <sub>3</sub> N <sub>4</sub>	1.5	(320 W, > 780 nm) Xe lamp	20% Methanol	101	unknown	[100]
1.8 wt% Phosphorene	g-C <sub>3</sub> N <sub>4</sub> NS	20	(300 W, > 400 nm) Xe lamp	18% Lactic acid	571	11.3	[101]

### 2.6.5 Metal organic framework (MOF) cocatalysts

The flexible structure endows the metal-organic framework (MOF) with various properties. Thus, MOF with an appropriate band structure, electric conductivity, surface area, and morphology can be synthesized and used as cocatalysts in PC-HER in theory.

In practice, Devarayapalli et al. exploited a facile microwave strategy to fabricate ZIF 67/g-C<sub>3</sub>N<sub>4</sub>, which was then utilized as a photocatalyst in PC-HER, to achieve a rate of 3.84 times higher than that of bare g-C<sub>3</sub>N<sub>4</sub>. [101]

## **2.7 Different nanostructures of g-C<sub>3</sub>N<sub>4</sub> for PC-HER**

Plenty of studies focused on the application of various nanostructured g-C<sub>3</sub>N<sub>4</sub> in PC-HER processes, which can be classified below.

### **2.7.1 Different morphologies of g-C<sub>3</sub>N<sub>4</sub> for PC-HER**

#### **2.7.1.1 g-C<sub>3</sub>N<sub>4</sub> nanosheets for PC-HER**

Large specific surface area, sufficient exposed active sites, and enhanced light absorption, all these edges of g-C<sub>3</sub>N<sub>4</sub> nanosheets are driving researchers to acquire routes to exfoliate bulk g-C<sub>3</sub>N<sub>4</sub>. The current developed strategies include thermal exfoliation, liquid exfoliation, lithium intercalation exfoliation, chemical exfoliation, ultrasonic exfoliation, and the mix of these ways. Specifically, thermal exfoliation has been widely exploited in previous reports because of its easiness and convenience and even became a standard for other strategies to compare.

In Yang's research,[102] five solvents were tested in the liquid exfoliation of g-C<sub>3</sub>N<sub>4</sub>. IPA and NMP (Figure 2.18) were proven to be adequate to gain stable dispersion. The obtained g-C<sub>3</sub>N<sub>4</sub> nanosheets, with a thickness of just 2 nm, helped distinctly advance the PC-HER activity of g-C<sub>3</sub>N<sub>4</sub> in 9.3 folds. Han and co-workers prepared ultrathin g-C<sub>3</sub>N<sub>4</sub> nanoplatelets by a deft ball-milling strategy.[103] The lateral size of the acquired 2D

materials is 2 – 6 nm and the thickness is only 0.35 – 0.7 nm. The enlarged specific surface area combined with the negative-shift conduction band helped boost the PC-HER to  $1365 \mu\text{mol}\cdot\text{h}^{-1}\cdot\text{g}^{-1}$ , which is 13.7 times as high as that of bulk g-C<sub>3</sub>N<sub>4</sub>. Ma et al. adopted an in-situ lithium intercalation way to synthesize ultrathin g-C<sub>3</sub>N<sub>4</sub> nanosheets.[36] In detail, LiCl was added to the precursor of g-C<sub>3</sub>N<sub>4</sub> before thermal polymerization, and the calcined product was ultrasonicated in water and ethanol, to make the bulk g-C<sub>3</sub>N<sub>4</sub> be exfoliated to nanosheets when LiCl was dissolved. The specific surface area achieved  $186.3 \text{ m}^2 \text{ g}^{-1}$ , and the thickness was about 2 – 3 nm, which promoted the PC-HER efficiency by 6.6 folds. Zhang and co-workers developed an easy way to prepare g-C<sub>3</sub>N<sub>4</sub> nanosheets (NS) at a large scale, which is to cover urea, the precursor of g-C<sub>3</sub>N<sub>4</sub>, with a block of melamine foam before polymerization.[104] The average thickness of the g-C<sub>3</sub>N<sub>4</sub> NS from this method is about 4.5 nm, and the PC-HER rate is ~ 6.7 times higher than that of bulk g-C<sub>3</sub>N<sub>4</sub> counterpart. Fang et al. took a similar strategy of covering the precursor of g-C<sub>3</sub>N<sub>4</sub>, melamine, with a nickel foam before calcination, to fabricate holey g-C<sub>3</sub>N<sub>4</sub> NS.[105] In this process, nickel foam can catalyze the derived NH<sub>3</sub> from melamine to transform to H<sub>2</sub>, which is then oxidized to become water molecules. With the participation of H<sub>2</sub>O molecules, gas molecules or bubbles (CO, NO, H<sub>2</sub>) may be generated, which would help shun aggregation of nanosheets. g-C<sub>3</sub>N<sub>4</sub> with 4 nm of the thickness and even  $240 \text{ m}^2/\text{g}$  of the specific

surface area can be obtained by this means, and the PC-HER activity can be raised to  $1871 \mu\text{mol}\cdot\text{h}^{-1}\cdot\text{g}^{-1}$ .

In summary, g-C<sub>3</sub>N<sub>4</sub> nanosheets can be realized by various strategies. Many of them can boost the PC-HER process by about one magnitude (Table 2.9). However, some other ways, like chemical exfoliation, are ineffective for PC-HER, perhaps due to their damage to the structure of g-C<sub>3</sub>N<sub>4</sub>.

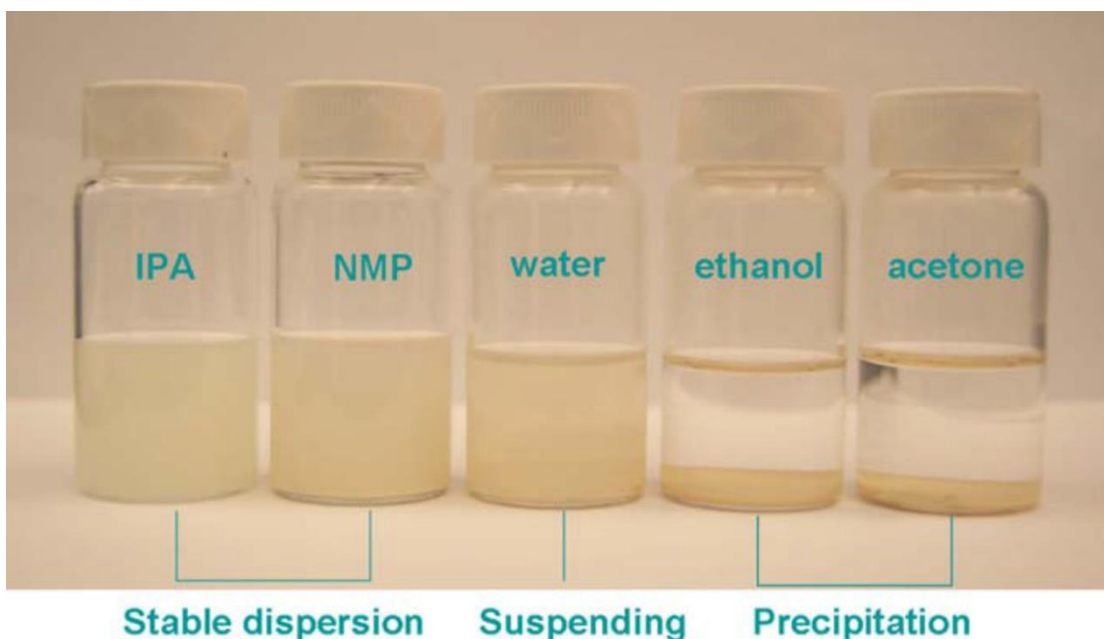


**Figure 2.18** Liquid exfoliation results of g-C<sub>3</sub>N<sub>4</sub> with different solvents.[102]

**Table 2.9** Different exfoliation strategies of g-C<sub>3</sub>N<sub>4</sub> for PC-HER.

Exfoliation strategy	Photocatalyst	Catalyst amount (mg)	Optical source	Sacrificial agent	H <sub>2</sub> evolution ( $\mu\text{mol h}^{-1} \text{g}^{-1}$ )	Enhanced degree	Ref
----------------------	---------------	-------------------------	----------------	----------------------	--	--------------------	-----

Thermal exfoliation	3 wt% Pt/g-C <sub>3</sub> N <sub>4</sub> NS	50	(350W, > 420 nm) Xe lamp	10% TEOA	1300	6.5	[102]
Liquid exfoliation	3 wt% Pt/g-C <sub>3</sub> N <sub>4</sub> NS	50	(350W, > 420 nm) Xe lamp	10% TEOA	1860	9.3	[102]
Ball milling	3 wt% Pt/g-C <sub>3</sub> N <sub>4</sub> NS	50	(300 W, >420 nm) Xe lamp	10% TEOA	1365	13.7	[103]
Lithium intercalation	0.6 wt% Pt/g-C <sub>3</sub> N <sub>4</sub> NS	100	(300 W, > 400 nm) Xe lamp	10% TEOA	1078	6.6	[36]
Melamine foam	3 wt% Pt/g-C <sub>3</sub> N <sub>4</sub> NS	10	(150 W, > 420 nm) Xe lamp	10% TEOA	2040	6.7	[104]
Nickel foam	3 wt% Pt/g-C <sub>3</sub> N <sub>4</sub> NS	20	(300 W, >420 nm) Xe lamp	10% TEOA	1871	31	[105]

### 2.7.1.2 Other g-C<sub>3</sub>N<sub>4</sub> morphologies for PC-HER

Except for bulk g-C<sub>3</sub>N<sub>4</sub> and g-C<sub>3</sub>N<sub>4</sub> nanosheets, there are also other morphologies with various advantages, including nanotubes, nanobelts, nanospheres, and quantum dots.

Zhu et al. used a water-induced way to transform g-C<sub>3</sub>N<sub>4</sub> nanosheets to nanotubes, and the PC-HER rate achieved 246  $\mu\text{mol}\cdot\text{h}^{-1}\cdot\text{g}^{-1}$  with the assistance of Ag-Cu bimetal cocatalysts.[106] Wu and co-workers synthesized C-O doped hierarchical porous g-C<sub>3</sub>N<sub>4</sub> nanobelts by a hydrothermal route. The PC-HER activity was even 79.9 folds higher than that of bulk g-C<sub>3</sub>N<sub>4</sub>. [107] Hollow g-C<sub>3</sub>N<sub>4</sub> nanospheres were fabricated with SiO<sub>2</sub> as a template by Zheng et al. and the excellent PC-HER performance can be owing to the red-shift of the optical absorption and the increased charge separation inside the shell.[108] In Wang's research, B doped g-C<sub>3</sub>N<sub>4</sub> quantum dots were prepared with the participation of NaCl/KCl, which was then located to the surface of g-C<sub>3</sub>N<sub>4</sub> by a hydrothermal method. The matched band structure of the heterojunction resulted in the prominent PC-HER activity.

The varieties of g-C<sub>3</sub>N<sub>4</sub> morphologies endow it with more flexibility, which can help broaden its applications.[109]

**Table 2.10** Different morphologies of g-C<sub>3</sub>N<sub>4</sub> for PC-HER.

Photocatalyst	Catalyst amount (mg)	Cocatalyst	Optical source	Sacrificial agent	H <sub>2</sub> evolution (μmol h <sup>-1</sup> g <sup>-1</sup> )	Enhanced degree	Ref
G-C <sub>3</sub> N <sub>4</sub> nanotubes	40	1 wt% Ag-Cu	(300 W, >420 nm) Xe lamp	10% TEA	246	Unknown	[106]
C-O g-C <sub>3</sub> N <sub>4</sub> nanobelts	5	3 wt% Pt	(300 W, >420 nm) Xe lamp	10% TEOA	18380	79.9	[107]
Hollow g-C <sub>3</sub> N <sub>4</sub> nanospheres	20	3 wt% Pt	(300 W, >455 nm) Xe lamp	10% TEOA	13750	Unknown	[108]
B-g-C <sub>3</sub> N <sub>4</sub> QDs/g-C <sub>3</sub> N <sub>4</sub>	50	1.5 wt% Pt	(300 W, >420 nm) Xe lamp	10% TEOA	1401	58 QD, 11	[109]

### 2.7.2 Porous g-C<sub>3</sub>N<sub>4</sub> for PC-HER

The dramatically improved specific surface area and exposed active sites of porous g-C<sub>3</sub>N<sub>4</sub> make it one of the hot research pursuits.

For the first time, Zhang et al. took urea as the precursor of g-C<sub>3</sub>N<sub>4</sub> and the as-fabricated material had a porous structure, leading to the high specific surface area and enhanced PC-HER performance.[110] Liang and co-workers penetrated urea into the melamine foam, which was then polymerized in a muffle furnace. The obtained 3D porous g-C<sub>3</sub>N<sub>4</sub> monolith showed a remarkable PC-HER activity due to its sufficient porosity and high specific surface area.[111] In Huang's research, the porous O-doped g-C<sub>3</sub>N<sub>4</sub> was acquired via pre-treating the precursor of g-C<sub>3</sub>N<sub>4</sub>, melamine, with H<sub>2</sub>O<sub>2</sub>. The evolved gases in the fabrication process

might result in the high porosity, which, combined with O-doping, helped enhance the PC-HER performance.[112] Porous g-C<sub>3</sub>N<sub>4</sub> was also synthesized via heating the mixture of melamine and LiCl. The ionic salt could be a soft template for the formation of abundant pores.[36] Gu and co-workers exploited a hydrothermal route before polymerization to prepare porous g-C<sub>3</sub>N<sub>4</sub> microspheres, with cyanuric chloride and melamine as the reactants. The fabricated porous structure also had narrower bandgap and lower impedance, facilitating the PC-HER process.[113] In Zhang's study, freeze-drying technology was introduced to help produce pores. In detail, the aqueous mixture of NH<sub>4</sub>Cl and dicyandiamide was firstly freeze-dried and then heated at 550 °C. The obtained g-C<sub>3</sub>N<sub>4</sub>, with both pores and defects, can have an enhanced PC-HER rate by 26 folds higher than that of bulk g-C<sub>3</sub>N<sub>4</sub>. [114] Wu et al. took a three-step procedure of hydrothermal heating, freeze-drying, and calcination, to prepare porous P-doped g-C<sub>3</sub>N<sub>4</sub> tubes from the mixture of dicyandiamide and phytic acid (Figure 2.19). The PC-HER performance achieved 2020 μmol·h<sup>-1</sup>·g<sup>-1</sup>, 22.4 times as high as that of pure g-C<sub>3</sub>N<sub>4</sub>. [115] Zhou and co-workers utilized CH<sub>4</sub>N<sub>2</sub>S and NH<sub>4</sub>Cl to synthesize porous S-doped g-C<sub>3</sub>N<sub>4</sub>. The released gases in the polymerization process helped form the porous structure. [116]

So many reports about the fabrication of various porous g-C<sub>3</sub>N<sub>4</sub> materials

with template-based and template-free routes fully demonstrate its significance for PC-HER enhancement (Table 2.11).

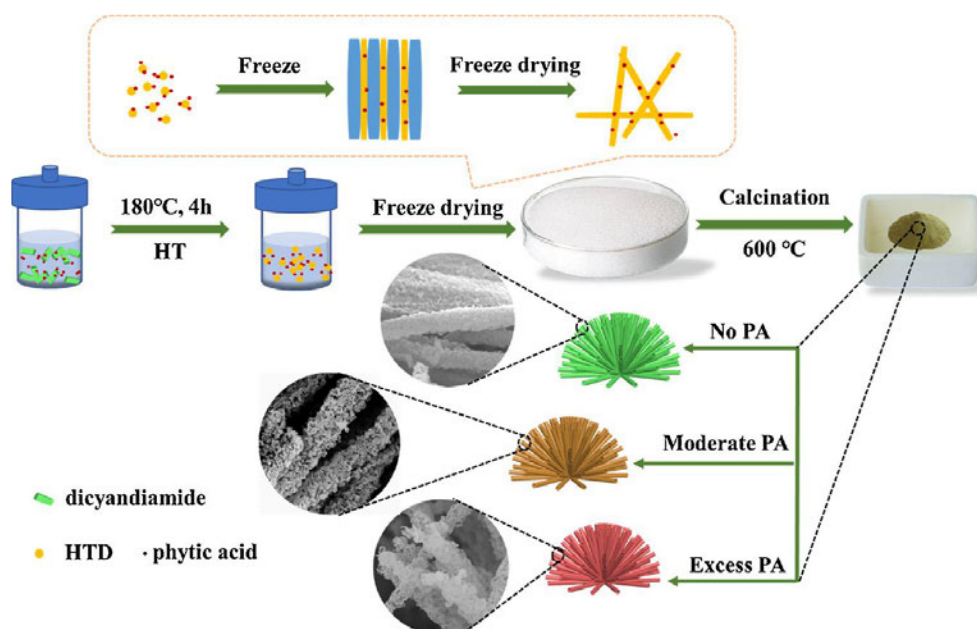


**Figure 2.19** The schematic procedure of synthesis of porous P-doped  $g\text{-C}_3\text{N}_4$  tubes.[115]

**Table 2.11** Different porous  $g\text{-C}_3\text{N}_4$  samples for PC-HER.

Photocatalyst	Catalyst amount (mg)	Cocatalyst	Optical source	Sacrificial agent	H <sub>2</sub> evolution ( $\mu\text{mol h}^{-1} \text{g}^{-1}$ )	Enhanced degree	Ref
Porous $g\text{-C}_3\text{N}_4$ from urea	80	Pt	(300 W, with filter) Xe lamp	10% TEOA	590	3 1, 2 3	[110]
3D Porous $g\text{-C}_3\text{N}_4$ Monolith	10	3 wt% Pt	(300 W, >420 nm) Xe lamp	10% TEOA	2900	2 84	[111]
O doped porous $g\text{-C}_3\text{N}_4$	50	3 wt% Pt	(300 W, >420 nm) Xe lamp	10% TEOA	1204	6 1	[112]
Porous $g\text{-C}_3\text{N}_4$ NS	100	0.6 wt% Pt	(300 W, > 400 nm) Xe lamp	10% TEOA	1078	6 6	[36]
Porous $g\text{-C}_3\text{N}_4$ microsphere	10	3 wt% Pt	(300 W, >420 nm) Xe lamp	15% TEOA	1800	112	[113]
Porous defected $g\text{-C}_3\text{N}_4$	10	3 wt% Pt	(300 W, >420 nm) Xe lamp	10% TEOA	2090	26	[114]
Porous P- $g\text{-C}_3\text{N}_4$ tubes	50	3 wt% Pt	(300 W, >420 nm) Xe lamp	10% TEOA	2020	22 4	[115]
Porous $g\text{-C}_3\text{N}_4$ NS	80	1 wt% Pt	(300 W, >420 nm) Xe lamp	10% TEOA	115 5	4	[117]
Porous $g\text{-C}_3\text{N}_4$ NS	15	Unknown	(300 W, >420 nm) Xe lamp	10% TEOA	367	5 3	[116]
Porous defective $g\text{-C}_3\text{N}_4$	50	3 wt% Pt	(300 W, > 400 nm) Xe lamp	20% TEOA	830 94	9 93	[118]

### 2.7.3 Crystalline g-C<sub>3</sub>N<sub>4</sub> for PC-HER

Graphitic carbon nitride derived from direct thermal polymerization always has structural defects like amino and cyano groups, which are harmful to PC-HER, since those defects may become reintegration centres of photo-generated electron-hole pairs. To overcome this drawback, the preparation of crystalline g-C<sub>3</sub>N<sub>4</sub> provides an alternative solution.

The successful fabrication of crystalline g-C<sub>3</sub>N<sub>4</sub> mostly involves ionothermal method.[119–121] In a typical procedure, the precursor of g-C<sub>3</sub>N<sub>4</sub> like melamine is heated to 500 °C, and the resulting material was then grounded with a eutectic mixture of LiCl and KCl. The obtained powder is then polymerized at 550 °C, and the mixed salts of LiCl/KCl can be washed away with deionized water.[121] There are also some reports that only took KCl as a restriction for forming the crystalline g-C<sub>3</sub>N<sub>4</sub>, which can avoid the complicated operation in a glove box due to the participation of lithium.[122] As shown in Table 2.12, more than 20 times enhancement on activity can be achieved with crystalline g-C<sub>3</sub>N<sub>4</sub> photocatalyst compared to pristine g-C<sub>3</sub>N<sub>4</sub>.

**Table 2.12** Crystalline g-C<sub>3</sub>N<sub>4</sub> for PC-HER.

Strategies	Photocatalyst	Catalyst amount (mg)	Optical source	Sacrificial agent	H <sub>2</sub> evolution (μmol h <sup>-1</sup> g <sup>-1</sup> )	Enhanced degree	Ref
KCl/LiCl	3 wt% Pt/g-C <sub>3</sub> N <sub>4</sub> crystal	50	(> 420 nm) Visible light	10% MeOH	420	26	[121]

## 2.7.4 Doped g-C<sub>3</sub>N<sub>4</sub> for PC-HER

Heteroatom doping is one of the essential tactics to enhance reaction activity of g-C<sub>3</sub>N<sub>4</sub> since it can adjust the band structure, broaden the optical absorption range, improve the electrical conductivity, and enlarge the specific surface area of g-C<sub>3</sub>N<sub>4</sub>. From the previous literature listed on the web of science (Figure 2.20), it can be found that there are 313 articles relevant to doped g-C<sub>3</sub>N<sub>4</sub>, and 80 out of them are concerning to PC-HER processes. Those elements contain Cl, I, O, S, N, P, C, B, Na, K, Mn, Fe, Co, Ni, Cu, Zn, Mo, Pd, and Eu.

IA																			0
H	IIA											IIIA	IVA	VA	VIA	VIIA		He	
Li 5	Be 1											B 43	C 19	N	O 35	F 5		Ne	
Na 8	Mg 1	IIIB	IVB	VB	VIB	VII B	VIII				IB	IIB	Al	Si 1	P 48	S 66	Cl 3	Ar	
K 7	Ca	Sc	Ti 4	V 1	Cr	Mn 3	Fe 18	Co 6	Ni 5	Cu 9	Zn 3	Ga	Ge	As	Se 3	Br	Kr		
Rb	Sr	Y 1	Zr 1	Nb	Mo 3	Tc	Ru	Rh	Pd 4	Ag 7	Cd	In	Sn	Sb	Te 1	I 2	Xe		
Cs 1	Ba	La- Lu	Hf	Ta	W 1	Re	Os	Ir	Pt 1	Au	Hg	Tl	Pb	Bi	Po	At	Rn		
		La	Ce 2	Pr	Nd	Pm	Sm	Eu 3	Gd	Tb	Dy	Ho	Er	Tm	Yb	Lu			

**Figure 2.20** The number of articles about doped g-C<sub>3</sub>N<sub>4</sub> from the web of science. The red number is specifically for PC-HER. (Searched on 01/02/2020)

According to these articles, strategies for the fabrication of doped g-C<sub>3</sub>N<sub>4</sub> can be summarized below. 1) Adding the precursor of the doping element to the precursor of g-C<sub>3</sub>N<sub>4</sub> before polymerization. For example, Zhang et al. mixed NaOH and melamine before heating the mixture at 650 °C to acquire Na doped g-C<sub>3</sub>N<sub>4</sub>. [123] Sagara and co-workers added dicyandiamide to the aqueous solution of BH<sub>3</sub>NH<sub>3</sub> and then polymerized the dry mixture in a muffle furnace to synthesize B doped g-C<sub>3</sub>N<sub>4</sub>. [124] 2) Using the substance containing the targeted doping element to prepare g-C<sub>3</sub>N<sub>4</sub>. For instance, Li et al. exploited H<sub>2</sub>O<sub>2</sub> to process g-C<sub>3</sub>N<sub>4</sub> by a hydrothermal method to obtain O doped g-C<sub>3</sub>N<sub>4</sub>. [125]

Most metal-atom doped g-C<sub>3</sub>N<sub>4</sub> materials share a similar structure, which is the metal atom being located on the six-fold cavity of g-C<sub>3</sub>N<sub>4</sub>. Bonds between the metal atoms and their adjacent N atoms are normally formed in the doped structure. Some exceptions also exist. In one study, K<sup>+</sup> is connected with amino species on the edges of g-C<sub>3</sub>N<sub>4</sub>, forming N-K bonds. [126] The doping atom of non-metal element doped g-C<sub>3</sub>N<sub>4</sub> is usually replacing some of C or N atoms of the g-C<sub>3</sub>N<sub>4</sub> structure. I, O, and S atoms are reported to replace the sp<sup>2</sup>-bonded N atoms in g-C<sub>3</sub>N<sub>4</sub> structure (C–N=C, N<sub>2</sub> in Figure 2.21), while N, P, and B atoms can take the place of C<sub>2</sub> atom as displayed in Figure 2.21.

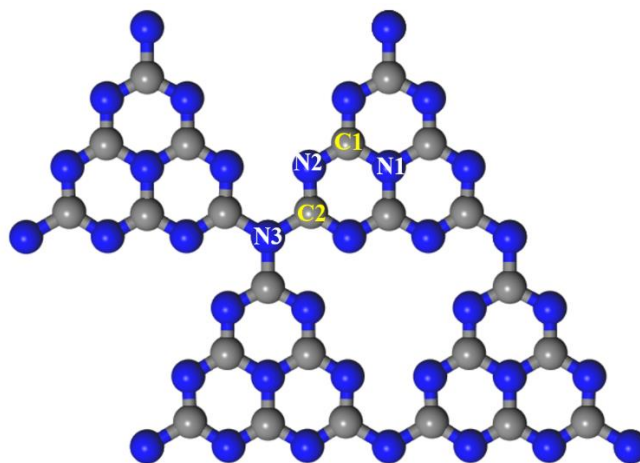


**Figure 2.21** Molecular framework of g-C<sub>3</sub>N<sub>4</sub>.

By adjusting the structure of g-C<sub>3</sub>N<sub>4</sub>, doped atoms can remarkably improve its physicochemical properties and thus enhance its PC-HER performance. Table 2.13 displays the PC-HER activities of various heteroatom doped g-C<sub>3</sub>N<sub>4</sub> and the escalation of PC-HER rates can be 1.5 to 11 times as high as that of pristine g-C<sub>3</sub>N<sub>4</sub>.

**Table 2.13** Doped g-C<sub>3</sub>N<sub>4</sub> for photocatalytic hydrogen evolution.

CB, VB (V vs SHE, pH=0) bandgap (eV)	Photocatalyst	Catalyst amount (mg)	Optical source	Sacrificial agent	H <sub>2</sub> evolution (μmol h <sup>-1</sup> g <sup>-1</sup> )	Enhanced degree	Ref
Unknown	3 wt% Pt/Cl doped g-C <sub>3</sub> N <sub>4</sub>	30	(300 W, > 400 nm) Xe lamp	10% TEOA	833	1.54	[70]
X, X, 2.82	3 wt% Pt/Br doped g-C <sub>3</sub> N <sub>4</sub>	50	(300 W, >420 nm) Xe lamp	10% TEOA	960	2.4	[127]
-0.71, 1.66, 2.37	3 wt% Pt/I doped g-C <sub>3</sub> N <sub>4</sub> NS	50	(300 W, >420 nm) Xe lamp	10% TEOA	890	2.3	[128]
-0.67, 1.82, 2.49	1.2 wt% Pt/O doped g-C <sub>3</sub> N <sub>4</sub>	100	(300 W, >420 nm) Xe lamp	10% TEOA	375	2.5	[125]
-1.06, 1.79, 2.85	6 wt% Pt/S doped g-C <sub>3</sub> N <sub>4</sub>	100	(300 W, >420 nm) Xe lamp	10% TEOA	333	8	[129]
-0.37, 2.28, 2.65	3 wt% Pt/N doped g-C <sub>3</sub> N <sub>4</sub>	80	(300 W, > 400 nm) Xe lamp	10% TEOA	554	5.6	[130]
-0.59, 2.12, 2.71	3 wt% Pt/P doped g-C <sub>3</sub> N <sub>4</sub>	100	(300 W, >420 nm) Xe lamp	10% TEOA	506	2.9	[131]
-0.45, 2.01, 2.46	3 wt% Pt/C-doped g-C <sub>3</sub> N <sub>4</sub>	10	(> 420 nm) Xe lamp	10% TEOA	1889	4.7	[132]
-0.50, 2.05, 2.55	1 wt% Pt/B doped g-C <sub>3</sub> N <sub>4</sub> NS	50	(300 W, > 400 nm) Xe lamp	10% TEOA	1880	1.6	[133]
Unknown	3 wt% Pt/Na doped g-C <sub>3</sub> N <sub>4</sub> NT	20	(300 W, >420 nm) Xe lamp	10% TEOA	7150	11	[123]
-1.15, 1.59, 2.74	3 wt% Pt/K doped g-C <sub>3</sub> N <sub>4</sub>	50	(300 W, > 400 nm) Xe lamp	10% TEOA	1337	5.6	[126]

X, X, 2 53	Fe doped g-C <sub>3</sub> N <sub>4</sub> NS	100	(300 W, >420 nm) Xe lamp	10% MeOH	536	1 8	[134]
X, X, 2 62	3 wt% Pt/Co doped g-C <sub>3</sub> N <sub>4</sub>	50	(300 W, >420 nm) Xe lamp	10% TEOA	560	3	[135]
Unknown	3 wt% Pt/Cu doped g-C <sub>3</sub> N <sub>4</sub> NT	50	(300 W, >420 nm) Xe lamp	10% TEOA	3020	13	[136]
-0 35, 2 21, 2 56	3 wt% Pt/Mo doped g-C <sub>3</sub> N <sub>4</sub>	50	(300 W, >420 nm) Xe lamp	10% TEOA	2009	9 6	[137]
Unknown	Pd doped g-C <sub>3</sub> N <sub>4</sub>	100	(300 W, >420 nm) Xe lamp	10% TEOA	3162	15 3	[138]
X, X, 2 55	Eu doped g-C <sub>3</sub> N <sub>4</sub>	50	(300 W) Xe lamp	20% TEOA	404	4	[139]
X, X, 2 8	1 wt% Pt/K-I-mpg-C <sub>3</sub> N <sub>4</sub>	50	(300 W, >420 nm) Xe lamp	5% MeOH	1612	2	[140]
-0 71, 2 06, 2 77	1 5 wt% Pt/Mo-Co-mpg-C <sub>3</sub> N <sub>4</sub>	100	(300 W, > 400 nm) Xe lamp	10% TEOA	694 5	8 6	[141]
X, X, 2 72	2 wt% Pt/Na-O-g-C <sub>3</sub> N <sub>4</sub>	50	(300 W) Xe lamp	25% EtOH	2200	6 9	[142]
X, X, 2 68	3 wt% Pt/K-S-g-C <sub>3</sub> N <sub>4</sub>	70	(300 W, >420 nm) Xe lamp	10% TEOA	1962 10	10	[69]

## 2.8 g-C<sub>3</sub>N<sub>4</sub> based heterostructure for PC-HER

Apart from various forms of g-C<sub>3</sub>N<sub>4</sub>, heterostructures formed between g-C<sub>3</sub>N<sub>4</sub> and other materials are another quite significant application mode for PC-HER. Those heterostructures include Schottky junctions, type II junctions, Z-scheme junctions, PN junctions, and van der Waals junctions. All the cocatalysts modified g-C<sub>3</sub>N<sub>4</sub> listed in Part 2.6 can be recognized as some kinds of heterojunctions. Besides, the combination of g-C<sub>3</sub>N<sub>4</sub> with other photocatalysts are also heterojunctions, which are the main focus in this part.

### 2.8.1 Schottky junction

The junction between a semiconductor and a metal or a metallic material is called Schottky junction. Therefore, most Schottky junctions are summarized in the part of metal (Part 2.6.1) or metallic cocatalysts. In this type of junctions, photo-excited electrons are usually transferred from semiconductors to the metal or metallic cocatalyst so that the reintegration

of photo-generated charges can be inhibited. There is also an exception, which is applied to the mechanism of localized surface plasmon resonance (LSPR). For example, in Zhang's research, Au nanorods were decorated on the surface of g-C<sub>3</sub>N<sub>4</sub> nanotubes. The hot electrons from the LSPR effect of Au nanorods can be injected into the CB of g-C<sub>3</sub>N<sub>4</sub> and then to participate in hydrogen evolution reactions.[143]

### **2.8.2 Type II junction**

Type II junctions are formed between two semiconductors, and solar light can help photoinduced electrons jump from the VB to the CB of both. Then the photo-stimulated electrons are transferred from the CB of the semiconductor with the more negative value to the CB of the other semiconductor. Meanwhile, the left photogenerated holes from the VB of the semiconductor with the more positive value are delivered to the VB of the other semiconductor. In this process, the reintegration of photo-excited electron-hole pairs can be effectively eased.

Except for most of those combinations of semiconductor cocatalyst/g-C<sub>3</sub>N<sub>4</sub> listed in Part 2.6, there are still the compositions of g-C<sub>3</sub>N<sub>4</sub> and other typical semiconductor-photocatalysts, having type II junctions.

Zhang et al. partly wrapped CdS nanowires with g-C<sub>3</sub>N<sub>4</sub>. The type II

junction between them can not only help impede the reintegration of photo-generated charges but also protect CdS from photo-corrosion.[144] Cao and co-workers synthesized a type II junction between CdS quantum dots and g-C<sub>3</sub>N<sub>4</sub> nanosheets by an in-situ solvothermal growth method, leading to effective charge separation.[145] In Tian's research, Zn<sub>0.8</sub>Cd<sub>0.2</sub>S/g-C<sub>3</sub>N<sub>4</sub> core-shell composites were prepared via a combined ultrasonication and hydrothermal route. Even without a cocatalyst, this type II junction could help boost the PC-HER rate of g-C<sub>3</sub>N<sub>4</sub> by 146 folds.[146] A CeO<sub>2</sub>/g-C<sub>3</sub>N<sub>4</sub> type II junction was also hybridized by Zou et al. and the (100) plane of CeO<sub>2</sub> could assist in facilitating interfacial interaction and photoelectrons transfer.[147]

All these connections conform to the mechanism of type II junctions abovementioned, whereas there is some difference for the junction of TiO<sub>2</sub>/g-C<sub>3</sub>N<sub>4</sub>. In Chai's work, under visible light illumination, only the electrons from g-C<sub>3</sub>N<sub>4</sub> could be motivated and then transmitted to the CB of TiO<sub>2</sub>, and no photoinduced charges of TiO<sub>2</sub> because of the wide bandgap.[15]

**Table 2.14** g-C<sub>3</sub>N<sub>4</sub> based type II junctions for PC-HER.

Photocatalyst	Catalyst amount (mg)	Cocatalyst	Optical source	Sacrificial agent	H <sub>2</sub> evolution (μmol h <sup>-1</sup> g <sup>-1</sup> )	Enhanced degree	Ref
CdS nanowires/g-C <sub>3</sub> N <sub>4</sub>	50	0.6 wt% Pt	(350 W, > 400 nm) Xe lamp	Na <sub>2</sub> S/Na <sub>2</sub> SO <sub>3</sub>	4152	Unknown	[144]
CdS QDs/g-C <sub>3</sub> N <sub>4</sub> NS	5	0.5 wt% Pt	(300 W, >420 nm) Xe lamp	L-ascorbic acid	4494	118	[145]

CdS QDs/g-C <sub>3</sub> N <sub>4</sub> nanosphere	20	3 wt% Pt	(300 W, >420 nm) Xe lamp	10% TEOA	30050	5	[148]
Zn <sub>0.8</sub> Cd <sub>0.2</sub> S/g-C <sub>3</sub> N <sub>4</sub>	20	None	(300 W, >420 nm) Xe lamp	Na <sub>2</sub> S/Na <sub>2</sub> SO <sub>3</sub>	2351 18	146	[146]
Cubic CeO <sub>2</sub> /g-C <sub>3</sub> N <sub>4</sub>	50	3 wt% Pt	(300 W, >420 nm) Xe lamp	10% TEOA	860	1 43	[147]
SrTiO <sub>3</sub> /g-C <sub>3</sub> N <sub>4</sub>	50	0.2 wt% Pt	(500 W) solar simulator	TEOA	552	1 84	[149]
TiO <sub>2</sub> /g-C <sub>3</sub> N <sub>4</sub>	100	Pt	(300 W, >420 nm) Xe lamp	10% TEOA	1780	1 62	[15]

### 2.8.3 Z-scheme junction

There are two types of Z-scheme junctions. The first one relies on the metal between the two semiconductors. For instance, in Zhao's report, Z-scheme Cd<sub>0.8</sub>Zn<sub>0.2</sub>S/Au/g-C<sub>3</sub>N<sub>4</sub> was synthesized, and the CB of Cd<sub>0.8</sub>Zn<sub>0.2</sub>S was in the middle of the CB and VB of g-C<sub>3</sub>N<sub>4</sub> (Figure 2.22).[150] The Au nanoparticles between Cd<sub>0.8</sub>Zn<sub>0.2</sub>S and g-C<sub>3</sub>N<sub>4</sub> acted as the recombination centres of the photoelectrons from Cd<sub>0.8</sub>Zn<sub>0.2</sub>S and the photo-generated holes of g-C<sub>3</sub>N<sub>4</sub> so that the remaining photoelectrons of g-C<sub>3</sub>N<sub>4</sub> were able to reduce H<sup>+</sup> to H<sub>2</sub>. In contrast, the residual photo-excited holes of Cd<sub>0.8</sub>Zn<sub>0.2</sub>S could be consumed by sacrificial agents.

The other kind of Z-scheme junction is very similar to the one described above. The only difference is no metal participation between two semiconductors and the photoelectrons from the first semiconductor with the CB value in the middle of the second semiconductor's CB and VB values can directly fall to the VB of the second semiconductor.

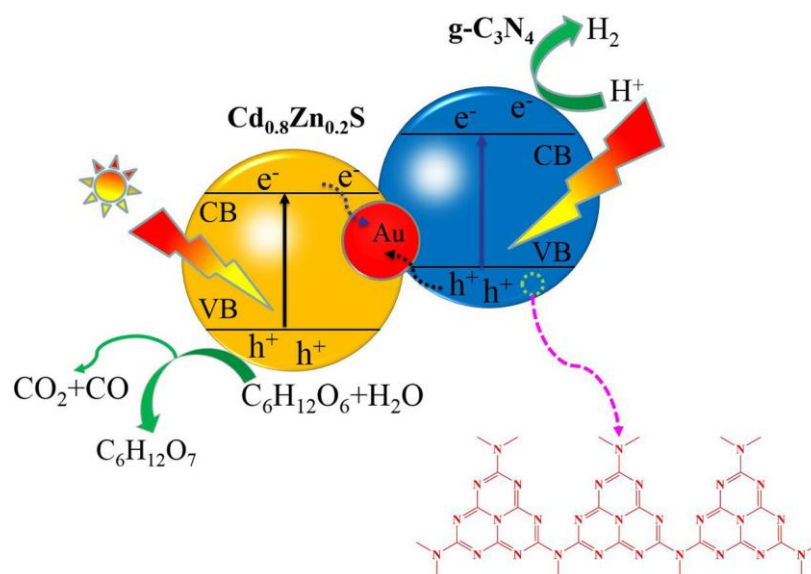


**Figure 2.22** The proposed mechanism of  $\text{Cd}_x\text{Zn}_{1-x}\text{S}/\text{Au}/\text{g-C}_3\text{N}_4$  for PC-HER.[150]

Katsumata and co-authors prepared  $\text{WO}_3/\text{g-C}_3\text{N}_4$  Z-scheme junction through grinding and calcination, which could aid to double the PC-HER activity of  $\text{g-C}_3\text{N}_4$ . [151] In Liu's report, the Z-scheme junction was formed between 0D  $\text{MoS}_2$  quantum dots and 2D  $\text{g-C}_3\text{N}_4$  and boosted the PC-HER rate by 1.3 folds. [13] Huang and co-authors unveiled that the adsorption of triethanolamine on the surface of  $\text{g-C}_3\text{N}_4$  would markedly uplift its Fermi level and thus switch type II junction of  $\text{W}_{18}\text{O}_{49}/\text{g-C}_3\text{N}_4$  to be Z-scheme, significantly boosting its PC-HER performance. [12] Moreover,  $\text{g-C}_3\text{N}_4$  based Z-scheme junctions were also realized in composite materials including  $\text{CuInS}_2/\text{g-C}_3\text{N}_4$ , [152]  $\text{MnIn}_2\text{S}_4/\text{g-C}_3\text{N}_4$ , [153]  $\text{LaFeO}_3/\text{g-C}_3\text{N}_4$ ,  $\text{LaFeO}_3/\text{g-C}_3\text{N}_4$ , [154] N doped carbon dots/ $\text{g-C}_3\text{N}_4$ , [11]  $\text{Bi}_4\text{NbO}_8\text{Cl}/\text{g-C}_3\text{N}_4$ , [10] et al., which could enhance the

PC-HER efficiency by 3~8 folds (Table 2.15).

**Table 2.15** g-C<sub>3</sub>N<sub>4</sub> based Z-scheme junctions for PC-HER.

Photocatalyst	Catalyst amount (mg)	Cocatalyst	Optical source	Sacrificial agent	H <sub>2</sub> evolution ( $\mu\text{mol h}^{-1} \text{g}^{-1}$ )	Enhanced degree	Ref
WO <sub>3</sub> /g-C <sub>3</sub> N <sub>4</sub>	40	2 wt% Pt	(300 W, >420 nm) Xe lamp	10% TEOA	110	2	[151]
0D (MoS <sub>2</sub> )/2D (g-C <sub>3</sub> N <sub>4</sub> )	50	2 wt% Pt	(300 W) Xe lamp	25% MeOH	577	1.3	[13]
W <sub>18</sub> O <sub>49</sub> /g-C <sub>3</sub> N <sub>4</sub>	50	3 wt% Pt	(300 W, > 400 nm) Xe lamp	10% TEOA	1020.3	1.57	[12]
Cd <sub>x</sub> Zn <sub>1-x</sub> S/Au/g-C <sub>3</sub> N <sub>4</sub>	50	None	(300 W, >420 nm) Xe lamp	Glucose	123	52.2	[150]
CuInS <sub>2</sub> /g-C <sub>3</sub> N <sub>4</sub>	50	1 wt% Pt	(300 W, >420 nm) Xe lamp	Na <sub>2</sub> S/Na <sub>2</sub> SO <sub>3</sub>	1290	3.3	[152]
MnIn <sub>2</sub> S <sub>4</sub> /g-C <sub>3</sub> N <sub>4</sub>	50	None	(300 W, > 400 nm) Xe lamp	Na <sub>2</sub> S/Na <sub>2</sub> SO <sub>3</sub>	200.8	8.2	[153]
LaFeO <sub>3</sub> /g-C <sub>3</sub> N <sub>4</sub>	20	1 wt% Pt	(125 W, > 420 nm) Xe lamp	10% MeOH	1152.34	5.6	[154]
MoS <sub>2</sub> QDs/g-C <sub>3</sub> N <sub>4</sub> /N-C dots	50	None	(300 W, >420 nm) Xe lamp	10% TEOA	212.41	Unknown	[11]
Bi <sub>4</sub> NbO <sub>8</sub> Cl/g-C <sub>3</sub> N <sub>4</sub>	100	1 wt% Pt	(300 W, >420 nm) Xe lamp	20% Lactic acid	287.71	6.85	[10]

## 2.8.4 PN junction

PN junction is structured in the interface of an n-type semiconductor, and a p-type one and the inner electric field from n to p can help photoelectrons transfer to n-type part and photo-excited holes to p-type material. As a result, the recombination of photoinduced electron-hole pairs can be efficaciously restrained. Meanwhile, PN junction is firstly a type II junction. Therefore, if the electron transfer direction of the type II junction coincides with the PN junction, the synergistic effect will occur and strongly boost the PC-HER process. If the directions are opposite, the functions of PN-junction and type II junction will offset each other.

g-C<sub>3</sub>N<sub>4</sub> is an n-type semiconductor, which can help create PN junction with a p-type semiconductor. In Liu's research, g-C<sub>3</sub>N<sub>4</sub> was partly reduced

to be p-type defected g-C<sub>3</sub>N<sub>4</sub> by NaBH<sub>4</sub>, which was then combined with pristine g-C<sub>3</sub>N<sub>4</sub> to form a PN junction.[155] The PC-HER results of the PN junction were 5 times higher than that of pure g-C<sub>3</sub>N<sub>4</sub>. Putri et al. produced PN junction with p-type B-doped graphene and n-type O-doped g-C<sub>3</sub>N<sub>4</sub>, also boosting the PC-HER performance by 4.1 folds.[120] Besides, p-type Cu<sub>3</sub>P[156] and NiO[79] were reported to combine with g-C<sub>3</sub>N<sub>4</sub> to form PN junction as well. Moreover, dual PN junctions of porous-CdS/Cu<sub>2</sub>O/g-C<sub>3</sub>N<sub>4</sub> was covered by Nekouei and co-authors.[157] As a narrow-bandgap material, Cu<sub>2</sub>O can produce photoelectrons very fast. On the one hand, the PN junction of p-type Cu<sub>2</sub>O and n-type porous Cu<sub>2</sub>O transferred photoelectrons from Cu<sub>2</sub>O to CdS, and on the other hand the PN junction of p-type Cu<sub>2</sub>O and n-type g-C<sub>3</sub>N<sub>4</sub> transmitted photoelectrons from Cu<sub>2</sub>O to g-C<sub>3</sub>N<sub>4</sub>. This is the so-called “dual PN junctions”, which could increase the PC-HER rates of g-C<sub>3</sub>N<sub>4</sub> by even 18.4 times.

**Table 2.16** g-C<sub>3</sub>N<sub>4</sub> based PN junctions for PC-HER.

Photocatalyst	Catalyst amount (mg)	Cocatalyst	Optical source	Sacrificial agent	H <sub>2</sub> evolution (μmol h <sup>-1</sup> g <sup>-1</sup> )	Enhanced degree	Ref
Defected g-C <sub>3</sub> N <sub>4</sub> /g-C <sub>3</sub> N <sub>4</sub>	25	3 wt% Pt	(300 W, L40 filter) Xe lamp	10% TEOA	4020	5	[155]
B-rGO/O-g-C <sub>3</sub> N <sub>4</sub>	30	3 wt% Pt	(500 W, AM 1.5 filter) Xe lamp	30% TEOA	273.1	4.1	[16]
Cu <sub>3</sub> P/g-C <sub>3</sub> N <sub>4</sub>	20	3 wt% Pt	(300 W, >420 nm) Xe lamp	10% TEOA	284	Unknown	[156]
NiO/g-C <sub>3</sub> N <sub>4</sub>	10	Ni <sub>2</sub> P	(300 W, >420 nm) Xe lamp	10% TEOA	504	Unknown	[79]
CdS/Cu <sub>2</sub> O/g-C <sub>3</sub> N <sub>4</sub>	20	None	(300 W, AM 1.5 filter) Xe lamp	20% MeOH	1840	18.4	[157]

### **2.8.5 Van der Waals junction**

Currently, with the rapid development of 2D nanomaterials, 2D/2D van der Waals junction has aroused rising concern in various research fields, which is formed by “face to face” contact of two types of 2D nanomaterials. The broad interface can maximize the interactions between the two materials so that the junction can be one of the high-efficiency candidates for PC-HER. Li et al. fabricated the van der Waals junction of 2D g-C<sub>3</sub>N<sub>4</sub> nanosheets and 2D g-C<sub>3</sub>N<sub>4</sub> nanofibers by a copolymerization method with a mixture of melamine and acidized melamine as the precursor.[158] The intimate contact of the junction led to shorter charge-transfer distances and spontaneous electron motions to accelerate PC-HER performance.

### **2.8.6 Summary of heterojunctions**

In summary, plenty of heterojunctions, including Schottky junctions, type II junctions, Z-scheme junctions, PN junctions, and van der Waals junctions, have been synthesized to gain PC-HER enhancement of g-C<sub>3</sub>N<sub>4</sub> with the edges in separating photogenerated electron-hole charges. It is noticeable that dual PN junctions have been obtained, which may encourage us to develop dual Z-scheme junction, dual Schottky junction, and even tertiary junctions. Besides, the combinations among those junctions are also a significant research area.

## 2.9 Other factors for g-C<sub>3</sub>N<sub>4</sub> based PC-HER

There are still other factors influencing g-C<sub>3</sub>N<sub>4</sub> based PC-HER processes, like the amounts of photocatalysts and light sources used in a reaction.

### 2.9.1 Quantity of photocatalysts

Compared with previous reports, it can be found that the amounts of photocatalysts added in a PC-HER process is also an essential factor in the PC-HER efficiency. As shown in Table 2.17, with increasing amounts of g-C<sub>3</sub>N<sub>4</sub>, H<sub>2</sub> evolution ( $\mu\text{mol}\cdot\text{h}^{-1}$ ) grows first and then goes down. The optimal quantity is 50 mg, while the PC-HER rate per gram photocatalysts ( $\mu\text{mol}\cdot\text{h}^{-1}\cdot\text{g}^{-1}$ ) diminishes. These results indicate that there is an optimum value of photocatalyst quantity for a particular PC-HER experiment and that the best amount of photocatalysts should still be optimized with considering economic effectiveness, especially with platinum as the cocatalyst.

**Table 2.17** Different amounts of g-C<sub>3</sub>N<sub>4</sub> for PC-HER.

Photocatalyst	Catalyst amount (mg)	Cocatalyst	Optical source	Sacrificial agent	H <sub>2</sub> evolution ( $\mu\text{mol}\cdot\text{h}^{-1}$ )	PC-HER rate ( $\mu\text{mol}\cdot\text{h}^{-1}\cdot\text{g}^{-1}$ )	Ref.
g-C <sub>3</sub> N <sub>4</sub>	10	3 wt% Pt	(300 W, >420 nm) Xe lamp	10% TEOA	10.24	1024	[111]
g-C <sub>3</sub> N <sub>4</sub>	20	3 wt% Pt	(300 W, >420 nm) Xe lamp	10% TEOA	13	650	[123]
g-C <sub>3</sub> N <sub>4</sub>	50	3 wt% Pt	(300 W, >420 nm) Xe lamp	10% TEOA	19.35	387	[128]
g-C <sub>3</sub> N <sub>4</sub>	100	3 wt% Pt	(300 W, >420 nm) Xe lamp	10% TEOA	17.4	174	[131]

## 2.9.2 Light sources

As shown in Table 2.18, the PC-HER rates of g-C<sub>3</sub>N<sub>4</sub> show quite different results with and without a cut-off filter. Besides, it has not been explored whether PC-HER laws are similar under different light sources. Therefore, the factor of light sources needs to be studied more in the future.

**Table 2.18** Different light sources of g-C<sub>3</sub>N<sub>4</sub> for PC-HER.

Photocatalyst	Catalyst amount (mg)	Cocatalyst	Optical source	Sacrificial agent	HER rate ( $\mu\text{mol}\cdot\text{h}^{-1}\cdot\text{g}^{-1}$ )	Ref.
g-C <sub>3</sub> N <sub>4</sub>	50	3 wt% Pt	(300 W) Xe lamp	10% TEOA	740	[74]
g-C <sub>3</sub> N <sub>4</sub>	50	3 wt% Pt	(300 W, >420 nm) Xe lamp	10% TEOA	387	[128]

## 2.10 Conclusions and perspectives

In conclusion, since Wang et al. firstly applied g-C<sub>3</sub>N<sub>4</sub> in PC-HER in 2009, a lot of g-C<sub>3</sub>N<sub>4</sub> based materials, including g-C<sub>3</sub>N<sub>4</sub> nanosheets, nanotubes, nanobelts, nanospheres, quantum dots, porous g-C<sub>3</sub>N<sub>4</sub>, crystalline g-C<sub>3</sub>N<sub>4</sub>, doped g-C<sub>3</sub>N<sub>4</sub>, g-C<sub>3</sub>N<sub>4</sub> based Schottky junctions, type II junctions, Z-scheme junctions, PN junctions, and van der Waals junctions, were developed to advance the reactivity of g-C<sub>3</sub>N<sub>4</sub>. The ways of these well-designed g-C<sub>3</sub>N<sub>4</sub> based photocatalysts acquiring their enhanced PC-HER performance contain increasing porosity, enlarging the specific surface area, improving the quantity and quality of active sites, shortening the bandgap, broadening the photoabsorption, adjusting the energy band,

strengthening the crystallinity, lowering the electrical impedance, and inhibiting the reintegration of the photogenerated electrons and holes. Furthermore, cocatalysts and sacrificial agents are also playing significant roles in the g-C<sub>3</sub>N<sub>4</sub> based PC-HER processes. While cocatalysts can transfer photoelectrons from g-C<sub>3</sub>N<sub>4</sub> to attached protons, sacrificial agents can effectively consume the photogenerated holes left on the surface of g-C<sub>3</sub>N<sub>4</sub>. Both of them can upgrade the PC-HER rate by several or even thousands of folds. Additionally, other factors, like the temperature of reaction solution, the amount of photocatalysts, and light sources, can also influence the PC-HER results.

Although so many achievements have been acquired in the past decade, the development of g-C<sub>3</sub>N<sub>4</sub> based PC-HER processes is still far from industrial applications, and arduous works in the following directions may be required to boost the reactivity to industrial-grade in the future.

i) Excellent and convenient noble-metal-free cocatalysts are desired to substitute platinum cocatalysts since platinum is too precious while other counterparts are not easy-prepared and stable enough. In recent years, there are abundant two-dimensional (2D) materials reported with good  $\Delta G_{H^*}$ . If sufficient exfoliated 2D cocatalysts and integration with g-C<sub>3</sub>N<sub>4</sub> were obtained, the PC-HER performance might be remarkably boosted.

Besides, single metal atom cocatalysts are still a critical research project, since they can not only maximize the atomic efficiency of the metals but also improve the co-catalytic ability of non-precious metals.

ii) Currently, TEOA is the best sacrificial agent for g-C<sub>3</sub>N<sub>4</sub> based PC-HER operations. However, it will be transformed into TEOA<sup>+</sup>, which is a by-product with little use and needs to be processed. The merit of TEOA being the top scavenger lies in its amino, which can protect g-C<sub>3</sub>N<sub>4</sub> from photo-corrosion. From this point of view, more other chemicals with amino groups can be tried to replace TEOA. Ideally, the new scavengers can be fully oxidized by photo-motivated holes with nitrogen as the by-product. Unlike TEOA<sup>+</sup>, nitrogen can be emitted to the air. Moreover, if the source of the new sacrificial agent candidate is life waste, the effect of “turning waste into treasure” can be gained.

iii) Based on the advanced g-C<sub>3</sub>N<sub>4</sub> photocatalysts as summarized above, more photocatalysts can be developed via their appropriate combination. For example, exfoliated g-C<sub>3</sub>N<sub>4</sub> or doped g-C<sub>3</sub>N<sub>4</sub> nanosheets can be piled with other 2D materials to form van der Waals junctions. In addition, Schottky junctions, type II junctions, Z-scheme junctions, or PN junctions can cooperate with van der Waals junctions to synergistically facilitate PC-HER processes. Last but not least, if exfoliated crystalline g-C<sub>3</sub>N<sub>4</sub> was

utilized to form van der Waals Z-scheme junctions, a very high PC-HER result might be observed.

iv) More factors need to be examined to optimize PC-HER conditions, like temperature, the concentration of photocatalysts, light sources, etc. Notably, the solar heat caused temperature rising, which must be carefully considered for practical PC-HER operations. If PC-HER capacity of a photocatalyst can dramatically increase with temperature, the infrared solar spectrum can participate in the PC-HER processes. As a result, PC-HER efficiency will be raised by a large extent due to the massive percentage of the infrared in the solar light (43%).

## References

- [1] A. Fujishima, K. Honda, Electrochemical Photolysis of Water at a Semiconductor Electrode, *Nature*. 238 (1972) 38–40.
- [2] J. Hong, Y. Wang, Y. Wang, W. Zhang, R. Xu, Noble-metal-free NiS/C<sub>3</sub>N<sub>4</sub> for efficient photocatalytic hydrogen evolution from water, *ChemSusChem*. 6 (2013) 2263–2268.
- [3] M. Wu, J.M. Yan, X.W. Zhang, M. Zhao, Q. Jiang, Ag<sub>2</sub>O modified g-C<sub>3</sub>N<sub>4</sub> for highly efficient photocatalytic hydrogen generation under visible light irradiation, *J. Mater. Chem. A*. 3 (2015) 15710–15714.

- [4] L. Yang, J. Liu, L. Yang, M. Zhang, H. Zhu, F. Wang, J. Yin,  $\text{Co}_3\text{O}_4$  imbedded g- $\text{C}_3\text{N}_4$  heterojunction photocatalysts for visible-light-driven hydrogen evolution, *Renew. Energy*. 145 (2020) 691–698.
- [5] A. Suryawanshi, P. Dhanasekaran, D. Mhamane, S. Kelkar, S. Patil, N. Gupta, S. Ogale, Doubling of photocatalytic  $\text{H}_2$  evolution from g- $\text{C}_3\text{N}_4$  via its nanocomposite formation with multiwall carbon nanotubes: Electronic and morphological effects, *Int. J. Hydrogen Energy*. 37 (2012) 9584–9589.
- [6] X. Li, Y. Zheng, A.F. Masters, T. Maschmeyer, A nano-engineered graphene/carbon nitride hybrid for photocatalytic hydrogen evolution, *J. Energy Chem*. 25 (2016) 225–227.
- [7] C. Cheng, S. Zong, J. Shi, F. Xue, Y. Zhang, X. Guan, B. Zheng, J. Deng, L. Guo, Facile preparation of nanosized MoP as cocatalyst coupled with g- $\text{C}_3\text{N}_4$  by surface bonding state for enhanced photocatalytic hydrogen production, *Appl. Catal. B Environ*. 265 (2020) 118620.
- [8] D. Zeng, T. Zhou, W.J. Ong, M. Wu, X. Duan, W. Xu, Y. Chen, Y.A. Zhu, D.L. Peng, Sub-5 nm Ultra-Fine FeP Nanodots as Efficient Co-Catalysts Modified Porous g- $\text{C}_3\text{N}_4$  for Precious-Metal-Free Photocatalytic Hydrogen Evolution under Visible Light, *ACS Appl. Mater. Interfaces*. (2019).
- [9] S. Fang, Y. Xia, K. Lv, Q. Li, J. Sun, M. Li, Effect of carbon-dots

- modification on the structure and photocatalytic activity of g-C<sub>3</sub>N<sub>4</sub>, *Appl. Catal. B Environ.* 185 (2016) 225–232.
- [10] Y. You, S. Wang, K. Xiao, T. Ma, Y. Zhang, H. Huang, Z-Scheme g-C<sub>3</sub>N<sub>4</sub>/Bi<sub>4</sub>NbO<sub>8</sub>Cl Heterojunction for Enhanced Photocatalytic Hydrogen Production, *ACS Sustain. Chem. Eng.* 6 (2018) 16219–16227.
- [11] Y. Jiao, Q. Huang, J. Wang, Z. He, Z. Li, A novel MoS<sub>2</sub> quantum dots (QDs) decorated Z-scheme g-C<sub>3</sub>N<sub>4</sub> nanosheet/N-doped carbon dots heterostructure photocatalyst for photocatalytic hydrogen evolution, *Appl. Catal. B Environ.* 247 (2019) 124–132.
- [12] Z.F. Huang, J. Song, X. Wang, L. Pan, K. Li, X. Zhang, L. Wang, J.J. Zou, Switching charge transfer of C<sub>3</sub>N<sub>4</sub>/W<sub>18</sub>O<sub>49</sub> from type-II to Z-scheme by interfacial band bending for highly efficient photocatalytic hydrogen evolution, *Nano Energy.* 40 (2017) 308–316.
- [13] Y. Liu, H. Zhang, J. Ke, J. Zhang, W. Tian, X. Xu, X. Duan, H. Sun, M. O Tade, S. Wang, 0D (MoS<sub>2</sub>)/2D (g-C<sub>3</sub>N<sub>4</sub>) heterojunctions in Z-scheme for enhanced photocatalytic and electrochemical hydrogen evolution, *Appl. Catal. B Environ.* 228 (2018) 64–74.
- [14] X. Wang, M. Kazuhiko, T. Arne, T. Kazuhiro, X. Gang, C.J. M., D. Kazunari, A. Markus, A metal-free polymeric photocatalyst for hydrogen production from water under visible light, *Nat. Mater.* 8

(2009) 76–80.

- [15] B. Chai, T. Peng, J. Mao, K. Li, L. Zan, Graphitic carbon nitride (g-C<sub>3</sub>N<sub>4</sub>)-Pt-TiO<sub>2</sub> nanocomposite as an efficient photocatalyst for hydrogen production under visible light irradiation, *Phys. Chem. Chem. Phys.* 14 (2012) 16745–16752.
- [16] L.K. Putri, B.J. Ng, W.J. Ong, H.W. Lee, W.S. Chang, S.P. Chai, Engineering nanoscale p-n junction: Via the synergetic dual-doping of p-type boron-doped graphene hybridized with n-type oxygen-doped carbon nitride for enhanced photocatalytic hydrogen evolution, *J. Mater. Chem. A*. 6 (2018) 3181–3194.
- [17] X.W. Guo, S.M. Chen, H.J. Wang, Z.M. Zhang, H. Lin, L. Song, T.B. Lu, Single-atom molybdenum immobilized on photoactive carbon nitride as efficient photocatalysts for ambient nitrogen fixation in pure water, *J. Mater. Chem. A*. 7 (2019) 19831–19837.
- [18] T. Niisoe, K.H. Harada, T. Hitomi, T. Watanabe, N.N. Hung, H. Ishikawa, Z. Wang, A. Koizumi, Environmental ecological modeling of human blood lead levels in East Asia, *Environ. Sci. Technol.* 45 (2011) 2856–2862.
- [19] C.H. Lai, Y.M. Lee, C.F. Tseng, C.Y. Liu, Resistance transition in NiO thin film and its temperature dependence, *Ferroelectrics*. 435 (2012) 155–160.
- [20] L. Li, W. Wang, L. He, J. Zhang, Z. Wu, B. Zhang, Y. Liu, Synthesis

- and characterization of p-type NiO films suitable for normally-off AlGaIn/GaN HFETs application, *Mater. Sci. Semicond. Process.* 67 (2017) 141–146.
- [21] J. Ran, B. Zhu, S.Z. Qiao, Phosphorene Co-catalyst Advancing Highly Efficient Visible-Light Photocatalytic Hydrogen Production, *Angew. Chemie - Int. Ed.* 56 (2017) 10373–10377.
- [22] Q. Han, B. Wang, J. Gao, L. Qu, Graphitic Carbon Nitride/Nitrogen-Rich Carbon Nanofibers: Highly Efficient Photocatalytic Hydrogen Evolution without Cocatalysts, *Angew. Chemie - Int. Ed.* 55 (2016) 10849–10853.
- [23] A. Science, E. Content, Air Pollution – Related Illness :, *Science* (80-. ). 804 (2014).
- [24] Y. Zhu, C. Lv, Z. Yin, J. Ren, X. Yang, C.L. Dong, H. Liu, R. Cai, Y.C. Huang, W. Theis, S. Shen, D. Yang, [001]-Oriented Hittorf's Phosphorus Nanorods/Polymeric Carbon Nitride Heterostructure for Boosting Wide-Spectrum-Responsive Photocatalytic Hydrogen Evolution from Pure Water, *Angew. Chemie - Int. Ed.* 030051 (2019).
- [25] B.D. Ravetz, A.B. Pun, E.M. Churchill, D.N. Congreve, T. Rovis, L.M. Campos, Photoredox catalysis using infrared light via triplet fusion upconversion, *Nature.* 565 (2019) 343–346.
- [26] M. Escudero, J.F. Marco, A. Cuesta, Surface decoration at the

- atomic scale using a molecular pattern: Copper adsorption on cyanide-Modified pt(111) electrodes, *J. Phys. Chem. C.* 113 (2009) 12340–12344.
- [27] X. Fan, L. Zhang, M. Wang, W. Huang, Y. Zhou, M. Li, R. Cheng, J. Shi, Constructing carbon-nitride-based copolymers via Schiff base chemistry for visible-light photocatalytic hydrogen evolution, *Appl. Catal. B Environ.* 182 (2016) 68–73.
- [28] S. Thaweesak, M. Lyu, P. Peerakiatkhajohn, T. Butburee, B. Luo, H. Chen, L. Wang, Two-dimensional g-C<sub>3</sub>N<sub>4</sub>/Ca<sub>2</sub>Nb<sub>2</sub>TaO<sub>10</sub> nanosheet composites for efficient visible light photocatalytic hydrogen evolution, *Appl. Catal. B Environ.* 202 (2017) 184–190.
- [29] X. She, J. Wu, J. Zhong, H. Xu, Y. Yang, R. Vajtai, J. Lou, Y. Liu, D. Du, H. Li, P.M. Ajayan, Oxygenated monolayer carbon nitride for excellent photocatalytic hydrogen evolution and external quantum efficiency, *Nano Energy.* 27 (2016) 138–146.
- [30] S. Guo, Y. Tang, Y. Xie, C. Tian, Q. Feng, W. Zhou, B. Jiang, P-doped tubular g-C<sub>3</sub>N<sub>4</sub> with surface carbon defects: Universal synthesis and enhanced visible-light photocatalytic hydrogen production, *Appl. Catal. B Environ.* 218 (2017) 664–671.
- [31] N.L. Panwar, S.C. Kaushik, S. Kothari, Role of renewable energy sources in environmental protection: A review, *Renew. Sustain. Energy Rev.* 15 (2011) 1513–1524.

- [32] V.G. Kunde, F.M. Flasar, D.E. Jennings, B. Bézard, D.F. Strobel, B.J. Conrath, C.A. Nixon, G.L. Bjoraker, P.N. Romani, R.K. Achterberg, A.A. Simon-Miller, P. Irwin, J.C. Brasunas, J.C. Pearl, M.D. Smith, G.S. Orton, P.J. Gierasch, L.J. Spilker, R.C. Carlson, A.A. Mamoutkine, S.B. Calcutt, P.L. Read, F.W. Taylor, T. Fouchet, P. Parrish, A. Barucci, R. Courtin, A. Coustenis, D. Gautier, E. Lellouch, A. Marten, R. Prangé, Y. Biraud, C. Ferrari, T.C. Owen, M.M. Abbas, R.E. Samuelson, F. Raulin, P. Ade, C.J. Césarsky, K.U. Grossman, A. Coradini, Jupiter's atmospheric composition from the Cassini thermal infrared spectroscopy experiment, *Science* (80-. ). 305 (2004) 1582–1586.
- [33] P. Poizot, F. Dolhem, Clean energy new deal for a sustainable world: From non-CO<sub>2</sub> generating energy sources to greener electrochemical storage devices, *Energy Environ. Sci.* 4 (2011) 2003–2019.
- [34] N.L. Rosi, J. Eckert, M. Eddaoudi, D.T. Vodak, J. Kim, M. O'Keeffe, O.M. Yaghi, Hydrogen storage in microporous metal-organic frameworks, *Science* (80-. ). 300 (2003) 1127–1129.
- [35] E. Kroke, M. Schwarz, E. Horath-Bordon, P. Kroll, B. Noll, A.D. Norman, Tri-s-triazine derivatives. Part I. From trichloro-tri-s-triazine to graphitic C<sub>3</sub>N<sub>4</sub> structures, *New J. Chem.* 26 (2002) 508–512.
- [36] L. Ma, H. Fan, J. Wang, Y. Zhao, H. Tian, G. Dong, *Applied*

- Catalysis B : Environmental Water-assisted ions in situ intercalation for porous polymeric graphitic carbon nitride nanosheets with superior photocatalytic hydrogen evolution performance, "Applied Catal. B, Environ. 190 (2016) 93–102.
- [37] K.S. Lakhi, D.H. Park, G. Singh, S.N. Talapaneni, U. Ravon, K. Al-Bahily, A. Vinu, Energy efficient synthesis of highly ordered mesoporous carbon nitrides with uniform rods and their superior CO<sub>2</sub> adsorption capacity, *J. Mater. Chem. A*. 5 (2017) 16220–16230.
- [38] K. Li, Y.Z. Lin, K. Wang, Y. Wang, Y. Zhang, Y. Zhang, F.T. Liu, Rational design of cocatalyst system for improving the photocatalytic hydrogen evolution activity of graphite carbon nitride, *Appl. Catal. B Environ.* 268 (2020) 118402.
- [39] Y. Li, W. Ho, K. Lv, B. Zhu, S.C. Lee, Carbon vacancy-induced enhancement of the visible light-driven photocatalytic oxidation of NO over g-C<sub>3</sub>N<sub>4</sub> nanosheets, *Appl. Surf. Sci.* 430 (2018) 380–389.
- [40] P. Sharma, Y. Sasson, A photoactive catalyst Ru-g-C<sub>3</sub>N<sub>4</sub> for hydrogen transfer reaction of aldehydes and ketones, *Green Chem.* 19 (2017) 844–852.
- [41] T. Giannakopoulou, I. Papailias, N. Todorova, N. Boukos, Y. Liu, J. Yu, C. Trapalis, Tailoring the energy band gap and edges' potentials of g-C<sub>3</sub>N<sub>4</sub>/TiO<sub>2</sub> composite photocatalysts for NO<sub>x</sub> removal, *Chem. Eng. J.* 310 (2017) 571–580.

- [42] Y. Zeng, C. Liu, L. Wang, S. Zhang, Y. Ding, Y. Xu, Y. Liu, S. Luo, A three-dimensional graphitic carbon nitride belt network for enhanced visible light photocatalytic hydrogen evolution, *J. Mater. Chem. A*. 4 (2016) 19003–19010.
- [43] Y. Zhu, Y. Xu, Y. Hou, Z. Ding, X. Wang, Cobalt sulfide modified graphitic carbon nitride semiconductor for solar hydrogen production, *Int. J. Hydrogen Energy*. 39 (2014) 11873–11879.
- [44] K.C. Devarayapalli, S.V.P. Vattikuti, T.V.M. Sreekanth, K.S. Yoo, P.C. Nagajyothi, J. Shim, Hydrogen production and photocatalytic activity of g-C<sub>3</sub>N<sub>4</sub>/Co-MOF (ZIF-67) nanocomposite under visible light irradiation, *Appl. Organomet. Chem.* 34 (2020) 1–9.
- [45] X. Li, H. Zhang, Y. Liu, X. Duan, X. Xu, S. Liu, H. Sun, S. Wang, Synergy of NiO quantum dots and temperature on enhanced photocatalytic and thermophoto hydrogen evolution, *Chem. Eng. J.* 390 (2020) 124634.
- [46] B. Zhu, P. Xia, Y. Li, W. Ho, J. Yu, Fabrication and photocatalytic activity enhanced mechanism of direct Z-scheme g-C<sub>3</sub>N<sub>4</sub> /Ag<sub>2</sub>WO<sub>4</sub> photocatalyst, *Appl. Surf. Sci.* 391 (2017) 175–183.
- [47] I. Papailias, T. Giannakopoulou, N. Todorova, D. Demotikali, T. Vaimakis, C. Trapalis, Effect of processing temperature on structure and photocatalytic properties of g-C<sub>3</sub>N<sub>4</sub>, *Appl. Surf. Sci.* 358 (2015) 278–286.

- [48] Z. Huang, F. Li, B. Chen, G. Yuan, Cycloaddition of CO<sub>2</sub> and epoxide catalyzed by amino- and hydroxyl-rich graphitic carbon nitride, *Catal. Sci. Technol.* 6 (2016) 2942–2948.
- [49] B. Zhu, J. Zhang, C. Jiang, B. Cheng, J. Yu, First principle investigation of halogen-doped monolayer g-C<sub>3</sub>N<sub>4</sub> photocatalyst, *Appl. Catal. B Environ.* 207 (2017) 27–34.
- [50] D. Jiang, L. Chen, J. Xie, M. Chen, Ag<sub>2</sub>S/g-C<sub>3</sub>N<sub>4</sub> composite photocatalysts for efficient Pt-free hydrogen production. the co-catalyst function of Ag/Ag<sub>2</sub>S formed by simultaneous photodeposition, *Dalt. Trans.* 43 (2014) 4878–4885.
- [51] F. Xue, M. Liu, C. Cheng, J. Deng, J. Shi, Localized NiS<sub>2</sub> Quantum Dots on g-C<sub>3</sub>N<sub>4</sub> Nanosheets for Efficient Photocatalytic Hydrogen Production from Water, *ChemCatChem.* 10 (2018) 5441–5448.
- [52] S.S. Shinde, A. Sami, J.H. Lee, Sulfur mediated graphitic carbon nitride/S-Se-graphene as a metal-free hybrid photocatalyst for pollutant degradation and water splitting, *Carbon N. Y.* 96 (2016) 929–936.
- [53] G. Liao, Y. Gong, L. Zhang, H. Gao, G.J. Yang, B. Fang, Semiconductor polymeric graphitic carbon nitride photocatalysts: The “holy grail” for the photocatalytic hydrogen evolution reaction under visible light, *Energy Environ. Sci.* 12 (2019) 2080–2147.
- [54] Y.S. Jun, E.Z. Lee, X. Wang, W.H. Hong, G.D. Stucky, A. Thomas,

- From melamine-cyanuric acid supramolecular aggregates to carbon nitride hollow spheres, *Adv. Funct. Mater.* 23 (2013) 3661–3667.
- [55] M.K. Bhunia, K. Yamauchi, K. Takanebe, Harvesting solar light with crystalline carbon nitrides for efficient photocatalytic hydrogen evolution, *Angew. Chemie - Int. Ed.* 53 (2014) 11001–11005.
- [56] Y.P. Yuan, L.S. Yin, S.W. Cao, L.N. Gu, G.S. Xu, P. Du, H. Chai, Y. Sen Liao, C. Xue, Microwave-assisted heating synthesis: A general and rapid strategy for large-scale production of highly crystalline g-C<sub>3</sub>N<sub>4</sub> with enhanced photocatalytic H<sub>2</sub> production, *Green Chem.* 16 (2014) 4663–4668.
- [57] X. Wang, K. Maeda, X. Chen, K. Takanebe, K. Domen, Y. Hou, X. Fu, M. Antonietti, Polymer semiconductors for artificial photosynthesis: Hydrogen evolution by mesoporous graphitic carbon nitride with visible light, *J. Am. Chem. Soc.* 131 (2009) 1680–1681.
- [58] Z. Zhao, Y. Dai, J. Lin, G. Wang, Highly-ordered mesoporous carbon nitride with ultrahigh surface area and pore volume as a superior dehydrogenation catalyst, *Chem. Mater.* 26 (2014) 3151–3161.
- [59] H. Yan, Soft-templating synthesis of mesoporous graphitic carbon nitride with enhanced photocatalytic H<sub>2</sub> evolution under visible light, *Chem. Commun.* 48 (2012) 3430–3432.

- [60] J. Liu, T. Zhang, Z. Wang, G. Dawson, W. Chen, Simple pyrolysis of urea into graphitic carbon nitride with recyclable adsorption and photocatalytic activity, *J. Mater. Chem.* 21 (2011) 14398–14401.
- [61] M.J. Bojdys, J.O. Müller, M. Antonietti, A. Thomas, Ionothermal synthesis of crystalline, condensed, graphitic carbon nitride, *Chem. - A Eur. J.* 14 (2008) 8177–8182.
- [62] V. Kumaravel, M.D. Imam, A. Badreldin, R.K. Chava, J.Y. Do, M. Kang, A. Abdel-Wahab, Photocatalytic hydrogen production: Role of sacrificial reagents on the activity of oxide, carbon, and sulfide catalysts, *Catalysts.* 9 (2019).
- [63] Y. Pellegrin, F. Odobel, Les donneurs d'électron sacrificiels pour la production de combustible solaire, *Comptes Rendus Chim.* 20 (2017) 283–295.
- [64] J. Liu, H. Xu, J. Yan, J. Huang, Y. Song, J. Deng, J. Wu, C. Ding, X. Wu, S. Yuan, H. Li, Efficient photocatalytic hydrogen evolution mediated by defect-rich 1T-PtS<sub>2</sub> atomic layer nanosheet modified mesoporous graphitic carbon nitride, *J. Mater. Chem. A.* 7 (2019) 18906–18914.
- [65] D. Zheng, G. Zhang, Y. Hou, X. Wang, Layering MoS<sub>2</sub> on soft hollow g-C<sub>3</sub>N<sub>4</sub> nanostructures for photocatalytic hydrogen evolution, *Appl. Catal. A Gen.* 521 (2016) 2–8.
- [66] Y. Hou, Y. Zhu, Y. Xu, X. Wang, Photocatalytic hydrogen

- production over carbon nitride loaded with WS<sub>2</sub> as cocatalyst under visible light, *Appl. Catal. B Environ.* 156–157 (2014) 122–127.
- [67] L. Yin, Y.P. Yuan, S.W. Cao, Z. Zhang, C. Xue, Enhanced visible-light-driven photocatalytic hydrogen generation over g-C<sub>3</sub>N<sub>4</sub> through loading the noble metal-free NiS<sub>2</sub> cocatalyst, *RSC Adv.* 4 (2014) 6127–6132.
- [68] J. Yi, X. She, Y. Song, M. Mao, K. Xia, Y. Xu, Z. Mo, J. Wu, H. Xu, H. Li, Solvothermal synthesis of metallic 1T-WS<sub>2</sub>: A supporting cocatalyst on carbon nitride nanosheets toward photocatalytic hydrogen evolution, *Chem. Eng. J.* 335 (2018) 282–289.
- [69] J. Bi, L. Zhu, J. Wu, Y. Xu, Z. Wang, X. Zhang, Y. Han, Optimizing electronic structure and charge transport of sulfur/potassium co-doped graphitic carbon nitride with efficient photocatalytic hydrogen evolution performance, *Appl. Organomet. Chem.* 33 (2019) 1–13.
- [70] L. Shi, F. Wang, J. Sun, The preparation of spherical mesoporous g-C<sub>3</sub>N<sub>4</sub> with highly improved photocatalytic performance for H<sub>2</sub> production and rhodamine B degradation, *Mater. Res. Bull.* 113 (2019) 115–121.
- [71] J.K. Nørskov, T. Bligaard, A. Logadottir, J.R. Kitchin, J.G. Chen, S. Pandelov, U. Stimming, Trends in the Exchange Current for Hydrogen Evolution, *J. Electrochem. Soc.* 152 (2005) J23.

- [72] S. Liang, Y. Xia, S. Zhu, S. Zheng, Y. He, J. Bi, M. Liu, L. Wu, Au and Pt co-loaded g-C<sub>3</sub>N<sub>4</sub> nanosheets for enhanced photocatalytic hydrogen production under visible light irradiation, *Appl. Surf. Sci.* 358 (2015) 304–312.
- [73] M. Song, Y. Wu, X. Wang, M. Liu, Y. Su, Switching charge transfer process of carbon nitride and bismuth vanadate by anchoring silver nanoparticle toward cocatalyst free water reduction, *J. Colloid Interface Sci.* 529 (2018) 375–384.
- [74] X. Li, W. Bi, L. Zhang, S. Tao, W. Chu, Q. Zhang, Y. Luo, C. Wu, Y. Xie, Single-Atom Pt as Co-Catalyst for Enhanced Photocatalytic H<sub>2</sub>Evolution, *Adv. Mater.* 28 (2016) 2427–2431.
- [75] S. Cao, H. Li, T. Tong, H.C. Chen, A. Yu, J. Yu, H.M. Chen, Single-Atom Engineering of Directional Charge Transfer Channels and Active Sites for Photocatalytic Hydrogen Evolution, *Adv. Funct. Mater.* 28 (2018) 1–9.
- [76] Z. Zeng, Y. Su, X. Quan, W. Choi, G. Zhang, N. Liu, B. Kim, S. Chen, H. Yu, S. Zhang, Single-atom platinum confined by the interlayer nanospace of carbon nitride for efficient photocatalytic hydrogen evolution, *Nano Energy.* 69 (2020) 104409.
- [77] G. Zhang, G. Li, X. Wang, Surface Modification of Carbon Nitride Polymers by Core-Shell Nickel/Nickel Oxide Cocatalysts for Hydrogen Evolution Photocatalysis, *ChemCatChem.* 7 (2015)

2864–2870.

- [78] J. Liu, Q. Jia, J. Long, X. Wang, Z. Gao, Q. Gu, Amorphous NiO as co-catalyst for enhanced visible-light-driven hydrogen generation over g-C<sub>3</sub>N<sub>4</sub> photocatalyst, *Appl. Catal. B Environ.* 222 (2018) 35–43.
- [79] J.W. Shi, Y. Zou, L. Cheng, D. Ma, D. Sun, S. Mao, L. Sun, C. He, Z. Wang, In-situ phosphating to synthesize Ni<sub>2</sub>P decorated NiO/g-C<sub>3</sub>N<sub>4</sub> p-n junction for enhanced photocatalytic hydrogen production, *Chem. Eng. J.* 378 (2019) 122161.
- [80] L. Yang, H. Li, Y. Yu, H. Yu, Study on the cocatalytic performance of nickel species in g-C<sub>3</sub>N<sub>4</sub> system for photocatalytic hydrogen evolution, *Catal. Commun.* 110 (2018) 51–54.
- [81] A. Kheradmand, Y. Zhu, W. Zhang, A. Marianov, Y. Jiang, Cobalt oxide on mesoporous carbon nitride for improved photocatalytic hydrogen production under visible light irradiation, *Int. J. Hydrogen Energy.* 44 (2019) 17930–17942.
- [82] Z. Chen, P. Sun, B. Fan, Z. Zhang, X. Fang, In situ template-free ion-exchange process to prepare visible-light-active g-C<sub>3</sub>N<sub>4</sub>/NiS hybrid photocatalysts with enhanced hydrogen evolution activity, *J. Phys. Chem. C.* 118 (2014) 7801–7807.
- [83] Y. Lu, D. Chu, M. Zhu, Y. Du, P. Yang, Exfoliated carbon nitride nanosheets decorated with NiS as an efficient noble-metal-free

- visible-light-driven photocatalyst for hydrogen evolution, *Phys. Chem. Chem. Phys.* 17 (2015) 17355–17361.
- [84] H. Zhao, H. Zhang, G. Cui, Y. Dong, G. Wang, P. Jiang, X. Wu, N. Zhao, A photochemical synthesis route to typical transition metal sulfides as highly efficient cocatalyst for hydrogen evolution: from the case of NiS/g-C<sub>3</sub>N<sub>4</sub>, *Appl. Catal. B Environ.* 225 (2018) 284–290.
- [85] B. Wang, J. Pan, Z. Jiang, Z. Dong, C. Zhao, J. Wang, C. Song, Y. Zheng, C. Li, The bimetallic iron–nickel sulfide modified g-C<sub>3</sub>N<sub>4</sub> nano-heterojunction and its photocatalytic hydrogen production enhancement, *J. Alloys Compd.* 766 (2018) 421–428.
- [86] H. Xu, J. Yi, X. She, Q. Liu, L. Song, S. Chen, Y. Yang, Y. Song, R. Vajtai, J. Lou, H. Li, S. Yuan, J. Wu, P.M. Ajayan, 2D heterostructure comprised of metallic 1T-MoS<sub>2</sub>/Monolayer O-g-C<sub>3</sub>N<sub>4</sub> towards efficient photocatalytic hydrogen evolution, *Appl. Catal. B Environ.* 220 (2018) 379–385.
- [87] Z. Liang, B. Sun, X. Xu, H. Cui, J. Tian, Metallic 1T-phase MoS<sub>2</sub> quantum dots/g-C<sub>3</sub>N<sub>4</sub> heterojunctions for enhanced photocatalytic hydrogen evolution, *Nanoscale.* 11 (2019) 12266–12274.
- [88] M. Shao, Y. Shao, S. Ding, J. Wang, J. Xu, Y. Qu, X. Zhong, X. Chen, W.F. Ip, N. Wang, B. Xu, X. Shi, X. Wang, H. Pan, Vanadium disulfide decorated graphitic carbon nitride for super-efficient solar-

- driven hydrogen evolution, *Appl. Catal. B Environ.* 237 (2018) 295–301.
- [89] M. Shao, W. Chen, S. Ding, K.H. Lo, X. Zhong, L. Yao, W.F. Ip, B. Xu, X. Wang, H. Pan,  $WX_y/g-C_3N_4$  ( $WX_y=W_2C$ ,  $WS_2$ , or  $W_2N$ ) Composites for Highly Efficient Photocatalytic Water Splitting, *ChemSusChem*. 12 (2019) 3355–3362.
- [90] J. Ran, G. Gao, F.T. Li, T.Y. Ma, A. Du, S.Z. Qiao,  $Ti_3C_2$  MXene co-catalyst on metal sulfide photo-absorbers for enhanced visible-light photocatalytic hydrogen production, *Nat. Commun.* 8 (2017) 1–10.
- [91] Y. Li, L. Ding, Y. Guo, Z. Liang, H. Cui, J. Tian, Boosting the Photocatalytic Ability of  $g-C_3N_4$  for Hydrogen Production by  $Ti_3C_2$  MXene Quantum Dots, *ACS Appl. Mater. Interfaces*. 11 (2019) 41440–41447.
- [92] A. Indra, A. Acharjya, P.W. Menezes, C. Merschjann, D. Hollmann, M. Schwarze, M. Aktas, A. Friedrich, S. Lochbrunner, A. Thomas, M. Driess, Boosting Visible-Light-Driven Photocatalytic Hydrogen Evolution with an Integrated Nickel Phosphide–Carbon Nitride System, *Angew. Chemie - Int. Ed.* 56 (2017) 1653–1657.
- [93] W. Wang, T. An, G. Li, D. Xia, H. Zhao, J.C. Yu, P.K. Wong, Earth-abundant  $Ni_2P/g-C_3N_4$  lamellar nanohybrids for enhanced photocatalytic hydrogen evolution and bacterial inactivation under

- visible light irradiation, *Appl. Catal. B Environ.* 217 (2017) 570–580.
- [94] D. Zeng, W. Xu, W.J. Ong, J. Xu, H. Ren, Y. Chen, H. Zheng, D.L. Peng, Toward noble-metal-free visible-light-driven photocatalytic hydrogen evolution: Monodisperse sub–15 nm Ni<sub>2</sub>P nanoparticles anchored on porous g-C<sub>3</sub>N<sub>4</sub> nanosheets to engineer 0D-2D heterojunction interfaces, *Appl. Catal. B Environ.* 221 (2018) 47–55.
- [95] P. Wen, K. Zhao, H. Li, J. Li, J. Li, Q. Ma, S.M. Geyer, L. Jiang, Y. Qiu, In situ decorated Ni<sub>2</sub>P nanocrystal co-catalysts on g-C<sub>3</sub>N<sub>4</sub> for efficient and stable photocatalytic hydrogen evolution via a facile co-heating method, *J. Mater. Chem. A.* 8 (2020) 2995–3004.
- [96] S.S. Yi, J.M. Yan, B.R. Wulan, S.J. Li, K.H. Liu, Q. Jiang, Noble-metal-free cobalt phosphide modified carbon nitride: An efficient photocatalyst for hydrogen generation, *Appl. Catal. B Environ.* 200 (2017) 477–483.
- [97] Y. Zeng, Y. Xia, W. Song, S. Luo, Visual observation of hydrogen bubble generation from monodisperse CoP QDs on ultrafine g-C<sub>3</sub>N<sub>4</sub> fiber under visible light irradiation, *J. Mater. Chem. A.* 7 (2019) 25908–25914.
- [98] Z. Sun, M. Fujitsuka, C. Shi, M. Zhu, A. Wang, T. Majima, Efficient Visible-Light-Driven Hydrogen Generation on g-C<sub>3</sub>N<sub>4</sub> Coupled with Iron Phosphide, *ChemPhotoChem.* 3 (2019) 540–544.

- [99] J. Wang, J. Chen, P. Wang, J. Hou, C. Wang, Y. Ao, Robust photocatalytic hydrogen evolution over amorphous ruthenium phosphide quantum dots modified g-C<sub>3</sub>N<sub>4</sub> nanosheet, *Appl. Catal. B Environ.* 239 (2018) 578–585.
- [100] M. Zhu, S. Kim, L. Mao, M. Fujitsuka, J. Zhang, X. Wang, T. Majima, Metal-Free Photocatalyst for H<sub>2</sub> Evolution in Visible to Near-Infrared Region: Black Phosphorus/Graphitic Carbon Nitride, *J. Am. Chem. Soc.* 139 (2017) 13234–13242.
- [101] J. Ran, W. Guo, H. Wang, B. Zhu, J. Yu, S.Z. Qiao, Metal-Free 2D/2D Phosphorene/g-C<sub>3</sub>N<sub>4</sub> Van der Waals Heterojunction for Highly Enhanced Visible-Light Photocatalytic H<sub>2</sub> Production, *Adv. Mater.* 30 (2018).
- [102] S. Yang, Y. Gong, J. Zhang, L. Zhan, L. Ma, Z. Fang, R. Vajtai, X. Wang, P.M. Ajayan, Exfoliated graphitic carbon nitride nanosheets as efficient catalysts for hydrogen evolution under visible light, *Adv. Mater.* 25 (2013) 2452–2456.
- [103] Q. Han, F. Zhao, C. Hu, L. Lv, Z. Zhang, N. Chen, L. Qu, Facile production of ultrathin graphitic carbon nitride nanoplatelets for efficient visible-light water splitting, 8 (2015) 1718–1728.
- [104] J. Zhang, Y. Hou, S. Wang, X. Zhu, C. Zhu, Z. Wang, C. Li, J. Jiang, H. Wang, M. Pan, C. Su, A facile method for scalable synthesis of ultrathin g-C<sub>3</sub>N<sub>4</sub> nanosheets for efficient hydrogen production,

- (2018) 18252–18257.
- [105] Z. Fang, Y. Hong, D. Li, B. Luo, B. Mao, W. Shi, One-Step Nickel Foam Assisted Synthesis of Holey G - Carbon Nitride Nanosheets for Efficient Visible-Light Photocatalytic H<sub>2</sub> Evolution, (2018).
- [106] Y. Zhu, A. Marianov, H. Xu, C. Lang, Y. Jiang, Bimetallic Ag-Cu Supported on Graphitic Carbon Nitride Nanotubes for Improved Visible-Light Photocatalytic Hydrogen Production, ACS Appl. Mater. Interfaces. 10 (2018) 9468–9477.
- [107] J. Wu, N. Li, X.H. Zhang, H. Bin Fang, Y.Z. Zheng, X. Tao, Heteroatoms binary-doped hierarchical porous g-C<sub>3</sub>N<sub>4</sub> nanobelts for remarkably enhanced visible-light-driven hydrogen evolution, Appl. Catal. B Environ. 226 (2018) 61–70.
- [108] D. Zheng, C. Pang, Y. Liu, X. Wang, Shell-engineering of hollow g-C<sub>3</sub>N<sub>4</sub> nanospheres via copolymerization for photocatalytic hydrogen evolution, Chem. Commun. 51 (2015) 9706–9709.
- [109] Y. Wang, Y. Li, J. Zhao, J. Wang, Z. Li, ScienceDirect heterojunction photocatalysts for hydrogen evolution under visible light, Int. J. Hydrogen Energy. 44 (2018) 618–628.
- [110] S. Chen, As featured in : Nanoscale Porous graphitic carbon nitride synthesized via direct polymerization of urea for efficient sunlight-driven photocatalytic hydrogen production †, (2012).
- [111] Q. Liang, Z. Li, X. Yu, Z. Huang, F. Kang, Macroscopic 3D Porous

Graphitic Carbon Nitride Monolith for Enhanced Photocatalytic Hydrogen Evolution, (2015) 4634–4639.

- [112] Z. Huang, J. Song, L. Pan, Z. Wang, Carbon nitride with simultaneous porous network and O-doping for efficient solar-energy-driven hydrogen evolution, *Nano Energy*. 12 (2015) 646–656.
- [113] Q. Gu, Y. Liao, L. Yin, J. Long, X. Wang, C. Xue, *Applied Catalysis B: Environmental* Template-free synthesis of porous graphitic carbon nitride microspheres for enhanced photocatalytic hydrogen generation with high stability, "Applied Catal. B, Environ. 165 (2015) 503–510.
- [114] D. Zhang, Y. Guo, Z. Zhao, *Applied Catalysis B: Environmental* Porous defect-modified graphitic carbon nitride via a facile one-step approach with significantly enhanced photocatalytic hydrogen evolution under visible light irradiation, *Appl. Catal. B Environ.* 226 (2018) 1–9.
- [115] M. Wu, J. Zhang, B. bei He, H. wen Wang, R. Wang, Y. sheng Gong, In-situ construction of coral-like porous P-doped g-C<sub>3</sub>N<sub>4</sub> tubes with hybrid 1D/2D architecture and high efficient photocatalytic hydrogen evolution, *Appl. Catal. B Environ.* 241 (2019) 159–166.
- [116] Y. Zhou, W. Lv, B. Zhu, F. Tong, J. Pan, J. Bai, Q. Zhou, H. Qin, Template-Free One-Step Synthesis of g-C<sub>3</sub>N<sub>4</sub> Nanosheets with

- Simultaneous Porous Network and S-Doping for Remarkable Visible-Light-Driven Hydrogen Evolution, *ACS Sustain. Chem. Eng.* 7 (2019) 5801–5807.
- [117] X. Gao, J. Feng, D. Su, Y. Ma, G. Wang, H. Ma, J. Zhang, In-situ exfoliation of porous carbon nitride nanosheets for enhanced hydrogen evolution, *Nano Energy.* 59 (2019) 598–609.
- [118] L. Jing, D. Wang, Y. Xu, M. Xie, J. Yan, M. He, Z. Song, H. Xu, H. Li, Porous defective carbon nitride obtained by a universal method for photocatalytic hydrogen production from water splitting, *J. Colloid Interface Sci.* 566 (2020) 171–182.
- [119] Z. Zeng, H. Yu, X. Quan, S. Chen, S. Zhang, Structuring phase junction between tri-s-triazine and triazine crystalline  $C_3N_4$  for efficient photocatalytic hydrogen evolution, *Appl. Catal. B Environ.* 227 (2018) 153–160.
- [120] L. Lin, W. Ren, C. Wang, A.M. Asiri, J. Zhang, X. Wang, Crystalline carbon nitride semiconductors prepared at different temperatures for photocatalytic hydrogen production, *Appl. Catal. B Environ.* 231 (2018) 234–241.
- [121] H. Ou, L. Lin, Y. Zheng, P. Yang, Y. Fang, X. Wang, Tri-s-triazine-Based Crystalline Carbon Nitride Nanosheets for an Improved Hydrogen Evolution, *Adv. Mater.* 29 (2017).
- [122] Y. Xu, X. He, H. Zhong, D.J. Singh, L. Zhang, R. Wang, Solid salt

- confinement effect: An effective strategy to fabricate high crystalline polymer carbon nitride for enhanced photocatalytic hydrogen evolution, *Appl. Catal. B Environ.* 246 (2019) 349–355.
- [123] L. Zhang, N. Ding, M. Hashimoto, K. Iwasaki, N. Chikamori, K. Nakata, Y. Xu, J. Shi, H. Wu, Y. Luo, D. Li, A. Fujishima, Q. Meng, Sodium-doped carbon nitride nanotubes for efficient visible light-driven hydrogen production, *Nano Res.* 11 (2018) 2295–2309.
- [124] N. Sagara, S. Kamimura, T. Tsubota, T. Ohno, Photoelectrochemical CO<sub>2</sub> reduction by a p-type boron-doped g-C<sub>3</sub>N<sub>4</sub> electrode under visible light, *Appl. Catal. B Environ.* 192 (2016) 193–198.
- [125] J. Li, B. Shen, Z. Hong, B. Lin, B. Gao, Y. Chen, A facile approach to synthesize novel oxygen-doped g-C<sub>3</sub>N<sub>4</sub> with superior visible-light photoreactivity, *Chem. Commun.* 48 (2012) 12017–12019.
- [126] Y. Wang, S. Zhao, Y. Zhang, J. Fang, Y. Zhou, S. Yuan, C. Zhang, W. Chen, One-pot synthesis of K-doped g-C<sub>3</sub>N<sub>4</sub> nanosheets with enhanced photocatalytic hydrogen production under visible-light irradiation, *Appl. Surf. Sci.* 440 (2018) 258–265.
- [127] Z.A. Lan, G. Zhang, X. Wang, A facile synthesis of Br-modified g-C<sub>3</sub>N<sub>4</sub> semiconductors for photoredox water splitting, *Appl. Catal. B Environ.* 192 (2016) 116–125.
- [128] Q. Han, C. Hu, F. Zhao, Z. Zhang, N. Chen, L. Qu, One-step

- preparation of iodine-doped graphitic carbon nitride nanosheets as efficient photocatalysts for visible light water splitting, *J. Mater. Chem. A.* 3 (2015) 4612–4619.
- [129] G. Liu, P. Niu, C. Sun, S.C. Smith, Z. Chen, G.Q. Lu, H.M. Cheng, Unique electronic structure induced high photoreactivity of sulfur-doped graphitic  $C_3N_4$ , *J. Am. Chem. Soc.* 132 (2010) 11642–11648.
- [130] J. Fang, H. Fan, M. Li, C. Long, Nitrogen self-doped graphitic carbon nitride as efficient visible light photocatalyst for hydrogen evolution, *J. Mater. Chem. A.* 3 (2015) 13819–13826.
- [131] Y. Zhou, L. Zhang, J. Liu, X. Fan, B. Wang, M. Wang, W. Ren, J. Wang, M. Li, J. Shi, Brand new P-doped g- $C_3N_4$ : Enhanced photocatalytic activity for  $H_2$  evolution and Rhodamine B degradation under visible light, *J. Mater. Chem. A.* 3 (2015) 3862–3867.
- [132] L. Zhang, Z. Jin, S. Huang, X. Huang, B. Xu, L. Hu, H. Cui, S. Ruan, Y.J. Zeng, Bio-inspired carbon doped graphitic carbon nitride with booming photocatalytic hydrogen evolution, *Appl. Catal. B Environ.* 246 (2019) 61–71.
- [133] S. Thaweesak, S. Wang, M. Lyu, M. Xiao, P. Peerakiatkhajohn, L. Wang, Boron-doped graphitic carbon nitride nanosheets for enhanced visible light photocatalytic water splitting, *Dalt. Trans.* 46 (2017) 10714–10720.

- [134] J. Gao, Y. Wang, S. Zhou, W. Lin, Y. Kong, A Facile One-Step Synthesis of Fe-Doped g-C<sub>3</sub>N<sub>4</sub> Nanosheets and Their Improved Visible-Light Photocatalytic Performance, *ChemCatChem*. 9 (2017) 1708–1715.
- [135] P.W. Chen, K. Li, Y.X. Yu, W. De Zhang, Cobalt-doped graphitic carbon nitride photocatalysts with high activity for hydrogen evolution, *Appl. Surf. Sci.* 392 (2017) 608–615.
- [136] X. Yan, Z. Jia, H. Che, S. Chen, P. Hu, J. Wang, L. Wang, A selective ion replacement strategy for the synthesis of copper doped carbon nitride nanotubes with improved photocatalytic hydrogen evolution, *Appl. Catal. B Environ.* 234 (2018) 19–25.
- [137] Y. Wang, Y. Zhang, S. Zhao, Z. Huang, W. Chen, Y. Zhou, X. Lv, S. Yuan, Bio-template synthesis of Mo-doped polymer carbon nitride for photocatalytic hydrogen evolution, *Appl. Catal. B Environ.* 248 (2019) 44–53.
- [138] N. Wang, J. Wang, J. Hu, X. Lu, J. Sun, F. Shi, Z.H. Liu, Z. Lei, R. Jiang, Design of Palladium-Doped g-C<sub>3</sub>N<sub>4</sub> for Enhanced Photocatalytic Activity toward Hydrogen Evolution Reaction, *ACS Appl. Energy Mater.* 1 (2018) 2866–2873.
- [139] J. Tang, W. Zhou, R. Guo, C. Huang, W. Pan, P. Liu, An exploration on in-situ synthesis of europium doped g-C<sub>3</sub>N<sub>4</sub> for photocatalytic water splitting, *Energy Procedia*. 158 (2019) 1553–1558.

- [140] Y. Guo, Q. Liu, Z. Li, Z. Zhang, X. Fang, Enhanced photocatalytic hydrogen evolution performance of mesoporous graphitic carbon nitride co-doped with potassium and iodine, *Appl. Catal. B Environ.* 221 (2018) 362–370.
- [141] W. Wu, Z. Ruan, J. Li, Y. Li, Y. Jiang, X. Xu, D. Li, Y. Yuan, K. Lin, In Situ Preparation and Analysis of Bimetal Co-doped Mesoporous Graphitic Carbon Nitride with Enhanced Photocatalytic Activity, *Nano-Micro Lett.* 11 (2019).
- [142] W. Fang, J. Liu, L. Yu, Z. Jiang, W. Shangguan, Novel (Na, O) co-doped g-C<sub>3</sub>N<sub>4</sub> with simultaneously enhanced absorption and narrowed bandgap for highly efficient hydrogen evolution, *Appl. Catal. B Environ.* 209 (2017) 631–636.
- [143] L. Zhang, N. Ding, L. Lou, K. Iwasaki, H. Wu, Y. Luo, D. Li, K. Nakata, A. Fujishima, Q. Meng, Localized Surface Plasmon Resonance Enhanced Photocatalytic Hydrogen Evolution via Pt@Au NRs/C<sub>3</sub>N<sub>4</sub> Nanotubes under Visible-Light Irradiation, *Adv. Funct. Mater.* 29 (2019) 1–10.
- [144] J. Zhang, Y. Wang, J. Jin, J. Zhang, Z. Lin, F. Huang, J. Yu, Efficient visible-light photocatalytic hydrogen evolution and enhanced photostability of core/shell CdS/g-C<sub>3</sub>N<sub>4</sub> nanowires, *ACS Appl. Mater. Interfaces.* 5 (2013) 10317–10324.
- [145] S.W. Cao, Y.P. Yuan, J. Fang, M.M. Shahjamali, F.Y.C. Boey, J.

- Barber, S.C. Joachim Loo, C. Xue, In-situ growth of CdS quantum dots on g-C<sub>3</sub>N<sub>4</sub> nanosheets for highly efficient photocatalytic hydrogen generation under visible light irradiation, *Int. J. Hydrogen Energy*. 38 (2013) 1258–1266.
- [146] F.Y. Tian, D. Hou, F. Tang, M. Deng, X.Q. Qiao, Q. Zhang, T. Wu, D.S. Li, Novel Zn<sub>0.8</sub>Cd<sub>0.2</sub>S@g-C<sub>3</sub>N<sub>4</sub> core-shell heterojunctions with a twin structure for enhanced visible-light-driven photocatalytic hydrogen generation, *J. Mater. Chem. A*. 6 (2018) 17086–17094.
- [147] W. Zou, Y. Shao, Y. Pu, Y. Luo, J. Sun, K. Ma, C. Tang, F. Gao, L. Dong, Enhanced visible light photocatalytic hydrogen evolution via cubic CeO<sub>2</sub> hybridized g-C<sub>3</sub>N<sub>4</sub> composite, *Appl. Catal. B Environ*. 218 (2017) 51–59.
- [148] D. Zheng, G. zhang, X. Wang, Integrating CdS quantum dots on hollow graphitic carbon nitride nanospheres for hydrogen evolution photocatalysis, *Appl. Catal. B Environ*. 179 (2015) 479–488.
- [149] J.T. Lee, Y.J. Chen, E.C. Su, M.Y. Wey, Synthesis of solar-light responsive Pt/g-C<sub>3</sub>N<sub>4</sub>/SrTiO<sub>3</sub> composite for improved hydrogen production: Investigation of Pt/g-C<sub>3</sub>N<sub>4</sub>/SrTiO<sub>3</sub> synthetic sequences, *Int. J. Hydrogen Energy*. 44 (2019) 21413–21423.
- [150] H. Zhao, X. Ding, B. Zhang, Y. Li, C. Wang, Enhanced photocatalytic hydrogen evolution along with byproducts suppressing over Z-scheme Cd<sub>x</sub>Zn<sub>1-x</sub>S/Au/g-C<sub>3</sub>N<sub>4</sub> photocatalysts

- under visible light, *Sci. Bull.* 62 (2017) 602–609.
- [151] H. Katsumata, Y. Tachi, T. Suzuki, S. Kaneco, Z-scheme photocatalytic hydrogen production over  $\text{WO}_3/\text{g-C}_3\text{N}_4$  composite photocatalysts, *RSC Adv.* 4 (2014) 21405–21409.
- [152] X. Li, K. Xie, L. Song, M. Zhao, Z. Zhang, Enhanced Photocarrier Separation in Hierarchical Graphitic- $\text{C}_3\text{N}_4$ -Supported  $\text{CuInS}_2$  for Noble-Metal-Free Z-Scheme Photocatalytic Water Splitting, *ACS Appl. Mater. Interfaces.* 9 (2017) 24577–24583.
- [153] W. Chen, Z.C. He, G.B. Huang, C.L. Wu, W.F. Chen, X.H. Liu, Direct Z-scheme 2D/2D  $\text{MnIn}_2\text{S}_4/\text{g-C}_3\text{N}_4$  architectures with highly efficient photocatalytic activities towards treatment of pharmaceutical wastewater and hydrogen evolution, *Chem. Eng. J.* 359 (2019) 244–253.
- [154] S. Acharya, S. Mansingh, K.M. Parida, The enhanced photocatalytic activity of  $\text{g-C}_3\text{N}_4\text{-LaFeO}_3$  for the water reduction reaction through a mediator free Z-scheme mechanism, *Inorg. Chem. Front.* 4 (2017) 1022–1032.
- [155] G. Liu, G. Zhao, W. Zhou, Y. Liu, H. Pang, H. Zhang, D. Hao, X. Meng, P. Li, T. Kako, J. Ye, In Situ Bond Modulation of Graphitic Carbon Nitride to Construct p–n Homojunctions for Enhanced Photocatalytic Hydrogen Production, *Adv. Funct. Mater.* 26 (2016) 6822–6829.

- [156] Z. Qin, M. Wang, R. Li, Y. Chen, SPECIAL ISSUE : Advanced Materials for Photoelectrochemical Cells Novel  $\text{Cu}_3\text{P} / \text{g-C}_3\text{N}_4$  p-n heterojunction photocatalysts for solar hydrogen generation, 61 (2018) 861–868.
- [157] F. Nekouei, S. Nekouei, M. Pouzesh, Y. Liu, Porous- $\text{CdS/Cu}_2\text{O/graphitic-C}_3\text{N}_4$  dual p-n junctions as highly efficient photo/catalysts for degrading ciprofloxacin and generating hydrogen using solar energy, Chem. Eng. J. 385 (2020) 123710.
- [158] H. Li, H. Tian, X. Wang, M. Pi, S. Wei, H. Zhu, D. Zhang, S. Chen, Self-Coupled  $\text{g-C}_3\text{N}_4$  van der Waals Heterojunctions for Enhanced Photocatalytic Hydrogen Production, ACS Appl. Energy Mater. 2 (2019) 4692–4699.

*Every reasonable effort has been made to acknowledge the owners of copyright material. I would be pleased to hear from any copyright owner who has been omitted or incorrectly acknowledged.*

## **Chapter 3 Solar-heat temperature effect on photocatalytic hydrogen evolution**

### **Abstract**

In photocatalytic hydrogen evolution reaction (PC-HER), solar heat (infrared) usually has no significant influence on the photoelectrons excitation. However, the solar heat impacts on PC-HER are urgently needed to be investigated with the consideration of the high proportion of infrared in the solar spectrum. In this Chapter, the solar-heat temperature-based PC-HER performances of different photocatalysts are studied and analyzed with the assistance of a series of temperature-based characterizations. Some essential conclusions are achieved from the study.

a) Pristine  $\text{TiO}_2$  P25 and  $\text{g-C}_3\text{N}_4$  have an increased PC-HER performance with temperature, while Pt nanoparticles (NPs) decorated  $\text{TiO}_2$  P25 and  $\text{g-C}_3\text{N}_4$  own an unstable or even decreased PC-HER efficiency with temperature. b) Pt NPs modified  $\text{g-C}_3\text{N}_4$  have an enhanced PC-HER performance from 25 to 65 °C under visible light irradiations. c) The lowered electrical impedance, a shortened bandgap, and the increased light absorption with temperature are beneficial factors for photocatalysts in the temperature-based PC-HER processes. d) The agglomeration of Pt NPs can be a significantly negative factor deteriorating the PC-HER performance at a higher temperature. e) UV light can aggravate the

thermal agglomeration of Pt NPs. This study outlines the positive and negative factors in solar-heat temperature-based PC-HER processes. It aims to help intrigue more creative studies to make PC-HER operations for industrialization.

### **3.1 Introduction**

The source of all energies on the Earth is ultimately sunlight, which contains 5% ultraviolet (UV) light (290 – 400 nm), 42% visible light (400 – 760 nm), and over 50% infrared light (760 – 5300 nm).[1–3] The direct exploitation of solar energy, therefore, is the cleanest and most sustainable way to provide power for our daily life. Photocatalytic hydrogen evolution reaction (PC-HER) is one of the most high-efficiency routes in utilizing solar energy, which transforms the sunlight into chemical energy stored in the H-H bonding of hydrogen molecules.[4–13] The key step of PC-HER lies in the excitation of photoelectrons by photons, where the photons must meet the requirement of having energy at least higher than the bandgap of a semiconductor.[7,14–18] Most photocatalysts currently used in laboratories have bandgap energies much more than 1.63 (1240/760) eV, which means that all the infrared of sunlight cannot be utilized for the electron motivation process. For example, cadmium sulfide (CdS), with a bandgap of 2.40 eV,[19–21] can only generate photoelectrons by incident photons less than 517 nm. Graphitic carbon nitride (g-C<sub>3</sub>N<sub>4</sub>), having a

bandgap of 2.70 eV,[22–27] only utilizes UV light and part of visible light (< 459 nm). Titanium dioxide (TiO<sub>2</sub>) and SrTiO<sub>3</sub>, as wide-bandgap semiconductors (3.2 eV),[28–33] can only exploit UV light (< 388 nm) to obtain their photoelectrons. As a result, the issue of how to utilize infrared for a PC-HER process is worth pondering.

It is well known that the main function of infrared irradiation is its huge thermal effect.[34–37] In PC-HER processes, this signifies that the reaction solution's temperature can be dramatically raised because of the enormous amounts of infrared light in the solar spectrum. In our tests, the temperature could achieve 57 °C within only 4 hours illumination with a 300 W Xenon lamp (Figure 3.1). This might provide a strategy to make use of infrared light if the PC-HER performance increases with temperature. However, very few reports focus on this point. In most PC-HER studies, a water-circulation system is employed to keep the temperature at a specific value to eliminate the interference of infrared thermal effect (solar heat) to the experimental results. This value is sometimes 25 °C,[38–40] which is seen as room temperature, and also sometimes 5 or 35 °C.[27,41–43] Reports usually do not provide more information about whether that is an optimal value or other explanations for choosing that temperature. Obviously, it would not be cost-effective to achieve a constant temperature at the industrial level. Thus, it is urgently

needed to explore the knowledge of the solar-heat temperatures on PC-HER so that appropriate tactics about solar heat can be determined.

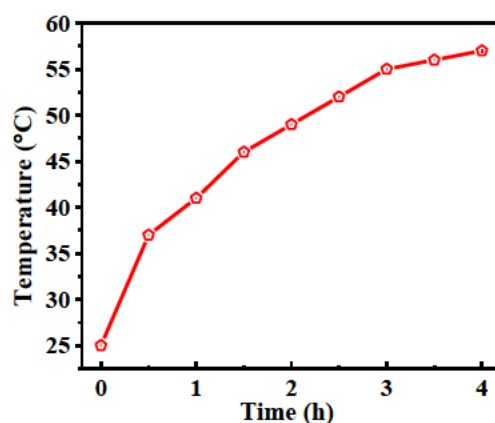


**Figure 3.1** Reaction solution temperature change versus illumination time with a 300 W Xenon lamp as a light source.

Herein, the solar-heat temperature effects were firstly tested under the full solar spectrum of a 300 W Xenon lamp as a solar simulator using  $\text{TiO}_2$  P25,  $\text{g-C}_3\text{N}_4$ , 1% Pt- $\text{TiO}_2$  P25, and 1% Pt- $\text{g-C}_3\text{N}_4$  as photocatalysts.  $\text{TiO}_2$  P25 and  $\text{g-C}_3\text{N}_4$  showed an increased PC-HER trend while the PC-HER rates of 1% Pt- $\text{TiO}_2$  P25, and 1% Pt- $\text{g-C}_3\text{N}_4$  were unstable or even decreased with temperature increase. A series of characterizations were conducted to explore the insights, and it was found that the thermal polymerization of platinum nanoparticles is mainly responsible for the unfavorable result. Besides, the PC-HER performance of 1% Pt- $\text{g-C}_3\text{N}_4$  was also evaluated under a 300 W Xenon lamp with a cutoff filter (> 420 nm) to impede UV light. The unexpectedly improved results with

temperatures from 25 to 65 °C were found and then explained.

## 3.2 Experimental

### 3.2.1 Chemicals and materials

TiO<sub>2</sub> P25, urea, sodium sulphate, ethylene glycol (EG), triethanolamine (TEOA), chloroplatinic acid, and Nafion solution were purchased from Sigma-Aldrich and used without further purification.

### 3.2.2 Fabrication of catalysts

The fabrication of g-C<sub>3</sub>N<sub>4</sub>: 10 g urea was placed in a crucible, which was then covered with a lid and transferred in a muffle furnace. The temperature was kept at 550 °C for 4 hours with a heating rate of 15 °C/min. The obtained bulk was pulverized in a hard plastic container with a stirrer bar by a vortex mixer.

Preparation of 1% Pt-TiO<sub>2</sub> P25 (or 1% Pt-g-C<sub>3</sub>N<sub>4</sub>): 100 mg TiO<sub>2</sub> P25 (or g-C<sub>3</sub>N<sub>4</sub>) was added in a mixed solution of 180 mL ultrapure water and 20 ml EG (or TEOA for 1% Pt-g-C<sub>3</sub>N<sub>4</sub>), followed by injecting 200 μL H<sub>4</sub>PtCl aqueous solution (5 mg Pt/mL) to the mixture. After a 5-minute ultrasonication, the mixed suspension was transferred to a black Teflon cell with a quartz light window, which was then sealed tightly. Nitrogen

gas was utilized to purge the air away from the cell for 30 minutes with vigorous stirring, after which the photo-deposition began with a 300 W Xenon lamp (Newport) as the light source. The temperature of the reaction solution was kept at 25 °C by a water circulation system. An hour later, the solution was filtered to obtain the powders, which were then washed several times with ultrapure water and absolute ethanol and vacuum-dried at room temperature.

### 3.2.3 Characterization techniques

Transmission electron microscopy images (TEM) were obtained from a Philips CM200 microscope (Germany) at 200 kV. UV-Vis diffuse reflectance tests were performed on a Cary 100 UV-Vis spectrophotometer (Agilent, USA) with BaSO<sub>4</sub> as the blank sample.

### 3.2.4 Photoelectrochemical tests

Time-dependent photocurrent, electrical impedance spectroscopy (EIS), and Mott-Schottky tests were performed on a Zennium electrochemical workstation (Zahner, Germany) in a standard three-electrode system with a 0.05 M Na<sub>2</sub>SO<sub>4</sub> (pH = 6.8) electrolyte solution, employing a Pt plate as the counter electrode and a Ag/AgCl electrode as the reference electrode. In terms of the photoanode, the sample film was fabricated on a fluorine-doped tin oxide (FTO) glass, which was ultrasonicated in ultrapure water,

acetone, and ethanol for 15 min in sequence and dried at 60 °C. Then 5 mg of the catalyst was mixed with 1 mL of absolute ethanol first. After an hour of ultrasonication, 10  $\mu$ L of Nafion solution was added to the mixture. The obtained slurry was ultrasonicated again for half an hour, before being dropped onto the pre-treated FTO glass via a spin-coating method, and the prepared electrode was dried at 100 °C for 24 h (catalyst loading  $\sim 0.60$   $\text{mg}\cdot\text{cm}^{-2}$ ). Photocurrents were obtained using a 300 W Xenon arc lamp with light passing through an AM 1.5 G filter into an optical fibre (output  $I_0 = 100$   $\text{mW}\cdot\text{cm}^{-2}$ ).

### 3.2.5 Solar-heat temperature effect measurements

The measurements of solar-heat temperature effect on photocatalytic hydrogen evolution were performed in a black Teflon cell with a quartz light window. The light source was a 300 W Xenon lamp (Newport). In a typical experiment, 50 mg photocatalysts were added in a mixed solution of 90 mL ultrapure water and 10 mL sacrificial agent (EG for  $\text{TiO}_2$  P25 and 1% Pt- $\text{TiO}_2$  P25, TEOA for g- $\text{C}_3\text{N}_4$  and 1% Pt-g- $\text{C}_3\text{N}_4$ ). After a 5-min ultrasonication, the mixed suspension was transferred in the reactor, which was then sealed tightly. Nitrogen gas was utilized to drive the air away from the reactor and the reaction solution for 30 min under vigorous stirring, after which the light source was switched on, and timing began. Meanwhile, the temperature of the reaction solution was kept at a constant

value using a water circulation system combined with a hot plate. The generated hydrogen was online examined by a 490 Micro GC (Agilent, USA) equipped with a thermal conductivity detector.

### 3.3 Results and discussions

The solar-heat temperature effects on PC-HER were firstly measured, with a circulation system and a hot plate to control the temperature. Figure 3.2a shows that the PC-HER rates of TiO<sub>2</sub> P25 increase with temperature from 25 to 65 °C under full-spectrum irradiations. EG was used as the sacrificial agent based on a previous report comparing different scavengers for various photocatalysts,[44] where EG was found to be the best one for TiO<sub>2</sub>. In our study, we also tried TEOA as the sacrificial agent for TiO<sub>2</sub> P25 and 1% Pt-TiO<sub>2</sub> P25. However, none of them showed any hydrogen evolution, which confirmed the correlation between a photocatalyst and a sacrificial agent. We can also find that the PC-HER rate of TiO<sub>2</sub> P25 achieves 152  $\mu\text{mol}\cdot\text{h}^{-1}\cdot\text{g}^{-1}$  at 65 °C, which is 6.1 folds that at 25 °C. Although it seems to be a significant increase, the improvement is negligible compared to TiO<sub>2</sub> P25 with 1% Pt as the cocatalyst. From Figure 3.2b, it can be found that the PC-HER rate of 1% Pt-TiO<sub>2</sub> P25 is 23949  $\mu\text{mol}\cdot\text{h}^{-1}\cdot\text{g}^{-1}$  at 25 °C, which is even up to 958 times that of pure TiO<sub>2</sub> P25 at 25 °C. Therefore, the research of solar-heat temperature effects on Pt-TiO<sub>2</sub> P25 is much more meaningful. However, as can be seen

from Figure 3.2b, the trend of 1% Pt-TiO<sub>2</sub> P25 is not continually growing with temperature. The PC-HER rate has a noticeable increase at 35 °C than that at 25 °C, even as high as 29945 μmol·h<sup>-1</sup>·g<sup>-1</sup>, but it plummets to 18656 μmol·h<sup>-1</sup>·g<sup>-1</sup> at 45 °C and then rises backward to 22761 μmol·h<sup>-1</sup>·g<sup>-1</sup> at 55 °C and 27490 μmol·h<sup>-1</sup>·g<sup>-1</sup> at 65 °C. However, this value at 65 °C is still 8% lower than the peak value obtained at 35 °C. We also investigated the solar-heat temperature effects on g-C<sub>3</sub>N<sub>4</sub> and 1% Pt-g-C<sub>3</sub>N<sub>4</sub>. Figure 3.3a displays that the PC-HER rates of g-C<sub>3</sub>N<sub>4</sub> move up, with temperature from 25 to 65 °C, and the value of 73.4 μmol·h<sup>-1</sup>·g<sup>-1</sup> at 65 °C is about 1.61 times as high as that at 25 °C. 1% Pt-g-C<sub>3</sub>N<sub>4</sub> has a PC-HER rate of 1684 μmol·h<sup>-1</sup>·g<sup>-1</sup> at 25 °C (Figure 3.3b), which is 37 folds that of pristine g-C<sub>3</sub>N<sub>4</sub> at the same temperature. An increase of ~ 7% can also be acquired at 35 °C than that at 25 °C for 1% Pt-g-C<sub>3</sub>N<sub>4</sub>, but the value at 45 °C considerably falls to just half that at 35 °C, which resembles the tendency of 1% Pt-TiO<sub>2</sub> P25. But different from 1% Pt-TiO<sub>2</sub> P25, the PC-HER rate of 1% Pt-g-C<sub>3</sub>N<sub>4</sub> continues a declining trend at 55 and 65 °C and drops to 777 μmol·h<sup>-1</sup>·g<sup>-1</sup> at 65 °C, which is 43% less than that of the peak value at 35 °C. Since, in most studies, g-C<sub>3</sub>N<sub>4</sub> based materials are only applied under a light source with a cutoff filter (> 420 nm), we also tested the solar-heat temperature effects of 1% Pt-g-C<sub>3</sub>N<sub>4</sub> using such a cutoff filter. As shown in Figure 3.3c, the enhancement with temperature from 25 to 65 °C is quite remarkable, but the PC-HER rate has a minor decrease at

75 °C. Besides, the rate of increase seems to slow down with temperature.

In summary, pure TiO<sub>2</sub> P25 and g-C<sub>3</sub>N<sub>4</sub> have enhanced PC-HER rates with increasing temperature. In contrast, the PC-HER rates of Pt nanoparticles modified TiO<sub>2</sub> P25 and g-C<sub>3</sub>N<sub>4</sub> are unstable or even decrease with temperature. Besides, under the light source with wavelength > 420 nm, 1% Pt-g-C<sub>3</sub>N<sub>4</sub> can see the growth of PC-HER rate with temperature from 25 to 65 °C, but the growth rate decreases with temperature increasing.

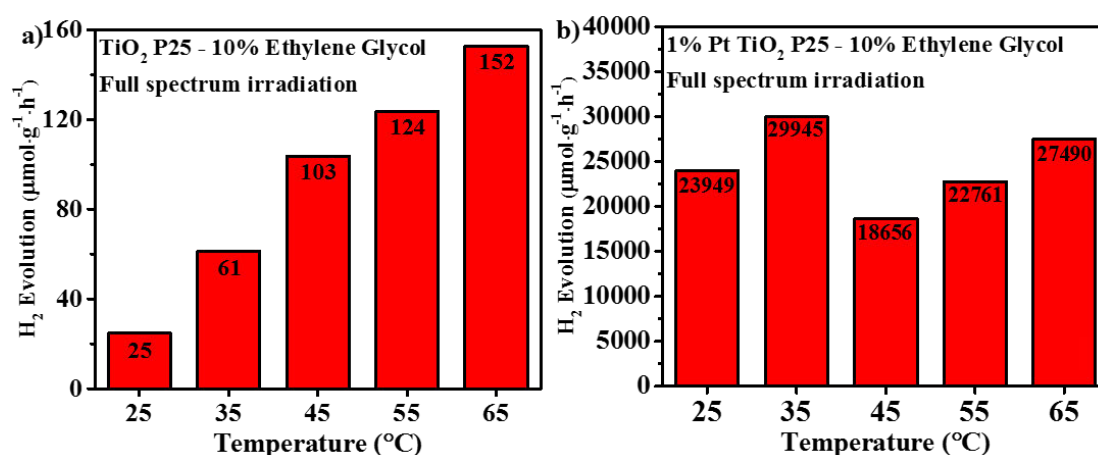


**Figure 3.2** The PC-HER rates under different temperatures of **a)** TiO<sub>2</sub> P25 and **b)** 1% Pt-TiO<sub>2</sub> P25.

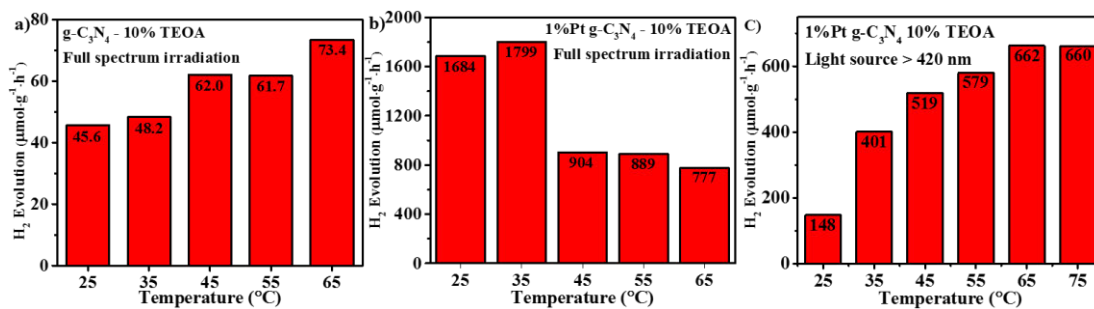


**Figure 3.3** The PC-HER rates at different temperatures of **a)** g-C<sub>3</sub>N<sub>4</sub>, **b)** 1% Pt-g-C<sub>3</sub>N<sub>4</sub>, and **c)** 1% Pt-g-C<sub>3</sub>N<sub>4</sub> with a cutoff filter (> 420 nm) for the light source.

According to the Arrhenius equation,[45,46] when other conditions are constant, the reaction rate should increase with temperature, unless the catalysts change. Therefore, it is speculated that some variations happened in the photocatalysts of 1% Pt-TiO<sub>2</sub> P25 and 1% Pt-g-C<sub>3</sub>N<sub>4</sub> when the temperature is increased.

To deeply understand what happened with those catalysts at different temperatures, we firstly explored their time-dependent photocurrent shifts with temperature. As displayed in Figure 3.4, all photocurrents of these four photocatalysts have gradual increases with temperature. The photocurrents at 65 °C are more than doubling those at 25 °C, respectively. However, these data are not consistent with the electrical resistance change of the electrochemical solution (0.5 M Na<sub>2</sub>SO<sub>4</sub>). As can be seen in Figure 3.5, the resistance is decreasing gradually with temperature, which

will inevitably cause the photocurrent to rise with temperature.

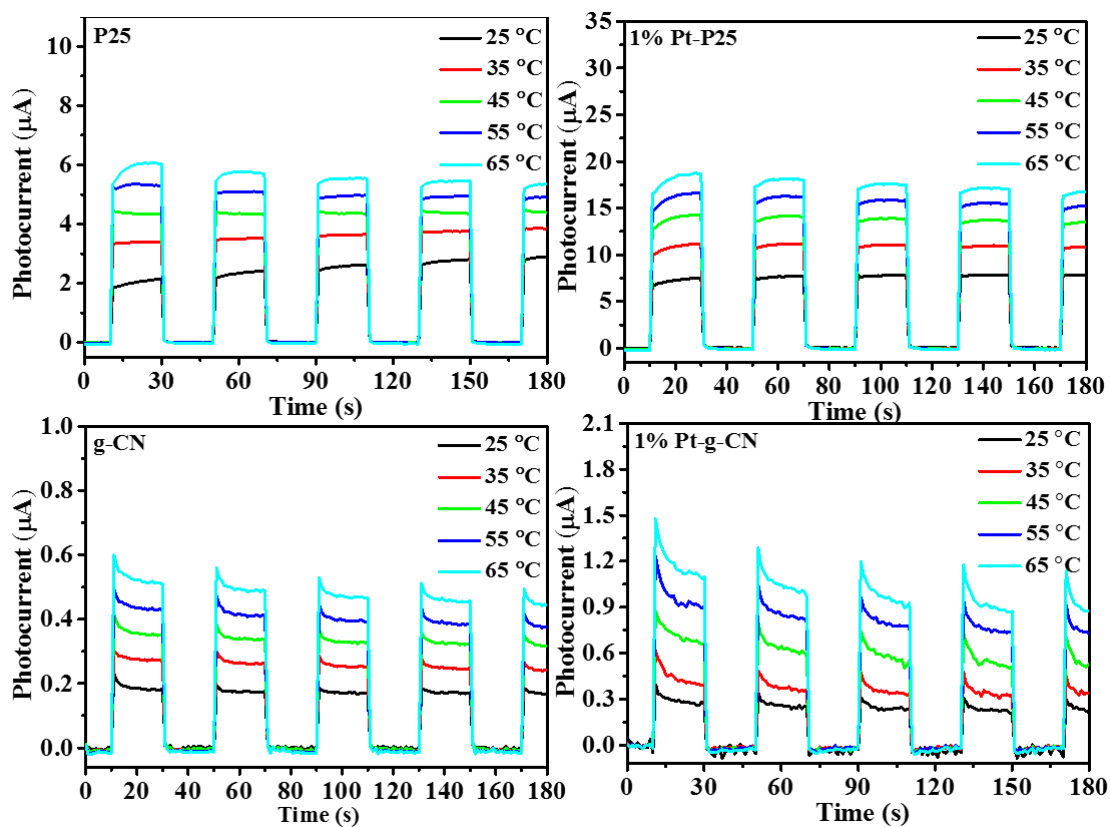


**Figure 3.4** The changes of time-dependent photocurrents of  $\text{TiO}_2$  P25, 1% Pt- $\text{TiO}_2$  P25, g- $\text{C}_3\text{N}_4$ , and 1% Pt-g- $\text{C}_3\text{N}_4$  with temperature.

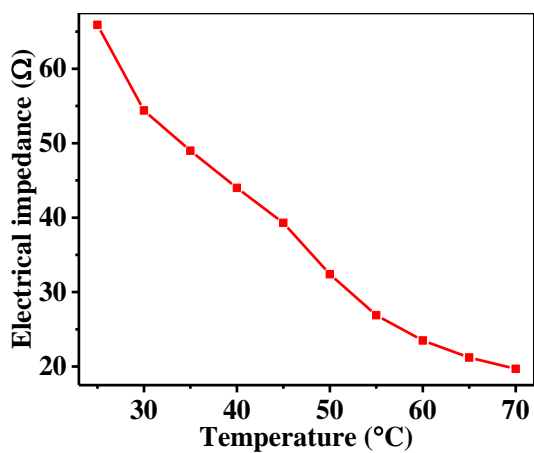


**Figure 3.5** The electrical impedance change of electrochemical solution (0.5 M  $\text{Na}_2\text{SO}_4$ ) with temperature.

After that, we continued the tests of EIS by the electrochemical system. Figure 3.6a clearly shows that the arc radii of TiO<sub>2</sub> P25 are reducing with temperature, indicating that the electrical impedance of TiO<sub>2</sub> P25 is shrinking with the temperature rising.[47,48] This result is reasonable. As the temperature goes up, the increased carrier (hole and electron) concentration of a semiconductor can lead to the decrease of its resistance. Figure 3.6b displays the EIS curves of 1% Pt-TiO<sub>2</sub> P25 at different temperatures. Compared to the curves of TiO<sub>2</sub> P25 in Figure 3.6a, 1% Pt-TiO<sub>2</sub> P25 has much smaller radii in the arc part, which is because of the much lower resistance of Pt nanoparticles in 1% Pt-TiO<sub>2</sub> P25. Moreover, unlike semiconductors, the resistance of a metal increases with temperature because the intensified vibration of metal cations under higher temperature will retard the movement of free electrons. However, the arc radius of 1% Pt-TiO<sub>2</sub> P25 still decreases with temperature going up, signifying that the EIS change of 1% Pt-TiO<sub>2</sub> P25 mainly originates from the decreased resistance of the semiconductor, TiO<sub>2</sub> P25. Figure 3.6c gives the EIS curves of g-C<sub>3</sub>N<sub>4</sub>, which resemble the results of TiO<sub>2</sub> P25 in Figure 3.6a. The curves of 1% Pt-g-C<sub>3</sub>N<sub>4</sub> (Figure 3.6d) only have slightly smaller arc radius than that of g-C<sub>3</sub>N<sub>4</sub>. This change is not so significant as the mutation from TiO<sub>2</sub> P25 to 1% Pt-TiO<sub>2</sub> P25 as described above, resulting from the fact that unlike TiO<sub>2</sub> P25 nanoparticle structure, the

nanosheet of g-C<sub>3</sub>N<sub>4</sub> has an extensive two dimensional (2D) surface and the wrinkles on the surface may cover Pt nanoparticles and weaken their impact on the EIS results. What is more, with the temperature rising, the arc radius of 1% Pt-g-C<sub>3</sub>N<sub>4</sub> also diminishes, again proving that the decreased electrical resistance of the semiconductor, g-C<sub>3</sub>N<sub>4</sub>, is mainly responsible for the EIS change of 1% Pt-g-C<sub>3</sub>N<sub>4</sub>.

In short, from the viewpoint of EIS change, all those four photocatalysts have a smaller electrical impedance, which should facilitate PC-HER efficiency.

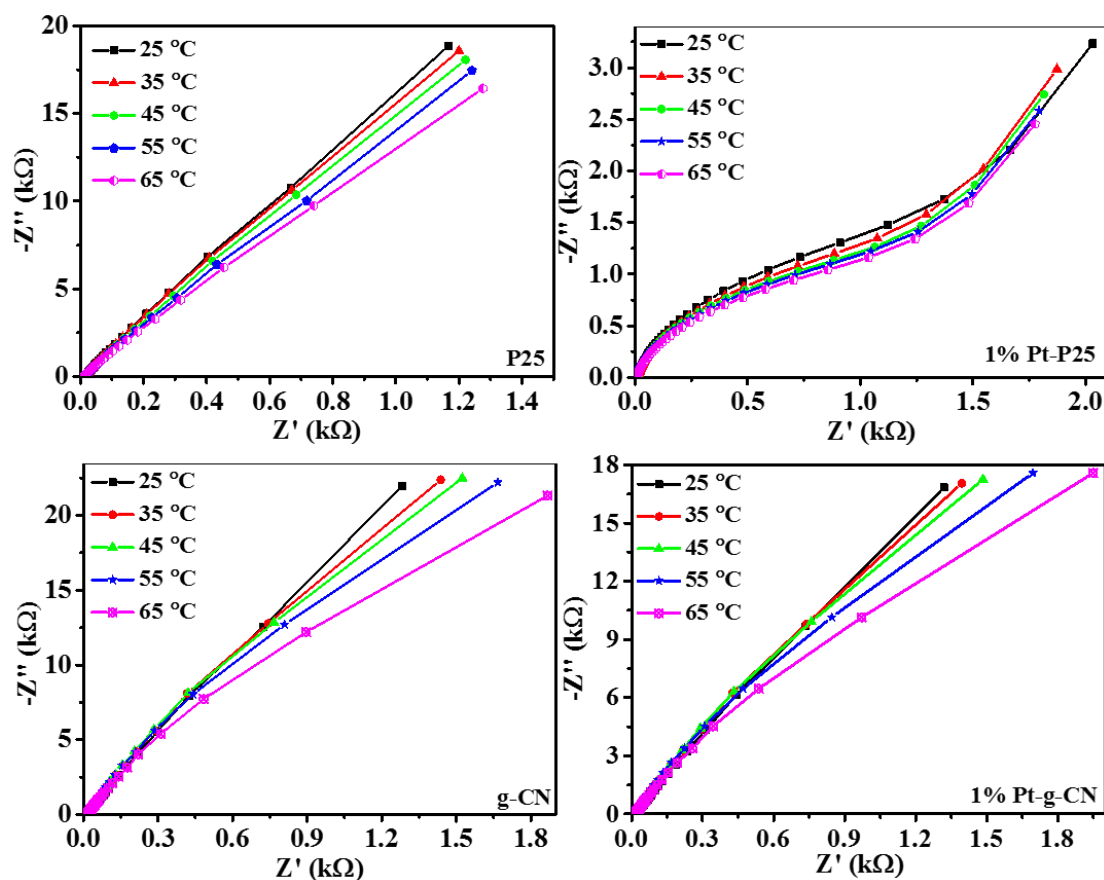


**Figure 3.6** The EIS changes TiO<sub>2</sub> P25, 1% Pt-TiO<sub>2</sub> P25, g-C<sub>3</sub>N<sub>4</sub>, and 1% Pt-g-C<sub>3</sub>N<sub>4</sub> with temperature.

To provide insights into the energy band shifts with temperature, UV-vis diffuse reflectance spectra of those four photocatalysts were employed. Figure 3.7a and b display that there are no significant changes in photoabsorption for both TiO<sub>2</sub> P25 and 1% Pt-TiO<sub>2</sub> P25 from 25 to 65 °C. However, from Figure 3.7c and d, we can find that the light absorption in the UV range of both g-C<sub>3</sub>N<sub>4</sub> and 1% Pt-g-C<sub>3</sub>N<sub>4</sub> intensifies with temperature, which can benefit the efficiency in PC-HER processes. According to the Kubelka-Munk theory, the bandgap changes with temperature were acquired and shown in Figure 3.7e, f, g, and h. The bandgap of TiO<sub>2</sub> P25 is stably 2.88 eV from 25 to 65 °C (Figure 3.7e), while that of 1% Pt-TiO<sub>2</sub> P25 is sustained at 2.28 eV (Figure 3.7f). Whereas, the bandgap of g-C<sub>3</sub>N<sub>4</sub> gradually narrows with the temperature rising and achieves 2.527 eV at 65 °C, which is 0.018 eV less than that at 25 °C (2.545 eV). Similarly, 1% Pt-g-C<sub>3</sub>N<sub>4</sub> sees the bandgap diminishing from 2.553 eV at 25 °C to 2.532 eV at 65 °C, which can help use photons with slightly lower energy to excite electrons.

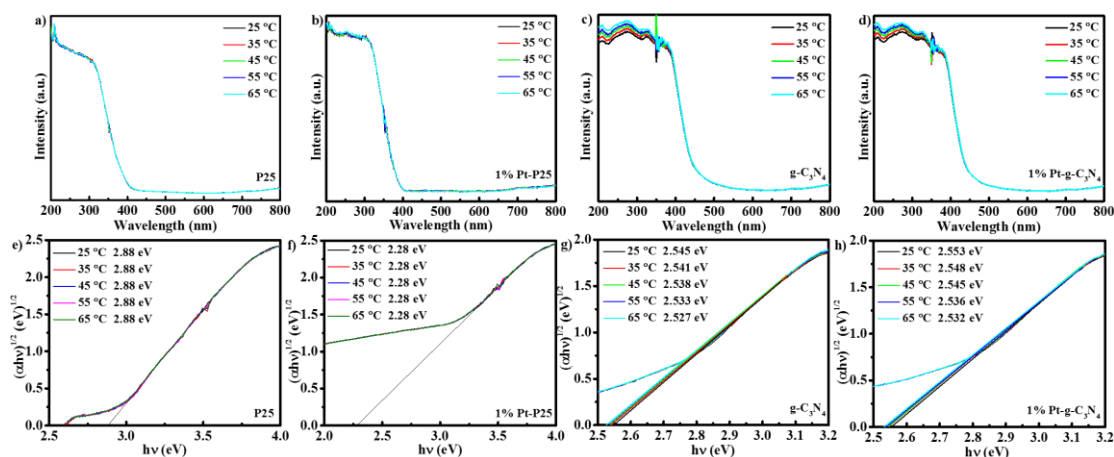


**Figure 3.7** The UV-vis diffuse reflectance spectra of **a)** TiO<sub>2</sub> P25, **b)** 1% Pt-TiO<sub>2</sub> P25, **c)** g-C<sub>3</sub>N<sub>4</sub>, and **d)** 1% Pt-g-C<sub>3</sub>N<sub>4</sub> with temperature, and their corresponding plots of  $(\alpha h\nu)^{1/2}$  versus bandgap energy (hv) of **e)** TiO<sub>2</sub> P25, **f)** 1% Pt-TiO<sub>2</sub> P25, **g)** g-C<sub>3</sub>N<sub>4</sub>, and **h)** 1% Pt-g-C<sub>3</sub>N<sub>4</sub>.

The Mott-Schottky (MS) curves were then conducted to determine the flat-band potentials, which can be approximated to the conduction band (CB) of those four n-type photocatalysts.[49–51] In Figure 3.8, it can be seen that the CB values of all those photocatalysts are becoming more negative with increased temperature (Figure 3.8a). In detail, the CB of TiO<sub>2</sub> P25 shifts from -0.29 eV at 25 °C to -0.41 eV at 65 °C, while the CB of 1% Pt-TiO<sub>2</sub> P25 changes from -0.50 eV at 25 °C to -0.41 eV at 65 °C. Apparently, the CB value of 1% Pt-TiO<sub>2</sub> P25 is more negative than that of TiO<sub>2</sub> P25 at the same temperature. This is because the Schottky junction formed between Pt and TiO<sub>2</sub> P25 makes the CB of TiO<sub>2</sub> P25 bend upward (Scheme 3.1). The MS curve changes of g-C<sub>3</sub>N<sub>4</sub> and 1% Pt-g-C<sub>3</sub>N<sub>4</sub> with temperature are akin to the results of TiO<sub>2</sub> P25 and 1% Pt-TiO<sub>2</sub> P25. The

CB of g-C<sub>3</sub>N<sub>4</sub> has gradual shifts from -0.33 eV at 25 °C to -0.41 eV at 65 °C with temperature, while the changes of 1% Pt-g-C<sub>3</sub>N<sub>4</sub> are -0.38 eV to -0.41 eV from 25 to 65 °C. Unlike 1% Pt-TiO<sub>2</sub> P25, the CB of 1% Pt-g-C<sub>3</sub>N<sub>4</sub> is only different from that of g-C<sub>3</sub>N<sub>4</sub> at 25 °C. At 35 – 65 °C, both g-C<sub>3</sub>N<sub>4</sub> and 1% Pt-g-C<sub>3</sub>N<sub>4</sub> share the same CB values. This indicates that, for 1% Pt-g-C<sub>3</sub>N<sub>4</sub>, the changes of semiconductor properties play the main role, which could again originate from the large 2D surface and wrinkles of g-C<sub>3</sub>N<sub>4</sub> covering Pt nanoparticles as described above.

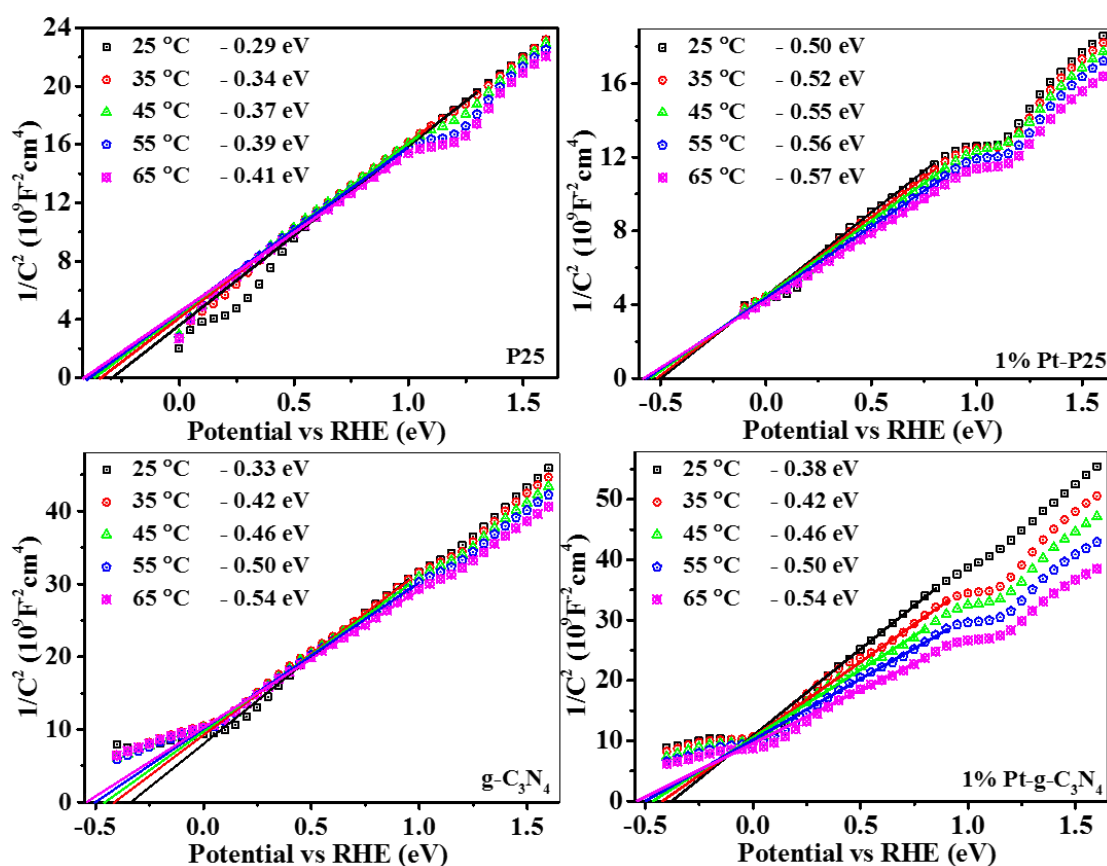
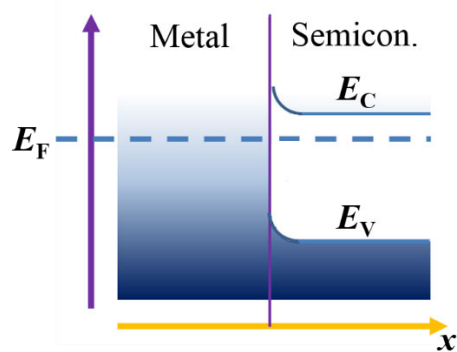


**Figure 3.8** The Mott-Schottky curves of a) TiO<sub>2</sub> P25, b) 1% Pt-TiO<sub>2</sub> P25, c) g-C<sub>3</sub>N<sub>4</sub>, and d) 1% Pt-g-C<sub>3</sub>N<sub>4</sub> with temperature.



Scheme 3.1 The structure of the Schottky junction.

Based on all the data from UV-vis spectra and MS curves, the energy bands of TiO<sub>2</sub> P25 and g-C<sub>3</sub>N<sub>4</sub> are calculated and summarized in Figure 3.9. It is clear that all CB and VB values are shifting toward a negative direction. The main difference between TiO<sub>2</sub> P25 and g-C<sub>3</sub>N<sub>4</sub> lies in that the bandgap of g-C<sub>3</sub>N<sub>4</sub> shortens with temperature, while there is no change of bandgap for TiO<sub>2</sub> P25.

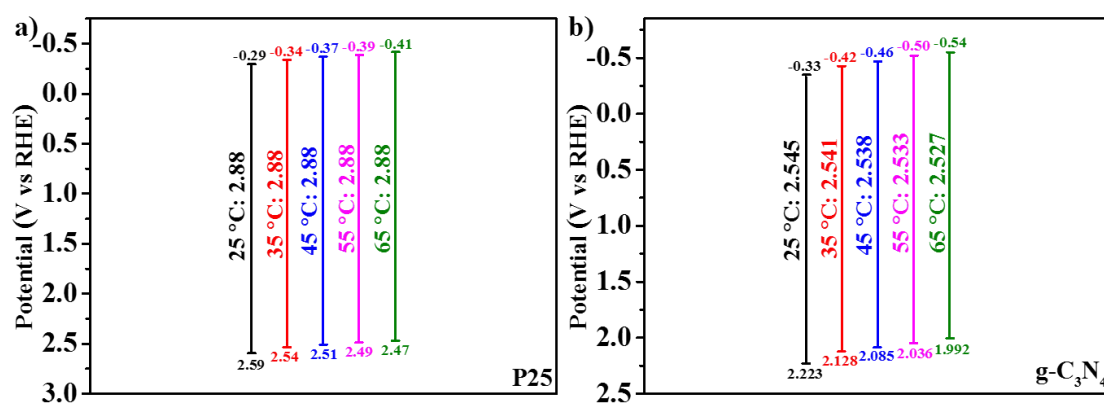


**Figure 3.9** The energy bands of a) TiO<sub>2</sub> P25 and b) g-C<sub>3</sub>N<sub>4</sub> under different temperatures.

To further figure out the unfavorable PC-HER results of Pt-based photocatalysts with temperature, we observed the morphologies of these photocatalysts after being used at different temperatures. Figure 3.10a shows 1% Pt-TiO<sub>2</sub> P25 morphologies at 25 – 65 °C. The size of the Pt nanoparticles (NPs) obtained at 25 °C is about 2 nm. At 35 °C, most of them keep the same size, but agglomeration occurs and makes the particle size into 3 nm. That explains why the PC-HER rate of 1% Pt-TiO<sub>2</sub> P25 can have an improvement from 25 to 35 °C, but this enhancement is not enormous (Figure 3.2b). Agglomeration continues to make the diameter of some nanoparticle grow to 8 nm at 45 °C, which accounts for the plunge of the PC-HER rate from 35 to 45 °C. Because the substrate of 1% Pt-TiO<sub>2</sub> P25 has a size about 25 nm, which does not support much larger nanoparticles, thus the agglomerated Pt NPs size is still ~ 8 nm at 55 and 65 °C. Therefore, the PC-HER results can keep increasing from 45 – 65 °C. The changed sizes of Pt NPs can primarily clarify the various PC-HER efficiency at different temperatures.

Unlike TiO<sub>2</sub> P25, g-C<sub>3</sub>N<sub>4</sub> nanosheet has a large surface, which provides enough space for attaching larger NPs. In Figure 3.10b, the size of the Pt NPs is about 3 nm at 25 °C. With the temperature rising, the agglomeration of Pt NPs keeps going seriously. At 65 °C, the agglomerated NPs with a diameter of ~ 18 nm can be found. These data can thoroughly explain the

going-down PC-HER performance of 1% Pt-g-C<sub>3</sub>N<sub>4</sub> with raised temperatures. However, under visible light (> 420 nm), no agglomeration and even no nanoparticles can be observed on the surface of g-C<sub>3</sub>N<sub>4</sub> (Figure 3.10c) from 25 to 55 °C. This is perhaps because the acquired Pt nanoclusters are beyond the resolution of our TEM setup. At 65 °C, Pt NPs about 4 nm emerge. At 75 °C, 8 nm Pt NPs can be found on the g-C<sub>3</sub>N<sub>4</sub> surface. These images elucidate the PC-HER performance of 1% Pt-g-C<sub>3</sub>N<sub>4</sub> at different temperatures with visible-light irradiations (firstly increasing then decreasing, Figure 3.3c). As to the reduced accelerating rate from 25 to 65 °C, it is perhaps the Pt nanoclusters are growing with temperature, until the Pt NPs appear at 65 °C (Figure 3.10c). Besides, the different solar-heat temperature-based PC-HER trends of 1% Pt-g-C<sub>3</sub>N<sub>4</sub> under full-spectrum and visible light indicate that the thermal agglomerations of Pt NPs can be severely aggravated under UV light.

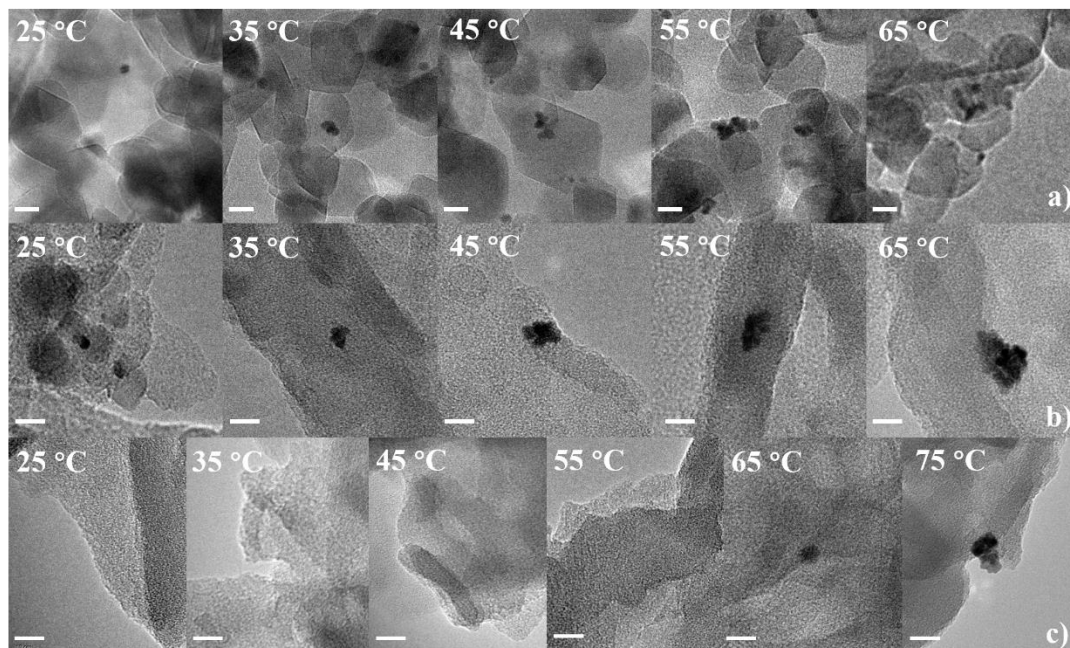


**Figure 3.10** The morphologies of Pt-based photocatalysts after being used under different temperatures. a) 1% Pt-TiO<sub>2</sub> P25. b) 1% Pt-g-C<sub>3</sub>N<sub>4</sub>. c) 1% Pt-g-C<sub>3</sub>N<sub>4</sub> under visible light irradiations (> 420 nm). All the scale bars are representing 10 nm.

### 3.4 Conclusions

From all the above results and discussion, some conclusions can be derived. 1) Pristine TiO<sub>2</sub> P25 and g-C<sub>3</sub>N<sub>4</sub> have increased PC-HER performances with temperature. 2) Pt NPs decorated TiO<sub>2</sub> P25 and g-C<sub>3</sub>N<sub>4</sub> own unstable or even decreased PC-HER efficiencies with temperature. 3) Pt NPs modified g-C<sub>3</sub>N<sub>4</sub> has enhanced PC-HER performances from 25 to 65 °C under visible light irradiations. 4) The lowered electrical impedance, shortened bandgap, and increased light absorption with temperature are

positive factors for those photocatalysts in temperature-based PC-HER processes. 5) The CB and VB values become more negative with temperature. 6) The agglomeration of Pt nanoparticles can be a significantly negative factor blocking the PC-HER performance on a higher temperature. 7) UV light can aggravate the thermal agglomeration of Pt NPs. Therefore, in the future, the issue of metal agglomeration with temperature must be solved for the industrial and practical application of PC-HER processes. Perhaps, single-atom catalysis will provide one alternative solution. This study summarizes the positive and negative factors for solar-heat temperature-based PC-HER processes. It aims to help inspire more studies to make PC-HER operations move forward toward industrialization.

## References

- [1] G.K. Mor, S. Kim, M. Paulose, O.K. Varghese, K. Shankar, J. Basham, C.A. Grimes, Visible to near-infrared light harvesting in TiO<sub>2</sub> nanotube array-P<sub>3</sub>HT based heterojunction solar cells, *Nano Lett.* 9 (2009) 4250–4257.
- [2] H. Choi, R. Nicolaescu, S. Paek, J. Ko, P. V. Kamat, Supersensitization of CdS quantum dots with a near-infrared organic dye: Toward the design of panchromatic hybrid-sensitized solar cells, *ACS Nano.* 5 (2011) 9238–9245.

- [3] G. Li, C. Guo, M. Yan, S. Liu, Cs<sub>x</sub>WO<sub>3</sub> nanorods: Realization of full-spectrum-responsive photocatalytic activities from UV, visible to near-infrared region, *Appl. Catal. B Environ.* 183 (2016) 142–148.
- [4] L. Yang, H. Li, Y. Yu, H. Yu, Study on the cocatalytic performance of nickel species in g-C<sub>3</sub>N<sub>4</sub> system for photocatalytic hydrogen evolution, *Catal. Commun.* 110 (2018) 51–54.
- [5] H. Xu, J. Yi, X. She, Q. Liu, L. Song, S. Chen, Y. Yang, Y. Song, R. Vajtai, J. Lou, H. Li, S. Yuan, J. Wu, P.M. Ajayan, 2D heterostructure comprised of metallic 1T-MoS<sub>2</sub>/Monolayer O-g-C<sub>3</sub>N<sub>4</sub> towards efficient photocatalytic hydrogen evolution, *Appl. Catal. B Environ.* 220 (2018) 379–385.
- [6] Y. Zeng, Y. Xia, W. Song, S. Luo, Visual observation of hydrogen bubble generation from monodisperse CoP QDs on ultrafine g-C<sub>3</sub>N<sub>4</sub> fiber under visible light irradiation, *J. Mater. Chem. A.* 7 (2019) 25908–25914.
- [7] A. Indra, A. Acharjya, P.W. Menezes, C. Merschjann, D. Hollmann, M. Schwarze, M. Aktas, A. Friedrich, S. Lochbrunner, A. Thomas, M. Driess, Boosting Visible-Light-Driven Photocatalytic Hydrogen Evolution with an Integrated Nickel Phosphide–Carbon Nitride System, *Angew. Chemie - Int. Ed.* 56 (2017) 1653–1657.
- [8] B. Zhu, J. Zhang, C. Jiang, B. Cheng, J. Yu, First principle investigation of halogen-doped monolayer g-C<sub>3</sub>N<sub>4</sub> photocatalyst,

- Appl. Catal. B Environ. 207 (2017) 27–34.
- [9] Q. Liang, Z. Li, X. Yu, Z. Huang, F. Kang, Macroscopic 3D Porous Graphitic Carbon Nitride Monolith for Enhanced Photocatalytic Hydrogen Evolution, (2015) 4634–4639.
- [10] M. Zhang, X. Bai, D. Liu, J. Wang, Y. Zhu, Enhanced catalytic activity of potassium-doped graphitic carbon nitride induced by lower valence position, Appl. Catal. B Environ. 164 (2015) 77–81.
- [11] T. Giannakopoulou, I. Papailias, N. Todorova, N. Boukos, Y. Liu, J. Yu, C. Trapalis, Tailoring the energy band gap and edges' potentials of g-C<sub>3</sub>N<sub>4</sub>/TiO<sub>2</sub> composite photocatalysts for NO<sub>x</sub> removal, Chem. Eng. J. 310 (2017) 571–580.
- [12] M.K. Bhunia, K. Yamauchi, K. Takanabe, Harvesting solar light with crystalline carbon nitrides for efficient photocatalytic hydrogen evolution, Angew. Chemie - Int. Ed. 53 (2014) 11001–11005.
- [13] S. Yang, Y. Gong, J. Zhang, L. Zhan, L. Ma, Z. Fang, R. Vajtai, X. Wang, P.M. Ajayan, Exfoliated graphitic carbon nitride nanosheets as efficient catalysts for hydrogen evolution under visible light, Adv. Mater. 25 (2013) 2452–2456.
- [14] L. Lin, W. Ren, C. Wang, A.M. Asiri, J. Zhang, X. Wang, Crystalline carbon nitride semiconductors prepared at different temperatures for photocatalytic hydrogen production, Appl. Catal. B Environ. 231 (2018) 234–241.

- [15] Z. Sun, M. Fujitsuka, C. Shi, M. Zhu, A. Wang, T. Majima, Efficient Visible-Light-Driven Hydrogen Generation on g-C<sub>3</sub>N<sub>4</sub> Coupled with Iron Phosphide, *ChemPhotoChem*. 3 (2019) 540–544.
- [16] Y.S. Jun, E.Z. Lee, X. Wang, W.H. Hong, G.D. Stucky, A. Thomas, From melamine-cyanuric acid supramolecular aggregates to carbon nitride hollow spheres, *Adv. Funct. Mater.* 23 (2013) 3661–3667.
- [17] P. Sharma, Y. Sasson, A photoactive catalyst Ru-g-C<sub>3</sub>N<sub>4</sub> for hydrogen transfer reaction of aldehydes and ketones, *Green Chem.* 19 (2017) 844–852.
- [18] J. Gao, Y. Wang, S. Zhou, W. Lin, Y. Kong, A Facile One-Step Synthesis of Fe-Doped g-C<sub>3</sub>N<sub>4</sub> Nanosheets and Their Improved Visible-Light Photocatalytic Performance, *ChemCatChem*. 9 (2017) 1708–1715.
- [19] B. Ma, J. Zhang, K. Lin, D. Li, Y. Liu, X. Yang, Improved photocatalytic hydrogen evolution of CdS using earth-abundant cocatalyst Mo<sub>2</sub>N with rod shape and large capacitance, *ACS Sustain. Chem. Eng.* 7 (2019) 13569–13575.
- [20] X. Lu, C.Y. Toe, F. Ji, W. Chen, X. Wen, R.J. Wong, J. Seidel, J. Scott, J.N. Hart, Y.H. Ng, Light-Induced Formation of MoO<sub>x</sub>S<sub>y</sub> Clusters on CdS Nanorods as Cocatalyst for Enhanced Hydrogen Evolution, *ACS Appl. Mater. Interfaces*. 12 (2020) 8324–8332.
- [21] L. Shang, B. Tong, H. Yu, G.I.N. Waterhouse, C. Zhou, Y. Zhao, M.

- Tahir, L.Z. Wu, C.H. Tung, T. Zhang, CdS Nanoparticle-Decorated Cd Nanosheets for Efficient Visible Light-Driven Photocatalytic Hydrogen Evolution, *Adv. Energy Mater.* 6 (2016) 1–7.
- [22] D. Jiang, L. Chen, J. Xie, M. Chen, Ag<sub>2</sub>S/g-C<sub>3</sub>N<sub>4</sub> composite photocatalysts for efficient Pt-free hydrogen production. the cocatalyst function of Ag/Ag<sub>2</sub>S formed by simultaneous photodeposition, *Dalt. Trans.* 43 (2014) 4878–4885.
- [23] G. Liu, P. Niu, C. Sun, S.C. Smith, Z. Chen, G.Q. Lu, H.M. Cheng, Unique electronic structure induced high photoreactivity of sulfur-doped graphitic C<sub>3</sub>N<sub>4</sub>, *J. Am. Chem. Soc.* 132 (2010) 11642–11648.
- [24] H. Li, H. Tian, X. Wang, M. Pi, S. Wei, H. Zhu, D. Zhang, S. Chen, Self-Coupled g-C<sub>3</sub>N<sub>4</sub> van der Waals Heterojunctions for Enhanced Photocatalytic Hydrogen Production, *ACS Appl. Energy Mater.* 2 (2019) 4692–4699.
- [25] Z. Zeng, Y. Su, X. Quan, W. Choi, G. Zhang, N. Liu, B. Kim, S. Chen, H. Yu, S. Zhang, Single-atom platinum confined by the interlayer nanospace of carbon nitride for efficient photocatalytic hydrogen evolution, *Nano Energy.* 69 (2020) 104409.
- [26] J. Tang, W. Zhou, R. Guo, C. Huang, W. Pan, P. Liu, An exploration on in-situ synthesis of europium doped g-C<sub>3</sub>N<sub>4</sub> for photocatalytic water splitting, *Energy Procedia.* 158 (2019) 1553–1558.
- [27] L. Yang, J. Liu, L. Yang, M. Zhang, H. Zhu, F. Wang, J. Yin, Co<sub>3</sub>O<sub>4</sub>

- imbedded g-C<sub>3</sub>N<sub>4</sub> heterojunction photocatalysts for visible-light-driven hydrogen evolution, *Renew. Energy*. 145 (2020) 691–698.
- [28] Y. Jin, D. Jiang, D. Li, P. Xiao, X. Ma, M. Chen, SrTiO<sub>3</sub> Nanoparticle/SnNb<sub>2</sub>O<sub>6</sub> Nanosheet 0D/2D Heterojunctions with Enhanced Interfacial Charge Separation and Photocatalytic Hydrogen Evolution Activity, *ACS Sustain. Chem. Eng.* 5 (2017) 9749–9757.
- [29] B. Han, L. Wu, J. Li, X. Wang, Q. Peng, N. Wang, X. Li, A nanoreactor based on SrTiO<sub>3</sub> coupled TiO<sub>2</sub> nanotubes confined Au nanoparticles for photocatalytic hydrogen evolution, *Int. J. Hydrogen Energy*. 45 (2019) 1559–1568.
- [30] H. He, J. Lin, W. Fu, X. Wang, H. Wang, Q. Zeng, Q. Gu, Y. Li, C. Yan, B.K. Tay, C. Xue, X. Hu, S.T. Pantelides, W. Zhou, Z. Liu, MoS<sub>2</sub>/TiO<sub>2</sub> Edge-On Heterostructure for Efficient Photocatalytic Hydrogen Evolution, *Adv. Energy Mater.* 6 (2016) 1–7.
- [31] L. Guo, Z. Yang, K. Marcus, Z. Li, B. Luo, L. Zhou, X. Wang, Y. Du, Y. Yang, MoS<sub>2</sub>/TiO<sub>2</sub> heterostructures as nonmetal plasmonic photocatalysts for highly efficient hydrogen evolution, *Energy Environ. Sci.* 11 (2018) 106–114.
- [32] Y. Pan, M. Wen, Noble metals enhanced catalytic activity of anatase TiO<sub>2</sub> for hydrogen evolution reaction, *Int. J. Hydrogen Energy*. 43 (2018) 22055–22063.

- [33] R. Tao, X. Li, X. Li, C. Shao, Y. Liu, TiO<sub>2</sub>/SrTiO<sub>3</sub>/g-C<sub>3</sub>N<sub>4</sub> ternary heterojunction nanofibers: Gradient energy band, cascade charge transfer, enhanced photocatalytic hydrogen evolution, and nitrogen fixation, *Nanoscale*. 12 (2020) 8320–8329.
- [34] X. Dai, L.B. Huang, Y. Du, J. Han, Q. Zheng, J. Kong, J. Hao, Self-Healing, Flexible, and Tailorable Triboelectric Nanogenerators for Self-Powered Sensors based on Thermal Effect of Infrared Radiation, *Adv. Funct. Mater.* 30 (2020) 1–10.
- [35] G. Li, X. Zhang, W. Zhao, W. Zhao, F. Li, K. Xiao, Q. Yu, S. Liu, Q. Zhao, Stable and Well-Organized Near-Infrared Platinum(II)-Acetylide-Based Metallacycles-Mediated Cancer Phototherapy, *ACS Appl. Mater. Interfaces*. 12 (2020) 20180–20190.
- [36] Z. Wang, Q. Shen, J. Zhang, M. Jiang, W. Chen, P. Tao, C. Song, B. Fu, T. Deng, W. Shang, Self-powered infrared detection using a graphene oxide film, *J. Mater. Chem. A*. 8 (2020) 9248–9255.
- [37] J.J. Li, S.C. Cai, E.Q. Yu, B. Weng, X. Chen, J. Chen, H.P. Jia, Y.J. Xu, Efficient infrared light promoted degradation of volatile organic compounds over photo-thermal responsive Pt-rGO-TiO<sub>2</sub> composites, *Appl. Catal. B Environ.* 233 (2018) 260–271.
- [38] Y. Zhang, Z. Peng, S. Guan, X. Fu, Novel B-NiS film modified CdS nanoflowers heterostructure nanocomposite: Extraordinarily highly efficient photocatalysts for hydrogen evolution, *Appl. Catal. B*

- Environ. 224 (2018) 1000–1008.
- [39] J. Jitputti, Y. Suzuki, S. Yoshikawa, Synthesis of TiO<sub>2</sub> nanowires and their photocatalytic activity for hydrogen evolution, *Catal. Commun.* 9 (2008) 1265–1271.
- [40] H. Ou, L. Lin, Y. Zheng, P. Yang, Y. Fang, X. Wang, Tri-s-triazine-Based Crystalline Carbon Nitride Nanosheets for an Improved Hydrogen Evolution, *Adv. Mater.* 29 (2017).
- [41] Q. Han, F. Zhao, C. Hu, L. Lv, Z. Zhang, N. Chen, L. Qu, Facile production of ultrathin graphitic carbon nitride nanoplatelets for efficient visible-light water splitting, 8 (2015) 1718–1728.
- [42] K. Li, Y.Z. Lin, K. Wang, Y. Wang, Y. Zhang, Y. Zhang, F.T. Liu, Rational design of cocatalyst system for improving the photocatalytic hydrogen evolution activity of graphite carbon nitride, *Appl. Catal. B Environ.* 268 (2020) 118402.
- [43] J. Chen, S. Shen, P. Guo, M. Wang, P. Wu, X. Wang, L. Guo, In-situ reduction synthesis of nano-sized Cu<sub>2</sub>O particles modifying g-C<sub>3</sub>N<sub>4</sub> for enhanced photocatalytic hydrogen production, *Appl. Catal. B Environ.* 152–153 (2014) 335–341.
- [44] V. Kumaravel, M.D. Imam, A. Badreldin, R.K. Chava, J.Y. Do, M. Kang, A. Abdel-Wahab, Photocatalytic hydrogen production: Role of sacrificial reagents on the activity of oxide, carbon, and sulfide catalysts, *Catalysts.* 9 (2019).

- [45] X. li Li, G. qing Yang, S. song Li, N. Xiao, N. Li, Y. qin Gao, D. Lv, L. Ge, Novel dual co-catalysts decorated Au@HCS@PdS hybrids with spatially separated charge carriers and enhanced photocatalytic hydrogen evolution activity, *Chem. Eng. J.* 379 (2020).
- [46] T. Shinagawa, K. Takanahe, New Insight into the Hydrogen Evolution Reaction under Buffered Near-Neutral pH Conditions: Enthalpy and Entropy of Activation, *J. Phys. Chem. C.* 120 (2016) 24187–24196.
- [47] X. Li, H. Zhang, Y. Liu, X. Duan, X. Xu, S. Liu, H. Sun, S. Wang, Synergy of NiO quantum dots and temperature on enhanced photocatalytic and thermophoto hydrogen evolution, *Chem. Eng. J.* 390 (2020) 124634.
- [48] X. Li, J. Wang, D. Xu, Z. Sun, Q. Zhao, W. Peng, Y. Li, G. Zhang, F. Zhang, X. Fan, NbSe<sub>2</sub> Nanosheet Supported PbBiO<sub>2</sub>Br as a High Performance Photocatalyst for the Visible Light-driven Asymmetric Alkylation of Aldehyde, *ACS Sustain. Chem. Eng.* 3 (2015) 1017–1022.
- [49] L. Yin, Y.P. Yuan, S.W. Cao, Z. Zhang, C. Xue, Enhanced visible-light-driven photocatalytic hydrogen generation over g-C<sub>3</sub>N<sub>4</sub> through loading the noble metal-free NiS<sub>2</sub> cocatalyst, *RSC Adv.* 4 (2014) 6127–6132.
- [50] Z. Zhao, Y. Dai, J. Lin, G. Wang, Highly-ordered mesoporous

carbon nitride with ultrahigh surface area and pore volume as a superior dehydrogenation catalyst, *Chem. Mater.* 26 (2014) 3151–3161.

- [51] A. Kheradmand, Y. Zhu, W. Zhang, A. Marianov, Y. Jiang, Cobalt oxide on mesoporous carbon nitride for improved photocatalytic hydrogen production under visible light irradiation, *Int. J. Hydrogen Energy.* 44 (2019) 17930–17942.

*Every reasonable effort has been made to acknowledge the owners of copyright material. I would be pleased to hear from any copyright owner who has been omitted or incorrectly acknowledged.*

## **Chapter 4 Synergy of NiO quantum dots and temperature on enhanced photocatalytic and thermophoto hydrogen evolution**

### **Abstract**

Solar-to-hydrogen holds a great promise as the sustainable energy solution, in which photocatalysis plays an important role. In the last Chapter, we studied the solar-heat influence on photocatalytic hydrogen evolution reaction (PC-HER). In this Chapter, a composite photocatalyst with NiO quantum dots (NiO QDs) in graphitic carbon nitride (g-CN) was synthesised and evaluated in photocatalytic (PC) and thermophotocatalytic HER processes under visible light irradiations. A sample of 9 wt% NiO QDs-g-CN achieved the highest PC-HER rate of  $130 \mu\text{mol}\cdot\text{g}^{-1}\cdot\text{h}^{-1}$  at ambient condition, 11 times higher than pristine g-CN. Meanwhile, the thermophotocatalytic HER rate reached  $260.2 \mu\text{mol}\cdot\text{g}^{-1}\cdot\text{h}^{-1}$  at  $55^\circ\text{C}$ . Photo-illumination led to the formation of C-O bond between g-CN and NiO QDs to bridge photoelectron transport for lowering the HER overpotential barriers and enhancing electrical conductivity. The higher thermophoto-induced HER can be ascribed to the increased electrical conductivity of NiO QDs-g-CN. This work underlines the importance of chemical binding in heterostructures and quantum confinement effects in QDs-based composites, and it also demonstrates the thermal sensitivity effect in thermophotocatalytic HER process.

## 4.1 Introduction

In recent decades, the depletion of fossil fuels[1–6] and increased environmental pollutions[7–12] urged researchers to develop new clean energy sources. With one of the most environmentally friendly methods and the cleanest energy product, photocatalytic (PC) hydrogen evolution reaction (HER) via water splitting has drawn widespread attention[13–18]. In this process, the key role is played by photocatalysts, which utilise photons for exciting electrons and holes to participate in redox reactions.

Graphitic carbon nitride (g-CN), with its suitable band structure, metal-free nature, easy fabrication and excellent chemical stability, is one of the most charming photocatalysts for PC-HER[19–26]. However, the high recombination rate of photo-excited electron-hole pairs causes its low performance[19–21]. Addition of cocatalysts has been an effective way to separate the photoinduced carriers for improving the photocatalytic activity[27–30]. While noble metal co-catalysts, platinum[27] or rhodium[31], can dramatically increase the PC-HER activity of g-CN, the iron[32], cobalt[33] or nickel-based[34,35] earth-abundant co-catalysts, provide cost-effective options. In particular, nickel-based catalysts have received more attention in recent years because of their outstanding activity[26,36].

Among them, nickel oxide is the most stable form with eminent electron transportation ability. Nevertheless, only a few investigations have been reported on its combination with g-CN for PC-HER[37,38]. Liu et al. prepared an amorphous NiO modified g-CN and used it in this area. The enriched active sites and extended visible light absorption remarkably promoted the PC-HER performance[38]. Li et al. studied the effect of nickel-based cocatalysts on g-CN. They reported that crystalline nickel oxide could greatly improve PC-HER activity because of the much lower impedance of NiO/g-CN[37]. However, no study has focused on the fabrication and application of NiO quantum dots (NiO QDs) on g-CN for PC-HER. With more exposed edges as catalytically active sites than NiO nanoparticles (NPs), NiO QDs appear to be a more favourable candidate as the cocatalyst in PC-HER.

Besides, considering that 43% of the solar spectrum falls within the infrared region[39], which has little ability for the photo-excitement of electrons. Then how to exploit this part of solar energy is up in the air. Given that the thermal effect is the main property of infrared lights[40], the reaction solution temperature will definitely go upwards in PC-HER. According to our tests, the temperature can reach 57 °C after 4 h irradiation using a Xenon lamp (refer to Figure 3.1). Therefore, finding the catalysts with evidently increased performance with temperature is

important. Taking into account that nickel oxide is a photosensitive semiconductor, whose resistance will decrease significantly with increasing temperature[41], it would be important to investigate the temperature effect on the performance of thermophoto reaction on NiO loaded on g-CN.

Hence, in this study, NiO QDs decorated g-CN was successfully synthesised by a refluxing method followed by a photo-illumination treatment. The as-prepared composite was used for PC-HER and thermophotocatalytic HER. The quantum confinement effects of NiO QDs and C-O single bonding formed via the photo illumination process led to faster electron transfer and lower over-potentials, resulting in the significantly enhanced PC-HER performance. In addition, the increased electron transfer ability of NiO at a higher temperature would synergistically help further improve the thermophoto performance of the as-synthesised catalyst.

## **4.2. Experimental**

### 4.2.1 Chemicals and materials

Urea (AR) was purchased from Chem-Supply, Australia. Nickel acetate tetrahydrate (98%), hexadecyl trimethyl ammonium bromide (CTAB,

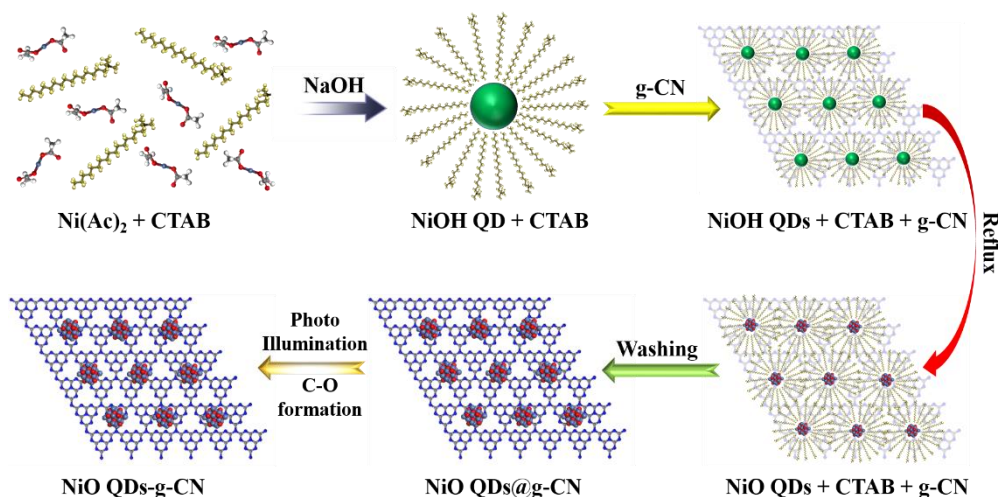
99%), ethylene glycol (EG, 99.8%), polyvinylpyrrolidone, sodium sulfate, sodium hydroxide, ethanol, acetone and methanol were supplied by Sigma-Aldrich, Australia. All the reagents were used directly without any further purification.

#### 4.2.2 Preparation of catalyst materials

Pristine g-CN powders were fabricated as below: 10 g of urea was placed in a furnace, heated to 550 °C at a heating rate of 15 °C min<sup>-1</sup> and kept for 4 h in air. The obtained chunk was ground to fine powders in a mortar.

Scheme 4.1 shows the typical synthesis of NiO QDs@g-CN and NiO QDs-g-CN. Typically, 61 mg of Ni(CH<sub>3</sub>COO)<sub>2</sub>·4H<sub>2</sub>O and 96 mg of CTAB were mixed in 70 mL of EG. Then 9.64 mL of NaOH solution (0.1 M in ethanol) was dropped in the mixture using a peristaltic pump. After 3-day stirring, 200 mg of g-CN was added. The mixture was sonicated for 1 h and then stirred for another day at ambient temperature. Subsequently, the mixed solution was refluxed for 3.5 h at the boiling point of EG, and the precipitate was then centrifuged, rinsed with ethanol and water for several times. The as-prepared composites were denoted as 9 wt% NiO QDs@g-CN, which were then transferred to the mixed solution of methanol (30 mL) and water (90 mL), and illuminated with a 300 W Xenon lamp for 4 h. The obtained precipitate was centrifuged and washed with ethanol and

water several times, and then dried in an oven of 60 °C. This sample was labelled as 9 wt% NiO QDs-g-CN. Other NiO QDs-g-CN samples were prepared similarly with different NiO loadings.



**Scheme 4.1** Schematic illustration of a refluxing route for the synthesis of NiO QDs@g-CN and NiO QDs-g-CN.  stands for nickel acetate,  CTAB,   $\text{Ni}(\text{OH})_2$  QD,  g-CN, and  NiO QD.

For comparison, a NiO nanoparticles (NPs) loaded on g-CN sample (NiO NPs-g-CN) was also prepared. For the preparation of NiO NPs, 4.35 g of  $\text{Ni}(\text{CH}_3\text{COO})_2 \cdot 4\text{H}_2\text{O}$  and 1.5 g of NaOH were dissolved in 30 mL and 75 mL of deionised (DI) water, respectively, followed by coprecipitation using polyvinylpyrrolidone (0.5 g) as a surfactant. The precipitate was obtained by centrifugation, rinsed with DI water and ethanol several times, and then dried at 60 °C for 24 h. Then, the collected precipitate was calcined at 300 °C for 2 h to obtain NiO NPs. In the following step, 200

mg of g-CN and 18 mg of NiO NPs were mixed in methanol and sonicated for 1 h, and then stirred for 24 h. The precipitate was collected by centrifugation, washed with water and ethanol, and then annealed at 300 °C in air for 2 h.

#### 4.2.3 Characterisation techniques

Transmission electron microscopy (TEM) and high angle annular dark-field scanning TEM (HAADF-STEM) images with elemental mapping were conducted on a Titan G2 60-300 at 200 and 80 kV, respectively. Powder X-ray diffraction (XRD) patterns were determined on a powder X-ray diffractometer (Miniflex, Rigaku) using Cu K $\alpha$  radiation. X-ray photoelectron spectroscopy (XPS) was measured on a Thermo Escalab 250 with an Al K $\alpha$  X-ray to determine the chemical states of the elements. Fourier transform infrared (FTIR) spectra were recorded on a Nicolet 6700 spectrometer. UV–vis diffuse reflectance spectra (DRS) were acquired on an Agilent Cary 100 UV–vis spectrophotometer equipped with an integrated sphere attachment. Photoluminescence (PL) spectra of the samples were obtained on a Cary Eclipse Fluorescence Spectrophotometer (Agilent, US).

#### 4.2.4 Photoelectrochemical tests

Electrochemical impedance spectroscopy (EIS), photocurrent, Mott-

Schottky and linear sweep voltammetry (LSV) curves were obtained on a Zennium electrochemical workstation (Zahner, Germany) in a standard three-electrode framework with a 0.05 M Na<sub>2</sub>SO<sub>4</sub> (pH = 6.8) electrolyte solution, employing a Pt plate as the counter electrode and an Ag/AgCl electrode as the reference electrode. As for the photoanode, the sample film was fabricated on a fluorine-doped tin oxide (FTO) glass, which was ultrasonicated in DI water, acetone and ethanol for 15 min in sequence and dried at 60 °C. Then 5 mg of the catalyst was mixed with 1 mL of absolute ethanol and 10 μL of Nafion solution homogeneously. The obtained slurry was dropped onto the pre-treated FTO glass via a spin-coating method, and the prepared electrode was dried at 100 °C for 24 h (catalyst loading ~ 0.60 mg·cm<sup>-2</sup>). Photocurrents were obtained using a 300W Xenon arc lamp with light passing through an AM 1.5 G filter into an optical fibre (output I<sub>0</sub> = 100 mW·cm<sup>-2</sup>).

#### 4.2.5 Photocatalytic activity evaluation

Photocatalytic H<sub>2</sub> production experiments were conducted in a stainless-steel reactor covered with a quartz window at ambient temperature. A 300W Xenon lamp (Newport) with a UV cutoff filter ( $\lambda > 400$  nm) was used as the light source. Typically, 50 mg of a photocatalyst was dispersed in a mixed solution (120 mL) containing DI water (90 mL) and methanol (30 mL). Prior to the irradiation, the suspensions were vigorously stirred

in the dark for 30 min, and the reaction vessel was degassed by purging with N<sub>2</sub> at the same time to form an anaerobic condition. The produced H<sub>2</sub> was analysed online by a gas chromatograph (Agilent 490 Micro GC) using a thermal conductivity detector. The apparent quantum efficiency (QE) was measured with a 420 nm filter. The focused intensity was tested with a light intensity meter. The QE was calculated according to the equation 4.1:

$$\text{QE}[\%] = \frac{\text{number of reacted electrons}}{\text{number of incident photons}} * 100 = \frac{\text{number of evolved H}_2 \text{ molecules} \times 2}{\text{number of incident photons}} * 100$$

Eq. 4.1

#### 4.2.6 Thermophoto activity evaluation

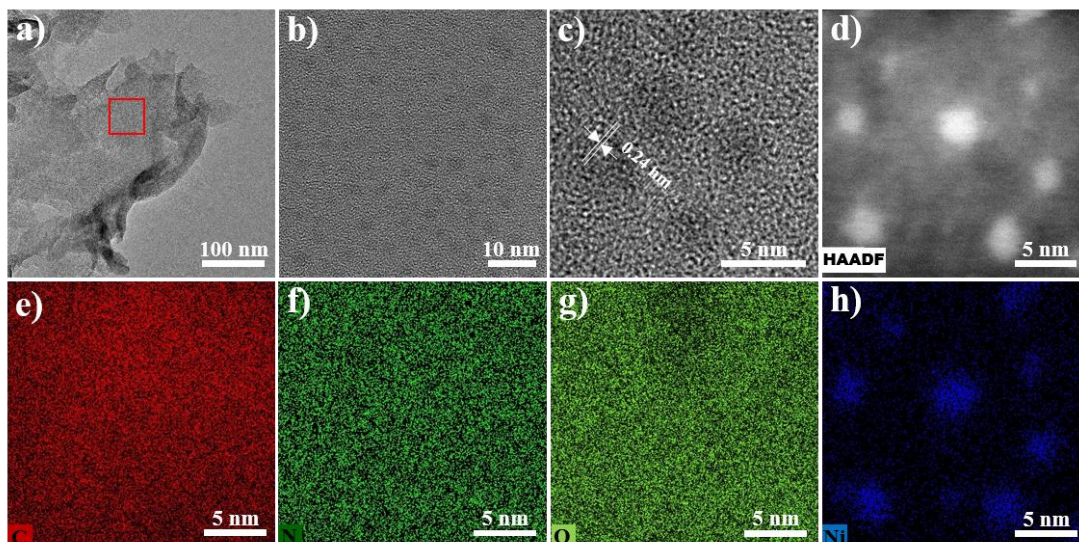
In the investigation of the temperature effect on photocatalytic activity of NiO QDs-g-CN, the solution temperature was controlled at 25, 35, 45, and 55 °C by both a heating plate and a circulating water system. After one hour of irradiation in the reactor, the produced H<sub>2</sub> was withdrawn to the online GC for detection.

### 4.3 Results and Discussion

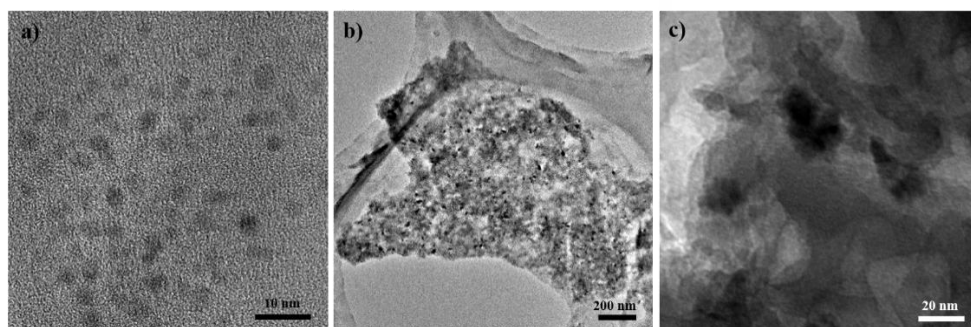
#### 4.3.1 Morphology, phase structure and composition of the catalysts

Figure 4.1a shows the TEM image of 9 wt% NiO QDs-g-CN, from which no evident particles can be found in the layered sheet-like g-CN. Small

dots in diameter of 2-4 nm can be observed on the surface of g-CN (Figure 4.1b) after amplifying the red frame section in Figure 4.1a. The HRTEM image (Figure 4.1c) shows the lattice distance of 0.24 nm that corresponds to the (111) plane of NiO, evidencing the successful fabrication of NiO QDs on g-CN. Figures 4.1d-h display the HAADF and corresponding elemental mapping. In detail, carbon, nitrogen and oxygen cover all the g-CN area, while nickel is just present on those small dots, indicating the formation of NiO QDs-g-CN and the uniform distribution of the QDs. Comparatively, TEM images of 9 wt% NiO QDs@g-CN (prepared without photo-illumination) and 9 wt% NiO NPs-g-CN are displayed in Figure 4.2. No evident morphological differences between NiO QDs@g-CN and NiO QDs-g-CN are shown, and NiO NPs with diameters of ~18-30 nm are evenly dispersed on NiO NPs-g-CN.



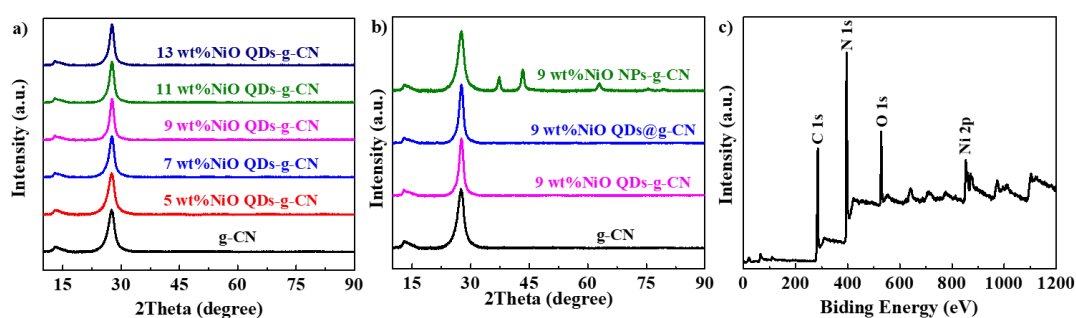
**Figure 4.1** Morphological characterisations of 9 wt% NiO QDs-g-CN. **a**, **b**) TEM images, **c**) high-resolution TEM image, **d**) HAADF image, and **e**, **f**, **g**, **h**) elemental mapping showing the distributions of carbon (red), nitrogen (olive), oxygen (green) and nickel (blue).



**Figure 4.2** TEM images of **a**) 9 wt% NiO QDs@g-CN and **b**) and **c**) 9 wt% NiO NPs-g-CN.

XRD patterns were investigated for the crystalline structure of g-CN and NiO QDs-g-CN at different ratios. In Figure 4.3a, only two peaks at about  $27.5^\circ$  and  $13.0^\circ$  can be found for all the samples, which stand for the

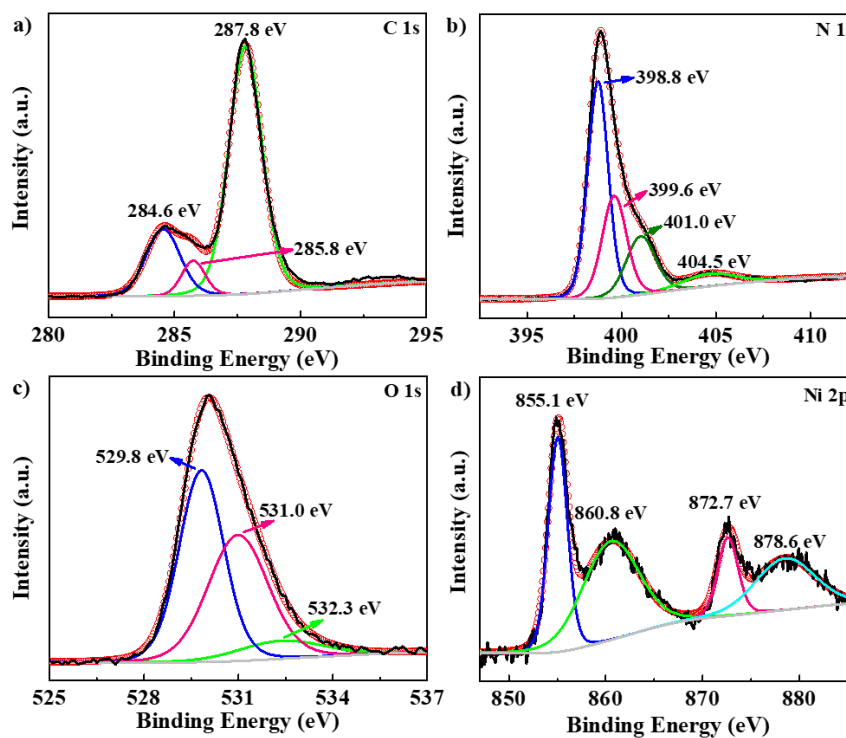
interplanar stacking of the conjugated double bonds for graphitic materials as the (002) crystal plane of 0.336 nm and the in-planar ordering of triazine units as the (100) plane at 0.675 nm, respectively.[24,42] The absence of NiO QDs peaks might be due to its quantum dot size, since a smaller particle size will usually reduce the continuity of the crystal lattice compared with a larger one, resulting in a weaker XRD peak intensity.[43] These results manifest that typical graphitic and layer-structured g-CN was well-formed as those in the previous reports[20,24,42] and that the addition of NiO QDs did not change the crystalline structure of g-CN. Additionally, XRD pattern (Figure 4.3b) of 9 wt% NiO QDs@g-CN is similar to that of 9 wt% NiO QDs-g-CN, while the peaks of NiO NPs on 9 wt% NiO NP-g-CN at 37.2°, 43.1°, 62.7°, 75.3°, and 79.3° can be clearly observed, corresponding to the (111), (200), (220), (311), and (222) plane diffractions of NiO (JCPDS No.47-1049)[38].



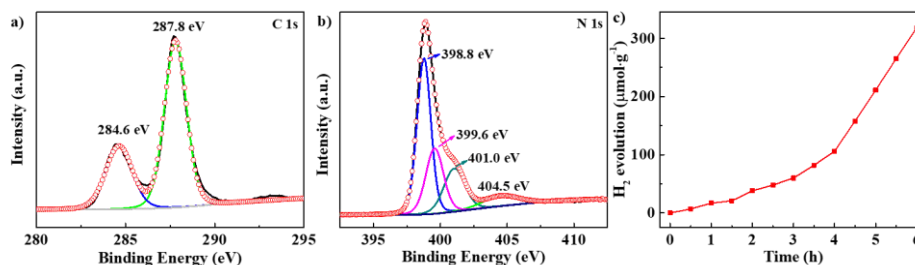
**Figure 4.3** a) XRD patterns of NiO QDs-g-CN with different ratios. b) XRD patterns of g-CN, 9 wt% NiO QDs@g-CN, 9 wt% NiO QDs-g-CN and 9 wt% NiO NPs-g-CN. c) XPS survey of 9 wt% NiO QDs-g-CN.

Figure 4.3c presents the XPS full-survey spectrum of 9 wt% NiO QDs-g-CN, containing elements of carbon, nitrogen, oxygen and nickel at binding energies of 287.3 (C 1s), 399.3 (N 1s), 529.8 (O 1s) and 855.1 eV (Ni 2p), respectively. Peaks of C 1s (Figure 4.4a) can be deconvoluted to three peaks at 284.6, 285.8 and 287.8 eV, respectively. The first and last peaks are in accordance with  $sp^2$  carbon bonded to the three nitrogen atoms in the g-CN lattice and unavoidably loaded graphitic carbon atoms, respectively[44,45], similar to g-CN (Figure 4.5a). The middle peak can be attributed to a carbon-oxygen single bond[46], indicating the formation of C-O bond between g-CN and NiO QDs. The new bonding could effectively improve the electron transportation between the interface of the two compounds[38], consistent with the EIS test reported in the following section. The four peaks in N 1s (Figure 4.4b) can be ascribed to the  $sp^2$ -bonded N atoms in graphite-like g-CN structure (C–N=C, 398.8 eV), tertiary groups (N–(C)<sub>3</sub>, 399.6 eV), amino-functional groups (C–N–H, 401.0 eV) and the typical  $\pi$ -excitation (404.5 eV) accordingly[45]. For O 1s (Figure 4.4c), the first peak (529.8 eV) originates from NiO QDs[47], while the second one (531.0 eV) is owing to the adsorbed H<sub>2</sub>O on the photocatalyst surface[48]. The third peak at 532.3 eV can be assigned to C–O single bond[49], which is in accordance with the results of C 1s (Figure 4.4a). In terms of Ni 2p (Figure 4.4d), the peak at 855.1 eV is

attributed to Ni 2p<sup>3/2</sup>, while the peak at 872.7 eV belongs to Ni 2p<sup>1/2</sup>, and the residual two peaks at 860.8 and 878.6 eV are the shakeup satellites[50].



**Figure 4.4** a) C1s of 9 wt% NiO QDs-g-CN, b) N1s of 9 wt% NiO QDs-g-CN, c) O 1s of 9 wt% NiO QDs-g-CN, and d) Ni 2p of 9 wt% NiO QDs-g-CN.



**Figure 4.5** a) C1s of g-CN. b) N1s of g-CN. c) Photocatalytic H<sub>2</sub> evolution on 9 wt% NiO QDs@g-CN.

In this study, the effect of photo-illumination treatment was investigated. A photocatalyst (NiO QDs@g-CN) without a photo-illumination treatment showed a very poor PC-HER performance (Figure 4.5c) in the first three hours, but it gradually presented a stable and good performance in the later several hours. XPS characterisation of NiO QDs-g-CN (after photo illumination of 4 h, Figure 4.4), NiO QDs@g-CN (before photo illumination, Figure 4.6) and g-CN (Figure 4.5a and b) suggested that the C-O bond is only present in NiO QDs-g-CN. Thus, it can be concluded that the C-O bond is formed in the photo illumination process and plays a critical role in the PC-HER performance (Figure 4.5c). Comparatively, the XPS spectrum of NiO NPs-g-CN was also acquired, as shown in Figure 4.7. The C-O bond was also found indicating that the main difference between NiO QDs-g-CN and NiO NPs-g-CN is lying on the sizes of QDs and NPs.

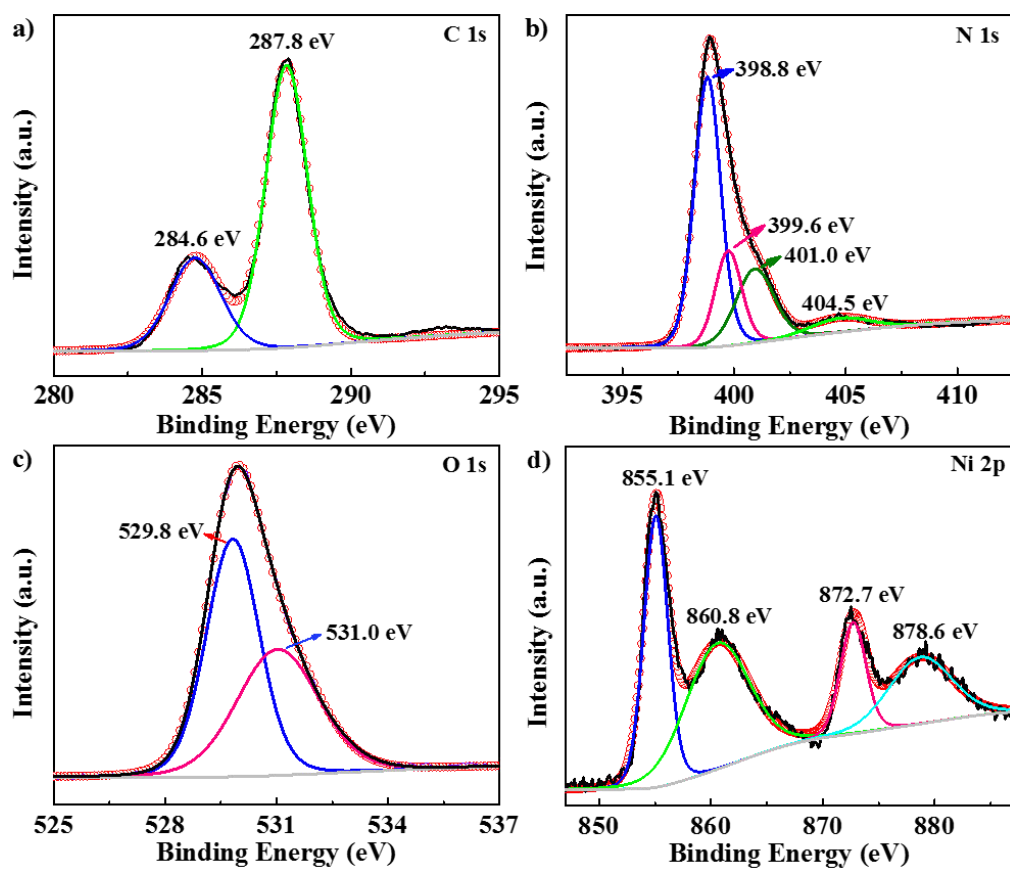


**Figure 4.6** XPS survey of 9 wt% NiO QDs@g-CN. **a)** C 1s, **b)** N 1s, **c)** O 1s, and **d)** Ni 2p.

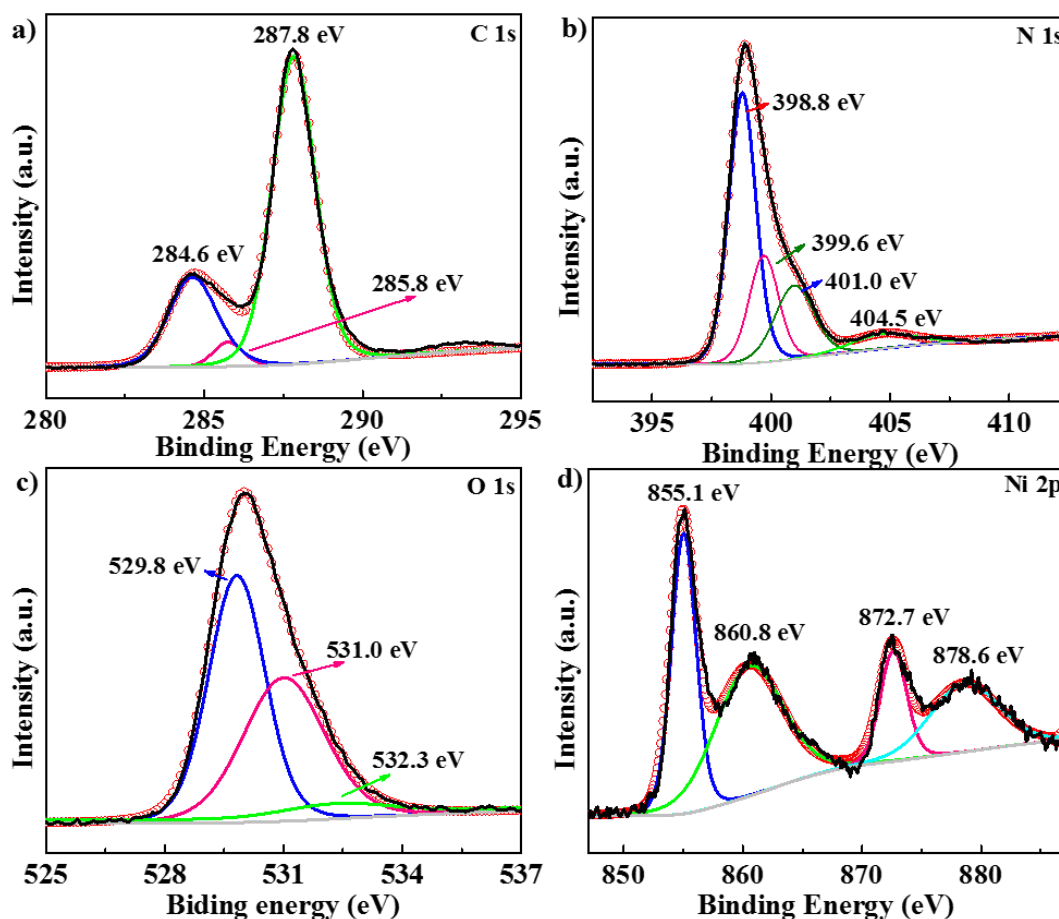


**Figure 4.7** XPS survey of 9 wt% NiO NPs-g-CN. a) C 1s, b) N 1s, c) O 1s, and d) Ni 2p.

To further verify the C-O bonds of NiO QDs-g-CN and NiO NPs-g-CN, we conducted FTIR of g-CN, NiO QDs@g-CN, NiO QDs-g-CN and NiO NPs-g-CN. Figure 4.8a displays that all these four samples show a similar spectrum, which is consistent with previously reported FTIR spectrum of g-CN[51]. When expanding the figure in the range of  $600\text{-}700\text{ nm}^{-1}$  (Figure 4.8b), a small broad peak for Ni-O bond can be found in NiO QDs@g-CN, NiO QDs-g-CN and NiO NPs-g-CN, but not in g-CN, demonstrating the existence of NiO in those three samples. More

importantly, when enlarging the figure in the range of 960-1110  $\text{nm}^{-1}$  (Figure 4.8c), a small sharp peak at  $\sim 1045 \text{ nm}^{-1}$  for C-O bond can only be found in NiO QDs-g-CN and NiO NPs-g-CN, but not in the other two samples, which complementarily proves the conclusion in XPS spectrum, that is the C-O bond only exists in NiO QDs-g-CN and NiO NPs-g-CN, but not in g-CN and NiO QDs@g-CN.

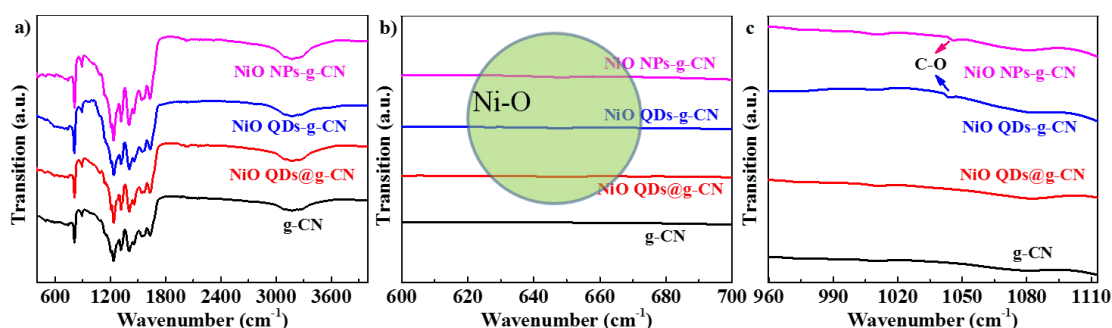


**Figure 4.8** FTIR spectrum of g-CN, NiO QDs@g-CN, NiO QDs-g-CN and NiO NPs-g-CN.

#### 4.3.2 Optical properties and bandstructure

UV-vis DRS was used to study the optical absorption and band structure of NiO QDs, g-CN, 9 wt% NiO QDs@g-CN, 9 wt% NiO QDs-g-CN and 9 wt% NiO NPs-g-CN. NiO QDs mainly absorb UV lights (Figure 4.9a), and the bandgap is 3.15 eV (Figure 4.9b), which is in the range of wide bandgap, consistent with previous reports[38,45]. NiO QDs@g-CN and NiO QDs-g-CN have an appreciable absorption increase in both the visible and ultraviolet regions than g-CN (Figure 4.9a). Only a mild

difference can be seen for NiO QDs@g-CN and NiO QDs-g-CN, indicating that the formation of the C-O bond in NiO QDs-g-CN does not significantly influence the optical property of the materials. This is perhaps because the formed C-O bonds appear mainly in the interfaces between g-CN and NiO QDs rather than their outside surfaces, which directly interact with photons. According to Kubelka-Munk theory, the bandgap energy was calculated as displayed in Figure 4.9b. Only a slight change can be found between g-CN (2.58 eV) and NiO QDs-g-CN (2.56 eV), while no difference was observed between NiO QDs@g-CN and NiO QDs-g-CN. For comparison, a little more absorption can be found for 9 wt% NiO NPs-g-CN in the range of 450 - 800 nm, and it has an obvious smaller bandgap of 2.47 eV.

Mott-Schottky (M-S) measurements were further conducted to determine the flat band potential values as well as the electronic band structure, using Equation 4.2.

$$1/C^2 = (2/\epsilon_r \epsilon_0 e N_d A^2) [(V - V_{fb}) - kT/e] \quad \text{Eq. 4.2}$$

Where  $V_{fb}$  (the flat band potential) can be obtained from the intercept of the plot tangents on X-axis when plotting  $1/C^2$  (C is the specific capacity) versus V (V is the applied potential).

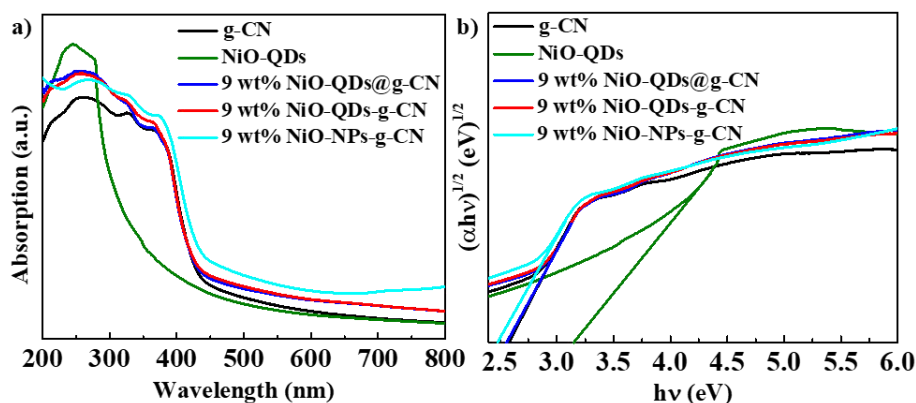


**Figure 4.9** a) UV-vis diffuse reflectance spectra and b) plots of  $(\alpha hv)^{1/2}$  versus bandgap energy ( $h\nu$ ) of g-CN, NiO QDs, 9 wt% NiO QDs@g-CN, 9 wt% NiO QDs-g-CN and 9 wt% NiO NPs-g-CN.

The positive slopes of the tangent lines in Figure 4.10a indicate that both g-CN and NiO QDs-g-CN are n-type semiconductors, for which the lowest potential of the conduction band (CB) can be extremely close to its flat-band potential. The flat band potential of NiO QDs-g-CN was calculated to be -1.11 V vs. SHE, the same as that of g-CN. From the UV-vis spectra and M-S tests, the valence band of 9 wt% NiO QDs-g-CN can be calculated to be 1.45 V vs. SHE, with CB of -1.11 V vs. SHE and bandgap energy of 2.56 eV, showing a slight change of the band structure (Figure 4.10b) after loading of NiO QDs.

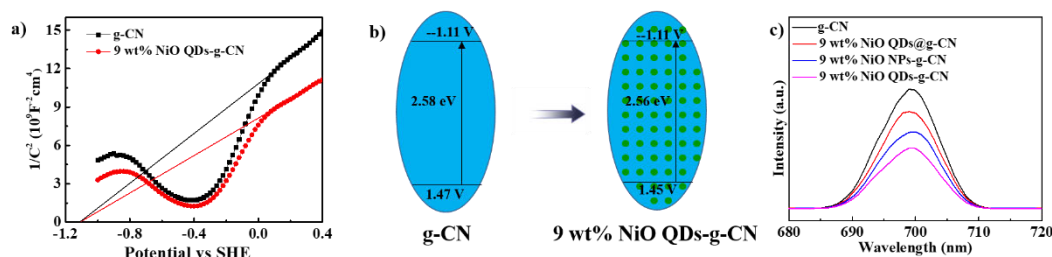


**Figure 4.10** a) Mott-Schottky curves of g-CN and 9 wt% NiO QDs-g-CN. b) Energy band structures of g-CN and 9 wt% NiO QDs-g-CN. c) PL spectra of g-CN, 9 wt% NiO QDs@g-CN, 9 wt% NiO QDs-g-CN and 9 wt% NiO NPs-g-CN.

Photoluminescence (PL) was performed to investigate the charge carrier separation, transfer, and recombination in g-CN, 9 wt% NiO QDs@g-CN, 9 wt% NiO QDs-g-CN and 9 wt% NiO NPs-g-CN (Figure 4.10c). All the photocatalysts exhibit similar emission trends at an excitation wavelength of 350 nm. The main emission peaks are centred at about 700 nm due to the recombination of the photoexcited electron-hole pairs derived from the intrinsic HOMO–LUMO transition. In terms of peak intensity, the order is g-CN > 9 wt% NiO QDs@g-CN > 9 wt% NiO NPs-g-CN > 9 wt% NiO QDs-g-CN. This observation indicates that both the addition of NiO QDs and NiO NPs can effectively promote the efficient charge transfer of g-CN, suppressing the recombination of photogenerated electrons and holes. More importantly, compared to 9 wt% NiO QDs@g-CN, the significantly lowered PL intensity of 9 wt% NiO QDs-g-CN should be due to the photoinduced C-O bond which favours electron transfer from g-CN to

NiO QDs. Lastly, the weaker intensity of 9 wt% NiO QDs-g-CN than that of 9 wt% NiO NPs-g-CN can be owing to the much larger interface between g-CN and NiO QDs of the former than the latter.

### 4.3.3 PC-HER activity and thermophoto HER

PC-HER tests were carried out on NiO QDs, g-CN and NiO QDs-g-CN with different NiO loading ratios. Figures 4.11a and b show that the NiO QD itself does not have the ability for PC-HER, which is consistent with its wide bandgap. For other samples, with the increasing content of NiO QDs, hydrogen production rate firstly increases and then decreases. At 9 wt%, NiO QDs-g-CN reaches the best performance at  $130 \mu\text{mol}\cdot\text{g}^{-1}\cdot\text{h}^{-1}$ , about 11 times as high as that of pristine g-CN ( $12 \mu\text{mol}\cdot\text{g}^{-1}\cdot\text{h}^{-1}$ ). This performance is among the top level of nickel-based cocatalysts decorated g-CN (Table 4.1), and the apparent quantum efficiency was also tested to be 0.7% under 420 nm light source. These results indicate that the addition of NiO QDs can significantly improve the photocatalytic ability of g-CN, but excessive loading of NiO QDs will reduce PC-HER performance. The stability tests of 9 wt% NiO QDs-g-CN in a 36-h photocatalytic run with 4-h intermittence present a 20% decrease of PC-HER rate after nine recycling runs (Figure 4.11c). TEM reveals that no apparent morphological change occurred on the catalyst before and after PC-HER tests (Figure 4.12). The loss of activity might be attributed to the photo-

corrosion of g-CN by photoinduced holes during the reaction process[52]. The PC-HER activities of 9 wt% NiO QDs-g-CN, 9 wt% NiO QDs@g-CN and 9 wt% NiO NPs-g-CN were also compared (Figure 4.11d). The 9 wt% NiO QDs@g-CN has an upshifting HER rate due to the formation of the C-O bond as described above. The dramatically higher HER ability of 9 wt% NiO QDs-g-CN in contrast to 9 wt% NiO QDs@g-CN evidently strengthens the significance of chemical bonding of the heterojunctions. The HER rate of 9 wt% NiO NPs-g-CN is  $74 \mu\text{mol}\cdot\text{g}^{-1}\cdot\text{h}^{-1}$ ,  $\sim 55\%$  of that on 9 wt% NiO QDs-g-CN, adequately demonstrating that NiO QDs facilitate PC-HER with much higher efficiency than NiO NPs as a cocatalyst.

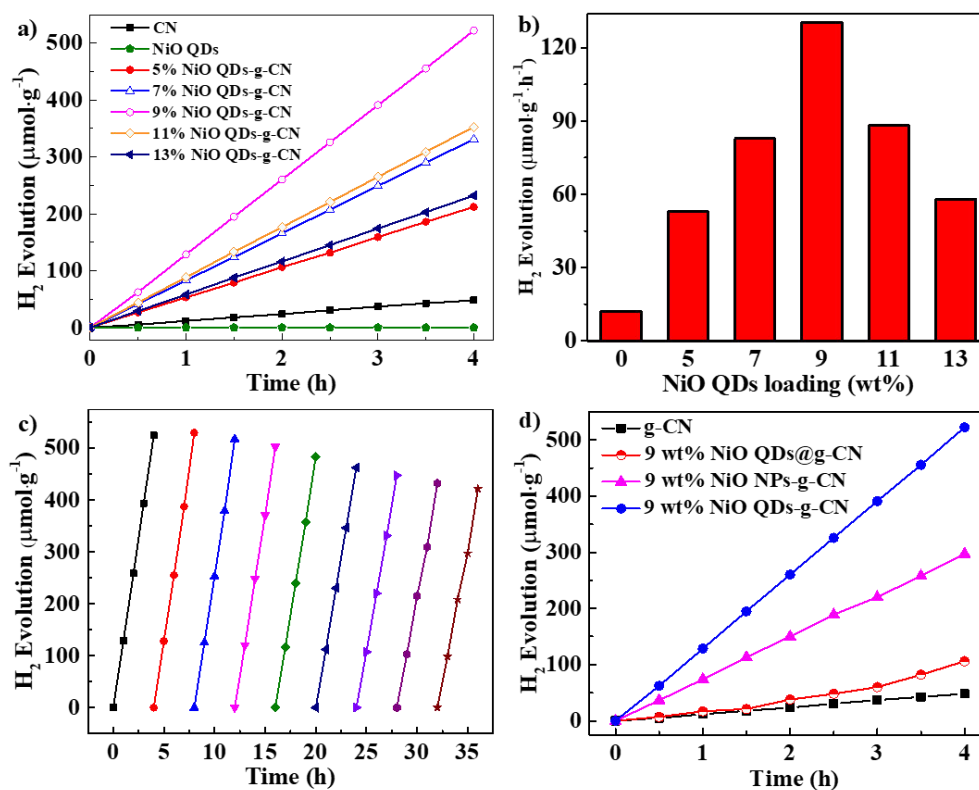


**Figure 4.11** a) Photocatalytic activity for H<sub>2</sub> evolution and b) average photocatalytic H<sub>2</sub> evolution rate over different samples under simulated solar light irradiations. c) The cycle runs for the photocatalytic H<sub>2</sub> evolution on 9 wt% NiO QDs-g-CN. d) Photocatalytic activity of H<sub>2</sub> evolution over g-CN, 9 wt% NiO QDs-g-CN, 9 wt% NiO QDs@g-CN, and 9 wt% NiO NPs-g-CN under simulated visible light irradiations.

**Table 4.1** Photocatalytic HER activities of graphitic carbon nitride modified with nickel-based cocatalysts.

Photocatalyst	Amount of photo-catalysts (mg)	Cocatalyst	Optimum loading	Hydrogen Evolution ( $\mu\text{mol}\cdot\text{h}^{-1}\cdot\text{g}^{-1}$ )	Reference
Ni(OH) <sub>2</sub> /g-C <sub>3</sub> N <sub>4</sub>	50	Ni(OH) <sub>2</sub>	0.5 mol%	152	[53]
NiS <sub>2</sub> /g-C <sub>3</sub> N <sub>4</sub>	10	NiS <sub>2</sub>	2 wt%	406	[54]
Ni(dmgh) <sub>2</sub> /g-C <sub>3</sub> N <sub>4</sub>	5	Ni(dmgh) <sub>2</sub>	3.5 wt%	236	[55]
Ni/NiO/g-C <sub>3</sub> N <sub>4</sub>	50	Ni/NiO	2.0 wt%	200	[56]
NiO/g-C <sub>3</sub> N <sub>4</sub>	50	Amorphous NiO	9 wt%	68.8	[57]
NiO/g-C <sub>3</sub> N <sub>4</sub>	40	NiO nanoparticles	--	82.9	[58]
NiO QDs-g-C <sub>3</sub> N <sub>4</sub>	50	NiO quantum dots	9 wt%	130	This work

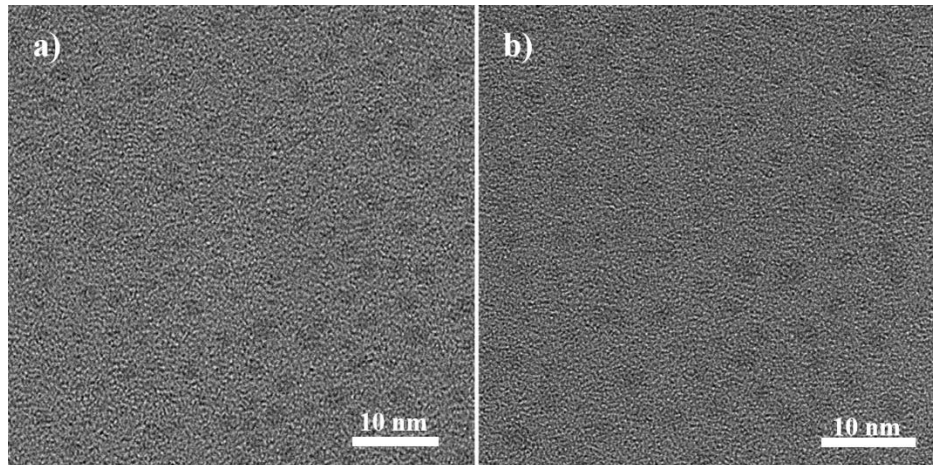


**Figure 4.12** TEM images of 9 wt% NiO QDs-g-CN **a)** before and **b)** after reactions.

In addition, thermophotocatalytic HER measurements were conducted over 9 wt% NiO QDs-g-CN (Figure 4.13a). The HER rate increased

almost linearly with a temperature increase from 25 to 55 °C, reaching 260.2  $\mu\text{mol}\cdot\text{g}^{-1}\cdot\text{h}^{-1}$  at 55 °C, which is nearly doubling the value at 25 °C. The increased rate of g-CN at the temperature of 55 °C, however, is only 1.25 times as high as that at 25 °C (Figure 4.13b), reflecting the eminent thermophoto performance of NiO QDs-g-CN. Afterwards, the stability test of 9 wt% NiO QDs-g-CN at 55 °C was carried out. After three-cycle runs (Figure 4.13c), a small loss can be found for the efficiency, which should result from minor agglomeration of NiO QDs, as shown in Figure 4.14a. No distinct change of 9 wt% NiO QDs-g-CN in UV-vis DRS test of before and after using at 55 °C (Figure 4.14b) also shows that it is relatively stable at this temperature.

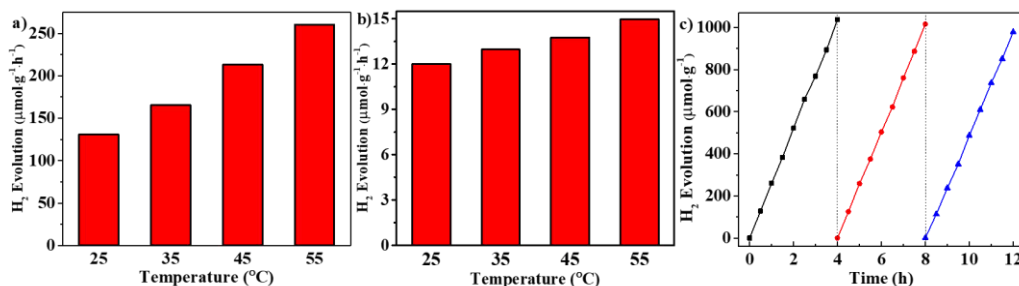


**Figure 4.13** Thermophoto H<sub>2</sub> evolution of **a)** 9 wt% NiO QDs-g-CN and **b)** g-CN at different temperatures. **c)** Cycle runs for thermophotocatalytic H<sub>2</sub> evolution on 9 wt% NiO QDs-g-CN at 55 °C.

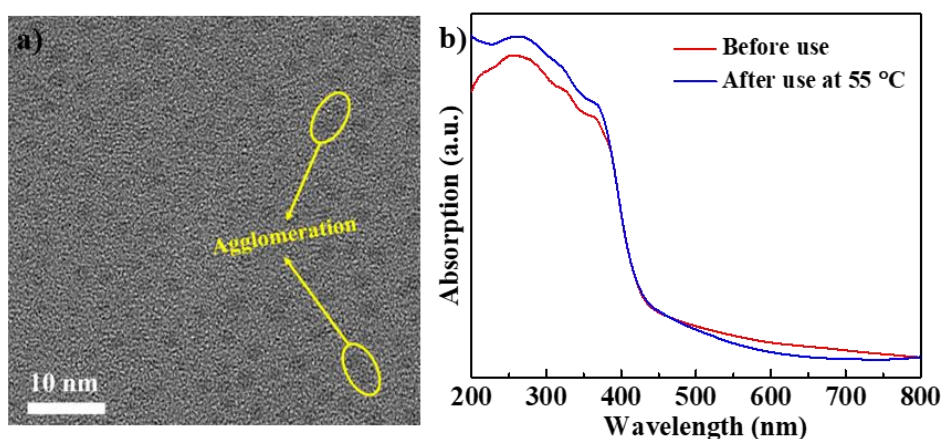


**Figure 4.14** a) TEM image of used 9 wt% NiO QDs-g-CN at 55 °C. b) UV-vis diffuse reflectance spectra of 9 wt% NiO QDs-g-CN before and after use at 55 °C.

#### 4.3.4 PC-HER and thermophoto HER mechanism

In order to clarify the mechanism, we firstly conducted tests of electrochemical impedance spectroscopy (EIS) of g-CN, 9 wt% NiO NPs-g-CN, 9 wt% NiO QDs@g-CN and 9 wt% NiO QDs-g-CN. As shown in Figure 4.15a, the Nyquist plot of g-CN shows a longer diameter than the other three NiO-loaded samples, indicating that the introduction of NiO led to a decreased resistance in the solid-state interface layer and a faster charge transfer in those composites. The shorter diameter of 9 wt% NiO QDs-g-CN than that of 9 wt% NiO QDs@g-CN can be attributed to the formation of C-O single bond between g-CN and NiO QDs, while the difference between 9 wt% NiO QDs-g-CN and 9 wt% NiO NPs-g-CN can be owing to the quantum confinement effect of NiO QDs, since with the

same amount of NiO, quantum size can dramatically increase the interface between NiO and g-CN, leading to faster charge transfer from g-CN towards NiO. These advantages of 9 wt% NiO QDs-g-CN will contribute to the suppression of charge recombination and a higher PC activity, which has been demonstrated in the PC-HER results.

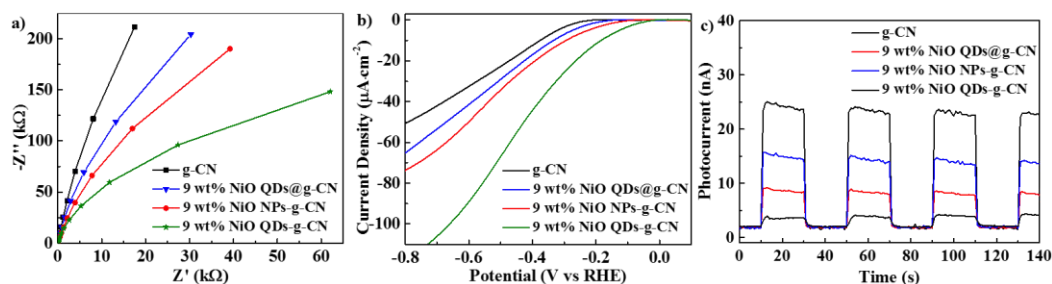


**Figure 4.15** Electrochemical characterisations. **a)** Nyquist plots of electrochemical impedance spectroscopy (EIS), **b)** polarisation curves and **c)** transient photocurrents of g-CN, 9 wt% NiO QDs@g-CN, 9 wt% NiO QDs-g-CN and 9 wt% NiO NPs-g-CN.

Electrochemical (EC) polarisation curves (Figure 4.15b) depict the electrocatalytic HER activity for g-CN and NiO QDs-g-CN, showing a significant cathodic current in a range of 0.1 – -0.8 V (versus RHE). The HER performance of the catalysts from the worst to the best can be ranked as below: g-CN < 9 wt% NiO QDs@g-CN < 9 wt% NiO NPs-g-CN < 9 wt% NiO QDs-g-CN, with onset potentials of -0.22, -0.17, -0.09 and -0.04 V vs RHE, respectively. The results suggest that 1) NiO plays a key role in decreasing the onset potential and increasing EC efficiency by acting as

an active site; 2) C-O single bond on NiO QDs-g-CN has a lower activation barrier for H<sub>2</sub> evolution than NiO QDs@g-CN; and 3) Improved kinetics of NiO QDs-g-CN as compared to that of NiO NPs-g-CN should be resulted from the quantum effect of NiO, which is because quantum sized NiO can provide more active sites than NiO NPs under the same amount.

Furthermore, the photoelectrochemical properties were studied on those four samples to explore the inherent mechanism of enhanced charge carrier separation and transportation. The photocurrent I-t curves for those samples were acquired under intermittent simulated sunlight (Figure 4.15c). Similar to the results of EIS and LSV, the I-t order of these samples from superior to inferior is also NiO QDs-g-CN, NiO NPs-g-CN, NiO QDs@g-CN and g-CN. This data indicates that NiO QDs can better promote the interfacial charge transfer with the g-CN than NiO NPs, which could also result from the larger interfacial face between g-CN and NiO QDs than that between g-CN and NiO NPs. Besides, the comparison of NiO QDs-g-CN and NiO QDs@g-CN proves the formed C-O bonds in NiO QDs-g-CN can help boost the charge transfer via interfaces as well.

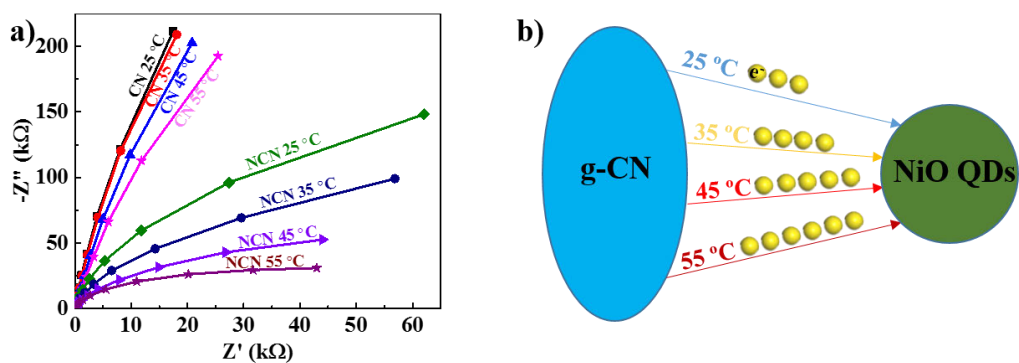


**Figure 4.16 a)** Nyquist plots of electrochemical impedance spectroscopy (EIS) for g-CN (CN) and 9 wt% NiO QDs-g-CN (NCN) under different temperatures, **b)** Mechanism of NiO QDs-g-CN under different temperatures.

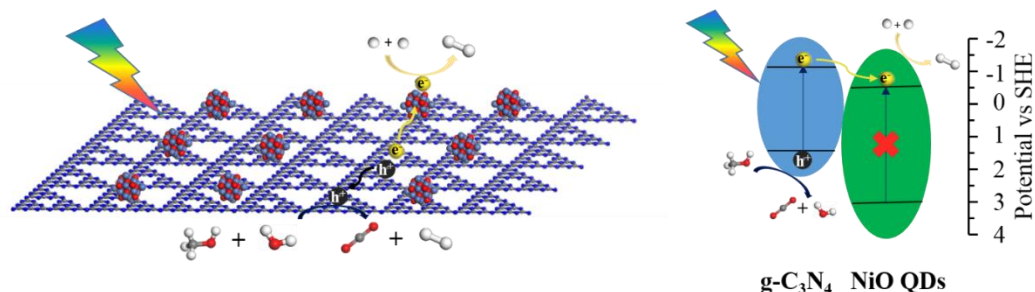
EIS of 9 wt% NiO QDs-g-CN and g-CN at different temperatures was also obtained to unveil the mechanism of the enhanced thermophotocatalytic HER performance. Figure 4.16a shows that, with a temperature increase, the diameters of EIS curves of g-CN and NiO QDs-g-CN reduce. More importantly, the diameter of EIS of NiO QDs-g-CN changes rapidly with the temperature, suggesting the more thermal sensitivity of NiO. The electrochemical impedance of NiO remarkably lessens with the increasing temperature[41]. Hence, more electrons can be effectively transferred to NiO QDs as the temperature increases, resulting in the better thermophotocatalytic HER performance of NiO QDs-g-CN.

The mechanisms of PC-HER and thermophoto HER over NiO QDs-g-CN are then illustrated in Scheme 4.2 and Figure 4.16b, respectively. The

conduction band (CB) and valence band (VB) energies of g-CN are -1.11 and 1.45 V vs SHE, respectively, with a bandgap energy of 2.56 eV (Figure 4.10b). Under photo illumination, excited electrons of the g-CN jump from the VB towards the CB, and then are transferred to the active sites, i.e. NiO QDs, via the C-O bond through the intimate contact interface. The separated electrons will then combine with  $H^+$  to evolve  $H_2$ , while the holes would be consumed by the sacrificial agent, methanol. In all these processes, no electrons of NiO can be excited because of its wide band structure. As a result, NiO QDs only act as a medium station for electrons, which can help inhibit the recombination of photoinduced electrons and holes. Besides, temperature rising results in a much better conductivity of NiO QDs-g-CN because of the thermal sensitivity of NiO, leading to more photogenerated electrons transferred from g-CN to NiO QDs, and eventually towards  $H^+$  to  $H_2$ .

In brief, the reduced electrochemical impedance and lowered overpotential, induced by the C-O bond between g-CN and NiO QDs, and the quantum confinement effect of NiO QDs mainly account for the enhanced PC-HER performance. Meanwhile, the increased electron transferability of the composite with the elevated temperature, based on the thermal sensitivity of NiO, is mainly responsible for the improved thermophoto HER performance. Besides, the uplifted photo absorbance

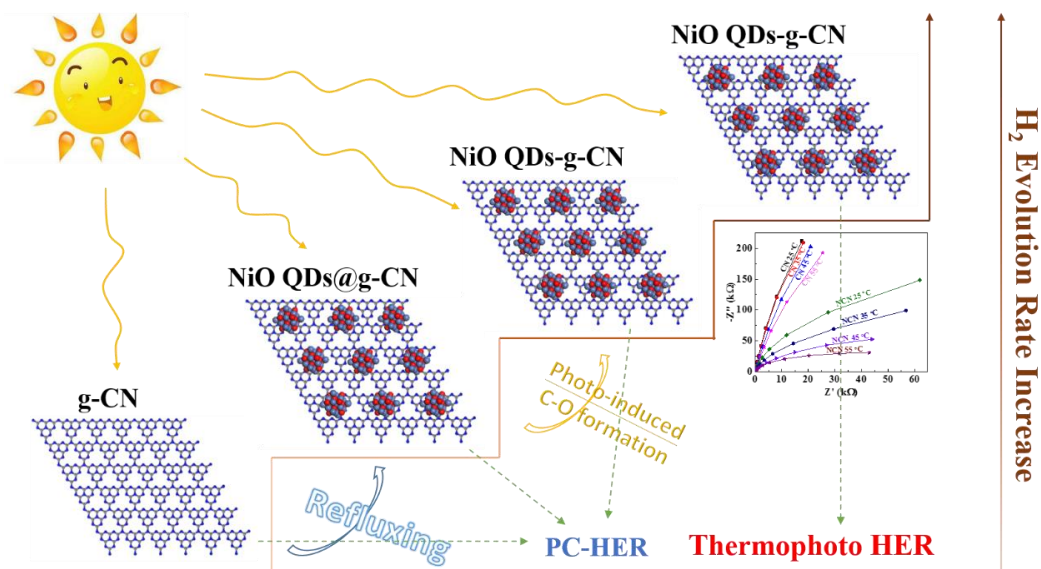
and the decreased bandgap of NiO QDs-g-CN also facilitate the PC-HER efficiency.



**Scheme 4.2** Mechanism of NiO QDs-g-CN for photocatalytic HER.

▨ stands for g-CN, ● NiO QD, ● methanol, ● CO<sub>2</sub>, ● H<sub>2</sub>O, ● H<sup>+</sup>, and ● H<sub>2</sub>.

Overall, the increase in HER rate goes through four stages, as shown in Scheme 4.3. In stage 2, the addition of NiO QDs slightly facilitates the PC-HER performance by improving both electrical and optical properties of the material, g-CN, while in stage 3, the photoinduced C-O bond is mainly responsible for the enhancement of PC-HER, via impacting the material's electrical property rather than optical property. And then, the HER rate achieves the best at 55 °C in stage 4, attributing to the thermal sensitivity of nickel oxide. Therefore, the synergy of NiO QDs and temperature help boost HER performance to a large extent.



**Scheme 4.3** The HER rate increase processes on NiO QDs-g-CN.

## 4 Conclusions

NiO QDs-g-CN was synthesised by a refluxing and photo-illumination method and utilised in PC-HER and thermophoto HER, showing excellent performances. Specially, C-O single bond was formed between g-CN and NiO QDs in photo illumination. The enhanced PC-HER performance is mainly attributed to the lowered HER overpotential barriers and the enhanced electrical conductivity, which are deeply owing to the emerging C-O single bond and the quantum size effect of NiO QDs. Besides, the improved light absorbance and narrowed bandgap of NiO QDs-g-CN also contribute to the enhanced HER performances. The photoinduced C-O bond is the key for the enhancement in PC-HER process, via impacting the material's electrical property rather than optical property. Enhanced thermophoto HER was observed as well and can be ascribed to the

significantly increased electrical conductivity of NiO QDs-g-CN. Therefore, NiO QDs and temperature synergistically boost the PC-HER performance of g-CN. This work suggests that chemical bonding is critical for effective heterostructures, and the thermal sensitivity influences thermophoto HER process.

## References

- [1] F. Mwasilu, J.J. Justo, E.K. Kim, T.D. Do, J.W. Jung, Electric vehicles and smart grid interaction: A review on vehicle to grid and renewable energy sources integration, *Renew. Sustain. Energy Rev.* 34 (2014) 501–516.
- [2] J. Aghaei, M.I. Alizadeh, Demand response in smart electricity grids equipped with renewable energy sources: A review, *Renew. Sustain. Energy Rev.* 18 (2013) 64–72.
- [3] N.L. Panwar, S.C. Kaushik, S. Kothari, Role of renewable energy sources in environmental protection: A review, *Renew. Sustain. Energy Rev.* 15 (2011) 1513–1524.
- [4] S.F. Tie, C.W. Tan, A review of energy sources and energy management system in electric vehicles, *Renew. Sustain. Energy Rev.* 20 (2013) 82–102.
- [5] M. Liserre, MARCO LISERRE, THILO SAUTER, and JOHN Y. HUNG, (2010) 18–37.

- [6] P. Poizot, F. Dolhem, Clean energy new deal for a sustainable world: From non-CO<sub>2</sub> generating energy sources to greener electrochemical storage devices, *Energy Environ. Sci.* 4 (2011) 2003–2019.
- [7] B. Brunekreef, S.T. Holgate, Air pollution and health, *Lancet*. 360 (2002) 1233–1242.
- [8] A. Science, E. Content, Air Pollution – Related Illness :, *Science* (80-. ). 804 (2014).
- [9] J. Lelieveld, J.S. Evans, M. Fnais, D. Giannadaki, A. Pozzer, The contribution of outdoor air pollution sources to premature mortality on a global scale, *Nature*. 525 (2015) 367–371.
- [10] E. Tagaris, K.J. Liao, A.J. Delucia, L. Deck, P. Amar, A.G. Russell, Potential impact of climate change on air pollution-related human health effects, *Environ. Sci. Technol.* 43 (2009) 4979–4988.
- [11] M. Cole, P. Lindeque, E. Fileman, C. Halsband, R. Goodhead, J. Moger, T.S. Galloway, Microplastic ingestion by zooplankton, *Environ. Sci. Technol.* 47 (2013) 6646–6655.
- [12] T. Niisoe, K.H. Harada, T. Hitomi, T. Watanabe, N.N. Hung, H. Ishikawa, Z. Wang, A. Koizumi, Environmental ecological modeling of human blood lead levels in East Asia, *Environ. Sci. Technol.* 45 (2011) 2856–2862.
- [13] X. Chen, S. Shen, L. Guo, S.S. Mao, Semiconductor-based photocatalytic hydrogen generation, *Chem. Rev.* 110 (2010) 6503–

6570.

- [14] N.L. Rosi, J. Eckert, M. Eddaoudi, D.T. Vodak, J. Kim, M. O’Keeffe, O.M. Yaghi, Hydrogen storage in microporous metal-organic frameworks, *Science* (80-. ). 300 (2003) 1127–1129.
- [15] C.H. Klangt, D.S. Bethunet, M.J. Heben, letters to nature " ’ 0 Iron cycle, 668 (1997) 1995–1997.
- [16] C.K. Ngaw, Q. Xu, T.T.Y. Tan, P. Hu, S. Cao, J.S.C. Loo, A strategy for in-situ synthesis of well-defined core-shell Au@TiO<sub>2</sub> hollow spheres for enhanced photocatalytic hydrogen evolution, *Chem. Eng. J.* 257 (2014) 112–121.
- [17] C. Ma, Y. Li, H. Zhang, Y. Chen, C. Lu, J. Wang, Photocatalytic hydrogen evolution with simultaneous photocatalytic reforming of biomass by Er<sup>3+</sup>: YAlO<sub>3</sub>/Pt-TiO<sub>2</sub> membranes under visible light driving, *Chem. Eng. J.* 273 (2015) 277–285.
- [18] Y. Li, L. Wang, T. Cai, S. Zhang, Y. Liu, Y. Song, X. Dong, L. Hu, Glucose-assisted synthesis 1D/2D nearly vertical CdS/MoS<sub>2</sub> heterostructures for efficient photocatalytic hydrogen evolution, *Chem. Eng. J.* 321 (2017) 366–374.
- [19] H. Xu, J. Yi, X. She, Q. Liu, L. Song, S. Chen, Y. Yang, Y. Song, R. Vajtai, J. Lou, H. Li, S. Yuan, J. Wu, P.M. Ajayan, 2D heterostructure comprised of metallic 1T-MoS<sub>2</sub>/Monolayer O-g-C<sub>3</sub>N<sub>4</sub> towards efficient photocatalytic hydrogen evolution, *Appl.*

- Catal. B Environ. 220 (2018) 379–385.
- [20] S. Thaweesak, M. Lyu, P. Peerakiatkhajohn, T. Butburee, B. Luo, H. Chen, L. Wang, Two-dimensional g-C<sub>3</sub>N<sub>4</sub>/Ca<sub>2</sub>Nb<sub>2</sub>TaO<sub>10</sub> nanosheet composites for efficient visible light photocatalytic hydrogen evolution, Appl. Catal. B Environ. 202 (2017) 184–190.
- [21] X. She, J. Wu, J. Zhong, H. Xu, Y. Yang, R. Vajtai, J. Lou, Y. Liu, D. Du, H. Li, P.M. Ajayan, Oxygenated monolayer carbon nitride for excellent photocatalytic hydrogen evolution and external quantum efficiency, Nano Energy. 27 (2016) 138–146.
- [22] G. Liu, G. Zhao, W. Zhou, Y. Liu, H. Pang, H. Zhang, D. Hao, X. Meng, P. Li, T. Kako, J. Ye, In Situ Bond Modulation of Graphitic Carbon Nitride to Construct p–n Homojunctions for Enhanced Photocatalytic Hydrogen Production, Adv. Funct. Mater. 26 (2016) 6822–6829.
- [23] Q. Liang, Z. Li, X. Yu, Z.H. Huang, F. Kang, Q.H. Yang, Macroscopic 3D Porous Graphitic Carbon Nitride Monolith for Enhanced Photocatalytic Hydrogen Evolution, Adv. Mater. 27 (2015) 4634–4639.
- [24] Q. Liang, Z. Li, Z.H. Huang, F. Kang, Q.H. Yang, Holey Graphitic Carbon Nitride Nanosheets with Carbon Vacancies for Highly Improved Photocatalytic Hydrogen Production, Adv. Funct. Mater. 25 (2015) 6885–6892.

- [25] Y. Kang, Y. Yang, L.C. Yin, X. Kang, G. Liu, H.M. Cheng, An Amorphous Carbon Nitride Photocatalyst with Greatly Extended Visible-Light-Responsive Range for Photocatalytic Hydrogen Generation, *Adv. Mater.* 27 (2015) 4572–4577.
- [26] A. Indra, A. Acharjya, P.W. Menezes, C. Merschjann, D. Hollmann, M. Schwarze, M. Aktas, A. Friedrich, S. Lochbrunner, A. Thomas, M. Driess, Boosting Visible-Light-Driven Photocatalytic Hydrogen Evolution with an Integrated Nickel Phosphide–Carbon Nitride System, *Angew. Chemie - Int. Ed.* 56 (2017) 1653–1657.
- [27] J. Ran, G. Gao, F.T. Li, T.Y. Ma, A. Du, S.Z. Qiao,  $\text{Ti}_3\text{C}_2$  MXene cocatalyst on metal sulfide photo-absorbers for enhanced visible-light photocatalytic hydrogen production, *Nat. Commun.* 8 (2017).
- [28] J. Ran, W. Guo, H. Wang, B. Zhu, J. Yu, S.Z. Qiao, Metal-Free 2D/2D Phosphorene/g- $\text{C}_3\text{N}_4$  Van der Waals Heterojunction for Highly Enhanced Visible-Light Photocatalytic  $\text{H}_2$  Production, *Adv. Mater.* 30 (2018) 2–7.
- [29] J. Ran, J. Qu, H. Zhang, T. Wen, H. Wang, S. Chen, L. Song, X. Zhang, L. Jing, R. Zheng, S.Z. Qiao, 2D Metal Organic Framework Nanosheet: A Universal Platform Promoting Highly Efficient Visible-Light-Induced Hydrogen Production, *Adv. Energy Mater.* 9 (2019) 1–8.
- [30] J. Ran, B. Zhu, S.Z. Qiao, Phosphorene Co-catalyst Advancing

Highly Efficient Visible-Light Photocatalytic Hydrogen Production, *Angew. Chemie - Int. Ed.* 56 (2017) 10373–10377.

- [31] Y. Sasaki, A. Iwase, H. Kato, A. Kudo, The effect of cocatalyst for Z-scheme photocatalysis systems with an  $\text{Fe}^{3+}/\text{Fe}^{2+}$  electron mediator on overall water splitting under visible light irradiation, *J. Catal.* 259 (2008) 133–137.
- [32] M. Yoshimizu, R. Kobayashi, M. Saegusa, T. Takashima, H. Funakubo, K. Akiyama, Y. Matsumoto, H. Irie, Photocatalytic hydrogen evolution over  $\beta$ -iron silicide under infrared-light irradiation, *Chem. Commun.* 51 (2015) 2818–2820.
- [33] Y. Li, Z. Yu, J. Meng, J. Xiao, Y. Li, Cobalt sulfide quantum dots modified  $\text{TiO}_2$  nanoparticles for efficient photocatalytic hydrogen evolution, *Int. J. Hydrogen Energy.* 39 (2014) 15387–15393.
- [34] Y. Liu, H. Zhang, J. Ke, J. Zhang, W. Tian, X. Xu, X. Duan, H. Sun, M. O Tade, S. Wang, 0D ( $\text{MoS}_2$ )/2D ( $\text{g-C}_3\text{N}_4$ ) heterojunctions in Z-scheme for enhanced photocatalytic and electrochemical hydrogen evolution, *Appl. Catal. B Environ.* 228 (2018) 64–74.
- [35] L. Zhang, B. Tian, F. Chen, J. Zhang, Nickel sulfide as cocatalyst on nanostructured  $\text{TiO}_2$  for photocatalytic hydrogen evolution, *Int. J. Hydrogen Energy.* 37 (2012) 17060–17067.
- [36] J. Xu, Y. Qi, L. Wang, In situ derived  $\text{Ni}_2\text{P}/\text{Ni}$  encapsulated in carbon/ $\text{g-C}_3\text{N}_4$  hybrids from metal–organic frameworks/ $\text{g-C}_3\text{N}_4$  for

- efficient photocatalytic hydrogen evolution, *Appl. Catal. B Environ.* 246 (2019) 72–81.
- [37] L. Yang, H. Li, Y. Yu, H. Yu, Study on the cocatalytic performance of nickel species in g-C<sub>3</sub>N<sub>4</sub> system for photocatalytic hydrogen evolution, *Catal. Commun.* 110 (2018) 51–54.
- [38] J. Liu, Q. Jia, J. Long, X. Wang, Z. Gao, Q. Gu, Amorphous NiO as cocatalyst for enhanced visible-light-driven hydrogen generation over g-C<sub>3</sub>N<sub>4</sub> photocatalyst, *Appl. Catal. B Environ.* 222 (2018) 35–43.
- [39] B.D. Ravetz, A.B. Pun, E.M. Churchill, D.N. Congreve, T. Rovis, L.M. Campos, Photoredox catalysis using infrared light via triplet fusion upconversion, *Nature.* 565 (2019) 343–346.
- [40] X. Meng, T. Wang, L. Liu, S. Ouyang, P. Li, H. Hu, T. Kako, H. Iwai, A. Tanaka, J. Ye, Photothermal conversion of CO<sub>2</sub> into CH<sub>4</sub> with H<sub>2</sub> over Group VIII nanocatalysts: An alternative approach for solar fuel production, *Angew. Chemie - Int. Ed.* 53 (2014) 11478–11482.
- [41] C.H. Lai, Y.M. Lee, C.F. Tseng, C.Y. Liu, Resistance transition in NiO thin film and its temperature dependence, *Ferroelectrics.* 435 (2012) 155–160.
- [42] Q. Han, B. Wang, J. Gao, L. Qu, Graphitic Carbon Nitride/Nitrogen-Rich Carbon Nanofibers: Highly Efficient Photocatalytic Hydrogen

- Evolution without Cocatalysts, *Angew. Chemie - Int. Ed.* 55 (2016) 10849–10853.
- [43] C.F. Holder, R.E. Schaak, Tutorial on Powder X-ray Diffraction for Characterising Nanoscale Materials, *ACS Nano*. 13 (2019) 7359–7365.
- [44] S. Cao, J. Jiang, B. Zhu, J. Yu, Shape-dependent photocatalytic hydrogen evolution activity over a Pt nanoparticle coupled g-C<sub>3</sub>N<sub>4</sub> photocatalyst, *Phys. Chem. Chem. Phys.* 18 (2016) 19457–19463.
- [45] Y. Fu, C. Liu, C. Zhu, H. Wang, Y. Dou, W. Shi, M. Shao, H. Huang, Y. Liu, Z. Kang, High-performance NiO/g-C<sub>3</sub>N<sub>4</sub> composites for visible-light-driven photocatalytic overall water splitting, *Inorg. Chem. Front.* 5 (2018) 1646–1652.
- [46] M. Tong, S. Liu, X. Zhang, T. Wu, H. Zhang, G. Wang, Y. Zhang, X. Zhu, H. Zhao, Two-dimensional CoNi nanoparticles@S,N-doped carbon composites derived from S,N-containing Co/Ni MOFs for high performance supercapacitors, *J. Mater. Chem. A*. 5 (2017) 9873–9881.
- [47] L. Li, W. Wang, L. He, J. Zhang, Z. Wu, B. Zhang, Y. Liu, Synthesis and characterisation of p-type NiO films suitable for normally-off AlGaN/GaN HFETs application, *Mater. Sci. Semicond. Process.* 67 (2017) 141–146.
- [48] S. Martha, A. Nashim, K.M. Parida, Facile synthesis of highly active

- g-C<sub>3</sub>N<sub>4</sub> for efficient hydrogen production under visible light, *J. Mater. Chem. A*. 1 (2013) 7816–7824.
- [49] C.H. Kim, B.H. Kim, K.S. Yang, TiO<sub>2</sub> nanoparticles loaded on graphene/carbon composite nanofibers by electrospinning for increased photocatalysis, *Carbon N. Y.* 50 (2012) 2472–2481.
- [50] J. ying Tang, R. tang Guo, W. guo Zhou, C. ying Huang, W. guo Pan, Ball-flower like NiO/g-C<sub>3</sub>N<sub>4</sub> heterojunction for efficient visible light photocatalytic CO<sub>2</sub> reduction, *Appl. Catal. B Environ.* 237 (2018) 802–810.
- [51] H. Zou, X. Yan, J. Ren, X. Wu, Y. Dai, D. Sha, J. Pan, J. Liu, Photocatalytic activity enhancement of modified g-C<sub>3</sub>N<sub>4</sub> by ionothermal copolymerisation, *J. Mater.* 1 (2015) 340–347.
- [52] M. Wang, S. Shen, L. Li, Z. Tang, J. Yang, Effects of sacrificial reagents on photocatalytic hydrogen evolution over different photocatalysts, *J. Mater. Sci.* 52 (2017) 5155–5164.
- [53] J. Yu, S. Wang, B. Cheng, Z. Lin, F. Huang, Noble metal-free Ni(OH)<sub>2</sub>-g-C<sub>3</sub>N<sub>4</sub> composite photocatalyst with enhanced visible-light photocatalytic H<sub>2</sub>- production activity, *Catal. Sci. Technol.* 3 (2013) 1782–1789.
- [54] L. Yin, Y.P. Yuan, S.W. Cao, Z. Zhang, C. Xue, Enhanced visible-light-driven photocatalytic hydrogen generation over g-C<sub>3</sub>N<sub>4</sub> through loading the noble metal-free NiS<sub>2</sub> cocatalyst, *RSC Adv.* 4

(2014) 6127–6132.

- [55] S.W. Cao, Y.P. Yuan, J. Barber, S.C.J. Loo, C. Xue, Noble-metal-free g-C<sub>3</sub>N<sub>4</sub> /Ni(dmgh)<sub>2</sub> composite for efficient photocatalytic hydrogen evolution under visible light irradiation, *Appl. Surf. Sci.* 319 (2014) 344–349.
- [56] G. Zhang, G. Li, X. Wang, Surface Modification of Carbon Nitride Polymers by Core-Shell Nickel/Nickel Oxide Cocatalysts for Hydrogen Evolution Photocatalysis, *ChemCatChem.* 7 (2015) 2864–2870.
- [57] J. Liu, Q. Jia, J. Long, X. Wang, Z. Gao, Q. Gu, Amorphous NiO as cocatalyst for enhanced visible-light-driven hydrogen generation over g-C<sub>3</sub>N<sub>4</sub> photocatalyst, *Appl. Catal. B Environ.* 222 (2018) 35–43.
- [58] L. Yang, H. Li, Y. Yu, H. Yu, Study on the cocatalytic performance of nickel species in g-C<sub>3</sub>N<sub>4</sub> system for photocatalytic hydrogen evolution, *Catal. Commun.* 110 (2018) 51–54.

*Every reasonable effort has been made to acknowledge the owners of copyright material. I would be pleased to hear from any copyright owner who has been omitted or incorrectly acknowledged.*

## Chapter 5 Solar-heat-assisted single-atom catalysis for photocatalytic hydrogen evolution

### Abstract

In the last Chapter, g-C<sub>3</sub>N<sub>4</sub> based composite photocatalysts were obtained and tested in photocatalytic hydrogen evolution reaction (PC-HER). In this Chapter, we focused our attention on g-C<sub>3</sub>N<sub>4</sub> based single-atom catalysis for PC-HER. It is noticeable that in PC-HER, the high cost of noble-metal-nanoparticle based cocatalysts and their agglomeration under solar heat (infrared) are severely impeding the practical PC-HER application. Herein, low-cost single-atom metal modified graphitic carbon nitride (g-CN) was synthesized and utilized in PC-HER and solar-heat-assisted PC-HER processes, where excellent performances were acquired. In PC-HER, profiting from the compromising  $\Delta G_{H^*}$  of SAAg-g-CN (No. 40 and 52 nitrogen atoms) between Ag and g-CN, the HER rate of 1 wt% SAAg-g-CN reaches 248  $\mu\text{mol}\cdot\text{h}^{-1}\cdot\text{g}^{-1}$ , 30.6 times higher than that of g-CN, 7.3 times higher than Ag nanoparticles decorated g-CN (AgNP-g-CN), and 3.0 times higher than Pt nanoparticles modified g-CN (PtNP-g-CN). More critically, descending HER performance was observed for nanoparticle-based cocatalysts modified g-CN in solar-heat-assisted PC-HER with the temperature rising; however, the HER rate of SAAg-g-CN increases with increasing reaction temperature. The HER rate of 1 wt%

SAAg-g-CN at 55 °C ( $498 \mu\text{mol}\cdot\text{h}^{-1}\cdot\text{g}^{-1}$ ) was even doubled as compared to that at 25 °C. This should be ascribed to the distinct structure of Ag single atoms. This work underlines the outstanding performance of single-atom catalysis originating from its unique structure, active sites, and photothermal stability. It provides an approach for overcoming nanoparticle agglomeration with temperature, and thus, to exploit solar heat effect (infrared) in PC-HER processes.

## 5.1 Introduction

Since the Honda-Fujishima effect was first discovered in 1972,[1] photocatalytic (PC) hydrogen evolution reaction (HER) via water splitting has been a research hotspot for about five decades.[2–6] However, its industrial application is still severely hampered by some major issues. One of them is the high cost of noble-metal based cocatalysts. It is known that a cocatalyst is almost indispensable for PC-HER, because of its function of inhibiting the recombination of photogenerated electron-hole pairs and providing active sites for reactants.[7–9] One of the most important parameters of the cocatalysts for effective HER is the Gibbs free energy of the intermediate state ( $\Delta G_{\text{H}^*}$ ),[10,11], which should be close to zero.[9] So far, platinum has been the best cocatalyst possessing a  $\Delta G_{\text{H}^*}$  of only -0.09 eV.[12] However, the scarcity and high cost of Pt limit its practical and industrial applications.[13,14] Thus, searching for other low-cost

alternatives with favorable  $\Delta G_{H^*}$  has become a grand challenge. However, Cu, Ag, Co, and Ni, with only 1% to even 1‰ cost of Pt, have the inferior co-catalytic ability for PC-HER due to their low-grade  $\Delta G_{H^*}$  (Cu, 0.19 eV; Ag, 0.51 eV; Co, -0.27 eV; Ni, -0.27 eV).[15] It was expected that single-atom catalysis (SAC) might offer a solution. First, extreme diffusion can maximize active sites and advance atomic efficiency to the highest level.[16–21] Secondly, single-atom cocatalysts promote the reactions following different mechanisms compared with nanoparticle cocatalysts.[22–26] It is intriguing to explore the changes in  $\Delta G_{H^*}$  after a single-atom cocatalyst is combined with the main catalyst.

Another challenging task of PC-HER is the exploitation of solar heat. In solar-energy-driven photocatalysis, over 43% of the solar spectrum in the infrared region is almost useless for the excitement of photo electron-hole pairs because of the low photon energy.[27] However, the infrared radiation induces the thermal effect in raising the reaction temperature in photocatalytic processes.[28] As indicated before, we found that, with a Xenon lamp, the reactor temperature increased from 25 to 57 °C after 4 h irradiations (Refer to Figure 3.1). Hence, it is feasible and highly beneficial to incorporate the thermal effect in a photocatalyst system. However, severe nanoparticle agglomeration with temperature can be detrimental to the reaction efficiency.[29–32] For instance, Esmailpour et

al. reported that the agglomerate size increases with higher temperature, unfavorable for fluidization.[33] Kister et al. found that Au nanoparticles grow according to temperature, apparently reducing atomic efficiency.[34] Accordingly, this issue will impede the use of solar heat. In most PC-HER experiments, cooling water is applied to keep the solution temperature constantly at 25 °C to avoid issues, which is quite uneconomic and unrealistic for the industrial level. Therefore, looking for strategies to overcome agglomeration and making use of solar heat in PC-HER are highly in demand. Single-atom cocatalysts may again offer a solution since chemical bond-based integration is often formed in SAC,[16–19,21] leading to a dense combination with the main catalyst, which may eliminate the chance of agglomeration and facilitate the use of solar heat.

Therefore, single-atom Cu, Ag, Ni, and Co are considered to be combined with graphitic carbon nitride, which is of feasible synthesis, proper band structure, nontoxicity, and chemical stability.[35–39] What is more, the six-fold cavity in its structure provides an ideal position for the loading of single atom cocatalysts.[40–43]

Herein, we fabricated single atom, Cu, Ag, Ni, and Co, modified g-CN via a facile two-step pyrolysis method and evaluated their performances in PC-HER processes. Single-atom Ag modified g-CN (denoted as SAAg-g-

CN) showed excellent performance, and the PC-HER rate even tripled that of Pt nanoparticles (NPs) decorated g-CN. Density functional theory (DFT) calculations revealed that, unlike NP cocatalysts, the SAAG cocatalyst does not directly serve as the active sites for PC-HER. Instead, it functions by escalating the  $\Delta G_{H^*}$  of No. 40 and No. 52 nitrogen atoms of g-CN. More importantly, SAC and NP photocatalysts were for the first time compared in the temperature based solar-heat-assisted PC-HER. The significantly enhanced performance of SAAG-g-CN with temperature is distinct from the descending trend with metal NP cocatalyst. This can be owing to its intrinsic N-Ag bonding based structure, which was illustrated by X-ray absorption near-edge structure (XANES), extended X-ray absorption fine structure (EXAFS), combined with DFT calculations.

## 5.2 Methods

### 5.2.1 Chemicals and materials

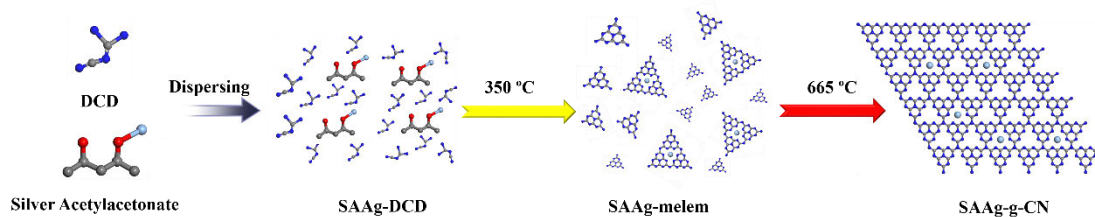
Cupric (II) acetylacetonate ( $C_{10}H_{14}CuO_4$ ), silver acetylacetonate ( $C_5H_7AgO_2$ ), nickel (II) acetylacetonate ( $C_{10}H_{14}NiO_4$ ), cobalt (II) acetylacetonate ( $C_{10}H_{14}CoO_4$ ), dicyandiamide ( $C_2H_4N_4$ , DCD), acetone, ethanol, ethylene glycol (EG), chloroplatinic acid, sodium sulfate and methanol were supplied by Sigma-Aldrich, Australia. The DCD was used after finely ground into fine powders with ball mill for 2 h. All the other

reagents were used directly without any further purification.

### 5.2.2 Fabrication of catalysts

Synthesis of g-C<sub>3</sub>N<sub>4</sub> (g-CN): DCD (10 g) was annealed for 7 h at 665 °C under an Ar flow of 50 mL·min<sup>-1</sup>. It was noted as g-CN after being carefully ground into fine powders.

Synthesis of single atom Ag modified g-CN (SAAg-g-CN): C<sub>5</sub>H<sub>7</sub>AgO<sub>2</sub> (C<sub>10</sub>H<sub>14</sub>CuO<sub>4</sub> for SACu-g-CN, C<sub>10</sub>H<sub>14</sub>NiO<sub>4</sub> for SANi-g-CN, or C<sub>10</sub>H<sub>14</sub>CoO<sub>4</sub> for SACo-g-CN) was sonicated for 2 h in the solution of acetone and ethanol (volume ratio 1:1). Then DCD fine powder was added into the above solution with a mass ratio of 1:200 (C<sub>5</sub>H<sub>7</sub>AgO<sub>2</sub> : DCD, 1.0 wt% SAAg-g-CN), and then the mixture was uniformly ground to dry powders. Subsequently, the mixture was heated at 350 °C for 3 h with Ar passing through the reaction chamber at a flow rate of 50 mL·min<sup>-1</sup>. Afterwards, the purple bulk was ground finely for 1 h, prior to annealing for 7 h at 665 °C under the Ar flow.



**Scheme 5.1** Schematic illustration of a two-step pyrolysis route for SAAg-g-CN synthesis.

Synthesis of Ag nanoparticles-g-CN (AgNP-g-CN): Firstly, pure g-CN was synthesized by the condensation method at 665 °C under Ar without the introduction of  $C_5H_7AgO_2$ , and then AgNP-g-CN was synthesized through a microwave method reported previously.[44] Briefly, the g-CN was mixed with  $C_5H_7AgO_2$  in ethanol and acetone solution, which was then transferred into EG. Subsequently, the solution was sonicated for 1 h before being placed in a microwave oven (1000 W) and heated for 2 min. The as-synthesized products were filtrated, washed, and then dried at 100 °C for 10 h.

Synthesis of PtNP-g-CN: Firstly, the prepared g-CN was ground and put into the mixed solution of methanol and deionized water (1:3). The chloroplatinic acid aqueous solution was added, and the whole system was illuminated with a 300 W Xenon lamp for 30 min. The as-synthesized products were filtrated and washed, followed by drying at 100 °C for 10 h.

### 5.2.3 Characterization techniques

Scanning electron microscopy (SEM) was conducted on an FEI Verios XHR SEM microscope. Transmission electron microscopy (TEM) and high angle annular dark-field scanning TEM (HAADF-STEM) images with elemental mapping were collected on a Titan G2 60-300 at 80 kV. The annular dark-field images (ADF) were received using a NionUltraSTEM100 microscope operated at 60 kV at a beam current of 60 pA. Powder X-ray diffraction (PXRD) patterns were measured on an Empyrean multipurpose research diffractometer (Panalytical Empyrean XRD) utilizing Cu K $\alpha$  radiation ( $\lambda = 1.5418 \text{ \AA}$ ) with a current of 40 mA and a voltage of 40 kV. X-ray photoelectron spectroscopy (XPS) was obtained on a Thermo Escalab 250 with an Al K $\alpha$  X-ray to determine the chemical states of the elements. UV–vis diffuse reflectance spectra (DRS) were carried out on an Agilent Cary 100 UV–vis spectrophotometer equipped with an integrated sphere attachment. Photoluminescence (PL) spectra of the samples were received on a Cary Eclipse Fluorescence Spectrophotometer (Agilent, US).

### 5.2.4 Photoelectrochemical tests

Electrochemical impedance spectroscopy (EIS) measurements were conducted on a Zennium electrochemical workstation (Zahner, Germany) in a standard three-electrode framework with a 0.05 M Na<sub>2</sub>SO<sub>4</sub> (pH = 6.8)

electrolyte solution, employing a Pt wire as the counter electrode and an Ag/AgCl electrode as the reference electrode. As for the photoanode, the sample film was fabricated on fluorine-doped tin oxide (FTO) glasses, which were ultrasonicated in DI water, acetone and ethanol for 15 min in sequence, and then dried at 60 °C. To be specific, 8 mg of the catalyst was mixed with 500  $\mu\text{L}$  of absolute ethanol and 25  $\mu\text{L}$  of Nafion solution homogeneously. The obtained slurry was then dropped onto the pre-treated FTO glass via a spin-coating method, and the prepared electrode was dried at 100 °C for 24 h (catalyst loading  $\sim 0.60 \text{ mg}\cdot\text{cm}^{-2}$ ).

#### 5.2.5 Photocatalytic activity evaluation

Photocatalytic  $\text{H}_2$  production experiments were conducted in a customized stainless-steel reactor covered with a quartz window at ambient temperature. A 300 W Xeon lamp (Newport) was used as the light source. Water circulation system was supplied to keep the temperature at 25 °C. Typically, 50 mg photocatalyst was dispersed in a mixed solution (120 mL) containing DI water (90 mL) and methanol (30 mL). Prior to the irradiations, the suspensions were vigorously stirred in dark for 30 min, and the reaction vessel was degassed by purging with  $\text{N}_2$  at the same time to maintain the anaerobic conditions. The produced  $\text{H}_2$  was analyzed in situ by a gas chromatograph (Agilent 490 Micro GC) using a thermal conductivity detector.

### 5.2.6 Temperature based solar-heat-assisted photocatalytic activity evaluation

For the investigation of solar-heat-assisted photocatalytic activity of SAAg-g-CN, the reaction solution was controlled at 25, 35, 45, and 55 °C by the cooperation of a heating plate and a circulating water system. After one hour of irradiation in the reactor, the produced H<sub>2</sub> was sent to the GC for detection.

### 5.2.7 Calculation methods

The geometry optimization, as well as the electronic calculation of the simulated models, were computed with DFT using the projected augmented wave[45] (PAW) approach.[46–48] The exchange and correlation potential were analyzed by a generalized gradient approximation of the Perdew-Burke-Ernzerhof (PBE).[49] The plane-wave cut-off energy for all the calculations is set to be 400 eV. The convergence criterion for electronic structure iteration was set to be  $1 \times 10^{-4}$  eV, and the structural optimization would be terminated by relaxing all atomic positions using the conjugate gradient algorithm until all forces were smaller than 0.03 eV/Å. Polarization effect was considered in all the cases. The k-space was sampled with gamma centered at  $2 \times 2 \times 1$  for SAAg-g-CN. The van der Waals (vdW) corrections were considered using the DFT-D3 method.[50]

The Gibbs free energy of hydrogen adsorption state ( $\Delta G_{H^*}$ ) can be estimated as

$$\Delta G_{H^*} = \Delta E_{H^*} + \Delta E_{ZPE} - T\Delta S \quad \text{Eq. 5.1}$$

where  $\Delta E_{H^*}$  is the hydrogen chemisorption energy, and  $\Delta E_{ZPE}$  is the difference corresponding to the zero-point energy between the adsorbed state and the gas phase. As the vibrational entropy of  $H^*$  in the adsorbed state is small, the entropy of adsorption of  $\frac{1}{2} H_2$  is  $\Delta S_H \approx -1/2 S_{H_2}^0$ , where  $S_{H_2}^0$  is the entropy of  $H_2$  in the gas phase at the standard condition ( $T=300K$ , 1 atm). Therefore, the overall corrections are taken as Eq.5.2.[15,20,51]  $\Delta E_{H^*}$  is the binding energy of H intermediate as estimated below (Eq 5.3). The free-energy barriers for hydrogen evolution on the Pt (111), Cu(111), Au (111) and Ag (111) surface were adopted from a previous study.[51]

$$\Delta G_{H^*} = \Delta E_{H^*} + 0.24 \text{ eV} \quad \text{Eq. 5.2}$$

$$\Delta E_{H^*} = E_{slab+H} - E_{slab} + 1/2 E_{H_2} \quad \text{Eq. 5.3}$$

### 5.3 Results and Discussion

Cu, Ag, Ni, and Co modified g-CN samples were respectively synthesized by a two-step pyrolysis method. Take the SAAg-g-CN as an example. The typical synthesis is shown in Scheme 5.1. The precursors of SAAg (silver acetylacetonate) and g-CN (dicyandiamide, denoted as DCD) were first

well dispersed. Then the two-step pyrolysis processes were conducted with an Ar flow at different temperatures. In the PC-HER tests, SAAg-g-CN proved a prominent performance, while others did not show any enhancement compared to g-CN (Figure 5.1a). Therefore, the following studies focused on SAAg-g-CN.

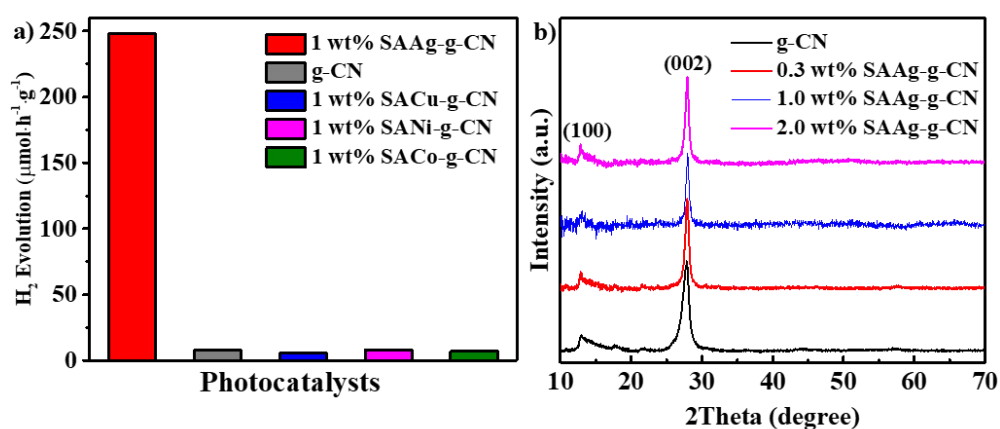


**Figure 5.1 a**, H<sub>2</sub> evolution rate of 1 wt% SAAg-g-CN, 1 wt% SACu-g-CN, 1 wt% SANi-g-CN, 1 wt% SACo-g-CN, and pure g-CN. **b**, XRD patterns of SAAg-g-CN with different ratios and pure g-CN.

The metal contents of the SAAg-g-CN samples were determined by an inductively coupled plasma atomic emission spectrometer (ICP-AES). The prepared materials were also analyzed by a variety of characterizations. X-ray diffraction (XRD) patterns of SAAg-g-CN with different Ag ratios and pure g-CN are shown in Figure 5.1b. The modification of g-CN with SAAg exerts no apparent influence on the

XRD peaks of g-CN, because of the low content of SAAG. The XRD peak of Ag was not found in SAAG-g-CN samples, indicating no apparent Ag nanoparticles attached on the g-CN sheets. The images of SEM (Figure 5.2a), TEM (Figure 5.2b) and high angle annular dark-field scanning TEM (HAADF-STEM, Figure 5.2c) of 1 wt% SAAG-g-CN show that a layered structure was fabricated with no Ag nanoparticles (NPs) attached on the surface of the sample. High-resolution TEM (HRTEM) image (Figure 5.2d), same as the red frame region from Figure 5.2b, further shows no metal aggregation on the as-synthesized material. The inset of energy dispersive X-ray (EDX) spectrum and HAADF-STEM image with corresponding elemental mapping images (Figure 5.2e) confirm the presence of carbon, nitrogen, and silver with the even distribution of the Ag element on the g-CN substrate. Moreover, the atomic dispersion of Ag atoms is revealed by aberration-corrected scanning transmission electron microscopy (AC-STEM) (Figure 5.2f), which displays the bright dots, corresponding to Ag atoms, are dispersed throughout the g-CN.

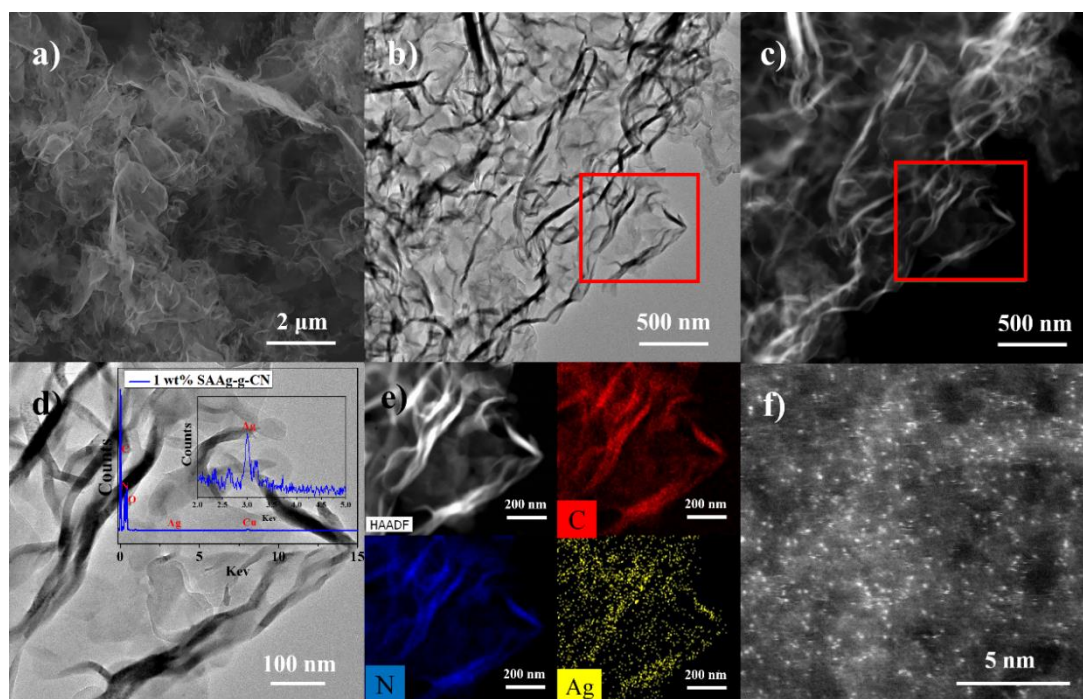


**Figure 5.2** Morphological characterizations of 1 wt% SAAg-g-CN. **a**, SEM image. **b**, TEM image. **c**, HAADF-STEM image. **d**, HRTEM image, inset showing the EDX spectroscopy. **e**, the element maps showing the distribution of carbon (red), nitrogen (blue) and silver (yellow). **f**, AC-STEM annular dark-field (ADF) image.

The structure of SAAg-g-CN was investigated by both experimental and computational techniques. In the optimized DFT framework (Figure 5.3a), single-atom Ag is trapped in the cavity of g-CN with N-Ag bonds at a length of  $\sim 2.408$  Å. Electrons are extracted from the Ag atom and to accumulate in nitrogen atoms near silver, as shown in the charge density distribution image (Figure 5.3b). The charge changes of each atom on both SAAg-g-CN and g-CN are listed in Table 5.1 (atom numbers shown in Figure 5.4) and 5.2 (atom numbers in Figure 5.5). The valence of Ag atom

as displayed in Table 5.1 is +0.6443 (the adverse of the net charge).

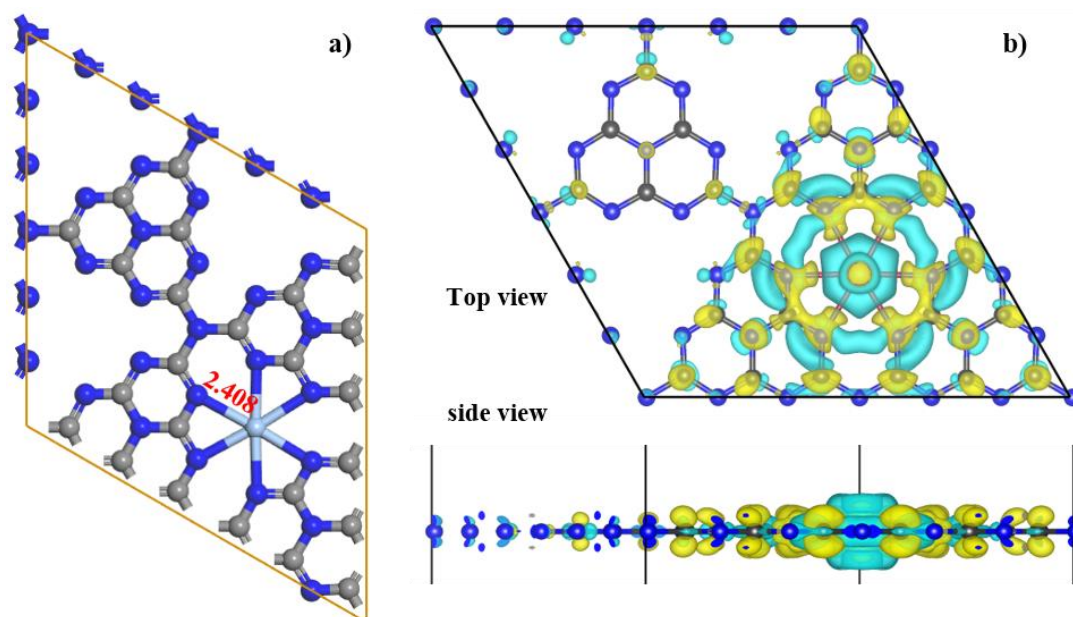


**Figure 5.3** a, An optimal structure of SAAg-g-CN. b, Charge density difference of SAAg-g-CN. The yellow and cyan areas represent the electron accumulated and depleted regions, respectively. The iso-surface value was set as 0.001 e/Å<sup>3</sup>.

**Table 5.1** Detailed data of each atom charge and net charge of SAAg-g-CN. (“-” represents “losing electrons”)

Atomic number	Charge	Net Charge
1	2.45	-1.55
2	2.74	-1.25
3	2.61	-1.38
4	2.65	-1.35

5	2.53	-1.46
6	2.52	-1.47
7	2.50	-1.49
8	2.32	-1.67
9	2.49	-1.50
10	2.46	-1.54
11	2.37	-1.63
12	2.32	-1.68
13	2.48	-1.52
14	2.49	-1.51
15	2.48	-1.52
16	2.30	-1.69
17	2.50	-1.50
18	2.32	-1.67
19	2.47	-1.53
20	2.29	-1.70
21	2.46	-1.54
22	2.44	-1.55
23	2.45	-1.55
24	2.57	-1.43
25	6.08	1.08
26	6.07	1.07

27	6.05	1.05
28	6.07	1.07
29	6.17	1.18
30	6.04	1.05
31	6.00	1.00
32	6.27	1.27
33	6.15	1.15
34	6.26	1.26
35	6.19	1.19
36	6.28	1.28
37	6.18	1.18
38	5.94	0.94
39	6.15	1.15
40	6.16	1.16
41	6.07	1.07
42	6.19	1.19
43	6.34	1.34
44	6.22	1.22
45	6.12	1.12
46	6.29	1.29
47	6.21	1.21
48	6.14	1.14

49	6.18	1.18
50	6.28	1.28
51	6.27	1.27
52	6.18	1.18
53	6.12	1.12
54	6.21	1.21
55	6.22	1.22
56	6.15	1.15
57	10.36	-0.64

---

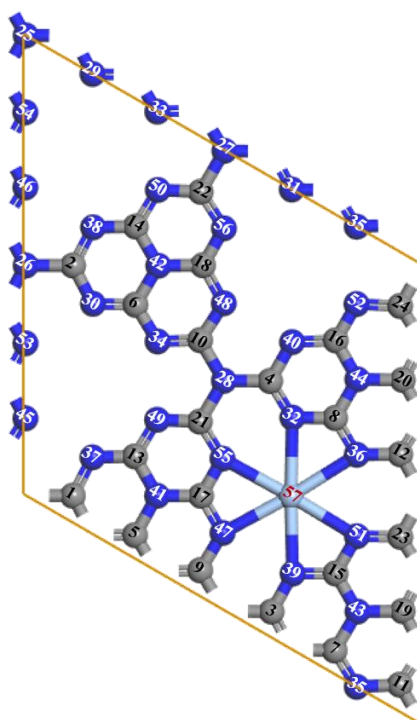


**Figure 5.4** Atomic numbers of SAAg-g-CN for Table 5.1.

**Table 5.2** Detailed data of each atom charge and net charge of g-CN. (“-” represents “losing electrons”)

Atomic number	Charge	Net Charge
1	2.71	-1.28
2	2.71	-1.28
3	2.72	-1.28
4	2.72	-1.28
5	2.52	-1.48
6	2.52	-1.48
7	2.52	-1.48
8	2.52	-1.48
9	2.46	-1.54
10	2.46	-1.54
11	2.46	-1.54
12	2.46	-1.54
13	2.49	-1.51
14	2.49	-1.51
15	2.49	-1.51
16	2.49	-1.51
17	2.35	-1.65
18	2.35	-1.65
19	2.35	-1.65

20	2.35	-1.65
21	2.57	-1.43
22	2.57	-1.43
23	2.57	-1.43
24	2.57	-1.43
25	6.05	1.05
26	6.05	1.05
27	6.05	1.05
28	6.05	1.05
29	6.06	1.06
30	6.06	1.06
31	6.06	1.06
32	6.06	1.06
33	6.25	1.25
34	6.25	1.25
35	6.25	1.25
36	6.25	1.25
37	5.93	0.93
38	5.93	0.93
39	5.93	0.93
40	5.93	0.93
41	6.19	1.19

42	6.19	1.19
43	6.19	1.19
44	6.19	1.19
45	6.10	1.10
46	6.10	1.10
47	6.10	1.10
48	6.10	1.10
49	6.14	1.14
50	6.14	1.14
51	6.14	1.14
52	6.14	1.14
53	6.14	1.14
54	6.14	1.14
55	6.14	1.14
56	6.14	1.14

---

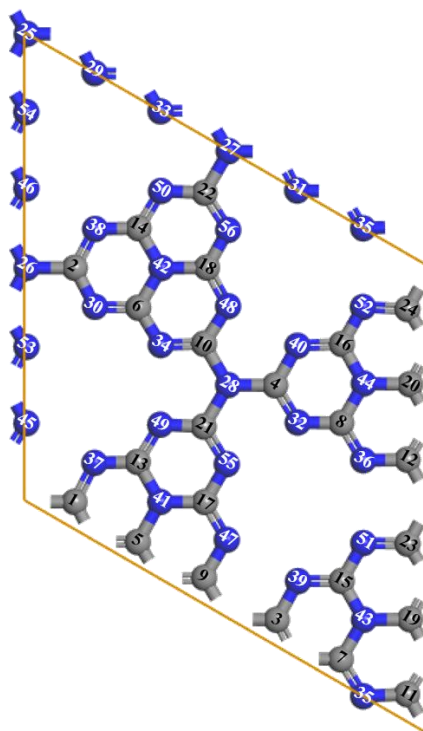


**Figure 5.5** Atomic numbers of g-CN for Table 5.2.

In the X-ray photoelectron spectroscopy (XPS) spectrum, the C 1s peak (Figure 5.6a) can be deconvoluted into two peaks at 287.8 and 284.4 eV, attributed to  $sp^2$  carbon bonded to the three nitrogen atoms in the carbon nitride lattice, and the unavoidably loaded graphitic carbon atoms, respectively.[7] The N1s spectrum in Figure 5.6b gives four asymmetrical peaks at 394.2, 395.0, 396.6 and 400.0 eV, ascribed to the C–N=C  $sp^2$ -bonded N atoms in the graphite-like g-CN structure, tertiary (N–(C)<sub>3</sub>) groups, amino-functional groups (C–N–H), and a typical  $\pi$ -excitation, accordingly.[52] The peaks of Ag 3d are presenting at 367.9 and 373.9 eV in Figure 5.6c, which suggest the oxidation state of Ag between  $Ag^+$  and metallic  $Ag^0$ , [53] consistent to the aforementioned DFT calculated

positive valence (+0.644).

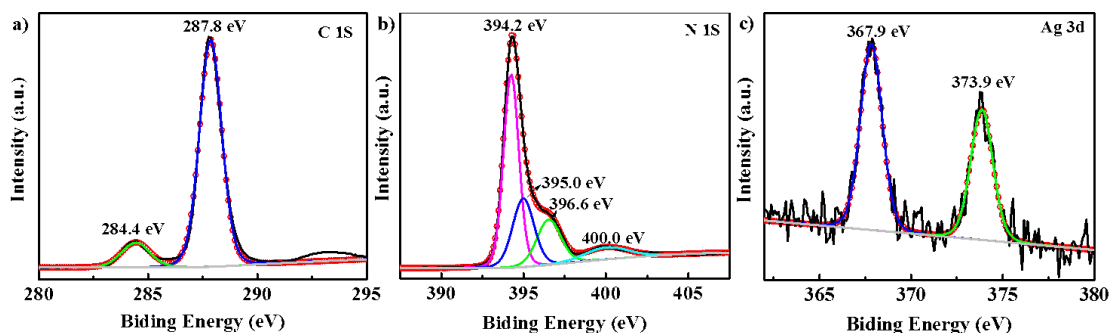


**Figure 5.6** XPS survey of 1.0 wt% SAAg-g-CN. **a**, C 1s, **b**, N 1s, **c**, Ag 3d of 1.0 wt% SAAg-g-CN.

The synchrotron-based XANES and EXAFS were further utilized to clarify the structure. In Figure 5.7a, the C K-edge curve of 1 wt% AgNP-g-CN is similar to that of g-CN, while the main peak ( $\pi^*$  C-N-C) of 1 wt% SAAg-g-CN has a right shift, indicating a less accumulated electron density of the carbon atoms.[7] According to the charge density list (Table 5.1), the difference between the charge sum of all 24 carbon atoms of SAAg-g-CN and g-CN (Table 5.2) is -1.14, manifesting the less negative charges of carbon for SAAg-g-CN, well in accordance with the C K-edge result. The two main peaks of N K-edge for g-CN (Figure 5.7b) are owing to  $\pi^*$  C-N-C and  $\pi^*$  N-3C ( $sp^3$  bridging N among three tri-s-triazine moieties).[54] The curve of 1 wt% AgNP-g-CN is still similar to that of g-CN. In comparison, 1 wt% SAAg-g-CN has left shifts for both the peaks, signifying more electrons accumulated on C-N=C  $sp^2$ -bonded N atoms

and  $sp^3$  bridging N among three tri-s-triazine moieties. In the charge lists (Table 5.1 and 2), the charge sum of the former N atoms (No. 29~35, 37, 38, 40, 45, 46, 49, 50, 52~54 and 56) for 1 wt% SAAg-g-CN minus that for g-CN is 1.03, also showing more negative charges of the former N, consistent with the experimental results. Similarly, the charge difference for latter N atoms (No. 25~28) is 0.08, positive as well, and in accordance with the XANES data. Furthermore, a new peak emerges at  $\sim 409$  eV for 1 wt% SAAg-g-CN, which may be ascribed to the formation of N-Ag bonds shown in the simulative structure (Figure 5.3a). The absorption edge energies of 1 wt% SAAg-g-CN in the XANES spectrum of Ag K-edge (Figure 5.7c) is slightly lower than that of Ag foil, indicating the oxidized state of Ag. It has been reported that Ag has lower binding energy with increasing oxidation state due to its core-level photo-emission.[55] This phenomenon also accords well with the positive valence of Ag (+0.644).

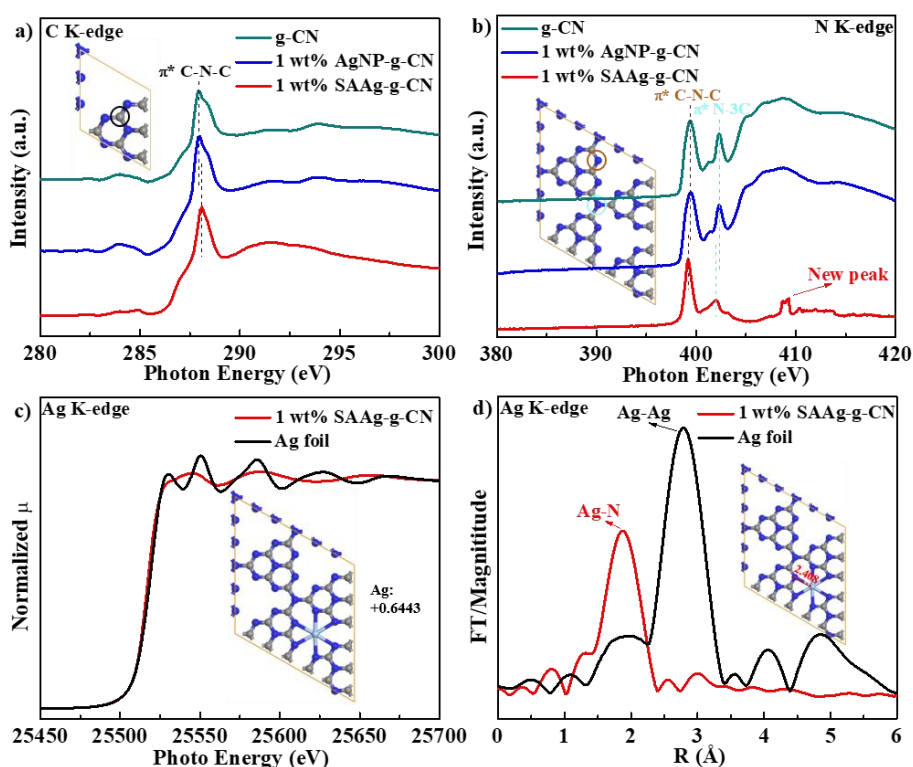


**Figure 5.7** **a**, C K-edge and **b**, N K-edge XANES of g-CN, 1 wt% AgNP-g-CN and 1 wt% SAAg-g-CN. **c**, Ag K-edge XANES of 1 wt% SAAg-g-CN and Ag foil. **d**, Fourier transforms of Ag K-edge EXAFS of 1 wt% SAAg-g-CN and Ag foil.

Lastly, the EXAFS of Ag K-edge for 1 wt% SAAg-g-CN (Figure 5.7d), together with its R, q, k space fitting results (Figure 5.8a, b, c), indicates that the quantitative coordination configuration of silver sites is 5.7, and the length of N-Ag is 2.39 Å (Table 5.3), which are remarkably different from those of Ag foil (Figure 5.8 d, e, and f and Table 5.3). The slight difference between fitting and computed results in the coordination number (5.7 versus 6) and bond length (2.39 versus 2.40 Å) is within a

reasonable range of error.[56] All the above XPS, XANES and EXAFS results adequately demonstrate that the structure of the SAAG-g-CN model in DFT calculation is plausible for the as-prepared SAAG-g-CN.

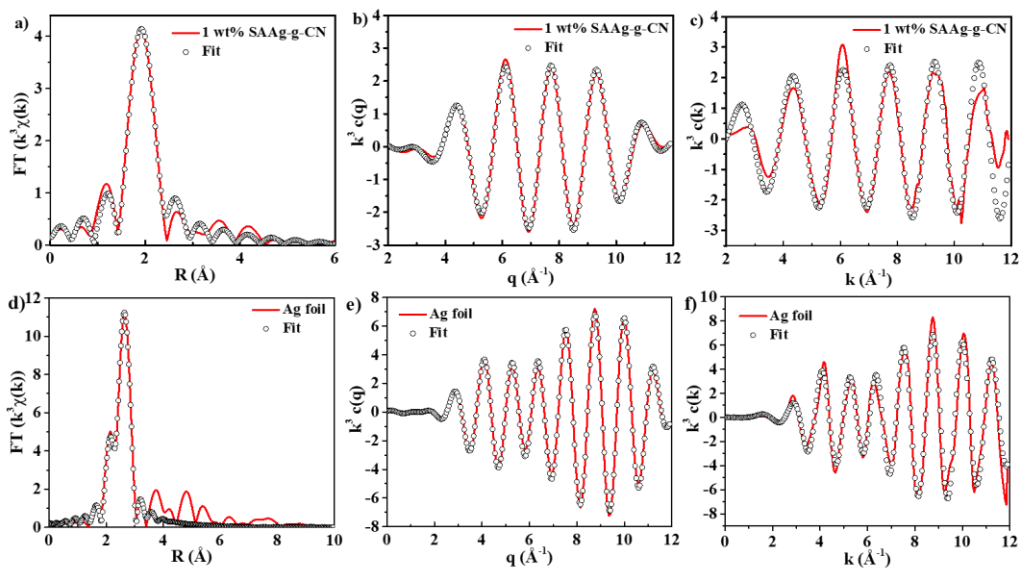


**Figure 5.8** The corresponding EXAFS **a**, **R**, **b**, **q**, and **c**, **k** space fitting curves of 1 wt% SAAG-g-CN. The corresponding EXAFS **d**, **R**, **e**, **q**, and **f**, **k** space fitting curves of Ag foil.

**Table 5.3** Structural parameters extracted from the Ag K-edge EXAFS fitting. ( $S_0^2 = 0.79^{[a]}$ )

Sample	Scattering Pair	CN <sup>[b]</sup>	R (Å) <sup>[c]</sup>	$\sigma^2$ ( $10^{-3}\text{\AA}^2$ ) <sup>[d]</sup>	$\Delta E_0$ (eV) <sup>[e]</sup>	R factor <sup>[f]</sup>
Ag foil	Ag-Ag	12*	2.87	0.006	0.06	0.001
1 wt% SAAG-g-CN	Ag-N	5.7	2.39	0.004	2.75	0.008

[a]  $S_0^2$  is the amplitude reduction factor. [b] CN is the coordination number.

[c] R is the interatomic distance (the bond length between central atoms

and surrounding coordination atoms). [d]  $\sigma^2$  is the Debye-Waller factor (a measure of thermal and static disorder in absorber-scatter distances). [e]  $\Delta E_0$  is the edge-energy shift (the difference between the zero kinetic energy value of the sample and that of the theoretical model). [f] R factor is used to value the goodness of the fitting, 1.0SAFe-SBA.

The photocatalytic H<sub>2</sub>-production efficiencies of the samples were further evaluated in the presence of 25% methanol by volume. As displayed in Figure 5.9a and Table 5.4, SAAg-g-CN demonstrated an excellent PC-HER activity. After 240 min of light irradiations, the average H<sub>2</sub>-evolution rate of 0.3 wt% SAAg-g-CN reaches 75  $\mu\text{mol}\cdot\text{h}^{-1}\cdot\text{g}^{-1}$ , which is 9 times higher than that of g-CN. At SAAg loading of 1 wt%, the PC-HER rate is raised to the optimal value of 248  $\mu\text{mol}\cdot\text{h}^{-1}\cdot\text{g}^{-1}$ , 30.6 times as high as that of g-CN, 7.3 times of 1.0 wt% AgNP-g-CN (34  $\mu\text{mol}\cdot\text{h}^{-1}\cdot\text{g}^{-1}$ ), 3.0 times of PtNP-g-CN (82  $\mu\text{mol}\cdot\text{h}^{-1}\cdot\text{g}^{-1}$ ), and much higher than the values of previously reported Pt or Ag NPs decorated g-CN under similar conditions (Table 5.5). However, a further increase in SAAg loading to 2.0 wt% does not lead to any further enhancement of hydrogen evolution (still 248  $\mu\text{mol}\cdot\text{h}^{-1}\cdot\text{g}^{-1}$ ), probably due to the emerged Ag clusters (Figure 5.9b).

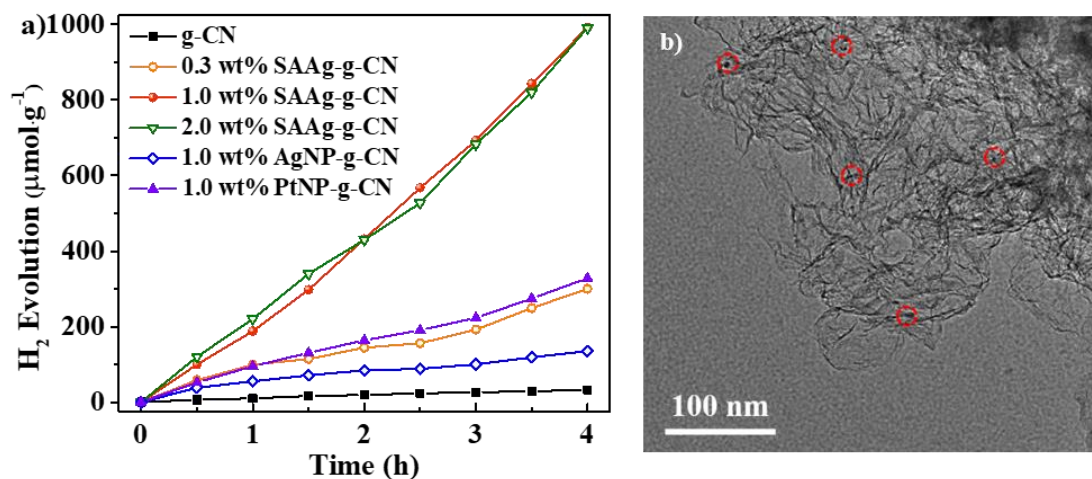


**Figure 5.9 a**, Photocatalytic activity for H<sub>2</sub> evolution over different samples under simulated solar light irradiations. **b**, TEM image of 2.0 wt% SAAg-g-CN.

**Table 5.4** H<sub>2</sub> evolution rates with different catalysts in Figure 5.9a.

Catalyst	H <sub>2</sub> evolution (μmol·h <sup>-1</sup> ·g <sup>-1</sup> )
g-CN	8.1
0.3 wt% SAAg-g-CN	75
1 wt% SAAg-g-CN	248
2 wt% SAAg-g-CN	248
1 wt% AgNP-g-CN	34
1 wt% PtNP-g-CN	75

**Table 5.5** A comparison of the photocatalytic H<sub>2</sub>-production activities for Ag or Pt modified g-C<sub>3</sub>N<sub>4</sub> photocatalysts with methanol as a sacrificial agent.

Catalyst	Optical source <sup>[a]</sup>	H <sub>2</sub> evolution ( $\mu\text{mol}\cdot\text{h}^{-1}\cdot\text{g}^{-1}$ )	Reference
8 wt% Ag/g-C <sub>3</sub> N <sub>4</sub>	300 W Xe lamp ( $\geq 420$ nm)	15	[57]
0.5% Ag QDs/g-C <sub>3</sub> N <sub>4</sub>	300 W Xe lamp ( $\geq 420$ nm)	18	[58]
1 wt% Pt/g-C <sub>3</sub> N <sub>4</sub>	Xe lamp ( $\geq 420$ nm)	11	[59]
3 wt% Pt/g-C <sub>3</sub> N <sub>4</sub>	Unknown ( $\geq 420$ nm)	16	[60]
1 wt% Pt/g-C <sub>3</sub> N <sub>4</sub>	300 W Xe lamp ( $\geq 400$ nm)	19	[61]
1 wt% Pt/g-C <sub>3</sub> N <sub>4</sub>	300 W Xe lamp ( $\geq 400$ nm)	20	[62]
1 wt% Pt/g-C <sub>3</sub> N <sub>4</sub>	300 W Xe lamp ( $\geq 400$ nm)	20	[63]
1 wt% Pt/g-C <sub>3</sub> N <sub>4</sub>	300 W Xe lamp ( $\geq 400$ nm)	20	[64]
0.5 wt% Pt/g-C <sub>3</sub> N <sub>4</sub>	450 W Hg lamp ( $\geq 400$ nm)	36	[65]
2 wt% Pt/g-C <sub>3</sub> N <sub>4</sub>	300 W Xe lamp (No filter)	53	[66]
1 wt% Pt/g-C <sub>3</sub> N <sub>4</sub>	Solar simulator (No filter)	140	[67]
1 wt% Pt/g-C <sub>3</sub> N <sub>4</sub>	500 W Xe lamp (No filter)	72	[68]
1 wt% AgNP-g-CN	300 W Xe lamp (No filter)	34	This work
1 wt% PtNP-g-CN	300 W Xe lamp (No filter)	82	This work
1 wt% SAAg-g-CN	300 W Xe lamp (No filter)	248	This work

[a] According to previously reported data of g-CN related catalysts, it is noticed that for optical source with filter of  $\lambda \geq 420$  nm, the photocatalytic

H<sub>2</sub> evolution reaction (PC-HER) rate times 3 to 5 can be comparative to that without an optical filter. For an optical source with a filter of  $\lambda \geq 400$  nm, the PC-HER rate times 2 to 4 can be comparative to that without an optical filter.

Figure 5.10a compares the relative photocatalytic activity of Ag modified samples based on per mg Ag atoms. The SAAg-g-CN shows a nearly stable activity at the Ag content less than 2.0 wt%, but a sharply declined activity at 2.0 wt% owing to the formation of clusters. The AgNP (TEM and HRTEM images in Figure 5.10 b and c) gives the worst activity. The stability of SAAg-g-CN in PC-HER was tested. No morphological change before and after use (Figure 5.11 a and b) was observed, demonstrating the reliable stability of the material. Figure 5.11c displays the H<sub>2</sub> evolution in a 12 h photocatalytic run with 4 h intermittence over the sample of 1 wt% SAAg-g-CN. No significant loss of activity occurred after three cycles.

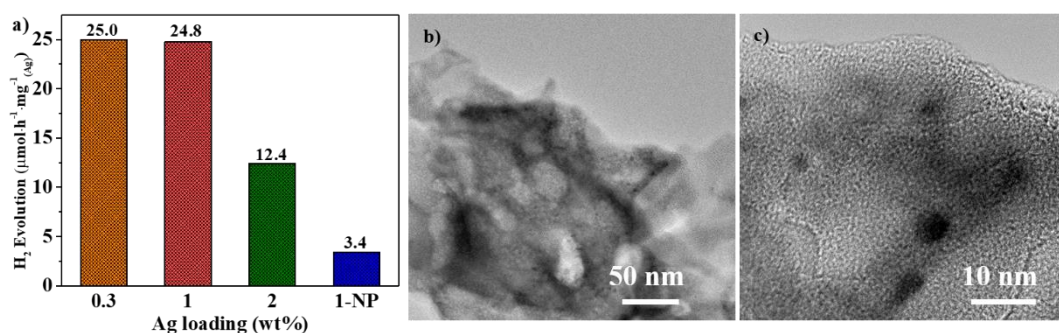


**Figure 5.10 a**, Comparison of photocatalytic activity of g-CN with various Ag contents normalized to per mg Ag atoms. **b**, TEM and **c**, HRTEM images of 1.0 wt% AgNP-g-CN.

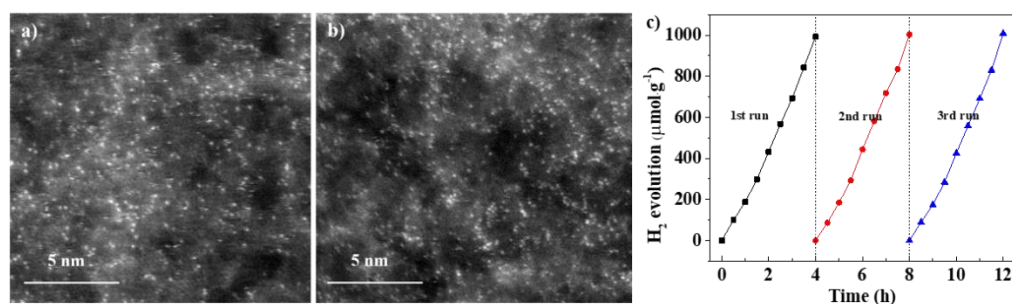


**Figure 5.11** AC-STEM of 1.0 wt% SAAg-g-CN **a**, before and **b**, after PC-HER reaction. **c**, Cycle runs for the photocatalytic H<sub>2</sub> evolution on 1.0% SAAg-g-CN.

The solar-heat-assisted PC-HER performance of 1 wt% SAAg-g-CN was then examined with the temperature being controlled from 25 to 55 °C using a water circulation system. In Figure 5.12a, the H<sub>2</sub>-production rate has a remarkable increase with increasing temperature and arrives at 498 μmol·h<sup>-1</sup>·g<sup>-1</sup> at 55 °C, doubling the value at 25 °C. Meanwhile, metal

nanoparticle cocatalysts were also tested, as shown in Figure 5.12b and c. The PC-HER rate of 1 wt% PtNP-g-CN (Figure 5.12b) remains the similar level at 25 and 35 °C but drops off at 45 and 55 °C, to the half value at 25 °C. Another catalyst, 1 wt% AgNP-g-CN (Figure 5.12c) shows the continuing decrease in the rates with the temperature rising. However, g-CN (Figure 5.12d) shows a similar behavior to SAAg-g-CN. These results demonstrate that an increased temperature can positively boost the PC-HER process on g-CN and SAAg-g-CN.

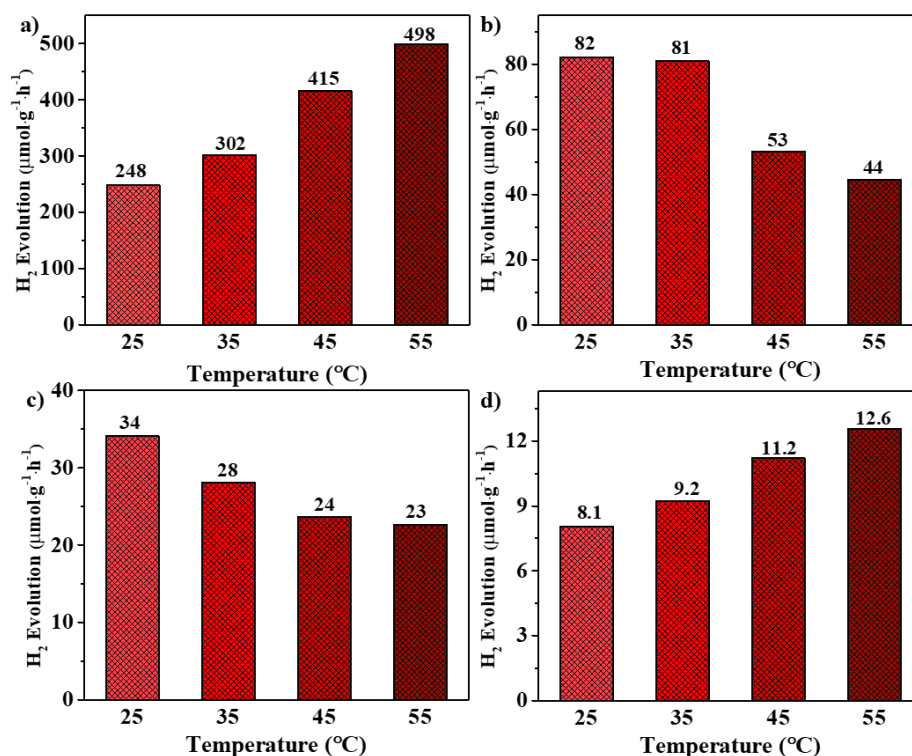


**Figure 5.12** Solar-heat-assisted H<sub>2</sub> evolution of **a**, 1 wt% SAAg-g-CN, **b**, 1.0 wt% PtNP-g-CN, **c**, 1.0 wt% AgNP-g-CN and **d**, g-CN at different temperatures.

TEM images of the used samples at different temperatures were acquired to explore the inhibition effect of solar-heat-assisted photocatalysis on NP-based cocatalysts. With the temperature rising, the growth and agglomeration of Pt NPs (Figure 5.13a-d) and Ag NPs (Figure 5.13e-h) became more and more serious, while no particles were found for SAAg-g-CN (Figure 5.13i-l). Therefore, it can be concluded that the growth and agglomeration of metal NP cocatalysts with temperature result in the decreased active sites for PC-HER.

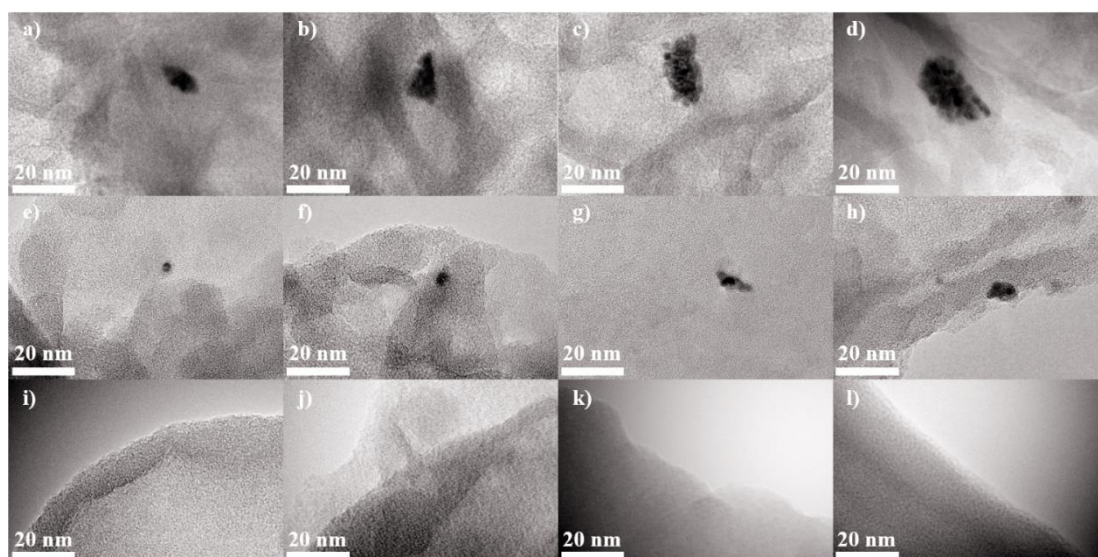


**Figure 5.13** TEM images of the used samples in different temperatures. **a**, 25 °C, **b**, 35 °C, **c**, 45 °C, **d**, 55 °C of 1 wt% PtNP-g-CN. **e**, 25 °C, **f**, 35 °C, **g**, 45 °C, **h**, 55 °C of 1 wt% AgNP-g-CN. **i**, 25 °C, **j**, 35 °C, **k**, 45 °C, **l**, 55 °C of 1 wt% SAAg-g-CN.

Then,  $\Delta G_{H^*}$  was calculated in DFT mode to unveil how SAAG-g-CN improves its capacity in PC-HER. Figure 5.14a displays the  $\Delta G_{H^*}$  of g-CN on atoms of No. 4, 16, 28, 40, 52. It can be seen that No. 4 and 16 carbon atoms, and No. 28 nitrogen atom connecting with three carbon atoms have positive values. In comparison, No. 52 and 40 nitrogen atoms (the hydrogen adsorption structure is shown in Figure 5.15a) own a negative value of -0.584 eV, which is the closest to zero. Thus, the  $\Delta G_{H^*}$  of g-CN is -0.584 eV, consistent with the previous report.[69] In terms of SAAG-g-CN, carbon atoms (Table 5.1) basically have positive valences, indicating that they are unfit for  $H^+$  adsorption. Therefore, the  $\Delta G_{H^*}$  values (Figure 5.14b) of representative nitrogen atoms (No. 32, 40, 44 and 52) and Ag atom (No. 57) are figured out. All of the five atoms own negative values, and No. 40 nitrogen atom (the hydrogen adsorption structure is shown in Figure 5.15b) is still the optimal one with a compromising value (-0.279 eV) of Ag (0.51 eV) and g-CN (-0.584 eV) (Figure 5.14c), explaining the outstanding performance of SAAG-g-CN. It is worth mentioning that the  $\Delta G_{H^*}$  of No. 52 nitrogen atom is also adjusted from -0.584 to -0.345 eV, which is helpful to PC-HER performance as well.

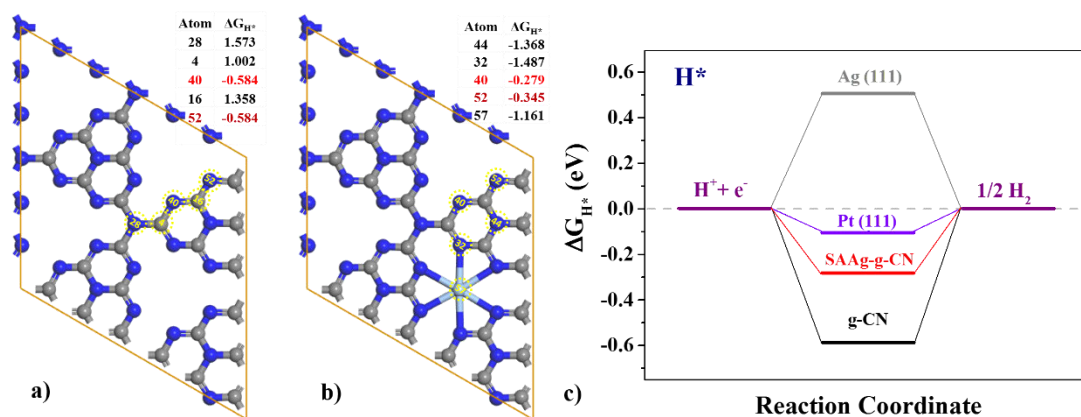


**Figure 5.14** **a**,  $\Delta G_{H^*}$  results of g-CN on atoms of No. 28, 4, 40, 16, 52. (blue for N and grey for C atoms) **b**,  $\Delta G_{H^*}$  results of SAAg-g-CN on atoms of No. 44, 32, 40, 52, 57. (light blue for Ag atoms) **c**, Calculated free-energy diagram of HER at the equilibrium potential for Ag (111), Pt (111), g-CN, and SAAg-g-CN.

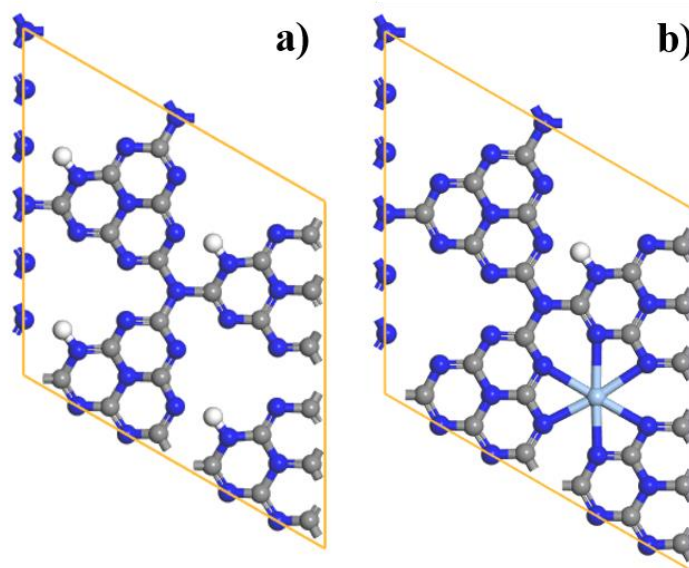


**Figure 5.15** Optimized hydrogen adsorption model of **a**, g-CN and **b**, SAAg-g-CN.

UV–vis diffuse reflectance spectra, photoluminescence (PL) spectra, and electrochemical impedance spectroscopy (EIS) of SAAg-g-CN were acquired. As displayed in Figure 5.16a, the steep edge near 385 nm can be assigned to the bandgap transition of g-CN, and the introduction of monoatomic Ag enhances the visible light absorption but slightly decreases UV absorption. According to the Kubelka-Munk theory, the bandgap energies of all the samples were plotted in Figure 5.16b. No significant shift in the bandgap energy (2.55 eV) of the composites can be found, indicating the addition of Ag single atom does not significantly affect the bandgap structure of g-CN. PL was performed to investigate the charge carrier separation, transfer, and capture in pure g-CN and 1 wt% SAAg-g-CN composite sample (Figure 5.16c). Both photocatalysts exhibit similar emission trends at room temperature at an excitation wavelength of 350 nm. For both g-CN and 1 wt% SAAg-g-CN, the main emission peaks are concentrated at about 700 nm due to the recombination of the photoexcited electron-hole pairs derived from the intrinsic HOMO–LUMO transition. Besides, 1 wt% SAAg-g-CN shows a lower PL intensity than g-CN, indicating the weaker recombination of photogenerated charges. This might contribute to the enhanced PC-HER performance. In Figure 5.16d, the Nyquist plots from typical EIS curves of g-CN and SAAg-g-CN show a slightly shorter curve diameter of SAAg-g-CN,[70] which cannot explain the significant enhanced PC-HER rate of

SAAg-g-CN. These characterizations jointly prove that the excellent performance of SAAg-g-CN should be attributed to the escalated  $\Delta G_{H^*}$ .

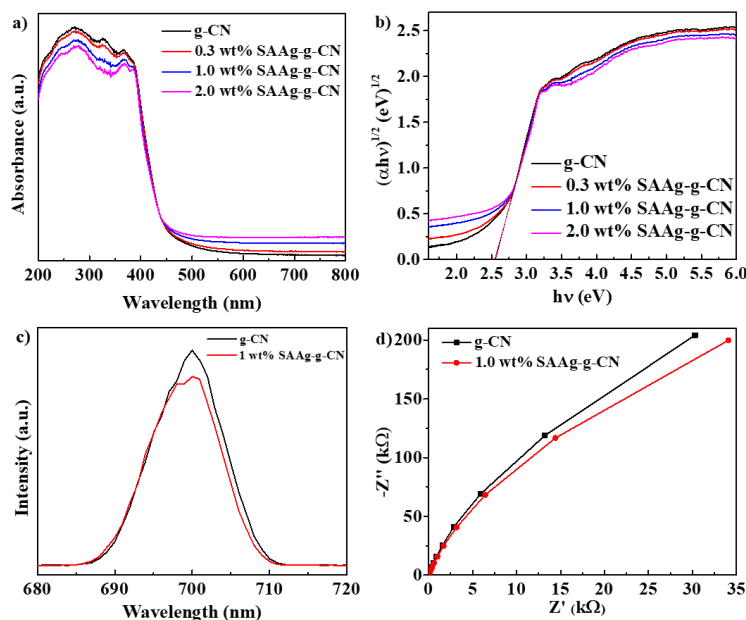
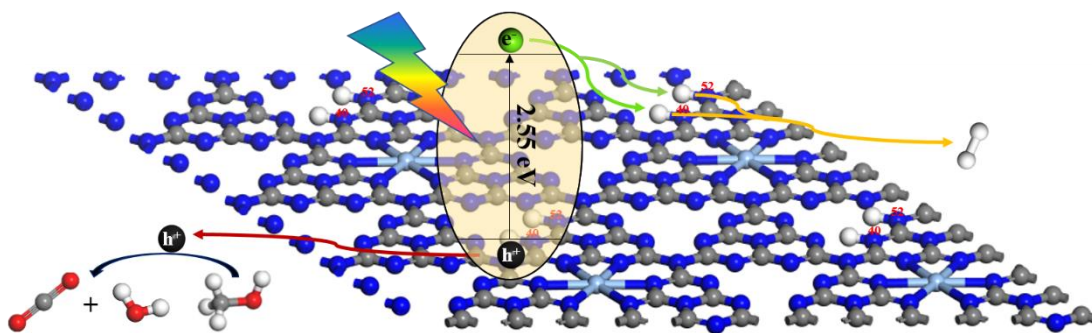


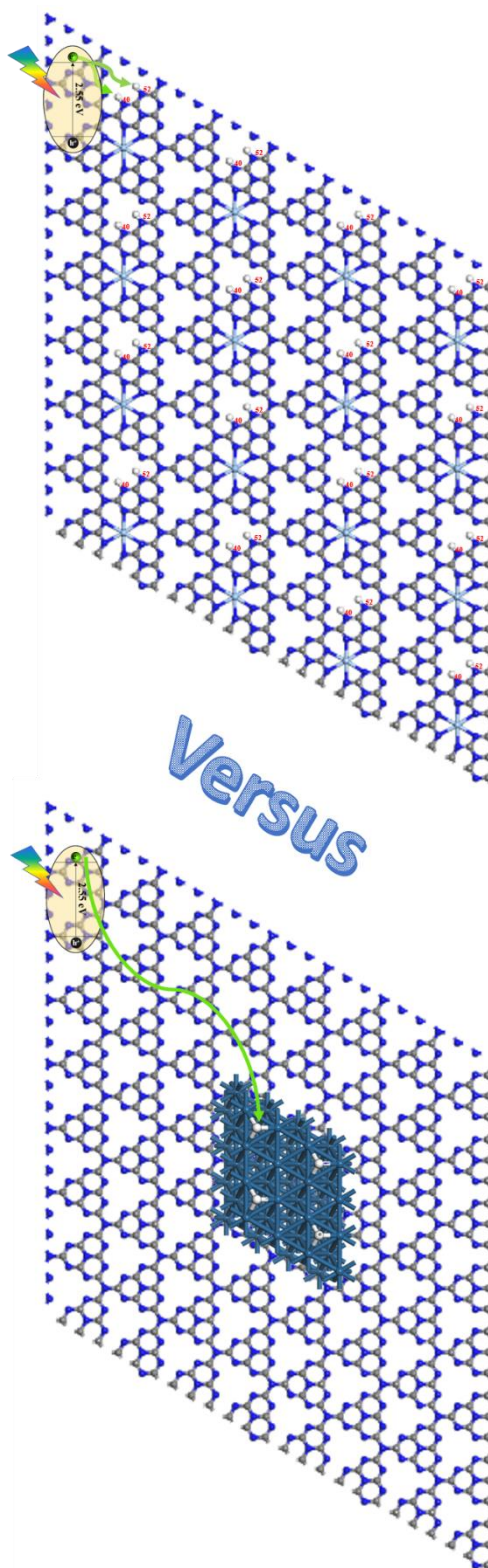
**Figure 5.16** **a**, UV-vis diffuse reflectance spectra and **b**, the plots of  $(\alpha hv)^{1/2}$  versus bandgap energy ( $h\nu$ ) of g-CN and different SAAg-g-CN samples. **c**, PL spectra of g-CN and 1.0 wt% SAAg-g-CN. **d**, Nyquist plots of electrochemical impedance spectroscopy (EIS) with different electrodes.

Based on all those experimental and calculation results, a mechanism of SAAg-g-CN is proposed, as shown in Scheme 5.2. SAAg is trapped in a six-fold cavity of g-CN with N-Ag bonding. Compared to g-CN (Figure 5.14a), in the framework of SAAg-g-CN (Figure 5.14b), the absolute value of  $\Delta G_{H^*}$  of the most efficient position for  $H_2$  evolution, No. 40

nitrogen atom, is reduced to less than half that of the counterpart in g-CN, while the  $|\Delta G_{H^*}|$  of No. 52 nitrogen atom also has an evident decrease, making it more powerful for PC-HER. Specifically,  $H^+$  is first attracted to the No. 40 and 52 nitrogen atoms and then combines with photo-excited electron to form H atom, while photogenerated holes are depleted by the sacrificial agent of methanol. Owing to the spatial adjacency, the obtained H atoms from No. 40 and 52 nitrogen atoms are inclined to combine before leaving the active sites, which may facilitate the desorption of the obtained  $H_2$  molecule from the catalyst, and thus boosts the PC-HER process. As to the reason why SAAg-g-CN with the  $\Delta G_{H^*}$  of only -0.279 eV surpasses the ability of PtNP-g-CN with the  $\Delta G_{H^*}$  of -0.09 eV, two other factors are applicable. First, as displayed in Scheme 5.3, Pt nanoparticles can only provide limited active sites compared to SAAg-g-CN, which has abundant No. 40 and 52 nitrogen atoms based active sites for  $H_2$  evolution. Second, a longer distance will be passed through for photoinduced electrons of PtNP-g-CN while ample short paths are available of SAAg-g-CN. More critically, the reinforced solar-heat-assisted PC-HER performance of SAAg-g-CN with temperature should be its unique merit compared with the metal NP co-catalytic system, deriving from its distinct N-Ag bond-based structure.



**Scheme 5.2** Schematic illustration of the mechanism of PC-HER on SAAg-g-CN (blue for N, grey for C, light blue for Ag, red for O and white for H atoms).



**Scheme 5.3** Schematic comparison of the mechanisms of PC-HER on SAAg-g-CN and NPt-g-CN (blue for N, grey for C, light blue for Ag, dark blue for Pt, red for O and white for H atoms).

## 4 Conclusion

In conclusion, single atom Ag modified g-CN was successfully synthesized via a facile two-step pyrolysis method and utilized in PC-HER processes with outstanding performances. The escalated  $\Delta G_{H^*}$  of No. 40 and 52 nitrogen atoms of SAAg-g-CN deriving from the individual structure endows the catalyst abundant active sites, shortened electron passing routes, and the ease for H<sub>2</sub> desorption, advancing the PC-HER process. What is more, this particular framework overshadows the metal NP cocatalyst weakness of growth and agglomeration with temperature. It endows SAAg-g-CN a prominent performance in solar-heat-assisted PC-HER. This work underlines the outstanding PC-HER and solar-heat-assisted PC-HER performance of SAC system stemming from its unique structure, reaction mechanism and tailored property. Specifically, it provides a route to utilize the thermal effect of infrared in the solar spectrum for PC-HER by SAC cocatalyst.

## References

- [1] A. Fujishima, K. Honda, Electrochemical Photolysis of Water at a Semiconductor Electrode, *Nature*. 238 (1972) 38–40.
- [2] I. Tsuji, H. Kato, H. Kobayashi, A. Kudo, Photocatalytic H<sub>2</sub> evolution reaction from aqueous solutions over band structure-controlled (AgIn)<sub>x</sub>Zn<sub>2(1-x)</sub>S<sub>2</sub> solid solution photocatalysts with

- visible-light response and their surface nanostructures, *J. Am. Chem. Soc.* 126 (2004) 13406–13413.
- [3] X. Wang, L. Yin, G. Liu, L. Wang, R. Saito, G.Q. Lu, H.M. Cheng, Polar interface-induced improvement in high photocatalytic hydrogen evolution over ZnO-CdS heterostructures, *Energy Environ. Sci.* 4 (2011) 3976–3979.
- [4] Y. Zhu, C. Lv, Z. Yin, J. Ren, X. Yang, C.L. Dong, H. Liu, R. Cai, Y.C. Huang, W. Theis, S. Shen, D. Yang, [001]-Oriented Hittorf's Phosphorus Nanorods/Polymeric Carbon Nitride Heterostructure for Boosting Wide-Spectrum-Responsive Photocatalytic Hydrogen Evolution from Pure Water, *Angew. Chemie - Int. Ed.* 030051 (2019).
- [5] Y. Liu, L. Wang, H. Feng, X. Ren, J. Ji, F. Bai, H. Fan, Microemulsion-Assisted Self-Assembly and Synthesis of Size-Controlled Porphyrin Nanocrystals with Enhanced Photocatalytic Hydrogen Evolution, *Nano Lett.* 19 (2019) 2614–2619.
- [6] X. Wang, L. Chen, S.Y. Chong, M.A. Little, Y. Wu, W.H. Zhu, R. Clowes, Y. Yan, M.A. Zwijnenburg, R.S. Sprick, A.I. Cooper, Sulfone-containing covalent organic frameworks for photocatalytic hydrogen evolution from water, *Nat. Chem.* 10 (2018) 1180–1189.
- [7] J. Ran, W. Guo, H. Wang, B. Zhu, J. Yu, S.Z. Qiao, Metal-Free 2D/2D Phosphorene/g-C<sub>3</sub>N<sub>4</sub> Van der Waals Heterojunction for

- Highly Enhanced Visible-Light Photocatalytic H<sub>2</sub> Production, *Adv. Mater.* 30 (2018) 2–7.
- [8] J. Ran, J. Qu, H. Zhang, T. Wen, H. Wang, S. Chen, L. Song, X. Zhang, L. Jing, R. Zheng, S.Z. Qiao, 2D Metal Organic Framework Nanosheet: A Universal Platform Promoting Highly Efficient Visible-Light-Induced Hydrogen Production, *Adv. Energy Mater.* 9 (2019) 1–8.
- [9] J. Ran, G. Gao, F.T. Li, T.Y. Ma, A. Du, S.Z. Qiao, Ti<sub>3</sub>C<sub>2</sub> MXene co-catalyst on metal sulfide photo-absorbers for enhanced visible-light photocatalytic hydrogen production, *Nat. Commun.* 8 (2017) 1–10.
- [10] W. Zhan, Y. Yuan, L. Sun, Y. Yuan, X. Han, Y. Zhao, Hierarchical NiO@N-Doped Carbon Microspheres with Ultrathin Nanosheet Subunits as Excellent Photocatalysts for Hydrogen Evolution, *Small.* 15 (2019) 1–8.
- [11] L. Zhang, Z.J. Zhao, M. Norouzi Banis, L. Li, Y. Zhao, Z. Song, Z. Wang, T.K. Sham, R. Li, M. Zheng, J. Gong, X. Sun, Selective atomic layer deposition of RuO<sub>x</sub> catalysts on shape-controlled Pd nanocrystals with significantly enhanced hydrogen evolution activity, *J. Mater. Chem. A.* 6 (2018) 24397–24406.
- [12] B. Hinnemann, P.G. Moses, J. Bonde, K.P. Jørgensen, J.H. Nielsen, S. Horch, I. Chorkendorff, J.K. Nørskov, Biomimetic hydrogen

- evolution: MoS<sub>2</sub> nanoparticles as catalyst for hydrogen evolution, *J. Am. Chem. Soc.* 127 (2005) 5308–5309.
- [13] Q. Yuan, D. Liu, N. Zhang, W. Ye, H. Ju, L. Shi, R. Long, J. Zhu, Y. Xiong, Noble-Metal-Free Janus-like Structures by Cation Exchange for Z-Scheme Photocatalytic Water Splitting under Broadband Light Irradiation, *Angew. Chemie - Int. Ed.* 56 (2017) 4206–4210.
- [14] X. Zhou, N. Liu, J. Schmidt, A. Kahnt, A. Osvet, S. Romeis, E.M. Zolnhofer, V.R.R. Marthala, D.M. Guldi, W. Peukert, M. Hartmann, K. Meyer, P. Schmuki, Noble-Metal-Free Photocatalytic Hydrogen Evolution Activity: The Impact of Ball Milling Anatase Nanopowders with TiH<sub>2</sub>, *Adv. Mater.* 29 (2017).
- [15] J.K. Nørskov, T. Bligaard, A. Logadottir, J.R. Kitchin, J.G. Chen, S. Pandelov, U. Stimming, Trends in the exchange current for hydrogen evolution, *J. Electrochem. Soc.* 152 (2005) 0–3.
- [16] X. Li, W. Bi, L. Zhang, S. Tao, W. Chu, Q. Zhang, Y. Luo, C. Wu, Y. Xie, Single-Atom Pt as Co-Catalyst for Enhanced Photocatalytic H<sub>2</sub> Evolution, *Adv. Mater.* 28 (2016) 2427–2431.
- [17] S. Cao, H. Li, T. Tong, H.C. Chen, A. Yu, J. Yu, H.M. Chen, Single-Atom Engineering of Directional Charge Transfer Channels and Active Sites for Photocatalytic Hydrogen Evolution, *Adv. Funct. Mater.* 28 (2018) 1–9.

- [18] B. Qiao, A. Wang, X. Yang, L.F. Allard, Z. Jiang, Y. Cui, J. Liu, J. Li, T. Zhang, Single-atom catalysis of CO oxidation using Pt<sub>1</sub>/FeO<sub>x</sub>, *Nat. Chem.* 3 (2011) 634–641.
- [19] X.F. Yang, A. Wang, B. Qiao, J. Li, J. Liu, T. Zhang, Single-atom catalysts: A new frontier in heterogeneous catalysis, *Acc. Chem. Res.* 46 (2013) 1740–1748.
- [20] J. Deng, H. Li, J. Xiao, Y. Tu, D. Deng, H. Yang, H. Tian, J. Li, P. Ren, X. Bao, Triggering the electrocatalytic hydrogen evolution activity of the inert two-dimensional MoS<sub>2</sub> surface via single-atom metal doping, *Energy Environ. Sci.* 8 (2015) 1594–1601.
- [21] G. Gao, Y. Jiao, E.R. Waclawik, A. Du, Single Atom (Pd/Pt) Supported on Graphitic Carbon Nitride as an Efficient Photocatalyst for Visible-Light Reduction of Carbon Dioxide, *J. Am. Chem. Soc.* 138 (2016) 6292–6297.
- [22] J. Hong, C. Jin, J. Yuan, Z. Zhang, Atomic Defects in Two-Dimensional Materials: From Single-Atom Spectroscopy to Functionalities in Opto-/Electronics, Nanomagnetism, and Catalysis, *Adv. Mater.* 29 (2017).
- [23] A. Wang, J. Li, T. Zhang, Heterogeneous single-atom catalysis, *Nat. Rev. Chem.* 2 (2018) 65–81
- [24] Y. Chen, S. Ji, W. Sun, W. Chen, J. Dong, J. Wen, J. Zhang, Z. Li, L. Zheng, C. Chen, Q. Peng, D. Wang, Y. Li, Discovering Partially

Charged Single-Atom Pt for Enhanced Anti-Markovnikov Alkene Hydrosilylation, *J. Am. Chem. Soc.* 140 (2018) 7407–7410.

- [25] M. Li, K. Duanmu, C. Wan, T. Cheng, L. Zhang, S. Dai, W. Chen, Z. Zhao, P. Li, H. Fei, Y. Zhu, R. Yu, J. Luo, K. Zang, Z. Lin, M. Ding, J. Huang, H. Sun, J. Guo, X. Pan, W.A. Goddard, P. Sautet, Y. Huang, X. Duan, Single-atom tailoring of platinum nanocatalysts for high-performance multifunctional electrocatalysis, *Nat. Catal.* 2 (2019) 495–503.
- [26] S. Chen, Z.N. Chen, W.H. Fang, W. Zhuang, L. Zhang, J. Zhang, Ag<sub>10</sub>Ti<sub>28</sub>-Oxo Cluster Containing Single-Atom Silver Sites: Atomic Structure and Synergistic Electronic Properties, *Angew. Chemie - Int. Ed.* 2 (2019) 10932–10935.
- [27] B.D. Ravetz, A.B. Pun, E.M. Churchill, D.N. Congreve, T. Rovis, L.M. Campos, Photoredox catalysis using infrared light via triplet fusion upconversion, *Nature.* 565 (2019) 343–346.
- [28] V.G. Kunde, F.M. Flasar, D.E. Jennings, B. B ézard, D.F. Strobel, B.J. Conrath, C.A. Nixon, G.L. Bjoraker, P.N. Romani, R.K. Achterberg, A.A. Simon-Miller, P. Irwin, J.C. Brasunas, J.C. Pearl, M.D. Smith, G.S. Orton, P.J. Gierasch, L.J. Spilker, R.C. Carlson, A.A. Mamoutkine, S.B. Calcutt, P.L. Read, F.W. Taylor, T. Fouchet, P. Parrish, A. Barucci, R. Courtin, A. Coustenis, D. Gautier, E. Lellouch, A. Marten, R. Prang é Y. Biraud, C. Ferrari, T.C. Owen,

- M.M. Abbas, R.E. Samuelson, F. Raulin, P. Ade, C.J. Césarsky, K.U. Grossman, A. Coradini, Jupiter's atmospheric composition from the Cassini thermal infrared spectroscopy experiment, *Science* (80-. ). 305 (2004) 1582–1586.
- [29] Y.Y. Won, S.P. Meeker, V. Trappe, D.A. Weitz, N.Z. Diggs, J.I. Emert, Effect of temperature on carbon-black agglomeration in hydrocarbon liquid with adsorbed dispersant, *Langmuir*. 21 (2005) 924–932.
- [30] Q. Shi, S. Li, S. Tian, Z. Huang, Y. Yang, Z. Liao, J. Sun, J. Wang, Y. Yang, Investigating Agglomeration Behaviors in High Temperature Gas-Solid Fluidized Beds with Liquid Injection, *Ind. Eng. Chem. Res.* 57 (2018) 5482–5494.
- [31] E. Varga, P. Pusztai, A. Oszkó, K. Báán, A. Erdohelyi, Z. Kónya, J. Kiss, Stability and Temperature-Induced Agglomeration of Rh Nanoparticles Supported by CeO<sub>2</sub>, *Langmuir*. 32 (2016) 2761–2770.
- [32] J.X. Dong, Z.F. Gao, Y. Zhang, B.L. Li, N.B. Li, H.Q. Luo, A selective and sensitive optical sensor for dissolved ammonia detection via agglomeration of fluorescent Ag nanoclusters and temperature gradient headspace single drop microextraction, *Biosens. Bioelectron.* 91 (2017) 155–161.
- [33] A.A. Esmailpour, R. Zarghami, N. Mostoufi, Effect of Temperature on the Nanoparticles Agglomerates Fluidization, (2015).

- [34] T. Kister, D. Monego, P. Mulvaney, A. Widmer-Cooper, T. Kraus, Colloidal Stability of Apolar Nanoparticles: The Role of Particle Size and Ligand Shell Structure, *ACS Nano*. 12 (2018) 5969–5977.
- [35] X. Chen, R. Shi, Q. Chen, Z. Zhang, W. Jiang, Y. Zhu, T. Zhang, Three-dimensional porous g-C<sub>3</sub>N<sub>4</sub> for highly efficient photocatalytic overall water splitting, *Nano Energy*. 59 (2019) 644–650.
- [36] Y. Zheng, J. Liu, J. Liang, M. Jaroniec, S.Z. Qiao, Graphitic carbon nitride materials: Controllable synthesis and applications in fuel cells and photocatalysis, *Energy Environ. Sci*. 5 (2012) 6717–6731.
- [37] X. Zhang, X. Xie, H. Wang, J. Zhang, B. Pan, Y. Xie, Enhanced photoresponsive ultrathin graphitic-phase C<sub>3</sub>N<sub>4</sub> nanosheets for bioimaging, *J. Am. Chem. Soc.* 135 (2013) 18–21.
- [38] G. Liu, P. Niu, C. Sun, S.C. Smith, Z. Chen, G.Q. Lu, H.M. Cheng, Unique electronic structure induced high photoreactivity of sulfur-doped graphitic C<sub>3</sub>N<sub>4</sub>, *J. Am. Chem. Soc.* 132 (2010) 11642–11648.
- [39] S. Han, X. Hu, W. Yang, Q. Qian, X. Fang, Y. Zhu, Constructing the Band Alignment of Graphitic Carbon Nitride (g-C<sub>3</sub>N<sub>4</sub>)/Copper(I) Oxide (Cu<sub>2</sub>O) Composites by Adjusting the Contact Facet for Superior Photocatalytic Activity, *ACS Appl. Energy Mater.* 2 (2019) 1803–1811.
- [40] X.W. Guo, S.M. Chen, H.J. Wang, Z.M. Zhang, H. Lin, L. Song, T.B. Lu, Single-atom molybdenum immobilized on photoactive

- carbon nitride as efficient photocatalysts for ambient nitrogen fixation in pure water, *J. Mater. Chem. A*. 7 (2019) 19831–19837.
- [41] W. Zhang, Q. Peng, L. Shi, Q. Yao, X. Wang, A. Yu, Z. Chen, Y. Fu, Merging Single-Atom-Dispersed Iron and Graphitic Carbon Nitride to a Joint Electronic System for High-Efficiency Photocatalytic Hydrogen Evolution, *Small*. 15 (2019) 1–8.
- [42] S. Wang, J. Li, Q. Li, X. Bai, J. Wang, Metal single-atom coordinated graphitic carbon nitride as an efficient catalyst for CO oxidation, *Nanoscale*. 12 (2020) 364–371.
- [43] Z. Chen, J. Zhao, C.R. Cabrera, Z. Chen, Computational Screening of Efficient Single - Atom Catalysts Based on Graphitic Carbon Nitride (g-C<sub>3</sub>N<sub>4</sub>) for Nitrogen Electroreduction , *Small Methods*. 3 (2019) 1800368.
- [44] S. Wang, S.P. Jiang, X. Wang, Microwave-assisted one-pot synthesis of metal/metal oxide nanoparticles on graphene and their electrochemical applications, *Electrochim. Acta*. 56 (2011) 3338–3344.
- [45] F. Han, Projector-Augmented Plane-Wave Method, *Probl. Solid State Phys. with Solut.* 50 (2011) 391–396.
- [46] G. Kresse, J. Hafner, Liquid-Metal — Amorphous-Semiconductor, *Phys. Rev. B*. 49 (1994) 14251.
- [47] G. Kresse, J. Hafner, Ab initio molecular dynamics for liquid metlas,

- Phys. Rev. B. 47 (1993) 558–561.
- [48] G. Kresse, J. Furthmüller, Y.J. Li, Y.J. Chen, J.C. Walmsley, R.H. Mathinsen, S. Dumoulin, H.J. Roven, S. Yip, T. Supervisor, S. Chen, Modeling Microstructural Effects on Deformation Resistance and Thermal Conductivity, Phys. Rev. B. 62 (2000) 11169–11186.
- [49] J.P. Perdew, K. Burke, M. Ernzerhof, Perdew, Burke, and Ernzerhof Reply, Phys. Rev. Lett. 80 (1998) 891.
- [50] J. Klime, D.R. Bowler, A. Michaelides, Van der Waals density functionals applied to solids, Phys. Rev. B - Condens. Matter Mater. Phys. 83 (2011) 1–13.
- [51] Y. Zheng, Y. Jiao, Y. Zhu, L.H. Li, Y. Han, Y. Chen, A. Du, M. Jaroniec, S.Z. Qiao, Hydrogen evolution by a metal-free electrocatalyst, Nat. Commun. 5 (2014) 1–8.
- [52] Y. Li, R. Jin, Y. Xing, J. Li, S. Song, X. Liu, M. Li, R. Jin, Macroscopic Foam-Like Holey Ultrathin  $g\text{-C}_3\text{N}_4$  Nanosheets for Drastic Improvement of Visible-Light Photocatalytic Activity, Adv. Energy Mater. 6 (2016) 3–7.
- [53] X. Sun, B.J. Tatarchuk, Photo-assisted adsorptive desulfurization of hydrocarbon fuels over  $\text{TiO}_2$  and  $\text{Ag}/\text{TiO}_2$ , Fuel. 183 (2016) 550–556.
- [54] S.N. Talapaneni, G.P. Mane, D.H. Park, K.S. Lakhi, K. Ramadass, S. Joseph, W.M. Skinner, U. Ravon, K. Al-Bahily, A. Vinu,

- Diaminotetrazine based mesoporous  $C_3N_6$  with a well-ordered 3D cubic structure and its excellent photocatalytic performance for hydrogen evolution, *J. Mater. Chem. A*. 5 (2017) 18183–18192.
- [55] H. Deng, Y. Yu, H. He, Water Effect on Preparation of Ag/Al<sub>2</sub>O<sub>3</sub> Catalyst for Reduction of NO<sub>x</sub> by Ethanol, *J. Phys. Chem. C*. 120 (2016) 24294–24301.
- [56] J.G. Parsons, K. Dokken, J.R. Peralta-Videa, J. Romero-Gonzalez, J.L. Gardea-Torresdey, X-ray absorption near edge structure and extended X-ray absorption fine structure analysis of standards and biological samples containing mixed oxidation states of chromium(III) and chromium(VI), *Appl. Spectrosc.* 61 (2007) 338–345.
- [57] M. Song, Y. Wu, X. Wang, M. Liu, Y. Su, Switching charge transfer process of carbon nitride and bismuth vanadate by anchoring silver nanoparticle toward cocatalyst free water reduction, *J. Colloid Interface Sci.* 529 (2018) 375–384.
- [58] T. Chen, W. Quan, L. Yu, Y. Hong, C. Song, M. Fan, L. Xiao, W. Gu, W. Shi, One-step synthesis and visible-light-driven H<sub>2</sub> production from water splitting of Ag quantum dots/g-C<sub>3</sub>N<sub>4</sub> photocatalysts, *J. Alloys Compd.* 686 (2016) 628–634.
- [59] X. Ding, Y. Li, J. Zhao, Y. Zhu, Y. Li, W. Deng, C. Wang, Enhanced photocatalytic H<sub>2</sub> evolution over CdS/Au/g-C<sub>3</sub>N<sub>4</sub> composite

- photocatalyst under visible-light irradiation, *APL Mater.* 3 (2015).
- [60] S. Yang, Y. Gong, J. Zhang, L. Zhan, L. Ma, Z. Fang, R. Vajtai, X. Wang, P.M. Ajayan, Exfoliated graphitic carbon nitride nanosheets as efficient catalysts for hydrogen evolution under visible light, *Adv. Mater.* 25 (2013) 2452–2456.
- [61] L. Ge, F. Zuo, J. Liu, Q. Ma, C. Wang, D. Sun, L. Bartels, P. Feng, Synthesis and efficient visible light photocatalytic hydrogen evolution of Polymeric g-C<sub>3</sub>N<sub>4</sub> coupled with CdS quantum dots, *J. Phys. Chem. C.* 116 (2012) 13708–13714.
- [62] L. Ge, C. Han, X. Xiao, L. Guo, Y. Li, Enhanced visible light photocatalytic hydrogen evolution of sulfur-doped polymeric g-C<sub>3</sub>N<sub>4</sub> photocatalysts, *Mater. Res. Bull.* 48 (2013) 3919–3925.
- [63] L. Ge, C. Han, Synthesis of MWNTs/g-C<sub>3</sub>N<sub>4</sub> composite photocatalysts with efficient visible light photocatalytic hydrogen evolution activity, *Appl. Catal. B Environ.* 117–118 (2012) 268–274.
- [64] L. Ge, C. Han, X. Xiao, L. Guo, Synthesis and characterization of composite visible light active photocatalysts MoS<sub>2</sub>-g-C<sub>3</sub>N<sub>4</sub> with enhanced hydrogen evolution activity, *Int. J. Hydrogen Energy.* 38 (2013) 6960–6969.
- [65] H. Yan, H. Yang, TiO<sub>2</sub>-g-C<sub>3</sub>N<sub>4</sub> composite materials for photocatalytic H<sub>2</sub> evolution under visible light irradiation, *J. Alloys Compd.* 509 (2011) 26–29.

- [66] X.L. Luo, G.L. He, Y.P. Fang, Y.H. Xu, Nickel sulfide/graphitic carbon nitride/strontium titanate (NiS/g-C<sub>3</sub>N<sub>4</sub>/SrTiO<sub>3</sub>) composites with significantly enhanced photocatalytic hydrogen production activity, *J. Colloid Interface Sci.* 518 (2018) 184–191.
- [67] K. Sridharan, E. Jang, J.H. Park, J.H. Kim, J.H. Lee, T.J. Park, Silver quantum cluster (Ag<sub>9</sub>)-grafted graphitic carbon nitride nanosheets for photocatalytic hydrogen generation and dye degradation, *Chem. - A Eur. J.* 21 (2015) 9126–9132.
- [68] M.A. Mohamed, M.F. M. Zain, L. Jeffery Minggu, M.B. Kassim, J. Jaafar, N.A. Saidina Amin, Y.H. Ng, Revealing the role of kapok fibre as bio-template for In-situ construction of C-doped g-C<sub>3</sub>N<sub>4</sub> @C, N co-doped TiO<sub>2</sub> core-shell heterojunction photocatalyst and its photocatalytic hydrogen production performance, *Appl. Surf. Sci.* 476 (2019) 205–220.
- [69] Y. Peng, B. Lu, L. Chen, N. Wang, J.E. Lu, Y. Ping, S. Chen, Hydrogen evolution reaction catalyzed by ruthenium ion-complexed graphitic carbon nitride nanosheets, *J. Mater. Chem. A.* 5 (2017) 18261–18269.
- [70] X. Li, J. Wang, D. Xu, Z. Sun, Q. Zhao, W. Peng, Y. Li, G. Zhang, F. Zhang, X. Fan, NbSe<sub>2</sub> Nanosheet Supported PbBiO<sub>2</sub>Br as a High Performance Photocatalyst for the Visible Light-driven Asymmetric Alkylation of Aldehyde, *ACS Sustain. Chem. Eng.* 3 (2015) 1017–

1022.

*Every reasonable effort has been made to acknowledge the owners of copyright material. I would be pleased to hear from any copyright owner who has been omitted or incorrectly acknowledged.*

## Chapter 6 g-C<sub>3</sub>N<sub>4</sub> self-based van der Waals type II junctions for photocatalytic hydrogen evolution

### Abstract

In the last two Chapters, graphitic carbon nitride (g-C<sub>3</sub>N<sub>4</sub>) based composites and single-atom catalysis were utilized in photocatalytic hydrogen evolution reaction (PC-HER). Herein, for improved PC-HER efficiency of g-C<sub>3</sub>N<sub>4</sub>, its self-based van der Waals (vdW) type II junctions are fabricated via a facile co-thermal-exfoliation method, with g-C<sub>3</sub>N<sub>4</sub> and heteroatom doped g-C<sub>3</sub>N<sub>4</sub> as precursors. The best candidate of g-C<sub>3</sub>N<sub>4</sub>/K doped g-C<sub>3</sub>N<sub>4</sub> nanosheets vdW type II junction has an outstanding PC-HER rate of 1243  $\mu\text{mol}\cdot\text{h}^{-1}\cdot\text{g}^{-1}$ , which is 1.5 times that of g-C<sub>3</sub>N<sub>4</sub> nanosheets (CNS) and K doped g-C<sub>3</sub>N<sub>4</sub> nanosheets (KCNS), and 8.9 times higher than that of bulk g-C<sub>3</sub>N<sub>4</sub>. The enhanced PC-HER performance could be ascribed to the synergistic effects of the shortened bandgap of KCNS than that of CNS, the enlarged specific surface area, the matched type II energy band structure, and the “face to face” vdW charge interaction. More importantly, the type II junctions were found superior to the type III junction, because the middle semiconductor in the type III junction could be degraded to the reintegration center of photo-motivated electron and hole pairs. This Chapter highlights the cooperative effect of different strategies in improving the PC-HER capacities of g-C<sub>3</sub>N<sub>4</sub>,

especially the application of vdW junctions, and discloses some unexpected but reasonable results.

## 6.1 Introduction

Fossil fuels, including petroleum, coal, natural gas, and shale oil, are currently the primary energy sources for the world.[1–5] However, those non-renewable energy sources will run out in the next ~ 200 years,[6–10] and the combustion products, e.g. CO<sub>2</sub>, and trace amounts of SO<sub>2</sub> and NO<sub>2</sub>, can lead to greenhouse effects[11–14] and environmental pollution.[15–17] Thus, clean energy is urgently required for sustainable human development. Photocatalytic hydrogen evolution reaction (PC-HER) offers a promising solution for solving the above issues, owing to the reproducibility and cleanliness of H<sub>2</sub>, and the environmental friendliness of PC-HER processes.[18–22]

In 2009, Wang et al. for the first time employed graphitic carbon nitride (g-C<sub>3</sub>N<sub>4</sub>) as the photocatalyst in a PC-HER system,[23] thereafter, this material has promptly become a superstar in photocatalysis owing to its easy preparation, suitable bandgap, non-toxicity, physicochemical firmness, and non-metal nature.[24–28] A large number of measures have been designed and exploited to continually advance its PC-HER to higher levels in the past decade. For example, exfoliating bulk g-C<sub>3</sub>N<sub>4</sub> into

nanosheets can remarkably enlarge the specific surface area and provide more active sites.[29–32] Doping heteroatoms to a g-C<sub>3</sub>N<sub>4</sub> framework can optimize its properties, like increasing its optical absorption, tuning its bandgap, modifying its electrical conductivity, and shifting its HOMO-LUMO sites.[33–40] Besides, type II junctions, formed by the connection of two types of semiconductors with a staggered band structure, can impede the reintegration of photo-motivated charges of both the two materials by transferring photoelectrons and holes from each other.[41–43] What is more, van der Waals (vdW) junctions, composed of several two-dimensional (2D) materials with a “face to face” contact, are gaining great attention in recent years because of their marvelous properties benefiting from the electronic interactions via massive intimate interfaces.[44,45]

If combining all those four strategies into a specific structure, we can collectively integrate all their advantages to boost the PC-HER process. Herein, g-C<sub>3</sub>N<sub>4</sub> self-based van der Waals type II and type III junctions were obtained via a thermal co-exfoliation method. Specifically, those composites contain g-C<sub>3</sub>N<sub>4</sub>/B-doped g-C<sub>3</sub>N<sub>4</sub> nanosheets (CN-BCN-S), g-C<sub>3</sub>N<sub>4</sub>/K-doped g-C<sub>3</sub>N<sub>4</sub> nanosheets (CN-KCN-S), B-doped g-C<sub>3</sub>N<sub>4</sub>/K-doped g-C<sub>3</sub>N<sub>4</sub> nanosheets (BCN-KCN-S), and g-C<sub>3</sub>N<sub>4</sub>/B doped g-C<sub>3</sub>N<sub>4</sub>/K-doped g-C<sub>3</sub>N<sub>4</sub> nanosheets (CN-BCN-KCN-S). Their enhanced PC-HER performances can be ascribed to the synergistic effects of shortened

bandgaps, an enlarged specific surface area, matched energy band structure, and “face to face” charge transfer. Moreover, this study, for the first time, discloses and explains the phenomenon that type II junctions are more efficient than type III junctions.

## 6.2 Experimental

### 6.2.1 Chemicals and materials

Urea, boric acid, potassium hydroxide, sodium sulfate, triethanolamine, chloroplatinic acid, and Nafion solution were purchased from Sigma-Aldrich and used without further purification.

### 6.2.2 Preparation of catalysts

Synthesis of g-C<sub>3</sub>N<sub>4</sub>: 10 g urea was placed in a crucible, which was then covered with a lid and transferred in a muffle furnace. The temperature was kept at 550 °C for 4 h with a heating rate of 15 °C/min. The obtained bulk was pulverized in a hard plastic container with a stirrer bar by a vortex mixer. The prepared powder was denoted as CN.

Fabrication of B-doped g-C<sub>3</sub>N<sub>4</sub> (or K-doped g-C<sub>3</sub>N<sub>4</sub>): 10 g urea and 3 mg boric acid (or 10 mg potassium hydroxide) were dissolved in 12 mL ultrapure water in a crucible. The mixture was stirred homogeneously,

dried at 100 °C and then transferred into a muffle furnace with a lid. The temperature was kept at 550 °C for 4 h with a heating rate of 15 °C/min. The acquired bulk was pulverized and then rinsed with ultrapure water several times by filtration and dried at 100 °C. The obtained material was pulverized again and denoted as BCN (or KCN).

Preparation of B, K co-doped g-C<sub>3</sub>N<sub>4</sub>: 10 g urea, 3 mg boric acid, and 10 mg potassium hydroxide were dissolved in 12 mL ultrapure water in a crucible. The mixture was stirred evenly, dried at 100 °C and then covered with a lid to be shifted into a muffle furnace. The temperature was kept at 550 °C for 4 h with a heating rate of 15 °C/min. The acquired bulk was still white crystal, which was the same as the state before polymerization. This is because the reaction of boric acid and potassium hydroxide happened in the dissolving and drying processes. The produced potassium metaborate with a boiling point at 1401 °C would thoroughly mix with urea, which protected the urea from being polymerized.

Fabrication of g-C<sub>3</sub>N<sub>4</sub> nanosheets (or B-doped g-C<sub>3</sub>N<sub>4</sub> nanosheets, or K doped g-C<sub>3</sub>N<sub>4</sub> nanosheets): 480 mg CN was put in a crucible with a lid, which was then transferred in a muffle furnace. The temperature was kept at 500 °C for 4 h with a heating rate of 15 °C/min. The obtained powder was denoted as CNS (or BCNS, or KCNS).

Preparation of the mixture of g-C<sub>3</sub>N<sub>4</sub> nanosheets and B-doped g-C<sub>3</sub>N<sub>4</sub> nanosheets (or the mixture of g-C<sub>3</sub>N<sub>4</sub> nanosheets and K-doped g-C<sub>3</sub>N<sub>4</sub> nanosheets, or the mixture of B-doped g-C<sub>3</sub>N<sub>4</sub> nanosheets and K-doped g-C<sub>3</sub>N<sub>4</sub> nanosheets): 120 mg CNS and 120 mg BCNS ( or 120 mg CNS and 120 mg KCNS, or 120 mg BCNS and 120 mg KCNS) were thoroughly mixed in a hard plastic container with a stirrer bar by a vortex mixer. The obtained mixture was denoted as CNS-BCNS (or CNS-KCNS, or BCNS-KCNS).

Preparation of the mixture of g-C<sub>3</sub>N<sub>4</sub> nanosheets, B-doped g-C<sub>3</sub>N<sub>4</sub> nanosheets and K-doped g-C<sub>3</sub>N<sub>4</sub> nanosheets: 80 mg CNS, 80 mg BCNS, and 80 mg KCNS were fully mixed in a hard plastic container with a stirrer bar by a vortex mixer. The obtained mixture was denoted as CNS-BCNS-KCNS.

Fabrication of g-C<sub>3</sub>N<sub>4</sub>/B-doped g-C<sub>3</sub>N<sub>4</sub> nanosheets-based van der Waals type II junction (or g-C<sub>3</sub>N<sub>4</sub>/K-doped g-C<sub>3</sub>N<sub>4</sub> nanosheets-based van der Waals type II junction, or B-doped g-C<sub>3</sub>N<sub>4</sub>/K-doped g-C<sub>3</sub>N<sub>4</sub> nanosheets-based van der Waals type II junction): 240 mg CN and 240 mg BCN (or 240 mg CN and 240 mg KCN, or 240 mg BCN and 240 mg KCN) were thoroughly mixed in a hard plastic container with a stirrer bar by a vortex

mixer. The mixture was then shifted in a muffle furnace, and the temperature was kept at 500 °C for 4 h with a heating rate of 15 °C/min. The obtained powder was denoted as CN-BCN-S (or CN-KCN-S, or BCN-KCNS).

Fabrication of g-C<sub>3</sub>N<sub>4</sub>/B-doped g-C<sub>3</sub>N<sub>4</sub>/K-doped g-C<sub>3</sub>N<sub>4</sub> nanosheets-based van der Waals type III junction: 160 mg CN, 160 mg BCN, and 160 mg KCN were thoroughly mixed in a hard plastic container with a stirrer bar by a vortex mixer. The mixture was then shifted in a muffle furnace, and the temperature was kept at 500 °C for 4 h with a heating rate of 15 °C/min. The obtained powder was denoted as CN-BCN-KCN-S.

### 6.2.3 Characterization of the materials

Transmission electron microscopy images (TEM) were acquired from a Philips CM200 microscope (Germany) at 200 kV. X-ray diffraction (XRD) analyses were operated using a powder X-ray diffractometer at 40 kV and 15 mA with Cu Ka radiation (Miniflex, Rigaku). X-ray photoelectron spectroscopy (XPS) measurements were conducted on an Axis Ultra (Kratos Analytical, UK) XPS spectrometer equipped with an Al Ka source (1486.6 eV). UV-Vis diffuse reflectance tests were performed on a Cary 100 UV-Vis spectrophotometer (Agilent, USA) with BaSO<sub>4</sub> as the blank sample.

#### 6.2.4 Photoelectrochemical tests

Mott-Schottky tests were performed on a Zennium electrochemical workstation (Zahner, Germany) in a normal three-electrode system with a 0.05 M Na<sub>2</sub>SO<sub>4</sub> (pH = 6.8) electrolyte solution. A platinum sheet served as the counter electrode and an Ag/AgCl electrode as the reference electrode. In terms of the photoanode, the sample film was synthesized on a fluorine-doped tin oxide (FTO) glass, which was ultrasonicated in ultrapure water, acetone, and ethanol for 15 min in order and dried at 60 °C. Then 5 mg of the catalyst was mixed with 1 mL of absolute ethanol and 10 μL of Nafion solution homogeneously. The acquired slurry was spin-coated onto the preprocessed FTO glass, and the prepared electrode was dried at 100 °C for 24 h (catalyst loading ~0.60 mg·cm<sup>-2</sup>).

#### 6.2.5 Photocatalytic measurements

Photocatalytic hydrogen evolution measurements were performed in a black Teflon cell with a quartz light window. The light source was a 300 W Xenon lamp (Newport) with a UV cut-off filter ( $\lambda > 420$  nm). In a typical experiment, 20 mg photocatalysts were added in a mixed solution of 90 mL ultrapure water and 10 mL triethanolamine (TEOA), followed by injecting 120 μL H<sub>4</sub>PtCl aqueous solution (5 mg Pt/ml) to the mixture to provide 3 wt% Pt cocatalysts. After a 5-minute ultrasonication, the mixed suspension was transferred in the reactor, which was then sealed

tightly. Nitrogen gas was utilized to purge the air in the reactor and the reaction solution for 30 min with vigorous stirring, after which the light source was switched on to start the reactions. Meanwhile, the temperature of the reaction system was kept at 25 °C with a water circulation system. The generated hydrogen was online examined by a 490 Micro GC (Agilent, USA) equipped with a thermal conductivity detector.

### 6.3 Results and discussions

Firstly, CN-KCN-S was taken as an example of the vdW type II junction, and its TEM image is exhibited in Figure 6.1. It can be found that 2D layers of CNS and KCNS were stacked together with an extensive interface.

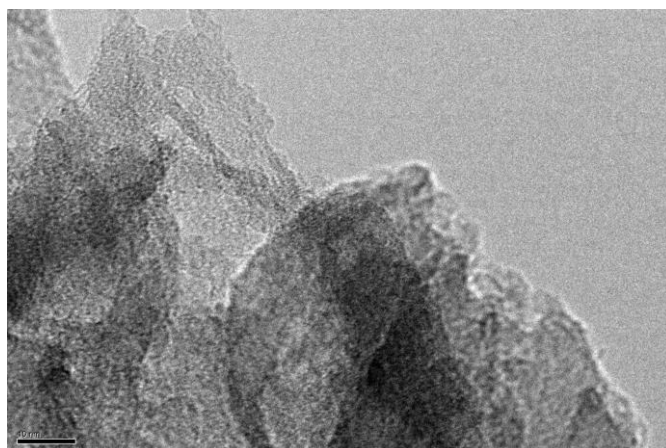


**Figure 6.1** TEM image of CN-KCN-S (vdW type II junction).

XRD was then explored to compare the crystal differences among all the

samples. The (100) peak at  $\sim 13.0^\circ$  (Figure 6.2a) results from the ordering of tri-s-triazine units at 0.675 nm within a g-C<sub>3</sub>N<sub>4</sub> plane, while the (002) peak at about  $27.5^\circ$  denotes the interlayer piling of the conjugated double bonds for graphitic materials, which is consistent with previously reported 0.33 nm of interlayer spacing.[35,46–48] From all the patterns in Figure 6.2, we can find that the (002) peak of nanosheets has a minor right-shift compared to the bulk counterparts, indicating a narrowed interlayer distance, which is corresponding to the data from the literature.[30,49,50] Figure 6.3 illustrates XRD patterns of the boron and potassium doping on g-C<sub>3</sub>N<sub>4</sub>. The bulk samples (Figure 6.3a) show that both boron doping and potassium doping can make a left shift of the (002) peak, indicating a widened layer-to-layer space. For B-doped g-C<sub>3</sub>N<sub>4</sub>, boron atoms are inclined to substitute carbon atoms in the architect of g-C<sub>3</sub>N<sub>4</sub>, as shown in Scheme 6.1a. Thus, the larger boron atom diameter than that of a carbon atom should be the reason for the wider interlayer distance of BCN. In terms of K-doped g-C<sub>3</sub>N<sub>4</sub>, potassium atoms are apt to be trapped in the six-fold cavity of the g-C<sub>3</sub>N<sub>4</sub> structure (Scheme 6.1b). Therefore, the left-shift of the (002) peak of KCN should be attributed to the larger radius of potassium atoms than that of carbon and nitrogen atoms. A similar trend of doping effect was shown in the nanosheet samples (Figure 6.3b). The smaller changes between doped CNS and pure CNS compared to the bulk group should be due to the right shift of nanosheets, as explained in Figure

6.2.

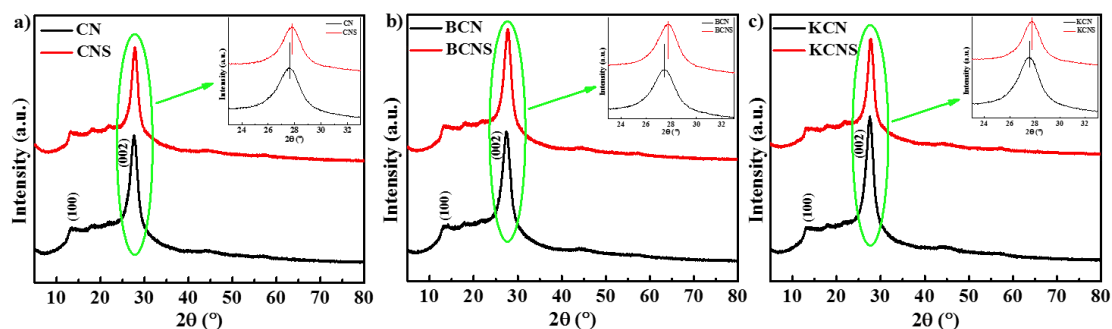


**Figure 6.2** The XRD patterns of bulk materials and nanosheets. **a)** CN vs. CNS, **b)** BCN vs. BCNS, and **c)** KCN vs. KCNS.

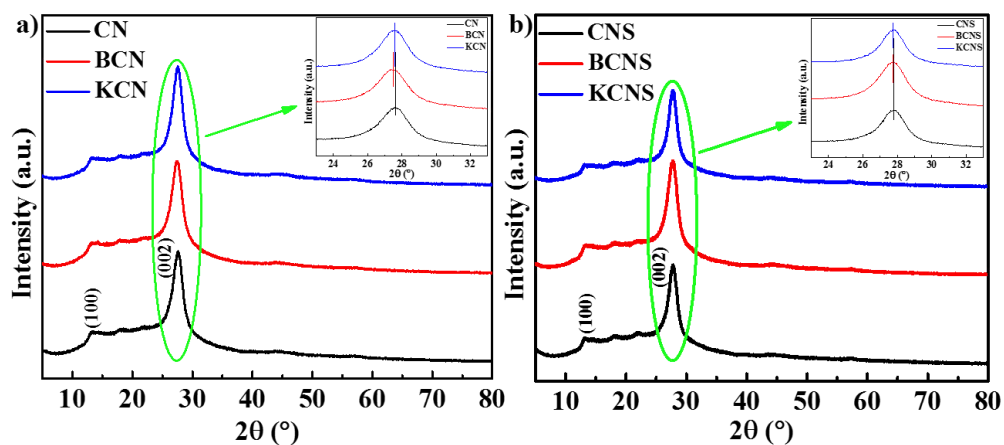
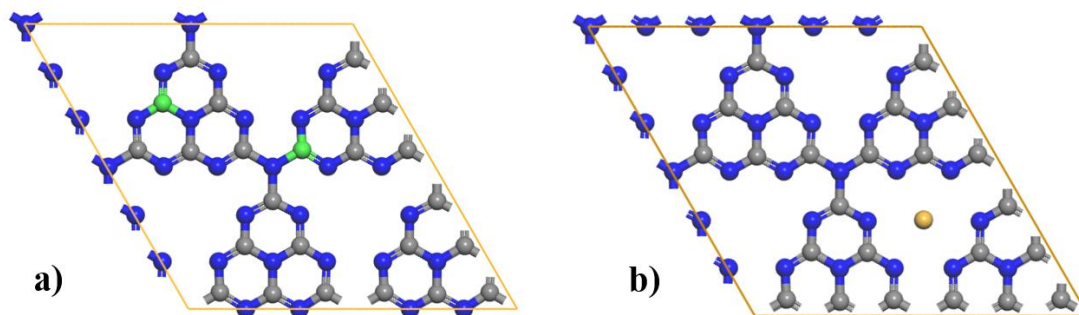


**Figure 6.3** The XRD patterns of doped  $g\text{-C}_3\text{N}_4$  and pristine  $g\text{-C}_3\text{N}_4$ . **a)** CN vs. BCN vs. KCN, and **b)** CNS vs. BCNS vs. KCNS.



**Scheme 6.1** The structure of a single-layer of **a)** B doped  $g\text{-C}_3\text{N}_4$ , and **b)** K doped  $g\text{-C}_3\text{N}_4$ . Blue for nitrogen atoms, grey for carbon atoms, green for boron atoms and yellow for potassium atoms.

A comprehensive study on vdW type II and III junctions, the mixture counterparts, and the corresponding nanosheets, is reflected in Figure 6.4. Compared to CNS and BCNS, the vdW type II junction of CN-BCN-S (Figure 6.4a) exhibits a left offset in the (002) peak, which may be the result of that the distance between CNS layer and BCNS layer is slightly wider than the interspace of single CNS or BCNS because of the weak vdW interaction of hetero layers. The mixture of CNS-BCNS also shows a minor left shift in the (002) peak, but it is not so significant as the change of CN-BCN-S. This indicates that minor vdW junctions can also be formed in CNS-BCNS; however, they are inefficient as compared to CN-BCN-S vdW junction. Similar tendencies can also be found in CN-KCN-S and BCN-KCN-S type II vdW junctions, and CN-BCN-KCN-S type III vdW junction.

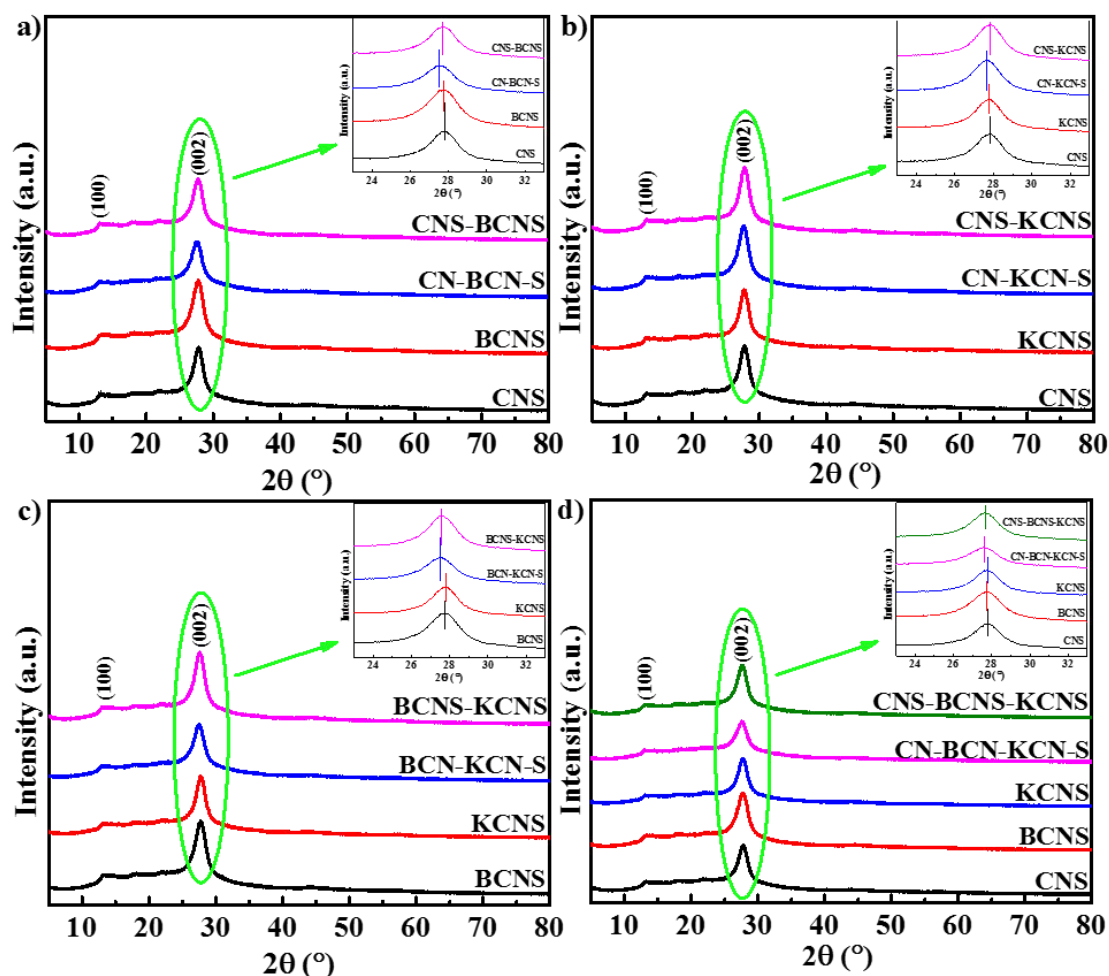


**Figure 6.4** The XRD pattern comparisons of vdW type II and III junctions, the mixture counterpart, and the corresponding nanosheets.

XPS studies were performed to get knowledge of the inner chemical bonding of BCNS and KCNS. The main C 1s peak of BCNS at 288.0 eV (Figure 6.5a) is the result of  $sp^2$  carbon jointed to the three nitrogen atoms ( $C-(N)_3$ ) in the  $g-C_3N_4$  grid. The other C 1s peak is from the unavoidable graphitic carbon atoms (C-C). The N 1s peak at 398.5 eV of BCNS (Figure 6.5b) accords with the  $sp^2$ -bonded N atoms in the graphite-like  $g-C_3N_4$  framework ( $C-N=C$ ). The peak of 399.6 eV results from the nitrogen

ternary groups (N-(C)<sub>3</sub>), while the peak at 401.0 eV signifies amino functional groups (C-N-H). Lastly, the one at 404.5 eV signifies the characteristic  $\pi$ -excitation.[31,51,52] There is only one B 1s peak of BCNS, which is at 191.5 eV, very close to the B 1s peak of h-BN, denoting the boron atom connected with three nitrogen atoms.[53,54] This is well consistent with the framework of a single-layer B doped g-C<sub>3</sub>N<sub>4</sub>, as shown in Scheme 6.1a. The C 1s (Figure 6.6a) and N 1s (Figure 6.6b) spectra of KCNS show no significant difference with those of BCNS. The two K 2p peaks at 296.1 and 294.4 eV consist of K 2p<sub>1/2</sub> and K 2p<sub>3/2</sub> separately, proving the successful loading of potassium in KCNS.[38,55]

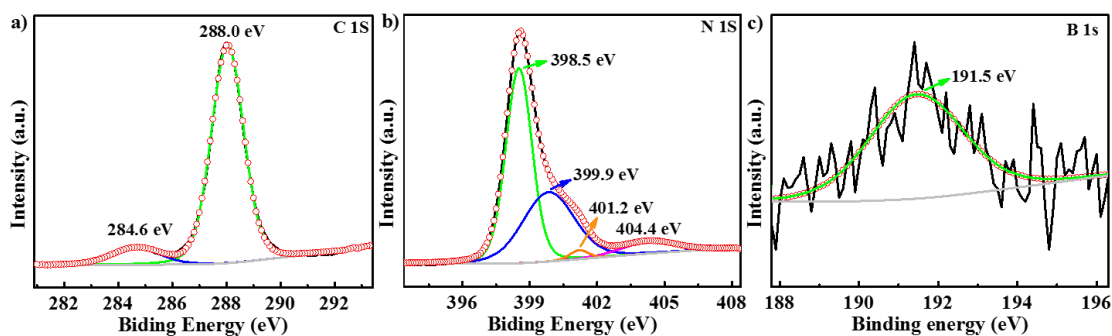


**Figure 6.5** The XPS spectra of BCNS. a) C 1s, b) N 1s, and c) B 1s.

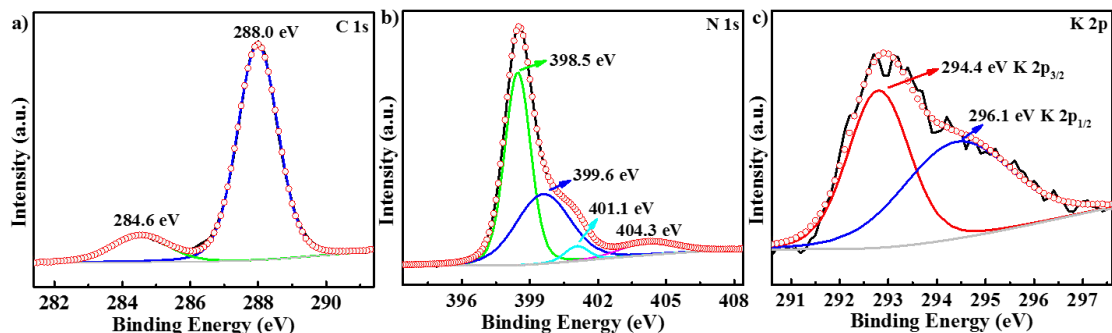


**Figure 6.6** The XPS spectra of KCNS. a) C 1s, b) N 1s, and c) K 2p.

All the above characterizations can demonstrate the successful fabrication of a sequence of g-C<sub>3</sub>N<sub>4</sub> based materials, especially g-C<sub>3</sub>N<sub>4</sub> self-based vdW type II and III junctions.

UV-vis diffuse reflectance spectra were then acquired to investigate the optical properties of the as-fabricated materials. Figure 6.7a, b, and c compare the nanosheets and bulk counterparts, from which it can be found that all the nanosheets have weak UV absorption. Besides, only KCNS has an obvious increase in the range of 450 – 800 nm compared to its bulk counterpart (KCN), which might be because, after thermal exfoliation, more potassium atoms can be exposed on the surface of KCNS. As a metal element, potassium atoms may help improve visible light absorption. The bandgap energies (Figure 6.7 d, e, and f) were then determined from the UV-vis diffuse reflectance data via the Kubelka-Munk equation of  $(\alpha h\nu)^n = k(h\nu - E_g)$  (where  $\alpha$ ,  $\nu$ ,  $k$ , and  $E_g$  stand for the absorption factor, optical frequency, proportionality constant, and bandgap energy, respectively;  $n = 2$  for direct bandgap semiconductors and  $n = 1/2$  for indirect bandgap semiconductors).[56] The widened bandgaps of nanosheets in comparison with bulk counterparts (Figure 6.7 d, e, and f) are consistent with previously reported data.[29,32,50] Figure 6.8 displays that the optical absorption intensity of these materials follows KCN > BCN > CN and

KCNS > BCNS > CNS and their bandgap orders are in an order of KCN (2.50 eV) < BCN (2.52 eV) < CN (2.58 eV) and KCNS (2.52 eV) < BCNS (2.56 eV) < CNS (2.65 eV). Obviously, the bandgap differences are enlarged in the nanosheets materials.

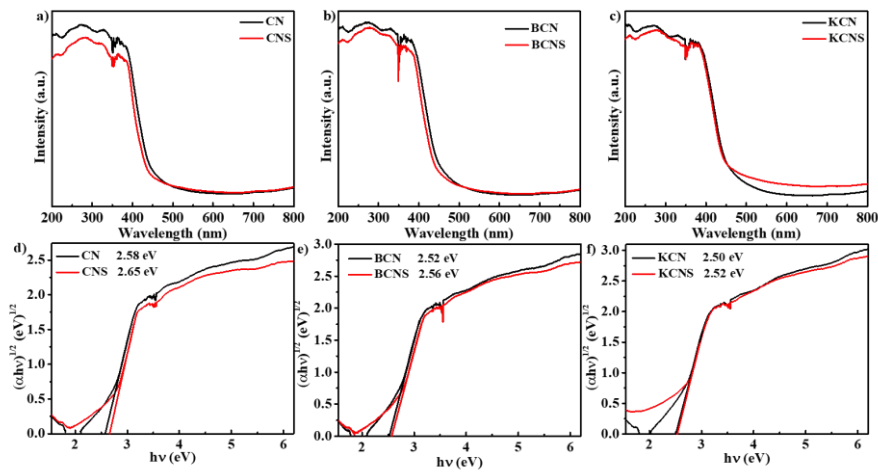


**Figure 6.7** UV-vis diffuse reflectance spectra of bulk materials and nanosheets. **a)** CN vs. CNS, **b)** BCN vs. BCNS, **c)** KCN vs. KCNS. The plots of  $(\alpha hv)^{1/2}$  vs. bandgap energy ( $h\nu$ ) of bulk materials and nanosheets. **d)** CN vs. CNS, **e)** BCN vs. BCNS, **f)** KCN vs. KCNS.

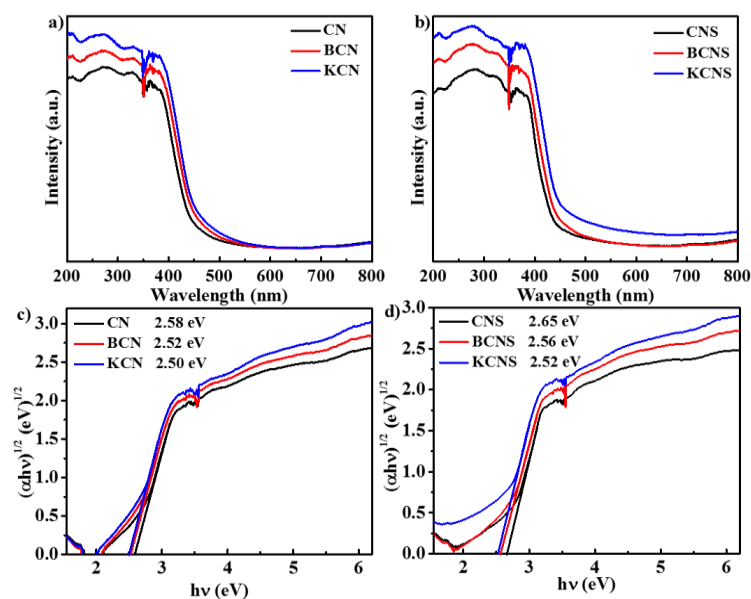


**Figure 6.8** UV-vis diffuse reflectance spectra of heteroatom-doping and non-doping  $g\text{-C}_3\text{N}_4$  based materials of **a)** CN vs. BCN vs. KCN, and **b)** CNS vs. BCNS vs. KCNS; and their corresponding plots of  $(\alpha h\nu)^{1/2}$  vs. bandgap energy ( $h\nu$ ) of **c)** CN vs. BCN vs. KCN, and **d)** CNS vs. BCNS vs. KCNS.

As for vdW type II junctions (Figure 6.9), binary mixtures (Figure 6.10), the vdW type III junction (Figure 6.11a and c), and the ternary mixture (Figure 6.11b and d), their absorption intensity and bandgap energy are among their corresponding nanosheet materials.

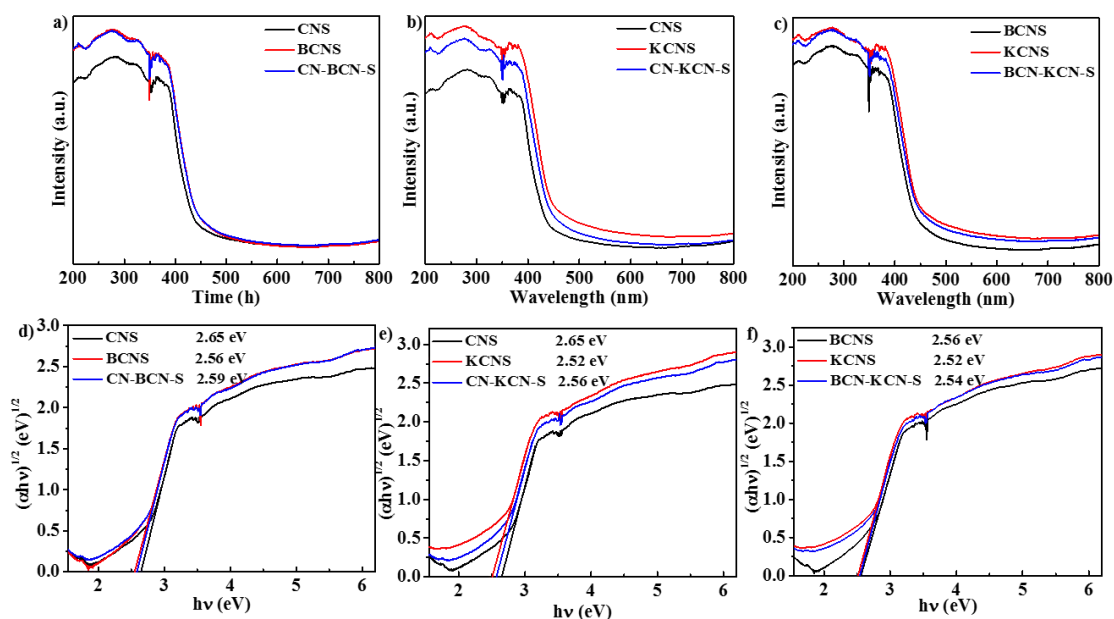


**Figure 6.9** UV-vis diffuse reflectance spectra of the vdW type II and corresponding nanosheet materials of **a)** CNS vs. BCNS vs. CN-BCN-S, **b)** CNS vs. KCNS vs. CN-KCN-S, and **c)** BCNS vs. KCNS vs. BCN-KCN-S; and their matching plots of  $(\alpha h\nu)^{1/2}$  vs. bandgap energy ( $h\nu$ ) of **d)** CNS vs. BCNS vs. CN-BCN-S, **e)** CNS vs. KCNS vs. CN-KCN-S, and **f)** BCNS vs. KCNS vs. BCN-KCN-S.

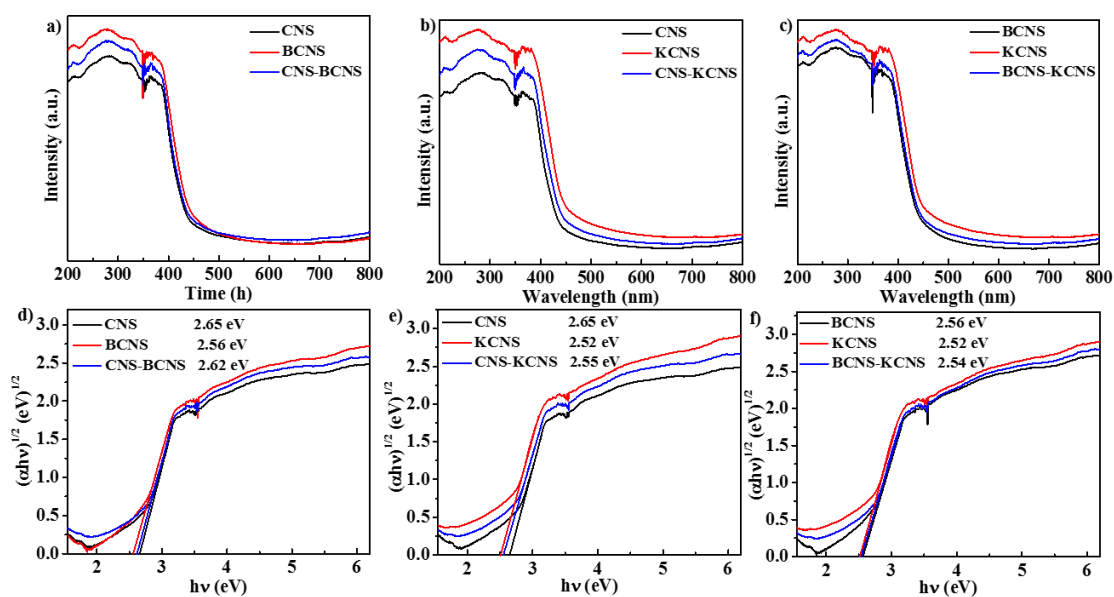


**Figure 6.10** UV-vis diffuse reflectance spectra of the mixture and corresponding nanosheet materials of **a)** CNS vs. BCNS vs. CNS-BCNS, **b)** CNS vs. KCNS vs. CNS-KCNS, and **c)** BCNS vs. KCNS vs. BCNS-KCNS; and their matching plots of  $(\alpha h\nu)^{1/2}$  vs. bandgap energy ( $h\nu$ ) of **d)** CNS vs. BCNS vs. CNS-BCNS, **e)** CNS vs. KCNS vs. CNS-KCNS, and **f)** BCNS vs. KCNS vs. BCNS-KCNS.

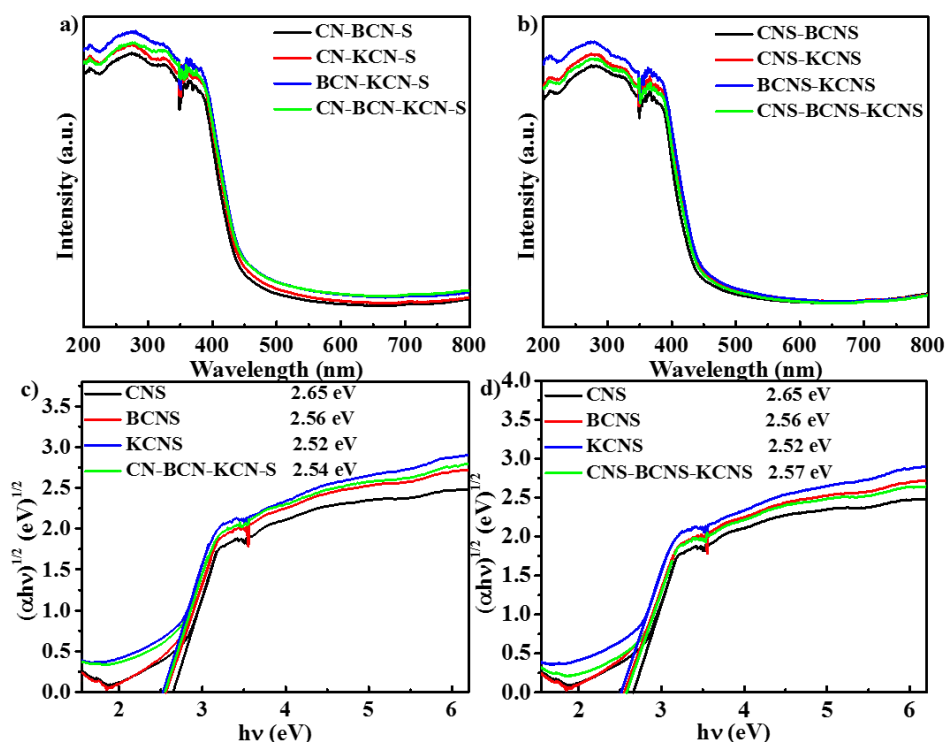


**Figure 6.11** UV-vis diffuse reflectance spectra of the vdW type III, the ternary mixture, and corresponding nanosheet materials of **a)** CNS vs. BCNS vs. KCNS vs. CN-BCN-KCN-S, and **b)** CNS vs. BCNS vs. KCNS vs. CNS-BCNS-KCNS; and their matching plots of  $(\alpha h\nu)^{1/2}$  vs. bandgap energy ( $h\nu$ ) of **c)** CNS vs. BCNS vs. KCNS vs. CN-BCN-KCN-S, and **d)** CNS vs. BCNS vs. KCNS vs. CNS-BCNS-KCNS.

Mott-Schottky (MS) tests were conducted to further determine their band structure. As can be seen from Figure 6.12 – 16, the tangent slopes of all curves are positive, manifesting that all the as-synthesized materials are n-type semiconductors. The intercept of the plot tangent and the X-axis in MS images can reflect the flat band position of the material. For n-type semiconductors, this value can be approximately viewed as the conduction

band (CB) position. Figure 6.12 makes it clear that the CB values of nanosheets are more negative than those of bulk counterparts, which accords well with previous reports. Figure 6.13 shows that the CB order is KCN (-1.04 V vs Ag/AgCl, pH = 6.8) < BCN (-0.93 V) < CN (-0.92 V), and obviously the differences in nanosheets group are more significant, which are KCNS (-1.17 V) < BCNS (-1.03 V) < CNS (-0.95 V). The vdW type II junctions (Figure 6.14) and the binary mixtures (Figure 6.15) have CB positions in between those of their matching nanosheets materials. Figure 6.16 reveals that the vdW type III junction and the ternary mixture also own CB values among those of their corresponding nanosheets semiconductors.

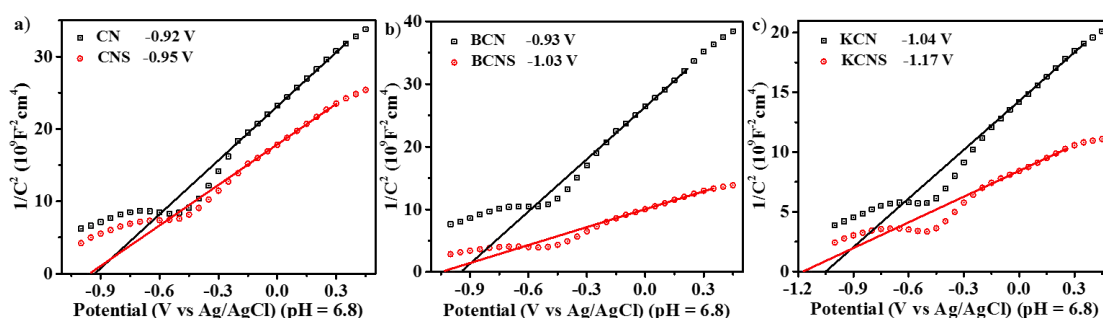


**Figure 6.12** The Mott-Schottky curves of bulk materials and corresponding nanosheets. **a)** CN vs. CNS, **b)** BCN vs. BCNS, **c)** KCN vs. KCNS.

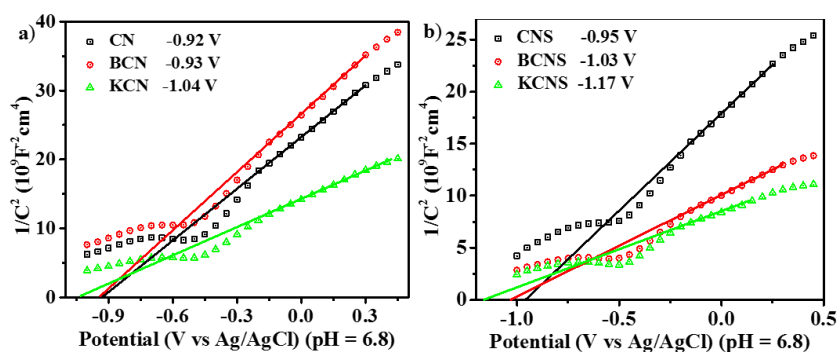


**Figure 6.13** UV-vis diffuse reflectance spectra of heteroatom-doping and non-doping  $g\text{-C}_3\text{N}_4$  based materials of **a)** CN vs. BCN vs. KCN, and **b)** CNS vs. BCNS vs. KCNS.

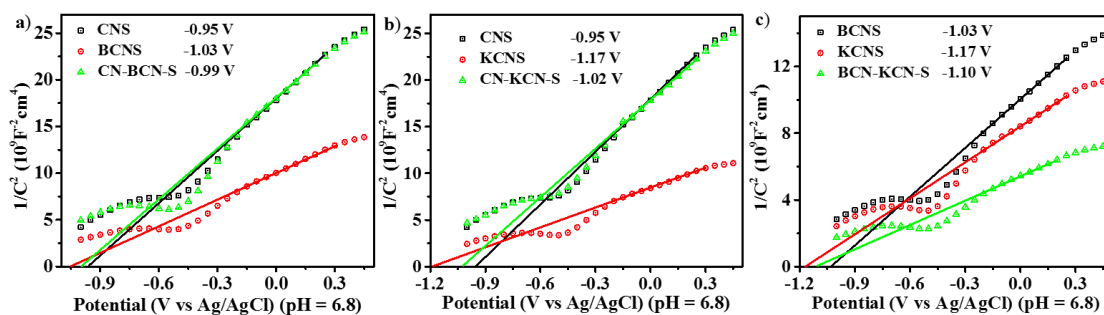


**Figure 6.14** The Mott-Schottky curves of the vdW type II and corresponding nanosheet materials of **a)** CNS vs. BCNS vs. CN-BCN-S, **b)** CNS vs. KCNS vs. CN-KCN-S, and **c)** BCNS vs. KCNS vs. BCN-KCN-S.

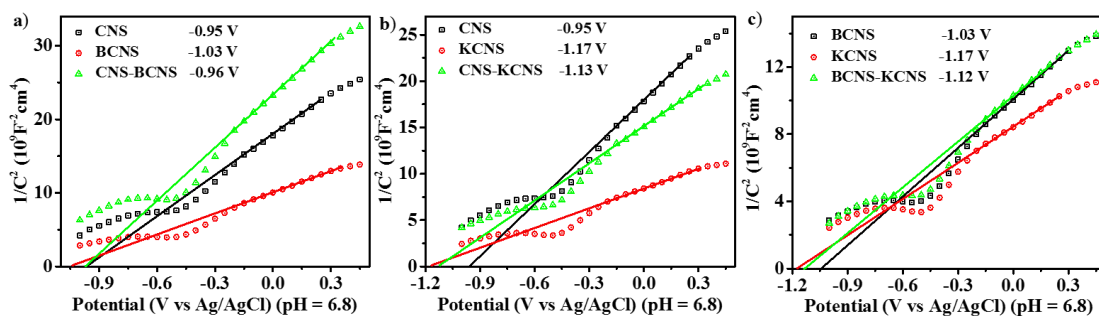


**Figure 6.15** The Mott-Schottky curves of the binary mixture and corresponding nanosheet materials of **a)** CNS vs. BCNS vs. CNS-BCNS, **b)** CNS vs. KCNS vs. CNS-KCNS, and **c)** BCNS vs. KCNS vs. BCNS-KCNS.

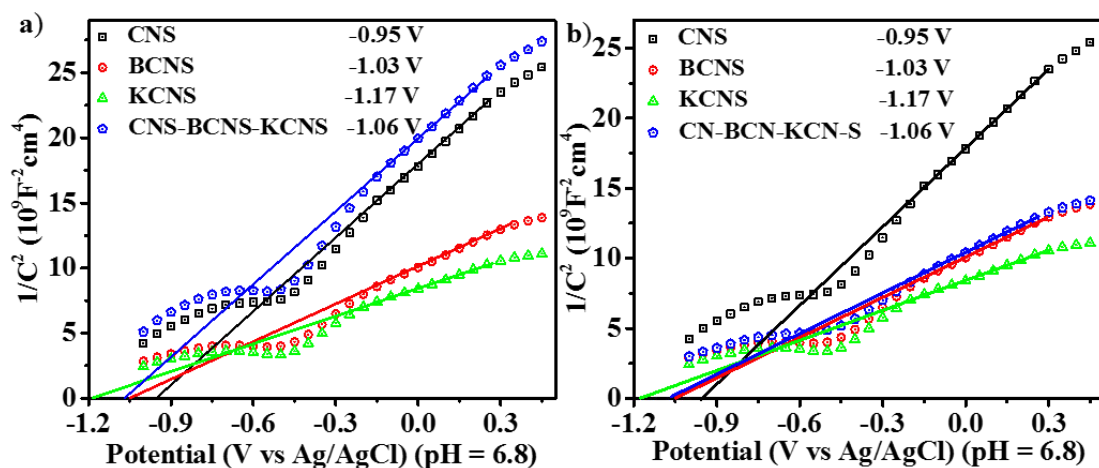


**Figure 6.16** UV-vis diffuse reflectance spectra of the vdW type III, the ternary mixture, and corresponding nanosheet materials of **a)** CNS vs. BCNS vs. KCNS vs. CN-BCN-KCN-S, and **b)** CNS vs. BCNS vs. KCNS vs. CNS-BCNS-KCNS.

Based on the above UV-vis and MS data, the energy band structures of nanosheets and bulk  $g\text{-C}_3\text{N}_4$  based semiconductors are shown in Figure

6.17. The CNS has a widened bandgap compared to CN, with a more negative CB position and more positive VB value (Figure 6.17a). Unlike CNS, BCNS and KCNS have wider bandgap than their bulk counterparts, while their CB and VB values are more negative than those of their matching counterparts. Figure 6.17b clearly shows that, from CNS to BCNS and then to KCNS, the bandgaps are gradually diminishing (2.65, 2.56, and 2.52 eV), and both the CB (-0.95, -1.03, -1.17 V vs Ag/AgCl, pH = 6.8) and VB (1.70, 1.53, 1.35 V vs Ag/AgCl, pH = 6.8) are decreasing step by step. These results fully manifest that perfect type II junctions can be formed between each two of them, and the perfect type III junction can be acquired by their combination. All those data about the energy band frame further confirmed the successful synthesis of those required g-C<sub>3</sub>N<sub>4</sub> based structures.

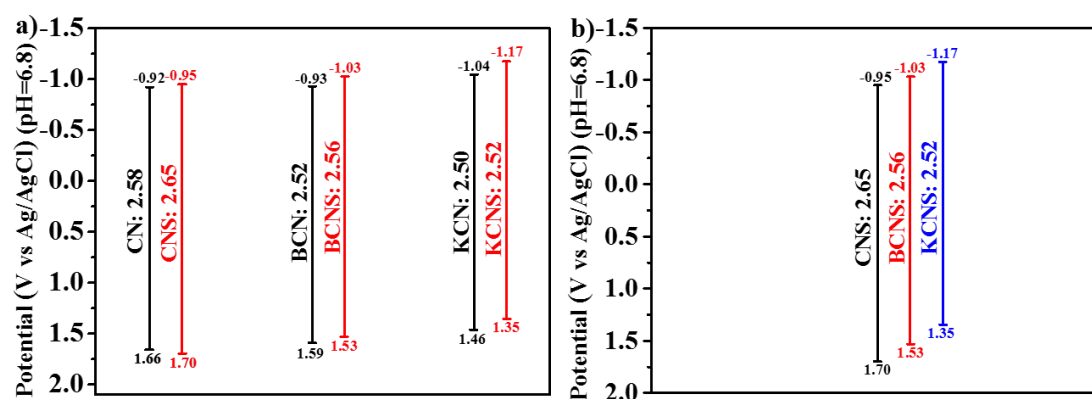


**Figure 6.17** The comparisons of energy band structures. **a)** Nanosheets vs. bulk counterparts. **b)** CNS vs. BCNS vs. KCNS.

PC-HER measurements were then performed to evaluate their activity (Figure 6.18). In the bulk group, we can find that both boron and potassium doping can help improve the PC-HER efficiency of g-C<sub>3</sub>N<sub>4</sub>, which can be mainly owing to the decreased bandgap and increased light absorption of BCN and KCN than those of CN (Figure 6.8). The nanosheet group has a remarkably enhanced PC-HER performance compared to the bulk group; however, their PC-HER rate order is KCNS > CNS > BCNS, which is different from the order of KCN > BCN > CN in the bulk community. This change may be lying in the changes in specific surface area. All the mixtures, including binary mixtures and the ternary mixture of CNS-BCNS-KCNS, have slightly better PC-HER efficiency than that of the nanosheets. This is perhaps because some junctions may also be formed in these mixtures at a lower level, leading to mitigated reintegration of photo-generated electrons and holes. However, no apparent regularity can be found among those mixtures, which may result from their randomly formed minor heterojunctions. The vdW junction group contains three vdW type II junctions and one vdW type III junction. The vdW type II junctions own significantly superior PC-HER rates to all the other g-C<sub>3</sub>N<sub>4</sub> based materials, as shown in Figure 6.18, which is the synergistic effect of enhanced light absorption (heteroatom doping effect), enlarged specific surface area (nanosheet effect), improved charge transfer

(type II junction effect), and the vast interface interaction (vdW junction effect). Among those three vdW type II junctions, CN-KCN-S owns the best PC-HER capacity of  $1243 \mu\text{mol}\cdot\text{h}^{-1}\cdot\text{g}^{-1}$ , 1.1 and 1.3 folds higher than that of CN-BCN-S and BCN-KCN-S, respectively (1.5 times that of CNS and KCNS, and 8.9 folds that of CN). The charge-transfer driving force of CN-KCN-S is more powerful than that of CN-BCN-S and BCN-KCN-S, as displayed in Figure 6.17b. Moreover, we also tried to exploit the same fabrication route to prepare boron and potassium co-doped  $g\text{-C}_3\text{N}_4$  to compare with BCN-KCN-S. However, the trial failed as described in the fabrication of photocatalysts part because the produced potassium metaborate with the boiling point at  $1401^\circ\text{C}$  would protect the urea from being polymerized. This reflects the flexibility of our synthesis approach from another point of view. Most importantly, the PC-HER rates of all three vdW type II junctions unexpectedly surpass that of the vdW type III junction, which might originate from the structure of vdW type III junction. As shown in Scheme 6.2, the transfer of electrons and holes in vdW type III junction can be viewed as two steps. After the first-step charge transfer (photoelectrons transfer from KCNS to BCNS, photo-generated holes transfer from CNS to BCNS), before the second-step charge transfer (photoelectrons transfer from BCNS to CNS, photo-generated holes transfer from BCNS to KCNS), the middle semiconductor (BCNS) can become the recombination center of photo-motivated electrons and holes,

causing the weaker performance of vdW type III junction compared to that of vdW type II junction.

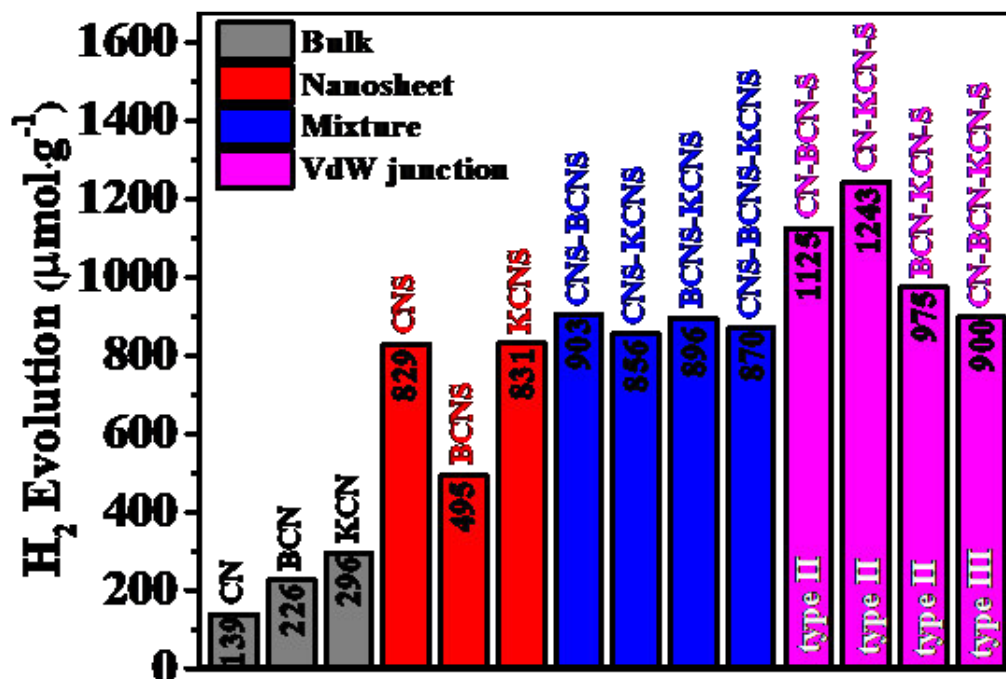
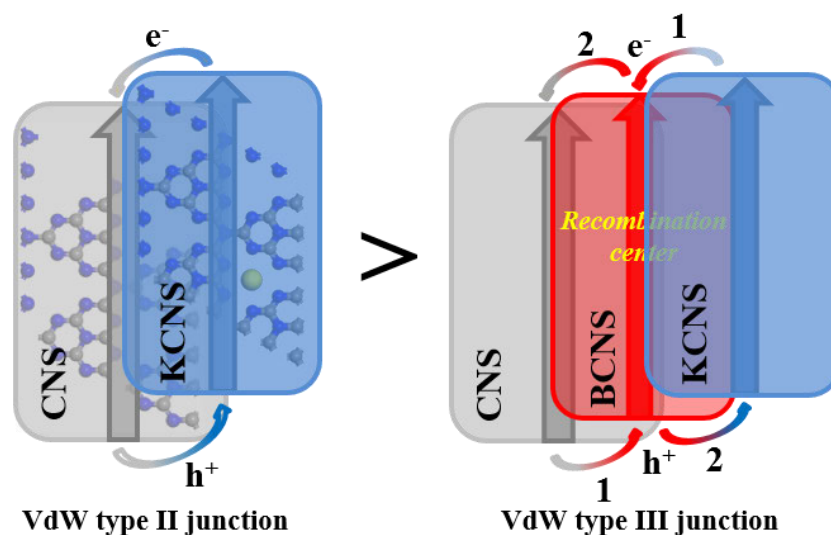
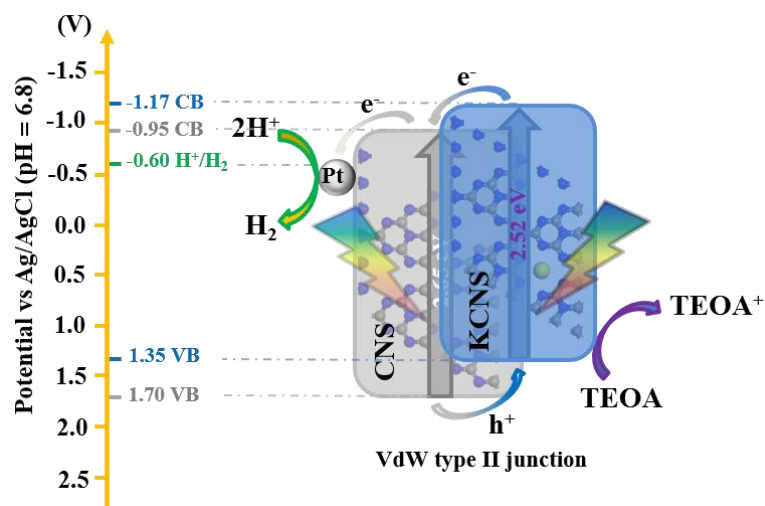


Figure 6.18 The PC-HER performance of all as-fabricated materials.



Scheme 6.2 The proposed mechanisms of the vdW type II junction and the vdW type III junction for the PC-HER process.

A mechanism of CN-KCN-S, the best candidate of the as-prepared vdW type II junctions, was then proposed in Scheme 6.3. Under visible light ( $> 420$  nm), photo-excited electrons were obtained in the CB positions of both CNS and KCNS. The photoelectrons from KCNS were then transferred to the CB of CNS via their vast “face to face” vdW contact and then went to the platinum cocatalyst together with the photoelectrons from the CNS. Afterwards, the hydrogen ions from water reacted with the electrons on platinum nanoparticles, so that hydrogen gas molecules were generated. Simultaneously, the photo-motivated holes from the VB of CNS firstly fell to the CB of KCNS, and were then, along with the photo-holes originating from KCNS, consumed by the sacrificial agent of TEOA. Herein, all the factors, including the cocatalyst, the sacrificial agent, the charge transfer in the type II structure, the shortened bandgap of KCNS than those of CNS, the large specific surface area of the nanosheets, and the vast “face to face” vdW contact, were synergistically contributing to the PC-HER process.



**Scheme 6.3** The proposed mechanism of the vdW type II junction for the PC-HER process.

## 6.4 Conclusion

In conclusion, g-C<sub>3</sub>N<sub>4</sub> self-based vdW type II junctions were prepared through a facile co-thermal-exfoliation method with g-C<sub>3</sub>N<sub>4</sub> and heteroatom doped g-C<sub>3</sub>N<sub>4</sub> as precursors. In the PC-HER processes, the best performance of the CN-KCN-S could be ascribed to the synergistic effects of shortened bandgaps of KCNS than that of CNS, enlarged specific surface area, matched type II energy band structure, and “face to face” vdW charge interaction. What is more, the type II junctions were found superior to the type III junction, and the drawback of the type III junction is that the middle semiconductor could be degenerated to the reintegration centre of photo-generated electron and hole pairs. This study strengthens the cooperative effect of different strategies in enhancing the

PC-HER capacities of g-C<sub>3</sub>N<sub>4</sub>, especially the application of vdW junctions, and discloses some unexpected but reasonable results.

## References

- [1] M. Höök, X. Tang, Depletion of fossil fuels and anthropogenic climate change-A review, *Energy Policy*. 52 (2013) 797–809.
- [2] G. Shaffer, S.M. Olsen, J.O.P. Pedersen, Long-term ocean oxygen depletion in response to carbon dioxide emissions from fossil fuels, *Nat. Geosci.* 2 (2009) 105–109.
- [3] R. York, Do alternative energy sources displace fossil fuels?, *Nat. Clim. Chang.* 2 (2012) 441–443.
- [4] B.M. Besancon, V. Hasanov, R. Imbault-Lastapis, R. Benesch, M. Barrio, M.J. Mørnvik, Hydrogen quality from decarbonized fossil fuels to fuel cells, *Int. J. Hydrogen Energy*. 34 (2009) 2350–2360.
- [5] R. a Berner, Fuels and Atmospheric Composition, *Nature*. 426 (2003) 323–326.
- [6] J. Tollefson, Energy crisis upsets platinum market, *Nature*. 451 (2008) 877.
- [7] R. Dalton, Californian labs feel the heat of energy crisis, *Nature*. 411 (2001) 227.
- [8] M.I. Qureshi, A.M. Rasli, K. Zaman, Energy crisis, greenhouse gas emissions and sectoral growth reforms: Repairing the fabricated

- mosaic, *J. Clean. Prod.* 112 (2016) 3657–3666.
- [9] S.C. Peter, Reduction of CO<sub>2</sub> to Chemicals and Fuels: A Solution to Global Warming and Energy Crisis, *ACS Energy Lett.* 3 (2018) 1557–1561.
- [10] K.W.J. Barnham, M. Mazzer, B. Clive, J. Wiley, S. Limited, Resolving the energy crisis : nuclear or photovoltaics ?, 5 (2006) 161–164.
- [11] Arctic ' greenhouse effect ' Crab hydrostatic, (n.d.) 383.
- [12] H.M. Worden, K.W. Bowman, J.R. Worden, A. Eldering, R. Beer, Satellite measurements of the clear-sky greenhouse effect from tropospheric ozone, *Nat. Geosci.* 1 (2008) 305–308.
- [13] H. Qiao, F. Zheng, H. Jiang, K. Dong, The greenhouse effect of the agriculture-economic growth-renewable energy nexus: Evidence from G20 countries, *Sci. Total Environ.* 671 (2019) 722–731.
- [14] M.J.S. Zuberi, S.F. Ali, Greenhouse effect reduction by recovering energy from waste landfills in Pakistan, *Renew. Sustain. Energy Rev.* 44 (2015) 117–131.
- [15] G. Mamba, A.K. Mishra, Graphitic carbon nitride (g-C<sub>3</sub>N<sub>4</sub>) nanocomposites: A new and exciting generation of visible light driven photocatalysts for environmental pollution remediation, *Appl. Catal. B Environ.* 198 (2016) 347–377.
- [16] X. Ren, C. Chen, M. Nagatsu, X. Wang, Carbon nanotubes as

- adsorbents in environmental pollution management: A review, *Chem. Eng. J.* 170 (2011) 395–410.
- [17] Z. Nasrollahi, M. sadat Hashemi, S. Bameri, V. Mohamad Taghvaei, Environmental pollution, economic growth, population, industrialization, and technology in weak and strong sustainability: using STIRPAT model, *Environ. Dev. Sustain.* 22 (2020) 1105–1122.
- [18] W. Wang, T. An, G. Li, D. Xia, H. Zhao, J.C. Yu, P.K. Wong, Earth-abundant Ni<sub>2</sub>P/g-C<sub>3</sub>N<sub>4</sub> lamellar nanohybrids for enhanced photocatalytic hydrogen evolution and bacterial inactivation under visible light irradiation, *Appl. Catal. B Environ.* 217 (2017) 570–580.
- [19] J. Li, B. Shen, Z. Hong, B. Lin, B. Gao, Y. Chen, A facile approach to synthesize novel oxygen-doped g-C<sub>3</sub>N<sub>4</sub> with superior visible-light photoreactivity, *Chem. Commun.* 48 (2012) 12017–12019.
- [20] D. Zeng, T. Zhou, W.J. Ong, M. Wu, X. Duan, W. Xu, Y. Chen, Y.A. Zhu, D.L. Peng, Sub-5 nm Ultra-Fine FeP Nanodots as Efficient Co-Catalysts Modified Porous g-C<sub>3</sub>N<sub>4</sub> for Precious-Metal-Free Photocatalytic Hydrogen Evolution under Visible Light, *ACS Appl. Mater. Interfaces.* (2019).
- [21] N. Wang, J. Wang, J. Hu, X. Lu, J. Sun, F. Shi, Z.H. Liu, Z. Lei, R. Jiang, Design of Palladium-Doped g-C<sub>3</sub>N<sub>4</sub> for Enhanced

- Photocatalytic Activity toward Hydrogen Evolution Reaction, *ACS Appl. Energy Mater.* 1 (2018) 2866–2873.
- [22] J. Ran, W. Guo, H. Wang, B. Zhu, J. Yu, S.Z. Qiao, Metal-Free 2D/2D Phosphorene/g-C<sub>3</sub>N<sub>4</sub> Van der Waals Heterojunction for Highly Enhanced Visible-Light Photocatalytic H<sub>2</sub> Production, *Adv. Mater.* 30 (2018).
- [23] X. Wang, M. Kazuhiko, T. Arne, T. Kazuhiro, X. Gang, C.J. M., D. Kazunari, A. Markus, A metal-free polymeric photocatalyst for hydrogen production from water under visible light, *Nat. Mater.* 8 (2009) 76–80.
- [24] Z. Huang, J. Song, L. Pan, Z. Wang, Carbon nitride with simultaneous porous network and O-doping for efficient solar-energy-driven hydrogen evolution, *Nano Energy.* 12 (2015) 646–656.
- [25] S. Cao, H. Li, T. Tong, H.C. Chen, A. Yu, J. Yu, H.M. Chen, Single-Atom Engineering of Directional Charge Transfer Channels and Active Sites for Photocatalytic Hydrogen Evolution, *Adv. Funct. Mater.* 28 (2018) 1–9.
- [26] Y. Lu, D. Chu, M. Zhu, Y. Du, P. Yang, Exfoliated carbon nitride nanosheets decorated with NiS as an efficient noble-metal-free visible-light-driven photocatalyst for hydrogen evolution, *Phys. Chem. Chem. Phys.* 17 (2015) 17355–17361.

- [27] Y.S. Jun, E.Z. Lee, X. Wang, W.H. Hong, G.D. Stucky, A. Thomas, From melamine-cyanuric acid supramolecular aggregates to carbon nitride hollow spheres, *Adv. Funct. Mater.* 23 (2013) 3661–3667.
- [28] S.S. Shinde, A. Sami, J.H. Lee, Sulfur mediated graphitic carbon nitride/S-Se-graphene as a metal-free hybrid photocatalyst for pollutant degradation and water splitting, *Carbon N. Y.* 96 (2016) 929–936.
- [29] S. Yang, Y. Gong, J. Zhang, L. Zhan, L. Ma, Z. Fang, R. Vajtai, X. Wang, P.M. Ajayan, Exfoliated graphitic carbon nitride nanosheets as efficient catalysts for hydrogen evolution under visible light, *Adv. Mater.* 25 (2013) 2452–2456.
- [30] K. Schwinghammer, M.B. Mesch, V. Duppel, C. Ziegler, J. Senker, B. V. Lotsch, Crystalline carbon nitride nanosheets for improved visible-light hydrogen evolution, *J. Am. Chem. Soc.* 136 (2014) 1730–1733.
- [31] Z. Fang, Y. Hong, D. Li, B. Luo, B. Mao, W. Shi, One-Step Nickel Foam Assisted Synthesis of Holey G - Carbon Nitride Nanosheets for Efficient Visible-Light Photocatalytic H<sub>2</sub> Evolution, (2018).
- [32] Q. Han, F. Zhao, C. Hu, L. Lv, Z. Zhang, N. Chen, L. Qu, Facile production of ultrathin graphitic carbon nitride nanoplatelets for efficient visible-light water splitting, 8 (2015) 1718–1728.
- [33] Y. Zhang, T. Mori, J. Ye, M. Antonietti, P doped g-C<sub>3</sub>N<sub>4</sub>(*J. AM.*

CHEM. SOC. 2010, 132, 6294–6295).pdf, (2010) 6294–6295.

- [34] J.W. Zhang, S. Gong, N. Mahmood, L. Pan, X. Zhang, J.J. Zou, Oxygen-doped nanoporous carbon nitride via water-based homogeneous supramolecular assembly for photocatalytic hydrogen evolution, *Appl. Catal. B Environ.* 221 (2018) 9–16.
- [35] L.J. Fang, X.L. Wang, J.J. Zhao, Y.H. Li, Y.L. Wang, X.L. Du, Z.F. He, H.D. Zeng, H.G. Yang, One-step fabrication of porous oxygen-doped g-C<sub>3</sub>N<sub>4</sub> with feeble nitrogen vacancies for enhanced photocatalytic performance, *Chem. Commun.* 52 (2016) 14408–14411.
- [36] L.K.B. Paragas, M.D.G. de Luna, R.A. Doong, Rapid removal of sulfamethoxazole from simulated water matrix by visible-light responsive iodine and potassium co-doped graphitic carbon nitride photocatalysts, *Chemosphere.* 210 (2018) 1099–1107.
- [37] P. Chen, P. Xing, Z. Chen, H. Lin, Y. He, Rapid and energy-efficient preparation of boron doped g-C<sub>3</sub>N<sub>4</sub> with excellent performance in photocatalytic H<sub>2</sub>-evolution, *Int. J. Hydrogen Energy.* 43 (2018) 19984–19989.
- [38] Y. Wang, S. Zhao, Y. Zhang, J. Fang, Y. Zhou, S. Yuan, C. Zhang, W. Chen, One-pot synthesis of K-doped g-C<sub>3</sub>N<sub>4</sub> nanosheets with enhanced photocatalytic hydrogen production under visible-light irradiation, *Appl. Surf. Sci.* 440 (2018) 258–265.

- [39] L. Zhang, Z. Jin, S. Huang, X. Huang, B. Xu, L. Hu, H. Cui, S. Ruan, Y.J. Zeng, Bio-inspired carbon doped graphitic carbon nitride with booming photocatalytic hydrogen evolution, *Appl. Catal. B Environ.* 246 (2019) 61–71.
- [40] Y. Zhou, L. Zhang, J. Liu, X. Fan, B. Wang, M. Wang, W. Ren, J. Wang, M. Li, J. Shi, Brand new P-doped g-C<sub>3</sub>N<sub>4</sub>: Enhanced photocatalytic activity for H<sub>2</sub> evolution and Rhodamine B degradation under visible light, *J. Mater. Chem. A.* 3 (2015) 3862–3867.
- [41] C. Cheng, S. Zong, J. Shi, F. Xue, Y. Zhang, X. Guan, B. Zheng, J. Deng, L. Guo, Facile preparation of nanosized MoP as cocatalyst coupled with g-C<sub>3</sub>N<sub>4</sub> by surface bonding state for enhanced photocatalytic hydrogen production, *Appl. Catal. B Environ.* 265 (2020) 118620.
- [42] Y. Zhu, Y. Xu, Y. Hou, Z. Ding, X. Wang, Cobalt sulfide modified graphitic carbon nitride semiconductor for solar hydrogen production, *Int. J. Hydrogen Energy.* 39 (2014) 11873–11879.
- [43] J. Hong, Y. Wang, Y. Wang, W. Zhang, R. Xu, Noble-metal-free NiS/C<sub>3</sub>N<sub>4</sub> for efficient photocatalytic hydrogen evolution from water, *ChemSusChem.* 6 (2013) 2263–2268.
- [44] J. Ran, W. Guo, H. Wang, B. Zhu, J. Yu, S.Z. Qiao, Metal-Free 2D/2D Phosphorene/g-C<sub>3</sub>N<sub>4</sub> Van der Waals Heterojunction for

- Highly Enhanced Visible-Light Photocatalytic H<sub>2</sub> Production, *Adv. Mater.* 30 (2018) 2–7.
- [45] H. Li, H. Tian, X. Wang, M. Pi, S. Wei, H. Zhu, D. Zhang, S. Chen, Self-Coupled g-C<sub>3</sub>N<sub>4</sub> van der Waals Heterojunctions for Enhanced Photocatalytic Hydrogen Production, *ACS Appl. Energy Mater.* 2 (2019) 4692–4699.
- [46] M. Wu, J.M. Yan, X.W. Zhang, M. Zhao, Q. Jiang, Ag<sub>2</sub>O modified g-C<sub>3</sub>N<sub>4</sub> for highly efficient photocatalytic hydrogen generation under visible light irradiation, *J. Mater. Chem. A.* 3 (2015) 15710–15714.
- [47] L. Yang, J. Liu, L. Yang, M. Zhang, H. Zhu, F. Wang, J. Yin, Co<sub>3</sub>O<sub>4</sub> imbedded g-C<sub>3</sub>N<sub>4</sub> heterojunction photocatalysts for visible-light-driven hydrogen evolution, *Renew. Energy.* 145 (2020) 691–698.
- [48] H. Xu, J. Yi, X. She, Q. Liu, L. Song, S. Chen, Y. Yang, Y. Song, R. Vajtai, J. Lou, H. Li, S. Yuan, J. Wu, P.M. Ajayan, 2D heterostructure comprised of metallic 1T-MoS<sub>2</sub>/Monolayer O-g-C<sub>3</sub>N<sub>4</sub> towards efficient photocatalytic hydrogen evolution, *Appl. Catal. B Environ.* 220 (2018) 379–385.
- [49] Y. Wang, X. Wang, M. Antonietti, Polymeric graphitic carbon nitride as a heterogeneous organocatalyst: From photochemistry to multipurpose catalysis to sustainable chemistry, *Angew. Chemie - Int. Ed.* 51 (2012) 68–89.

- [50] L. Ma, H. Fan, J. Wang, Y. Zhao, H. Tian, G. Dong, *Applied Catalysis B : Environmental* Water-assisted ions in situ intercalation for porous polymeric graphitic carbon nitride nanosheets with superior photocatalytic hydrogen evolution performance, “*Applied Catal. B, Environ.* 190 (2016) 93–102.
- [51] J. Liu, Q. Jia, J. Long, X. Wang, Z. Gao, Q. Gu, Amorphous NiO as cocatalyst for enhanced visible-light-driven hydrogen generation over g-C<sub>3</sub>N<sub>4</sub> photocatalyst, *Appl. Catal. B Environ.* 222 (2018) 35–43.
- [52] A. Suryawanshi, P. Dhanasekaran, D. Mhamane, S. Kelkar, S. Patil, N. Gupta, S. Ogale, Doubling of photocatalytic H<sub>2</sub> evolution from g-C<sub>3</sub>N<sub>4</sub> via its nanocomposite formation with multiwall carbon nanotubes: Electronic and morphological effects, *Int. J. Hydrogen Energy.* 37 (2012) 9584–9589.
- [53] S. Thaweesak, S. Wang, M. Lyu, M. Xiao, P. Peerakiatkhajohn, L. Wang, Boron-doped graphitic carbon nitride nanosheets for enhanced visible light photocatalytic water splitting, *Dalt. Trans.* 46 (2017) 10714–10720.
- [54] N. Sagara, S. Kamimura, T. Tsubota, T. Ohno, Photoelectrochemical CO<sub>2</sub> reduction by a p-type boron-doped g-C<sub>3</sub>N<sub>4</sub> electrode under visible light, *Appl. Catal. B Environ.* 192 (2016) 193–198.

- [55] M. Zhang, X. Bai, D. Liu, J. Wang, Y. Zhu, Enhanced catalytic activity of potassium-doped graphitic carbon nitride induced by lower valence position, *Appl. Catal. B Environ.* 164 (2015) 77–81.
- [56] Y. Liu, H. Zhang, J. Ke, J. Zhang, W. Tian, X. Xu, X. Duan, H. Sun, M. O Tade, S. Wang, 0D (MoS<sub>2</sub>)/2D (g-C<sub>3</sub>N<sub>4</sub>) heterojunctions in Z-scheme for enhanced photocatalytic and electrochemical hydrogen evolution, *Appl. Catal. B Environ.* 228 (2018) 64–74.

*Every reasonable effort has been made to acknowledge the owners of copyright material. I would be pleased to hear from any copyright owner who has been omitted or incorrectly acknowledged.*

## Chapter 7 Conclusions and perspectives

### 7.1 Conclusions

In this thesis, the solar-heat-based temperature factor was investigated for PC-HER using different nanomaterials as photocatalysts. Meanwhile, novel g-C<sub>3</sub>N<sub>4</sub> based nanostructures, including NiO quantum dots decorated g-C<sub>3</sub>N<sub>4</sub>, single-atom Ag modified g-C<sub>3</sub>N<sub>4</sub>, and K doped g-C<sub>3</sub>N<sub>4</sub>/g-C<sub>3</sub>N<sub>4</sub> van der Waals type II junction, were developed and applied in the PC-HER processes. Various characterization techniques combined with density functional theory (DFT) calculations were utilized to explore the structures and properties of these composites. The loading amounts, substance ratios, and reaction temperatures were optimized to maximize the PC-HER efficiency. The electrochemical tests and photoluminescence experiments were taken to probe the inner mechanisms of the enhanced PC-HER performance of these materials. This PhD study not only helps broaden the sources of photocatalysts for PC-HER but also assists in better understanding the PC-HER process of g-C<sub>3</sub>N<sub>4</sub> based nanomaterials from varying aspects.

Through the comprehensive studies, some important conclusions can be made as below.

### 7.1.1 Literature review

- ❖ Since Wang et al. firstly applied g-C<sub>3</sub>N<sub>4</sub> in PC-HER in 2009, a lot of g-C<sub>3</sub>N<sub>4</sub> based materials, including g-C<sub>3</sub>N<sub>4</sub> nanosheets, nanotubes, nanobelts, nanospheres, quantum dots, porous g-C<sub>3</sub>N<sub>4</sub>, crystalline g-C<sub>3</sub>N<sub>4</sub>, doped g-C<sub>3</sub>N<sub>4</sub>, g-C<sub>3</sub>N<sub>4</sub> based Schottky junctions, type II junctions, Z-scheme junctions, PN junctions, and van der Waals junctions, have been developed to advance the reactivity of g-C<sub>3</sub>N<sub>4</sub>.
- ❖ The well-designed g-C<sub>3</sub>N<sub>4</sub> based photocatalysts acquiring their enhanced PC-HER performance contain increasing porosity, enlarging the specific surface area, improving the quantity and quality of active sites, shortening the bandgap, broadening the photoabsorption, adjusting the energy band, strengthening the crystallinity, lowering the electrical impedance, and inhibiting the reintegration of the photogenerated electrons and holes.
- ❖ Cocatalysts and sacrificial agents are also playing significant roles in the g-C<sub>3</sub>N<sub>4</sub> based PC-HER processes. While cocatalysts can transfer photoelectrons from g-C<sub>3</sub>N<sub>4</sub> to attached protons, sacrificial agents can effectively consume the photogenerated holes on the surface of g-C<sub>3</sub>N<sub>4</sub>. Both of them can upgrade the PC-HER rate by several or even thousands of folds.
- ❖ Other factors, like the temperature of reaction solution, the amount of

photocatalysts, and light sources, can also influence the PC-HER results.

### **7.1.2 Solar-heat temperature effect on photocatalytic hydrogen evolution**

- ❖ Pristine TiO<sub>2</sub> P25 and g-C<sub>3</sub>N<sub>4</sub> have increased PC-HER performances when the temperature is increased.
- ❖ Pt nanoparticles decorated TiO<sub>2</sub> P25 and g-C<sub>3</sub>N<sub>4</sub> own an unstable or even decreased PC-HER efficiency with the temperature rising.
- ❖ Pt nanoparticles modified g-C<sub>3</sub>N<sub>4</sub> has an enhanced PC-HER performance from 25 to 65 °C under visible light irradiations.
- ❖ The lowered electrical impedance, shortened bandgap, and increased light absorption with temperature are positive factors for those photocatalysts in temperature-based PC-HER processes.
- ❖ The conduction bands and valence bands become more negative at escalated temperatures.
- ❖ The agglomeration of Pt nanoparticles can be a significantly negative factor to the PC-HER performance at a higher temperature.
- ❖ UV light can aggravate the thermal agglomeration of Pt nanoparticles.

### **7.1.3 Synergy of NiO quantum dots and temperature on enhanced**

## **photocatalytic and thermophoto hydrogen evolution**

- ❖ C-O single bond can be formed between g-C<sub>3</sub>N<sub>4</sub> and NiO quantum dots under illuminations.
- ❖ The enhanced photocatalytic hydrogen evolution is mainly attributed to the lowered overpotential barriers and improved electrical conductivity, which are profoundly originated from the emerging C-O bond and the quantum size effect of NiO quantum dots.
- ❖ The improved absorption and narrowed bandgap of NiO quantum dots modified g-C<sub>3</sub>N<sub>4</sub> also contribute to the enhanced photocatalytic performances.
- ❖ Enhanced thermophoto catalytic hydrogen evolution can be ascribed to the significantly increased electrical conductivity of NiO quantum dots decorated g-C<sub>3</sub>N<sub>4</sub>, originating from the apparently reduced resistance of NiO.

### **7.1.4 Solar-heat-assisted single-atom catalysis for photocatalytic hydrogen evolution**

- ❖ Single-atom Ag modified g-C<sub>3</sub>N<sub>4</sub> (SAAg-g-CN) was successfully synthesized via a facile two-step pyrolysis method and utilized in photocatalytic hydrogen evolution processes with outstanding

performances.

- ❖ The upgraded  $\Delta G_{H^*}$  of No. 40 and 52 nitrogen atoms of SAAG-g-CN derived from the individual structure endows the catalyst abundant active sites, shortened electron transfer paths, and the ease for  $H_2$  desorption, therefore promoting the photocatalytic hydrogen evolution (PC-HER) processes.
- ❖ The unique structure of SAAG-g-CN overshadows the weakness of metal-nanoparticle-based cocatalysts, i.e. the growth and agglomeration with temperature. It endows the material a prominent performance in solar-heat-assisted PC-HER.

### **7.1.5 g-C<sub>3</sub>N<sub>4</sub> self-based van der Waals type II junctions for photocatalytic hydrogen evolution**

- ❖ g-C<sub>3</sub>N<sub>4</sub> self-based van der Waals (vdW) type II and type III junctions were designed and prepared through a facile co-thermal-exfoliation method using g-C<sub>3</sub>N<sub>4</sub> and heteroatom doped g-C<sub>3</sub>N<sub>4</sub> as precursors.
- ❖ In the PC-HER processes, the best material of g-C<sub>3</sub>N<sub>4</sub>/K doped g-C<sub>3</sub>N<sub>4</sub> nanosheet (CN-KCN-S) based vdW type II junction possessed synergistic effects of shortened bandgaps of KCNS than that of CNS, the enlarged specific surface area, the matched type II energy band structure, and the “face to face” vdW charge interaction.

- ❖ The type II junctions were found superior to the type III junction, which originated from the drawbacks of the type III junction that the middle semiconductor could be degenerated to the reintegration centre of photogenerated electrons and holes.

## 7.2 Perspectives

In the process of photocatalytic hydrogen evolution, many factors need to be carefully considered and optimized.

From the beginning point, the increased reaction temperature caused by solar heat (infrared light), whether all photocatalysts share a similar trend at different temperatures should be further explored. How to incorporate and utilize the infrared light to the photocatalytic operations is still one of the grand challenges for practical industrialization of PC-HER, which requires more investigations.

In terms of new photocatalysts for enhancing the PC-HER efficiency of g-C<sub>3</sub>N<sub>4</sub> based materials, rational design may consider the combination of following directions. As summarized in Chapter 2 of this thesis, currently there are abundant g-C<sub>3</sub>N<sub>4</sub> based materials, including g-C<sub>3</sub>N<sub>4</sub> nanosheets, nanotubes, nanobelts, nanospheres, quantum dots, porous g-C<sub>3</sub>N<sub>4</sub>, crystalline g-C<sub>3</sub>N<sub>4</sub>, doped g-C<sub>3</sub>N<sub>4</sub>, g-C<sub>3</sub>N<sub>4</sub> based Schottky junctions, type

II junctions, Z-scheme junctions, PN junctions, and van der Waals junctions. Their proper combination and alignment can be enormous and provide more creative and prominent composite photocatalysts.

As to the cocatalysts for g-C<sub>3</sub>N<sub>4</sub> based PC-HER processes, more earth-abundant materials are needed to be studied to substitute the noble-metal based cocatalysts. For example, plenty of two-dimensional materials are developed and reported to be potential candidates for the cocatalysts of PC-HER in recent years. More investigations should be devoted to this area.

When discussing the sacrificial agents for PC-HER, we should keep in mind that there is a precise correlation between photocatalysts and sacrificial agents. For example, ethylene glycol can make the PC-HER performance of TiO<sub>2</sub> to increase several levels. Triethanolamine is most suitable for g-C<sub>3</sub>N<sub>4</sub> and can help protect g-C<sub>3</sub>N<sub>4</sub> from photo-corrosion. In my opinion, perhaps some other chemicals or even waste can better play this role for g-C<sub>3</sub>N<sub>4</sub>. That is urea or human urine, because of the structure proximity of g-C<sub>3</sub>N<sub>4</sub> and urea.

To deeply explore the mechanism of g-C<sub>3</sub>N<sub>4</sub> based materials for photocatalytic hydrogen evolution, we should also make many efforts on

this reaction from the atomic level or the point of electronic orbitals.

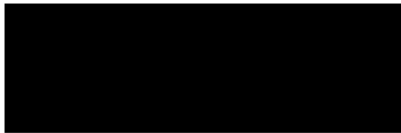
Lastly, for the industrialization of PC-HER, more practical parameters should be taken into account. For instance, we must find an appropriate site for the establishment of a photocatalytic factory. Perhaps, Perth in Western Australia may provide such an ideal location, because both average 8 h sunshine throughout the year and the strong UV light make it the best location for capturing solar energy. Besides, it is quite a beautiful and environmentally friendly place, which fits the theme of environmental protection and clean energy of photocatalytic hydrogen evolution.

## APPENDIX I: ATTRIBUTION TABLES

**A. Xiaojie Li**, Huayang Zhang, Yazhi Liu, Xiaoguang Duan, Xinyuan Xu, Shaomin Liu, Hongqi Sun, Shaobin Wang. Synergy of NiO quantum dots and temperature on enhanced photocatalytic and thermophoto hydrogen evolution. *Chemical Engineering Journal*, 2020, 390, 124634.

Authors and full affiliations:

	Conception and design	Experiments conduction & data acquisition	Data processing & analysis	Interpretation & discussion	Manuscript writing, revision and finalisation	Final Approval
Huayang Zhang		×		×		
I acknowledge that these represent my contribution to the above research output. Sign: 						
Yazhi Liu				×		
I acknowledge that these represent my contribution to the above research output. Sign: 						
Xiaoguang Duan				×		

I acknowledge that these represent my contribution to the above research output.						
Sign:						
						
Xinyuan Xu		×				
I acknowledge that these represent my contribution to the above research output.						
Sign:						
						
Shaomin Liu				×		
I acknowledge that these represent my contribution to the above research output.						
Sign:						
						
Hongqi Sun				×	×	
I acknowledge that these represent my contribution to the above research output.						
Sign:						
						
Shaobin Wang				×	×	

I acknowledge that these represent my contribution to the above research output.

Sign:



Contribution Statement:

To Whom It May Concern,

I, Xiaojie Li, contributed research idea, conception design, experimental methods, experiment conduction, data acquisition, data processing, data analysis, data interpretation, manuscript writing and revision to the paper/publication entitled “Synergy of NiO quantum dots and temperature on enhanced photocatalytic and thermophoto hydrogen evolution”.

Sign:



I, as a Co-Author, endorse that this level of contribution by the candidate indicated above is appropriate.

Huayang Zhang

Sign:



Yazi Liu

Sign:



Xiaoguang Duan

Sign:



Xinyuan Xu

Sign:



Shaomin Liu

Sign:



Hongqi Sun

Sign:



Shaobin Wang

Sign:



## APPENDIX II: COPYRIGHT PERMISSION STATEMENTS



### Royal Society of Chemistry - License Terms and Conditions

This is a License Agreement between Xiaojie Li / Curtin University ("You") and Royal Society of Chemistry ("Publisher") provided by Copyright Clearance Center ("CCC"). The license consists of your order details, the terms and conditions provided by Royal Society of Chemistry, and the CCC terms and conditions.

All payments must be made in full to CCC.

Order Date	07-Jul-2020	Type of Use	Republish in a thesis/dissertation
Order license ID	1046653-1	Publisher	ROYAL SOCIETY OF CHEMISTRY
ISSN	1460-4744	Portion	Chart/graph/table/figure

#### LICENSED CONTENT

Publication Title	Chemical Society reviews	Country	United Kingdom of Great Britain and Northern Ireland
Author/Editor	Royal Society of Chemistry (Great Britain)	Rightholder	Royal Society of Chemistry
Date	01/01/1972	Publication Type	e-Journal
Language	English	URL	http://www.rsc.org/csr

#### REQUEST DETAILS

Portion Type	Chart/graph/table/figure	Distribution	Worldwide
Number of charts / graphs / tables / figures requested	1	Translation	Original language of publication
Format (select all that apply)	Print, Electronic	Copies for the disabled?	No
Who will republish the content?	Academic institution	Minor editing privileges?	No
Duration of Use	Life of current edition	Incidental promotional use?	No
Lifetime Unit Quantity	Up to 9,999	Currency	AUD
Rights Requested	Main product		

#### NEW WORK DETAILS

Title	Photochemical and Thermal Energy Transformation for Hydrogen Generation	Institution name	Curtin University
Instructor name	Xiaojie Li	Expected presentation date	2020-07-15

#### ADDITIONAL DETAILS

Order reference number	N/A	The requesting person / organization to appear on the license	Xiaojie Li / Curtin University
------------------------	-----	---	--------------------------------

#### REUSE CONTENT DETAILS

Title, description or numeric reference of the portion(s)	Photochemical and Thermal Energy Transformation for Hydrogen Generation	Title of the article/chapter the portion is from	Heterogeneous photocatalyst materials for water splitting
Editor of portion(s)	N/A	Author of portion(s)	Royal Society of Chemistry (Great Britain)
Volume of serial or monograph	N/A	Issue, if republishing an article from a serial	N/A
Page or page range of portion	1-7	Publication date of portion	2008-11-18

Granted permission from ref [16] for the reprinted **Figure 1.1**. Copyright (2008) Royal Society of Chemistry.

## A metal-free polymeric photocatalyst for hydrogen production from water under visible light

SPRINGER NATURE

Author: Xinchun Wang et al  
 Publication: Nature Materials  
 Publisher: Springer Nature  
 Date: Nov 9, 2008

Copyright © 2008, Springer Nature

## Order Completed

Thank you for your order.

This Agreement between Xiaojie Li ("You") and Springer Nature ("Springer Nature") consists of your license details and the terms and conditions provided by Springer Nature and Copyright Clearance Center.

Your confirmation email will contain your order number for future reference.

License Number 4863481246497

[Printable Details](#)

License date Jul 07, 2020

## Licensed Content

Licensed Content Publisher Springer Nature  
 Licensed Content Publication Nature Materials  
 Licensed Content Title A metal-free polymeric photocatalyst for hydrogen production from water under visible light  
 Licensed Content Author Xinchun Wang et al  
 Licensed Content Date Nov 9, 2008

## Order Details

Type of Use Thesis/Dissertation  
 Requestor type academic/university or research institute  
 Format print and electronic  
 Portion figures/tables/illustrations  
 Number of figures/tables/illustrations 1  
 High-res required no  
 Will you be translating? no  
 Circulation/distribution 1 - 29  
 Author of this Springer Nature content no

## About Your Work

Title Photochemical and Thermal Energy Transformation for Hydrogen Generation  
 Institution name Curtin University  
 Expected presentation date Jul 2020

## Additional Data

Portions Figure 1

## Requestor Location

Xiaojie Li  
Curtin University

## Requestor Location

Peth, other 6102  
Australia  
Attn: Xiaojie Li

## Tax Details

## \$ Price

Total 0.00 USD

Total: 0.00 USD

CLOSE WINDOW

ORDER MORE

Granted permission from ref [17] for the reprinted **Figure 1.2**. Copyright (2008) Springer Nature.

The screenshot shows the RightsLink interface for an article. At the top, there are logos for Copyright Clearance Center and RightsLink, along with navigation links for Home, Help, Email Support, and a user profile for Xiaojie Li. The main content area displays the article title, author list (Xiaojie Li, Huayang Zhang, Yazhi Liu, Xiaoguang Duan, Xinyuan Xu, Shaomin Liu, Hongqi Sun, Shaobin Wang), publication (Chemical Engineering Journal), publisher (Elsevier), and date (15 June 2020). Below this, there is a copyright notice: © 2020 Elsevier B.V. All rights reserved. A large text block provides a disclaimer: "Please note that, as the author of this Elsevier article, you retain the right to include it in a thesis or dissertation, provided it is not published commercially. Permission is not required, but please ensure that you reference the journal as the original source. For more information on this and on your other retained rights, please visit: <https://www.elsevier.com/about/our-business/policies/copyright#Author-rights>". At the bottom of this block are "BACK" and "CLOSE WINDOW" buttons. The footer contains copyright information and contact details for Copyright Clearance Center, Inc.

Granted permission from ref [45] for the reprinted **Figure 2.2**. Copyright (2020) Elsevier B.V.

The screenshot shows a journal article page. The article title is "Energy efficient synthesis of highly ordered mesoporous carbon nitrides with uniform rods and their superior CO<sub>2</sub> adsorption capacity†". The authors listed are Krijpal S. Lakhi, Dae-Hwan Park, Gurwinder Singh, Siddulu N. Talapaneni, Ugo Ravon, Khalid Al-Bahily, and Ajayan Vinu. The article is from the Journal of Materials Chemistry A, Issue 31, 2017. A "Check for updates" button is visible. On the right side, there is a "Cited by" tab, and a pop-up window displays the article title and citation information: "Energy efficient synthesis of highly ordered mesoporous carbon nitrides with uniform rods and their superior CO<sub>2</sub> adsorption capacity" by K. S. Lakhi, D. Park, G. Singh, S. N. Talapaneni, U. Ravon, K. Al-Bahily and A. Vinu, *J. Mater. Chem. A*, 2017, 5, 16220. DOI: 10.1039/C6TA10716H. The pop-up also mentions the article is licensed under a Creative Commons Attribution 3.0 Unported Licence.

Granted permission from ref [37] for the reprinted **Figure 2.3**.



### Fabrication and photocatalytic activity enhanced mechanism of direct Z-scheme g-C<sub>3</sub>N<sub>4</sub>/Ag<sub>2</sub>WO<sub>4</sub> photocatalyst

Author: Bicheng Zhu, Pengfei Xia, Yao Li, Wingkei Ho, Jiaguo Yu

Publication: Applied Surface Science

Publisher: Elsevier

Date: 1 January 2017

© 2016 Elsevier B.V. All rights reserved.

#### Order Completed

Thank you for your order.

This Agreement between Xiaojie Li ("You") and Elsevier ("Elsevier") consists of your license details and the terms and conditions provided by Elsevier and Copyright Clearance Center.

Your confirmation email will contain your order number for future reference.

License Number 4963430417634

[Printable Details](#)

License date Jul 07, 2020

#### Licensed Content

Licensed Content Publisher Elsevier  
 Licensed Content Publication Applied Surface Science  
 Licensed Content Title Fabrication and photocatalytic activity enhanced mechanism of direct Z-scheme g-C<sub>3</sub>N<sub>4</sub>/Ag<sub>2</sub>WO<sub>4</sub> photocatalyst  
 Licensed Content Author Bicheng Zhu, Pengfei Xia, Yao Li, Wingkei Ho, Jiaguo Yu  
 Licensed Content Date Jan 1, 2017  
 Licensed Content Volume 391  
 Licensed Content Issue n/a  
 Licensed Content Pages 9  
 Journal Type S&T

#### Order Details

Type of Use reuse in a thesis/dissertation  
 Portion figures/tables/illustrations  
 Number of figures/tables/illustrations 1  
 Format both print and electronic  
 Are you the author of this Elsevier article? No  
 Will you be translating? No

#### About Your Work

Title Photochemical and Thermal Energy Transformation for Hydrogen Generation  
 Institution name Curtin University  
 Expected presentation date Jul 2020

#### Additional Data

Portions Fig. 3

#### Requestor Location

Xiaojie Li  
 Curtin University  
 Requestor Location Perth, other 6102  
 Australia  
 Attn: Xiaojie Li

#### Tax Details

Publisher Tax ID GB 494 6272 12

#### Price

Total 0.00 AUD

Total: 0.00 AUD

[CLOSE WINDOW](#)

[ORDER MORE](#)

Granted permission from ref [46] for the reprinted **Figure 2.4**. Copyright (2016) Elsevier B.V.

Effect of processing temperature on structure and photocatalytic properties of g-C<sub>3</sub>N<sub>4</sub>

Author: I. Papailias, T. Giannakopoulou, N. Todorova, D. Demotikali, T. Vaimakis, C. Trapalis

Publication: Applied Surface Science

Publisher: Elsevier

Date: 15 December 2015

Copyright © 2015 Elsevier B.V. All rights reserved.

## Order Completed

Thank you for your order.

This Agreement between Xiaojie Li ("You") and Elsevier ("Elsevier") consists of your license details and the terms and conditions provided by Elsevier and Copyright Clearance Center.

Your confirmation email will contain your order number for future reference.

License Number 4863440252721

[Printable Details](#)

License date Jul 07, 2020

## Licensed Content

Licensed Content Publisher Elsevier  
 Licensed Content Publication Applied Surface Science  
 Licensed Content Title Effect of processing temperature on structure and photocatalytic properties of g-C<sub>3</sub>N<sub>4</sub>  
 Licensed Content Author I. Papailias, T. Giannakopoulou, N. Todorova, D. Demotikali, T. Vaimakis, C. Trapalis  
 Licensed Content Date Dec 15, 2015  
 Licensed Content Volume 358  
 Licensed Content Issue n/a  
 Licensed Content Pages 9  
 Journal Type S&T

## Order Details

Type of Use reuse in a thesis/dissertation  
 Portion figures/tables/illustrations  
 Number of figures/tables/illustrations 1  
 Format both print and electronic  
 Are you the author of this Elsevier article? No  
 Will you be translating? No

## About Your Work

Title Photochemical and Thermal Energy Transformation for Hydrogen Generation  
 Institution name Curtin University  
 Expected presentation date Jul 2020

## Additional Data

Portions Fig. 8

## Requestor Location

Xiaojie Li  
 Curtin University  
 Requestor Location Perth, other 6102  
 Australia  
 Attn: Xiaojie Li

## Tax Details

Publisher Tax ID GB 494 6272 12

## \$ Price

Total 0.00 AUD

Total: 0.00 AUD

[CLOSE WINDOW](#)[ORDER MORE](#)

Granted permission from ref [47] for the reprinted **Figure 2.5**. Copyright (2015) Elsevier B.V.

## Royal Society of Chemistry - License Terms and Conditions

This is a License Agreement between Xiaojie Li / Curtin University ("You") and Royal Society of Chemistry ("Publisher") provided by Copyright Clearance Center ("CCC"). The license consists of your order details, the terms and conditions provided by Royal Society of Chemistry, and the CCC terms and conditions.

All payments must be made in full to CCC.

Order Date	07-Jul-2020	Type of Use	Republish in a thesis/dissertation
Order license ID	1046614-1	Publisher	Royal Society of Chemistry
ISSN	2044-4761	Portion	Chart/graph/table/figure

### LICENSED CONTENT

Publication Title	Catalysis Science & Technology	Country	United Kingdom of Great Britain and Northern Ireland
Author/Editor	Royal Society of Chemistry (Great Britain)	Rightsholder	Royal Society of Chemistry
Date	01/01/2011	Publication Type	e-Journal
Language	English		

### REQUEST DETAILS

Portion Type	Chart/graph/table/figure	Distribution	Worldwide
Number of charts / graphs / tables / figures requested	1	Translation	Original language of publication
Format (select all that apply)	Print, Electronic	Copies for the disabled?	No
Who will republish the content?	Academic institution	Minor editing privileges?	No
Duration of Use	Life of current edition	Incidental promotional use?	No
Lifetime Unit Quantity	Up to 9,999	Currency	AUD
Rights Requested	Main product		

### NEW WORK DETAILS

Title	Photochemical and Thermal Energy Transformation for Hydrogen Generation	Institution name	Curtin University
Instructor name	Xiaojie Li	Expected presentation date	2020-07-15

### ADDITIONAL DETAILS

Order reference number	N/A	The requesting person / organization to appear on the license	Xiaojie Li / Curtin University
------------------------	-----	---	--------------------------------

### REUSE CONTENT DETAILS

Title, description or numeric reference of the portion(s)	Photochemical and Thermal Energy Transformation for Hydrogen Generation	Title of the article/chapter the portion is from	Cycloaddition of CO <sub>2</sub> and epoxide catalyzed by amino- and hydroxyl-rich graphitic carbon nitride
Editor of portion(s)	N/A	Author of portion(s)	Royal Society of Chemistry (Great Britain)
Volume of serial or monograph	N/A	Issue, if republishing an article from a serial	N/A
Page or page range of portion	13-80	Publication date of portion	2015-11-26

Granted permission from ref [48] for the reprinted **Figure 2.6**. Copyright (2015) Royal Society of Chemistry.



### Carbon vacancy-induced enhancement of the visible light-driven photocatalytic oxidation of NO over g-C<sub>3</sub>N<sub>4</sub> nanosheets

Author: Yuhan Li,Wingkei Ho,Kangle Lv,Bicheng Zhu,Shun Cheng Lee

Publication: Applied Surface Science

Publisher: Elsevier

Date: 1 February 2018

© 2017 Elsevier B.V. All rights reserved.

#### Order Completed

Thank you for your order.

This Agreement between Xiaojie Li ("You") and Elsevier ("Elsevier") consists of your license details and the terms and conditions provided by Elsevier and Copyright Clearance Center.

Your confirmation email will contain your order number for future reference.

License Number 4863441436403

[Printable Details](#)

License date Jul 07, 2020

#### Licensed Content

Licensed Content Publisher Elsevier

Licensed Content Publication Applied Surface Science

Licensed Content Title Carbon vacancy-induced enhancement of the visible light-driven photocatalytic oxidation of NO over g-C<sub>3</sub>N<sub>4</sub> nanosheets

Licensed Content Author Yuhan Li,Wingkei Ho,Kangle Lv,Bicheng Zhu,Shun Cheng Lee

Licensed Content Date Feb 1, 2018

Licensed Content Volume 430

Licensed Content Issue n/a

Licensed Content Pages 10

Journal Type S&T

#### Order Details

Type of Use reuse in a thesis/dissertation

Portion figures/tables/illustrations

Number of figures/tables/illustrations 1

Format both print and electronic

Are you the author of this Elsevier article? No

Will you be translating? No

#### About Your Work

Title Photochemical and Thermal Energy Transformation for Hydrogen Generation

Institution name Curtin University

Expected presentation date Jul 2020

#### Additional Data

Portions Fig. 6

#### Requestor Location

Xiaojie Li  
Curtin University

Requestor Location Peth, other 6102  
Australia  
Attn: Xiaojie Li

#### Tax Details

Publisher Tax ID GB 494 6272 12

#### \$ Price

Total 0.00 AUD

Total: 0.00 AUD

[CLOSE WINDOW](#)

[ORDER MORE](#)

Granted permission from ref [39] for the reprinted **Figure 2.7**. Copyright (2017) Elsevier B.V.



### First principle investigation of halogen-doped monolayer g-C<sub>3</sub>N<sub>4</sub> photocatalyst

Author: Bicheng Zhu, Jinfeng Zhang, Chuanjia Jiang, Bei Cheng, Jiaguo Yu

Publication: Applied Catalysis B: Environmental

Publisher: Elsevier

Date: 15 June 2017

© 2017 Elsevier B.V. All rights reserved.

#### Order Completed

Thank you for your order.

This Agreement between Xiaojie Li ("You") and Elsevier ("Elsevier") consists of your license details and the terms and conditions provided by Elsevier and Copyright Clearance Center.

Your confirmation email will contain your order number for future reference.

License Number 4863450532320

[Printable Details](#)

License date Jul 07, 2020

#### Licensed Content

Licensed Content Publisher Elsevier  
 Licensed Content Publication Applied Catalysis B: Environmental  
 Licensed Content Title First principle investigation of halogen-doped monolayer g-C<sub>3</sub>N<sub>4</sub> photocatalyst  
 Licensed Content Author Bicheng Zhu, Jinfeng Zhang, Chuanjia Jiang, Bei Cheng, Jiaguo Yu  
 Licensed Content Date Jun 15, 2017  
 Licensed Content Volume 207  
 Licensed Content Issue n/a  
 Licensed Content Pages 8  
 Journal Type S&T

#### Order Details

Type of Use reuse in a thesis/dissertation  
 Portion figures/tables/illustrations  
 Number of figures/tables/illustrations 2  
 Format both print and electronic  
 Are you the author of this Elsevier article? No  
 Will you be translating? No

#### About Your Work

Title Photochemical and Thermal Energy Transformation for Hydrogen Generation  
 Institution name Curtin University  
 Expected presentation date Jul 2020

#### Additional Data

Portions Fig. 1 and 3

#### Requestor Location

Xiaojie Li  
Curtin University

#### Tax Details

Publisher Tax ID GB 494 6272 12

#### Requestor Location

Peth, other 6102  
Australia  
Attn: Xiaojie Li

#### Price

Total 0.00 AUD

Total: 0.00 AUD

[CLOSE WINDOW](#)

[ORDER MORE](#)

Granted permission from ref [49] for the reprinted **Figure 2.8** and **2.9**.

Copyright (2017) Elsevier B.V.

The screenshot shows the RightsLink interface for a paper. At the top, there are navigation links: Home, Help, Email Support, and a user profile for Xiaojie Li. The main content area displays the paper's title, author (Yann Pellegrin, Fabrice Odobel), publication (Comptes Rendus Chimie), publisher (Elsevier), and date (March 2017). Below this, the Creative Commons Attribution-NonCommercial-No Derivatives License (CC BY NC ND) is detailed, explaining that the article is published under these terms and providing instructions for non-commercial use. There are 'BACK' and 'CLOSE WINDOW' buttons at the bottom of the license information. A footer contains copyright information for 2020 Copyright Clearance Center, Inc., along with links to privacy statements and terms and conditions.

Granted permission from ref [63] for the reprinted **Eq. 2.13**. Copyright (2016) Académie des sciences.

The screenshot shows the article page for 'Photocatalytic Hydrogen Production: Role of Sacrificial Reagents on the Activity of Oxide, Carbon, and Sulfide Catalysts' in the journal Catalysts. The page includes a sidebar with 'Submit to this Journal', 'Review for this Journal', and 'Edit a Special Issue' buttons. The article menu lists options like 'Abstract', 'Open Access and Permissions', 'Share and Cite', 'Article Metrics', 'Related Articles', and 'Order Article Reprints'. The main content area features the article title, authors (Vignesh Kumaravel, Muhammad Danyal Imam, Ahmed Badreldin, Rama Krishna Chava, Jeong Yeon Do, Misook Kang, and Ahmed Abdel-Wahab), and their affiliations. It also includes the article's DOI, publication date (18 March 2019), and buttons for 'View Full-Text', 'Download PDF', 'Browse Figures', and 'Cite This Paper'.

Granted permission from ref [62] for the reprinted **Figure 2.10** and **2.11**. Open access.

Single-Atom Pt as Co-Catalyst for Enhanced Photocatalytic H<sub>2</sub> Evolution

Author: Yi Xie, Changzheng Wu, Yi Luo, et al

Publication: Advanced Materials

Publisher: John Wiley and Sons

Date: Jan 29, 2016

© 2016 WILEY-VCH Verlag GmbH &amp; Co. KGaA, Weinheim

## Order Completed

Thank you for your order.

This Agreement between Xiaojie Li ("You") and John Wiley and Sons ("John Wiley and Sons") consists of your license details and the terms and conditions provided by John Wiley and Sons and Copyright Clearance Center.

Your confirmation email will contain your order number for future reference.

License Number 4863451406377

[Printable Details](#)

License date Jul 07, 2020

## Licensed Content

Licensed Content Publisher John Wiley and Sons

Licensed Content Publication Advanced Materials

Licensed Content Title Single-Atom Pt as Co-Catalyst for Enhanced Photocatalytic H<sub>2</sub> Evolution

Licensed Content Author Yi Xie, Changzheng Wu, Yi Luo, et al

Licensed Content Date Jan 29, 2016

Licensed Content Volume 28

Licensed Content Issue 12

Licensed Content Pages 5

## Order Details

Type of use Dissertation/Thesis

Requestor type University/Academic

Format Print and electronic

Portion Figure/table

Number of figures/tables 1

Will you be translating? No

## About Your Work

Title Photochemical and Thermal Energy Transformation for Hydrogen Generation

Institution name Curtin University

Expected presentation date Jul 2020

## Additional Data

Portions Figure 1

## Requestor Location

Xiaojie Li  
Curtin University

## Tax Details

Publisher Tax ID EU826007151

## Requestor Location

Peth, other 6102  
Australia  
Attn: Xiaojie Li

## \$ Price

Total 0.00 AUD

Would you like to purchase the full text of this article? If so, please continue on to the content ordering system located here: [Purchase PDF](#)  
If you click on the buttons below or close this window, you will not be able to return to the content ordering system.

Total: 0.00 AUD

[CLOSE WINDOW](#)[ORDER MORE](#)

Granted permission from ref [74] for the reprinted **Figure 2.13**. Copyright (2016) WILEY-VCH Verlag GmbH & Co. KGaA, Weinheim.



### Amorphous NiO as co-catalyst for enhanced visible-light-driven hydrogen generation over g-C<sub>3</sub>N<sub>4</sub> photocatalyst

Author: Jianni Liu, Qiaohui Jia, Jinlin Long, Xuxu Wang, Ziwei Gao, Quan Gu

Publication: Applied Catalysis B: Environmental

Publisher: Elsevier

Date: March 2018

© 2017 Elsevier B.V. All rights reserved.

#### Order Completed

Thank you for your order.

This Agreement between Xiaojie Li ("You") and Elsevier ("Elsevier") consists of your license details and the terms and conditions provided by Elsevier and Copyright Clearance Center.

Your confirmation email will contain your order number for future reference.

License Number 4863611134589 [Printable Details](#)

License date Jul 07, 2020

#### Licensed Content

Licensed Content Publisher Elsevier  
 Licensed Content Publication Applied Catalysis B: Environmental  
 Licensed Content Title Amorphous NiO as co-catalyst for enhanced visible-light-driven hydrogen generation over g-C<sub>3</sub>N<sub>4</sub> photocatalyst  
 Licensed Content Author Jianni Liu, Qiaohui Jia, Jinlin Long, Xuxu Wang, Ziwei Gao, Quan Gu  
 Licensed Content Date Mar 1, 2018  
 Licensed Content Volume 222  
 Licensed Content Issue n/a  
 Licensed Content Pages 9  
 Journal Type S&T

#### Order Details

Type of Use reuse in a thesis/dissertation  
 Portion figures/tables/illustrations  
 Number of figures/tables/illustrations 1  
 Format both print and electronic  
 Are you the author of this Elsevier article? No  
 Will you be translating? No

#### About Your Work

Title Photochemical and Thermal Energy Transformation for Hydrogen Generation  
 Institution name Curtin University  
 Expected presentation date Jul 2020

#### Additional Data

Portions Scheme 1

#### Requestor Location

Xiaojie Li  
 Curtin University

#### Tax Details

Publisher Tax ID GB 494 6272 12

#### Requestor Location

Peth, other 6102  
 Australia  
 Attn: Xiaojie Li

#### Price

Total 0.00 AUD

Total: 0.00 AUD

[CLOSE WINDOW](#)

[ORDER MORE](#)

Granted permission from ref [78] for the reprinted **Figure 2.14**. Copyright (2017) Elsevier B.V.



### In-situ phosphating to synthesize Ni<sub>2</sub>P decorated NiO/g-C<sub>3</sub>N<sub>4</sub> p-n junction for enhanced photocatalytic hydrogen production

**Author:** Jian-Wen Shi, Yajun Zou, Linhao Cheng, Dandan Ma, Diankun Sun, Siman Mao, Lvwei Sun, Chi He, Zeyan Wang  
**Publication:** Chemical Engineering Journal  
**Publisher:** Elsevier  
**Date:** 15 December 2019

© 2019 Elsevier B.V. All rights reserved.

#### Order Completed

Thank you for your order.

This Agreement between Xiaojie Li ("You") and Elsevier ("Elsevier") consists of your license details and the terms and conditions provided by Elsevier and Copyright Clearance Center.

Your confirmation email will contain your order number for future reference.

License Number 4863560948072 [Printable Details](#)

License date Jul 07, 2020

#### Licensed Content

**Licensed Content Publisher** Elsevier  
**Licensed Content Publication** Chemical Engineering Journal  
**Licensed Content Title** In-situ phosphating to synthesize Ni<sub>2</sub>P decorated NiO/g-C<sub>3</sub>N<sub>4</sub> p-n junction for enhanced photocatalytic hydrogen production  
**Licensed Content Author** Jian-Wen Shi, Yajun Zou, Linhao Cheng, Dandan Ma, Diankun Sun, Siman Mao, Lvwei Sun, Chi He, Zeyan Wang  
**Licensed Content Date** Dec 15, 2019  
**Licensed Content Volume** 378  
**Licensed Content Issue** n/a  
**Licensed Content Pages** 1  
**Journal Type** S&T

#### Order Details

**Type of Use** reuse in a thesis/dissertation  
**Portion** figures/tables/illustrations  
**Number of figures/tables/illustrations** 1  
**Format** both print and electronic  
**Are you the author of this Elsevier article?** No  
**Will you be translating?** No

#### About Your Work

**Title** Photochemical and Thermal Energy Transformation for Hydrogen Generation  
**Institution name** Curtin University  
**Expected presentation date** Jul 2020

#### Additional Data

**Portions** Scheme 1

#### Requester Location

Xiaojie Li  
Curtin University

#### Tax Details

**Publisher Tax ID** GB 494 6272 12

#### Requester Location

Peth, other 6102  
Australia  
Attn: Xiaojie Li

#### Price

**Total** 0.00 AUD

Total: 0.00 AUD

[CLOSE WINDOW](#)

[ORDER MORE](#)

Granted permission from ref [79] for the reprinted **Figure 2.15**. Copyright (2019) Elsevier B.V.

## Royal Society of Chemistry - License Terms and Conditions

This is a License Agreement between Xiaojie Li / Curtin University ("You") and Royal Society of Chemistry ("Publisher") provided by Copyright Clearance Center ("CCC"). The license consists of your order details, the terms and conditions provided by Royal Society of Chemistry, and the CCC terms and conditions.

All payments must be made in full to CCC.

Order Date	07-Jul-2020	Type of Use	Republish in a thesis/dissertation
Order license ID	1046708-1	Publisher	Royal Society of Chemistry
ISSN	2050-7496	Portion	Chart/graph/table/figure

### LICENSED CONTENT

Publication Title	Journal of materials chemistry. A, Materials for energy and sustainability	Country	United Kingdom of Great Britain and Northern Ireland
Author/Editor	Royal Society of Chemistry (Great Britain)	Rightsholder	Royal Society of Chemistry
Date	01/01/2013	Publication Type	e-Journal
Language	English	URL	http://pubs.rsc.org/en/journals/journaliss...

### REQUEST DETAILS

Portion Type	Chart/graph/table/figure	Distribution	Worldwide
Number of charts / graphs / tables / figures requested	1	Translation	Original language of publication
Format (select all that apply)	Print, Electronic	Copies for the disabled?	No
Who will republish the content?	Academic institution	Minor editing privileges?	No
Duration of Use	Life of current edition	Incidental promotional use?	No
Lifetime Unit Quantity	Up to 9,999	Currency	AUD
Rights Requested	Main product		

### NEW WORK DETAILS

Title	Photochemical and Thermal Energy Transformation for Hydrogen Generation	Institution name	Curtin University
Instructor name	Xiaojie Li	Expected presentation date	2020-07-15

### ADDITIONAL DETAILS

Order reference number	N/A	The requesting person / organization to appear on the license	Xiaojie Li / Curtin University
------------------------	-----	---	--------------------------------

### REUSE CONTENT DETAILS

Title, description or numeric reference of the portion(s)	Photochemical and Thermal Energy Transformation for Hydrogen Generation	Title of the article/chapter the portion is from	Ag <sub>2</sub> O modified g-C <sub>3</sub> N <sub>4</sub> for highly efficient photocatalytic hydrogen generation under visible light irradiation
Editor of portion(s)	N/A	Author of portion(s)	Royal Society of Chemistry (Great Britain)
Volume of serial or monograph	N/A	Issue, if republishing an article from a serial	N/A
Page or page range of portion	13-80	Publication date of portion	2015-06-22

Granted permission from ref [3] for the reprinted **Figure 2.16**. Copyright (2015) Royal Society of Chemistry.

Copyright Clearance Center RightsLink Home Help Email Support Xiaojie Li

**Metal-Free Photocatalyst for H<sub>2</sub> Evolution in Visible to Near-Infrared Region: Black Phosphorus/Graphitic Carbon Nitride**  
Author: Mingshan Zhu, Sooyeon Kim, Liang Mao, et al  
Publication: Journal of the American Chemical Society  
Publisher: American Chemical Society  
Date: Sep 1, 2017  
Copyright © 2017, American Chemical Society

**PERMISSION/LICENSE IS GRANTED FOR YOUR ORDER AT NO CHARGE**

This type of permission/license, instead of the standard Terms & Conditions, is sent to you because no fee is being charged for your order. Please note the following:

- Permission is granted for your request in both print and electronic formats, and translations.
- If figures and/or tables were requested, they may be adapted or used in part.
- Please print this page for your records and send a copy of it to your publisher/graduate school.
- Appropriate credit for the requested material should be given as follows: "Reprinted (adapted) with permission from (COMPLETE REFERENCE CITATION), Copyright (YEAR) American Chemical Society." Insert appropriate information in place of the capitalized words.
- One-time permission is granted only for the use specified in your request. No additional uses are granted (such as derivative works or other editions). For any other uses, please submit a new request.

If credit is given to another source for the material you requested, permission must be obtained from that source.

BACK CLOSE WINDOW

© 2020 Copyright - All Rights Reserved | Copyright Clearance Center, Inc. | Privacy statement | Terms and Conditions  
Comments? We would like to hear from you. E-mail us at [customercare@copyright.com](mailto:customercare@copyright.com)

Granted permission from ref [100] for the reprinted **Figure 2.17**.  
Copyright (2017) American Chemical Society.



### Exfoliated Graphitic Carbon Nitride Nanosheets as Efficient Catalysts for Hydrogen Evolution Under Visible Light

Author: Shubin Yang, Yongji Gong, Jinshui Zhang, et al

Publication: Advanced Materials

Publisher: John Wiley and Sons

Date: Mar 1, 2013

Copyright © 2013 WILEY-VCH Verlag GmbH & Co. KGaA, Weinheim

#### Order Completed

Thank you for your order.

This Agreement between Xiaojie Li ("You") and John Wiley and Sons ("John Wiley and Sons") consists of your license details and the terms and conditions provided by John Wiley and Sons and Copyright Clearance Center.

Your confirmation email will contain your order number for future reference.

License Number 4863601080772

[Printable Details](#)

License date Jul 07, 2020

#### Licensed Content

Licensed Content Publisher John Wiley and Sons  
 Licensed Content Publication Advanced Materials  
 Licensed Content Title Exfoliated Graphitic Carbon Nitride Nanosheets as Efficient Catalysts for Hydrogen Evolution Under Visible Light  
 Licensed Content Author Shubin Yang, Yongji Gong, Jinshui Zhang, et al  
 Licensed Content Date Mar 1, 2013  
 Licensed Content Volume 25  
 Licensed Content Issue 17  
 Licensed Content Pages 5

#### Order Details

Type of use Dissertation/Thesis  
 Requestor type University/Academic  
 Format Print and electronic  
 Portion Figure/table  
 Number of figures/tables 1  
 Will you be translating? No

#### About Your Work

Title Photochemical and Thermal Energy Transformation for Hydrogen Generation  
 Institution name Curtin University  
 Expected presentation date Jul 2020

#### Additional Data

Portions Figure S1

#### Requestor Location

Xiaojie Li  
 Curtin University

#### Tax Details

Publisher Tax ID EU826007151

#### Requestor Location

Peth, other 6102  
 Australia  
 Attn: Xiaojie Li

#### Price

Total 0.00 AUD

Would you like to purchase the full text of this article? If so, please continue on to the content ordering system located here: [Purchase PDF](#)  
 If you click on the buttons below or close this window, you will not be able to return to the content ordering system.

Total: 0.00 AUD

[CLOSE WINDOW](#)

[ORDER MORE](#)

Granted permission from ref [102] for the reprinted **Figure 2.18**.

Copyright (2013) WILEY-VCH Verlag GmbH & Co. KGaA, Weinheim.


**In-situ construction of coral-like porous P-doped g-C<sub>3</sub>N<sub>4</sub> tubes with hybrid 1D/2D architecture and high efficient photocatalytic hydrogen evolution**

Author: Mao Wu, Jin Zhang, Bei-bei He, Huan-wen Wang, Rui Wang, Yan-sheng Gong

Publication: Applied Catalysis B: Environmental

Publisher: Elsevier

Date: February 2019

© 2018 Elsevier B.V. All rights reserved.

**Order Completed**

Thank you for your order.

This Agreement between Xiaojie Li ("You") and Elsevier ("Elsevier") consists of your license details and the terms and conditions provided by Elsevier and Copyright Clearance Center.

Your confirmation email will contain your order number for future reference.

 License Number: 4863460681663 [Printable Details](#)

License date: Jul 07, 2020

**Licensed Content**

Licensed Content Publisher	Elsevier
Licensed Content Publication	Applied Catalysis B: Environmental
Licensed Content Title	In-situ construction of coral-like porous P-doped g-C <sub>3</sub> N <sub>4</sub> tubes with hybrid 1D/2D architecture and high efficient photocatalytic hydrogen evolution
Licensed Content Author	Mao Wu, Jin Zhang, Bei-bei He, Huan-wen Wang, Rui Wang, Yan-sheng Gong
Licensed Content Date	Feb 1, 2019
Licensed Content Volume	241
Licensed Content Issue	n/a
Licensed Content Pages	8
Journal Type	S&T

**Order Details**

Type of Use	reuse in a thesis/dissertation
Portion	figures/tables/illustrations
Number of figures/tables/illustrations	1
Format	both print and electronic
Are you the author of this Elsevier article?	No
Will you be translating?	No

**About Your Work**

Title	Photochemical and Thermal Energy Transformation for Hydrogen Generation
Institution name	Curtin University
Expected presentation date	Jul 2020

**Additional Data**

Portions	Scheme 1
----------	----------

**Requestor Location**

Requestor Location	Xiaojie Li Curtin University
Requestor Location	Peth, other 6102 Australia Attrn: Xiaojie Li

**Tax Details**

Publisher Tax ID	GB 494 6272 12
------------------	----------------

**Price**

Total	0.00 AUD
-------	----------

**Total: 0.00 AUD**
[CLOSE WINDOW](#)
[ORDER MORE](#)

 Granted permission from ref [115] for the reprinted **Figure 2.19**.

Copyright (2018) Elsevier B.V.



### Enhanced photocatalytic hydrogen evolution along with byproducts suppressing over Z-scheme Cd x Zn1-x S/Au/g-C3N4 photocatalysts under visible light

Author: He Zhao,Xiaoling Ding,Bing Zhang,Yingxuan Li,Chuanyi Wang

Publication: Science Bulletin

Publisher: Elsevier

Date: 15 May 2017

© 2017 Science China Press. Published by Elsevier B.V. and Science China Press. All rights reserved.

#### Order Completed

Thank you for your order.

This Agreement between Xiaojie Li ("You") and Elsevier ("Elsevier") consists of your license details and the terms and conditions provided by Elsevier and Copyright Clearance Center.

Your confirmation email will contain your order number for future reference.

License Number 4863461107275 [Printable Details](#)

License date Jul 07, 2020

#### Licensed Content

**Licensed Content Publisher** Elsevier  
**Licensed Content Publication** Science Bulletin  
**Licensed Content Title** Enhanced photocatalytic hydrogen evolution along with byproducts suppressing over Z-scheme Cd x Zn1-x S/Au/g-C3N4 photocatalysts under visible light  
**Licensed Content Author** He Zhao,Xiaoling Ding,Bing Zhang,Yingxuan Li,Chuanyi Wang  
**Licensed Content Date** May 15, 2017  
**Licensed Content Volume** 62  
**Licensed Content Issue** 9  
**Licensed Content Pages** 8  
**Journal Type** S&T

#### Order Details

**Type of Use** reuse in a thesis/dissertation  
**Portion** figures/tables/illustrations  
**Number of figures/tables/illustrations** 1  
**Format** both print and electronic  
**Are you the author of this Elsevier article?** No  
**Will you be translating?** No

#### About Your Work

**Title** Photochemical and Thermal Energy Transformation for Hydrogen Generation  
**Institution name** Curtin University  
**Expected presentation date** Jul 2020

#### Additional Data

**Portions** Figure 6

#### Requestor Location

Xiaojie Li  
Curtin University

#### Tax Details

**Publisher Tax ID** GB 494 6272 12

#### Requestor Location

Peth, other 6102  
Australia  
Attn: Xiaojie Li

#### \$ Price

**Total** 0.00 AUD

**Total: 0.00 AUD**

[CLOSE WINDOW](#)

[ORDER MORE](#)

Granted permission from ref [150] for the reprinted **Figure 2.22.**

Copyright (2017) Science China Press.

Copyright Clearance Center RightsLink

Home Help Email Support Xiaoje Li

**Synergy of NiO quantum dots and temperature on enhanced photocatalytic and thermophoto hydrogen evolution**

**Author:** Xiaoje Li, Huayang Zhang, Yazhi Liu, Xiaoguang Duan, Xinyuan Xu, Shaomin Liu, Hongqi Sun, Shaobin Wang

**Publication:** Chemical Engineering Journal

**Publisher:** Elsevier

**Date:** 15 June 2020

© 2020 Elsevier B.V. All rights reserved.

Please note that, as the author of this Elsevier article, you retain the right to include it in a thesis or dissertation, provided it is not published commercially. Permission is not required, but please ensure that you reference the journal as the original source. For more information on this and on your other retained rights, please visit: <https://www.elsevier.com/about/our-business/policies/copyright#Author-rights>

BACK CLOSE WINDOW

© 2020 Copyright - All Rights Reserved | Copyright Clearance Center, Inc. | Privacy statement | Terms and Conditions  
Comments? We would like to hear from you. E-mail us at [customercare@copyright.com](mailto:customercare@copyright.com)

Granted permission for the reprinted **Chapter 4**. Copyright (2020) Elsevier B.V.

**Table Appendix II-1.** Granted permissions for reprinted figures.

Order Date	Article Title	Publication	Type of Use	Order Status	License Number
07-Jul-2020	Heterogeneous photocatalyst materials for water splitting	Chemical Society Reviews	Thesis/Dissertation	Granted	1046653-1
07-Jul-2020	A metal-free polymeric photocatalyst for hydrogen production from water under visible light	Nature Materials	Thesis/Dissertation	Completed	4863481246497
07-Jul-2020	Fabrication and photocatalytic activity enhanced mechanism of direct Z-scheme g-C <sub>3</sub> N <sub>4</sub> /Ag <sub>2</sub> WO <sub>4</sub> photocatalyst	Applied Surface Science	Thesis/Dissertation	Completed	4863430417634

07-Jul-2020	Effect of processing temperature on structure and photocatalytic properties of g-C <sub>3</sub> N <sub>4</sub>	Applied Surface Science	Thesis/Dissertation	Completed	486344025 2721
07-Jul-2020	Cycloaddition of CO <sub>2</sub> and epoxide catalyzed by amino- and hydroxyl-rich graphitic carbon nitride	Catalysis Science & Technology	Thesis/Dissertation	Granted	1046614-1
07-Jul-2020	Carbon vacancy-induced enhancement of the visible light-driven photocatalytic oxidation of NO over g-C <sub>3</sub> N <sub>4</sub> nanosheets	Applied Surface Science	Thesis/Dissertation	Completed	486344143 6403
07-Jul-2020	First principle investigation of halogen-doped monolayer g-C <sub>3</sub> N <sub>4</sub> photocatalyst	Applied Catalysis B: Environmental	Thesis/Dissertation	Completed	486345053 2320
07-Jul-2020	Single-Atom Pt as Co-Catalyst for Enhanced Photocatalytic H <sub>2</sub> Evolution	Advanced Materials	Thesis/Dissertation	Completed	486345140 6377
07-Jul-2020	Amorphous NiO as co-catalyst for enhanced visible-light-driven hydrogen generation over g-C <sub>3</sub> N <sub>4</sub> photocatalyst	Applied Catalysis B: Environmental	Thesis/Dissertation	Completed	486361113 4589
07-Jul-2020	In-situ phosphating to synthesize Ni <sub>2</sub> P decorated NiO/g-C <sub>3</sub> N <sub>4</sub> p-n junction for enhanced photocatalytic hydrogen production	Chemical Engineering Journal	Thesis/Dissertation	Completed	486356094 8072

---

07-Jul- 2020	Ag <sub>2</sub> O modified g-C <sub>3</sub> N <sub>4</sub> for highly efficient photocatalytic hydrogen generation under visible light irradiation	Journal of materials chemistry. A, Materials for energy and sustainability	Thesis/Dis sertation	Granted	1046708-1
07-Jul- 2020	Exfoliated graphitic carbon nitride nanosheets as efficient catalysts for hydrogen evolution under visible light	Advanced Materials	Thesis/Dis sertation	Completed	486360108 0772
07-Jul- 2020	In-situ construction of coral-like porous P-doped g-C <sub>3</sub> N <sub>4</sub> tubes with hybrid 1D/2D architecture and high efficient photocatalytic hydrogen evolution	Applied Catalysis B: Environmental	Thesis/Dis sertation	Completed	486346068 1663
07-Jul- 2020	Enhanced photocatalytic hydrogen evolution along with byproducts suppressing over Z-scheme Cd <sub>x</sub> Zn <sub>1-x</sub> S/Au/g-C <sub>3</sub> N <sub>4</sub> photocatalysts under visible light	Science Bulletin	Thesis/Dis sertation	Completed	486346110 7275

---